

Mineral Scale Prediction Modelling:

**Precipitation of CaCO₃ Scale in CO₂-Water Alternating Gas
Production Systems**

Duarte Jorge Alves de Carvalho e Silva

Submitted for the degree of Doctor of Philosophy

Heriot-Watt University

School of Energy, Geoscience, Infrastructure and Society

September 2017

The copyright in this thesis is owned by the author. Any quotation from the thesis or use of any of the information contained in it must acknowledge this thesis as the source of the quotation or information.

Abstract

The injection of CO₂ in oil reservoirs for tertiary oil recovery is one of the main Enhanced Oil Recovery (EOR) processes and it is widely used in the oil and gas industry. To prevent early gas breakthrough, CO₂ is commonly injected in alternated slugs with water, in a process known as CO₂ Water Alternating Gas (CO₂ WAG). When such processes are carried out in carbonate reservoirs, there is the potential for calcite (CaCO₃) dissolution in the reservoir and its subsequent re-precipitation in production systems, thus posing a flow assurance risk that must be carefully managed.

A new thermodynamic model that addresses all of the major steps involved in the precipitation of CaCO₃ scale in CO₂ WAG production systems is proposed, including: i) the dissolution of injected CO₂ into the reservoir brine; ii) the rock-brine interactions and the dissolution of CaCO₃ rock; iii) the reactive flow and transport of aqueous components in the reservoir; iv) the partition of components between the liquid, vapour, and water phases; and v) the precipitation of CaCO₃ scale as a function of decreasing pressure (and temperature) in CO₂ WAG production systems (i.e. in the well and in topside equipment). Thus, an aqueous electrolyte model has been implemented and coupled with a Vapour-Liquid Equilibrium (VLE) model, a multiphase flash model, and a reactive transport model. The non-ideal behaviour of the aqueous and hydrocarbon phases (vapour and liquid) has been modelled by using respectively the Pitzer equations and an Equation of State (EOS) (Soave-Redlich-Kwong, SRK, and Peng-Robinson, PR, EOS, have been used, among others). The implementation of these models has been validated by comparing results with experimental data and/or with results obtained by using industry standard software.

In addition, the impact of VLE, multiphase flash, and reactive transport calculations on the precipitation of CaCO₃ scale has been investigated, by considering commonly available production data. Also, a procedure had been devised to address each step involved in the precipitation of CaCO₃ scale in CO₂ WAG production wells individually, and together in an integrated approach. In fact, this work focuses on building the boundaries for the CaCO₃ scaling system, thus allowing to define, and work on, worst case scenarios. This gives the required information – both qualitatively and quantitatively – to manage CaCO₃ scale in CO₂ WAG production wells.

To my parents, Ana and Joaquim.

Acknowledgements

I would like to express my sincere gratitude to my supervisor and mentor Professor Ken Sorbie. Leonardo da Vinci said that “poor is the pupil who does not surpass his master”, and, indeed, I am now poorer than the day I started my PhD. But I am also richer, as I drank every drop of knowledge and – every time I could handle – wisdom from him. The time spent with Professor Sorbie was of immeasurable value – a treasure I take humbly from my years in Edinburgh. For this, above all else, I am grateful. I would also like to extent my gratitude to my second supervisor Professor Eric Mackay. More than the much appreciated insights for my PhD project, Professor Mackay has been an inspiration to me for his noble conduct. Eric always gave me a hand when things were going well, and two hands when life dictated that things were to go less well.

In addition, I would like to sincerely thank Galp Energia for their financial support through my scholarship. I would also like to thank FAST JIP sponsors for their valuable input on my project, and CMG Ltd for supplying the WinProp license used in this work.

My life in Edinburgh would not have been the same without my friends Luis, Wissem, Bouja, Mohamed, and Alfonso. I thank them for all the happy moments we shared together, and I look forward to sharing many more of these in the future. Further, I would like to thank all my colleges in the FAST group, students and staff, for creating such an enjoyable working environment, and for always making me feel welcomed in Scotland. It has been a pleasure, and indeed a privilege, to have spent these years alongside such bright minds, and, most importantly, alongside friends.

My deepest thank you goes to Ilaria, my companion in this great adventure called life, who made the dark nights of my PhD – “black as the pit from pole to pole”, and which are inherent to all great endeavours –, look like a sunny day in Edinburgh. Her love and support are in every single word of this manuscript.

Finally, my parents Ana and Joaquim need no words of acknowledgment, my gratitude goes beyond words, and they know.

Research Thesis Submission

Name:	Duarte Jorge Alves de Carvalho e Silva		
School:	School of Energy, Geoscience, Infrastructure and Society		
Version: (i.e. First, Resubmission, Final)		Degree Sought:	PhD, Petroleum Engineering

Declaration

In accordance with the appropriate regulations I hereby submit my thesis and I declare that:

- 1) the thesis embodies the results of my own work and has been composed by myself
- 2) where appropriate, I have made acknowledgement of the work of others and have made reference to work carried out in collaboration with other persons
- 3) the thesis is the correct version of the thesis for submission and is the same version as any electronic versions submitted*.
- 4) my thesis for the award referred to, deposited in the Heriot-Watt University Library, should be made available for loan or photocopying and be available via the Institutional Repository, subject to such conditions as the Librarian may require
- 5) I understand that as a student of the University I am required to abide by the Regulations of the University and to conform to its discipline.
- 6) I confirm that the thesis has been verified against plagiarism via an approved plagiarism detection application e.g. Turnitin.

* Please note that it is the responsibility of the candidate to ensure that the correct version of the thesis is submitted.

Signature of Candidate:		Date:
-------------------------	--	-------

Submission

Submitted By (name in capitals):	
Signature of Individual Submitting:	
Date Submitted:	

For Completion in the Student Service Centre (SSC)

Received in the SSC by (name in capitals):		
1.Method of Submission (Handed in to SSC; posted through internal/external mail):		
2.E-thesis Submitted (mandatory for final theses)		
Signature:		Date:

Contents

1. Introduction	9
1.1 Background in oilfield scale	9
1.2 CaCO ₃ scale in CO ₂ Water Alternating Gas	12
1.3 Objectives and outline of the dissertation	14
2. Literature review.....	16
2.1 Aqueous electrolyte systems	16
2.2 Vapour-liquid equilibrium.....	18
2.3 Multiphase flash calculations	20
2.4 Reactive transport.....	23
3. Aqueous electrolyte model.....	24
3.1 Thermodynamic model.....	25
3.1.1 Equilibrium constants	25
3.1.2 System of equations for scale prediction calculations	26
3.1.3 Pitzer electrolyte model.....	33
3.2 Results and discussion	38
3.2.1 Pitzer electrolyte model.....	38
3.2.2 General scale prediction calculations	42
3.2.3 Solubility of CaCO ₃ scale	43
3.2.4 Co-precipitation of CaCO ₃ with FeCO ₃ and FeS	49
3.2.5 Mixing of two chemically incompatible waters.....	54
3.3 Conclusions and recommendations	57
4. Vapour-Liquid Equilibrium.....	59
4.1 Thermodynamic models	60
4.1.1 γ – φ approach	60
4.1.2 φ – φ approach	61
4.1.3 Equations of State (EOS) and fugacity coefficients.....	63
4.1.4 Søreide and Whitson solubility model	67
4.1.5 Duan et al. CO ₂ solubility model	68
4.2 Results and discussion	71
4.2.1 Solubility of CO ₂ in water and brine	71

4.2.2	Solubility of CO ₂ , H ₂ S, and CH ₄ gas mixtures in water	79
4.2.3	Impact of VLE calculations on scale prediction modelling	81
4.2.4	CaCO ₃ scale formation due to de-pressurisation	83
4.3	Conclusions and recommendations	85
5.	Multiphase flash calculations	88
5.1	Petroleum reservoir fluids	89
5.2	Calculation of reservoir fluids composition from surface samples	92
5.2.1	Re-conciliation of separator outlet streams and the principle of mass conservation.....	92
5.2.2	Oil-Gas-Water (OGW) flash	95
5.2.3	Coupling OGW with scale predictions: equilibration of fluids with reservoir rock	97
5.3	Calculation of scale precipitation profiles in production systems.....	98
5.3.1	Coupling OGW with scale predictions: precipitation of scale in the production system.....	98
5.4	Calculation of scaling profiles in the production system that agree with the water chemistry measured at surface sampling points	100
5.5	Results and discussion	102
5.5.1	Oil-Gas-Water (OGW) flash	102
5.5.2	Calculation of reservoir fluid compositions from surface samples.....	103
5.5.3	Calculation of scale precipitation profiles in production systems	106
5.5.4	Example of a calculation in a CO ₂ and H ₂ S-rich environment	113
5.5.5	Field case example	117
5.5.6	Calculation of scaling profiles in the production system that agree with the water chemistry measured at surface sampling points	122
5.6	Conclusions and recommendations	128
6.	Reactive transport	130
6.1	1D reactive transport model	131
6.2	Studying the effect of kinetics in the reactive transport model	131
6.3	Reactive transport coupled with scale predictions in production systems	134
6.4	Results and discussion	135
6.4.1	Model validation with laboratory data	135
6.4.2	CaCO ₃ scale in CO ₂ -WAG.....	139
6.4.3	Study of the effect of kinetics on CaCO ₃ scale in CO ₂ -WAG	147

6.4.4	Siderite (FeCO_3) scavenging H_2S in the reservoir	150
6.5	Conclusions and recommendations	156
7.	Conclusions and recommendations	158
8.	Bibliography	161
9.	Appendix	173

List of publications

Silva, D. J., Sorbie, K. S., Mackay, E. J., *Coupling Reactive Transport, Vapour-Liquid Equilibrium, and Scale Prediction Calculations to Model the Precipitation of CaCO₃ in CO₂ Water Alternating Gas Production Wells*, (in preparation).

Silva, D. J., Sorbie, K. S., Mackay, E. J., *Carbonate and Sulphide Scale Prediction Modelling: Coupling of Oil-Gas-Water Flash Algorithm with Scale Prediction Calculations*, (in preparation).

Silva, D. J., Sorbie, K. S., Mackay, E. J., *Modelling CaCO₃ Scale in CO₂ Water Alternating Gas CO₂-WAG Processes*, SPE International Oilfield Scale Conference and Exhibition (Paper #SPE-179893-MS), Aberdeen, Scotland, UK (2016).

Silva, D. J., Sorbie, K. S., Mackay, E. J., *Thermodynamic Model Development Relevant to Calcium Carbonate Scale Mitigation in CO₂ Water Alternating Gas Schemes*, Rio Oil & Gas Expo and Conference (Paper #IBP 1927_14), Rio de Janeiro, Brazil (2014).

Ribeiro, A. S., Silva, D. J., E. J. Mackay, Sorbie, K. S., *The impact of Vapour/Liquid-Equilibria Calculations on Scale-Prediction Modelling*, SPE Production & Operations, 32 (2017).

Ribeiro, A. S., Silva, D. J., E. J. Mackay, Sorbie, K. S., *The impact of Vapour-Liquid Equilibria VLE Calculations on Scale Prediction Modelling*, SPE International Oilfield Scale Conference and Exhibition (Paper #SPE-179885-MS), Aberdeen, Scotland, UK (2016).

Verri, G., Sorbie, K. S., Silva, D. J., *A rigorous general workflow for accurate prediction of carbonate and sulphide scaling profiles in oil and gas wells*, Journal of Petroleum Science and Engineering, 156, 679-681 (2017).

Verri, G., Sorbie, K. S., Singleton, M. A., Silva, D. J., Hinrichsen, C., Wang, Q., Chang, F. F., *A New Approach to Combined Sulphide and Carbonate Scale Predictions Applied to Different Field Scenarios*, SPE International Conference on Oilfield Chemistry, Texas, US (2017).

Notation

Capital letters

A	Area
AARD	Average of the Absolute of the Relative Error
AQ	Aqueous
ARD	Absolute of the Relative Error
A_ϕ	Debye-Hückel parameter in the Pitzer model
BIP	Binary Interaction Parameter
CMG	Computer Modelling Group
CPA EOS	Cubic-Plus-Association Equation of State
D	Dielectric constant
Da	Damköhler number
D_i	Dispersion coefficient of component i
EOS	Equation of State
ESD EOS	Elliott-Suresh-Donohue Equation of State
F	Feed
FAST	Flow Assurance and Scale Team
G	Gibbs Energy
GC	Gas chromatography
G^{Em}	Total excess Gibbs energy in molality
$H_{i,j}$	Henry's constant for solute i in solvent j
HW FAST	Heriot-Watt Flow Assurance and Scale Team
I	Ionic strength
ICP-EOS	Inductively Coupled Plasma–Optical Emission Spectrometry
K	Stoichiometric equilibrium constant
K^0	Thermodynamic equilibrium constant
K_{im}	Partition coefficient of component i in phase m
K_{sp}	Stoichiometric solubility product
K_{sp}^0	Thermodynamic solubility product
L	Liquid
M	Molarity (mol/L)

MM	Molecular Mass
NA	Non-Aqueous
NR	Newton-Raphson
OGW	Oil-Gas-Water
P (and p)	Pressure (in bar)
P_c	Critical pressure
PR EOS	Peng-Robinson Equation of State
PRSV EOS	Peng-Robinson Equation of State modified by Stryjek-Vera
PT EOS	Patel-Teja Equation of State
PV	Pore Volume
PVT	Pressure-Volume-Temperature
Q_v	Volumetric flowrate
R_i	Reaction rate of component i
RK EOS	Reddlich-Kwong Equation of State
SAFT	Statistical Association Fluid Theory
SR	Saturation Ratio
SRK EOS	Reddlich-Kwong Equation of State modified by Soave
SSW	Synthetic Seawater
T	Temperature (in K)
TBP	True Boiling Point
TBT	Tube Blocking Test
T_c	Critical temperature
T_r	Reduced temperature
UNIQUAC	Activity model (short for UNIversal QUAsiChemical)
V	Volume
VLE	Vapour-Liquid Equilibrium
VPT EOS	Patel-Teja Equation of State modified by Valderrama
WAG	Water Alternating Gas
Z	Compressibility factor

Lower case letters

a_{H_2O}	Activity of component water
a_i	Activity of component i
c_i	Concentration of component i
d_w	Density of the solvent
f_i	Fugacity of component i
f_i^0	Standard state fugacity of component i
k_{ij}	Binary interaction coefficient between components i and j
k_1	Forward rate constant
k_2	Reverse rate constant
m_i	Molality of component i
n_i	Number of moles of component i
v_i	Velocity of component i
v_i^∞	Partial molar volume of component i at infinite dilution
x_i	Aqueous molar fraction of component i
y_i	Gaseous molar fraction of component i
z	Charge of ions

Greek characters

γ	Activity coefficient
γ_i	Activity coefficient of component i
θ_{ij}	Parameter in the Pitzer model
${}^E\theta_{ij}$	Parameter in the Pitzer model
λ_{ij}	Second virial coefficient in the equation for the total excess Gibbs energy
μ	Chemical potential
μ_i	Chemical potential of component i
μ_i^0	Standard chemical potential of component i
μ_{ijk}	Third virial coefficient in the equation for the total excess Gibbs energy
ξ_{Nca}	Ternary parameter in the Pitzer model
ρ	Density

- v_i Stoichiometric coefficient of component i ; number of ions per molecule of electrolyte [Equation (3.45)]
- ϕ Osmotic coefficient [Equations (3.50) and (3.51)]; fugacity coefficient; porosity [Equation (6.14)]
- φ Fugacity coefficient
- Ω Saturation ratio
-

Universal constants

- e Electronic charge (1.602×10^{-19} C)
- k Boltzman constant (1.381×10^{-23} J K $^{-1}$)
- R Ideal gas constant (8.314462×10^{-5} m 3 bar K $^{-1}$ mol $^{-1}$)
- N_0 Avogadro number (6.022×10^{23} mol $^{-1}$)
- ε_0 Permittivity of vacuum (8.85419×10^{-12} C 2 N $^{-1}$ m $^{-2}$)
-

1. Introduction

1.1 Background in oilfield scale

Oilfield scales are mineral compounds that result from precipitation reactions in supersaturated aqueous solutions and that pose a potential flow assurance risk to oil and gas production. The formation of oilfield scales is dependent on temperature, pressure, pH, aqueous chemical composition, etc. Barium sulphate, BaSO_4 , and calcium carbonate, CaCO_3 , are two examples of common oilfield scales.

There are two principal scenarios for scale formation in oilfield operations: *mixing of two chemically incompatible waters* and “*autoscaling*”. Scale can form when two waters with different chemical compositions are brought together. For example, BaSO_4 can form when seawater, which is rich in sulphate ions, SO_4^{2-} , is mixed with a formation water rich in barium ions, Ba^{2+} . Or, scale can form when seawater is mixed with produced water for Produced Water Re-Injection (PWRI). Other common examples of scale formation due to mixing of two chemically incompatible waters can be found in Mackay, 2003. On the other hand, “*autoscaling*” occurs for a single source brine when scale forms due to changes in conditions, such as a change in temperature, pressure, salinity, pH, etc., which inevitably occurs in oilfield operations. For example, CaCO_3 scale can form in production systems due to a decrease in pressure, as will be discussed below.

The formation of scale does not always pose an issue to flow assurance. For example, scale formation deep in the reservoir is not considered a flow assurance problem, indeed this actually helps to reduce the scaling problem at the producer well. However, scale formation in the near-wellbore matrix, in injection or production wells, or in surface equipment can pose a serious flow assurance issue, and it must be carefully addressed. There are two principal approaches to tackle scale-related issues: removal of scale should scale occur, and/or prevention of scale formation.

Scale removal techniques may be classified into mechanical and chemical techniques. Mechanical techniques use, for example, mill and hammer tools to remove scale from wellbore tubulars. However, these techniques are obviously not applicable to treat scale in the formation matrix. On the other hand, chemical techniques are used to dissolve

scale – for example, a strong acid such as hydrochloric acid (HCl) can be used to dissolve CaCO_3 scale –, or to chelate scaling ions by using a chelating agent such as ethylene diamine tetraacetic acid (EDTA) and its derivatives. Chemical techniques can be used to treat scale in the formation matrix, and, in this case, the treatment is commonly referred to as a *stimulation* treatment.

Preventing scale formation can be accomplished by predicting and preventing the occurrence of supersaturated solutions. For example, desulphation or removal of hardness from injection waters can render injection and formation waters chemically compatible, i.e. scale *does not* form upon mixing of waters, and thus prevent scale from occurring. In some cases, the desulphated brine system may still produce some mineral scale but in lesser quantities and at lower saturation ratios (SR; see below). In addition, scale prevention can be achieved by using *scale inhibitors* in supersaturated solutions.

Scale inhibitors (SI) are molecules that inhibit the nucleation and crystal growth stages of scale formation by adhering to the surface of the scale crystals and stereo-chemically hindering further growth of the crystals. SIs can be classified into two main groups: phosphonate and polymer-based types. Phosphonate-based SIs have generally a better scale inhibition efficiency, and are more easily detected experimentally than polymer-based SIs. However, there has been an effort in the oil and gas industry to replace phosphonate-based SIs by polymer-based SIs due to environmental constraints. Also, polymer SIs are being produced which can function just as well as or better than phosphonates for certain scaling problems.

SIs are usually deployed either by *continuous injection* or in near well downhole *squeeze treatments*. In continuous injection, SIs are injected continuously into the wellbore or into a topside system. However, this solution does not “protect” the well or production system upstream of the injection point. Alternatively, SIs can be injected into the near-well reservoir formation in a squeeze treatment. In a squeeze treatment, production is stopped and a solution containing a SI (or a *blend* of SIs) is injected into the formation. An overflush is then usually applied to push the SI fluid slug into the reservoir formation away from the well. Then, there is a soaking period – typically between 6 to 24 hours – to allow SIs to adsorb and/or precipitate into the formation rock, after which production is resumed. SIs are then slowly “released” from the formation rock into the brine, and

the objective of the treatment is to maintain the concentration of the SI in the brine above a previously determined threshold level (the Minimum Inhibitor Concentration [MIC], which is determined experimentally) for a certain period of time. The duration of the squeeze treatment (the “squeeze lifetime”) varies between a couple of weeks to typically one or two years, depending on the system. This way, the well is protected against scale formation during the lifetime of the squeeze treatment. The squeeze lifetime is more often measured against how much water can be produced from the well in which the concentration of the SI, $[SI]$, is $>$ MIC. If the $[SI] >$ MIC, then the well is seen as being “protected” and when it drops below this value ($[SI] <$ MIC), then the well should be re-treated with SI.

The selection of SIs follows several steps, including compatibility tests, thermal stability tests, static and dynamic inhibition efficiency tests, and core flood tests. These tests are carried out to screen SIs for specific field conditions, and thus select the best option for that particular environment. In detail, thermal and compatibility tests are carried out to assess if SIs can be used in a particular environment, or not. Then, static and dynamic inhibition efficiency tests are carried out to rank SIs according to their MIC. Obviously, strictly put, a SI with a lower MIC is preferable to one with a higher MIC, since less quantity of inhibitor is required to inhibit the same scaling system. After selecting a SI based on these tests, a core flood test is carried out to derive the SI *pseudo-adsorption isotherm*. This isotherm is then used as input to design squeeze treatments in specialised software (e.g. Squeeze 10 developed and distributed by the FAST group at Heriot-Watt University). If the SI deployment mechanism is continuous injection, then core flood tests are not necessary.

Scale formation in oilfields is typically integrated in a cycle of scale management. For example, such a cycle could include: i) risk assessment ii) product selection iii) treatment design iv) treatment implementation v) monitoring and tracking vi) review and back to risk assessment. As noted here, this cycle should involve close monitoring of the system, squeeze process improvement and optimisation and a successively more efficient scale management.

1.2 CaCO₃ scale in CO₂ Water Alternating Gas

CO₂ Water Alternating Gas, or CO₂ WAG, is an Enhanced Oil Recovery (EOR) process that consists in the alternated injection of water and CO₂ in the reservoir for tertiary oil recovery. Injecting CO₂ in the reservoir is a common EOR technique in the oil and gas industry (e.g. Christensen et al., 2001, Alvarado and Manrique, 2010, Verma, 2015). In particular, I highlight the projects in the ultra-deep water pre-salt cluster of the Santos Basin offshore Brazil that have been developed to include CO₂ WAG techniques (Galp, 2016). This work has been stimulated by the proposed application of CO₂ WAG in the Santos Basin, Brazil.

CO₂ can be injected in the reservoir in either miscible or immiscible floods, depending on the conditions of the system. In a miscible CO₂ flood, gas and oil form one phase causing the volume of the oil to swell, and thus displacing residual oil. Water is usually used in a WAG scheme to prevent early gas breakthrough by stabilizing the gas front, which otherwise may be prone to unstable viscous fingering.

Tackling scale formation in EOR processes and particularly in CO₂ WAG schemes can be addressed by using the same broad approach as for *conventional* scale formation. However, each EOR process has its own specificities with respect to scale formation. Production wells in carbonate reservoirs with a CO₂-rich environment such as in CO₂ WAG processes are prone to CaCO₃ precipitation and deposition, which poses one of the most common flow assurance risks in upstream oilfield operations (e.g. Yuan et al., 2001, Fleming et al., 2007, Pizarro and Branco, 2012). This process can be explained as follows: i) in the reservoir, injected CO₂ dissolves in the aqueous phase causing a decrease in pH to acidic levels; ii) at lower pH levels, CaCO₃ rock buffers the system by dissolving Ca²⁺ and CO₃²⁻ ions (actually bicarbonate ions , HCO₃²⁻, mostly form), thus establishing a new thermodynamic equilibrium between rock and brine; iii) these components are then transported to production systems, and, as the brine enters the production system and travels along the tubing, the pressure gradually reduces causing the evolution of CO₂ from the aqueous phase to the vapour phase and a consequent increase in the pH; and iv) at higher pH levels, CaCO₃ scale becomes over-saturated and re-precipitates.

There are two main commercial software used by companies to perform scale prediction calculations in the oil and gas industry, namely Scalechem – developed and distributed

by OLI Systems, USA – and Multiscale – developed by NTNU and distributed by Expro Petrotech, Norway (e.g. Collins et al., 2004, Ramstad et al., 2005, Simpson et al., 2005, Jordan et al., 2008, Jones et al., 2006, Jordan and Mackay, 2007, Gomes et al., 2012, Zhang et al., 2015). These software can be used to predict scale formation in general, and CaCO_3 scale in particular, for a variety of scale formation mechanisms – mixing of waters, auto-scaling, evaporation-induced, etc. –, and, indeed, they have been used successfully in the past for this purpose. However, these software have limitations that need to be carefully addressed. For example, these models are limited by the availability of experimental data that supports their calculations, especially in less common scaling environments (e.g. sour environments that can potentiate the precipitation of “exotic” scales such as ZnS and PbS , or alkaline environments which are characteristic of Alkaline-Surfactant-Polymer (ASP) EOR processes and that can potentiate silicate scaling). Another example is the extent of their PVT capabilities: these software do not possess the same PVT capabilities as, for example, PVTSIM Nova (developed by Calsep, Denmark) or HydraFLASH (developed by Heriot-Watt University, Scotland), albeit a state-of-the-art PVT model is key for scale predictions, especially when acid gases such as CO_2 and H_2S are involved.

With respect to modelling the formation of CaCO_3 scale in CO_2 WAG processes, I identify two key limitations of these software that I am going to address here. First, these software do not have the built-in capability of calculating the *correct* CaCO_3 scaling profile in CO_2 -rich production systems from commonly available production data – I propose in Chapter 5 an innovative procedure for this calculation. I emphasise that this calculation is important for the design of scale treatments, including squeeze treatments, such that scale formation is not over or under-estimated (both over and under-estimation of scale can have significant additional costs). Second, these software do not model the reactive flow of fluid in porous media, and therefore do not account for processes that may have a significant impact on the precipitation of scale in production systems – I propose in Chapter 6 a model that couples scale prediction and reactive transport calculations. In addition, I propose in Chapter 5 a new approach to interpret modelling results for auto-scaling processes, based on the cumulative amount of scale formed, and I explain why this approach should be used instead of the “traditional” approach. This approach can then be used to improve scale management strategies.

1.3 Objectives and outline of the dissertation

The objective of this work is to model the precipitation of CaCO_3 scale in CO_2 WAG production systems. To this end, processes taking place in the reservoir and in production systems must be modelled and coupled together. In particular, the following processes are considered:

In the reservoir

- i) CO_2 dissolution in the aqueous phase.
- ii) Aqueous acid equilibrium, including the equilibrium established in the carbonate system, i.e. the equilibrium established between the species $\text{CO}_2/\text{HCO}_3^-/\text{CO}_3^{2-}$ (note that this equilibrium quantifies the decrease in pH levels).
- iii) Rock-brine equilibrium, including the dissolution (and precipitation) of CaCO_3 rock.
- iv) Transport of aqueous components, including the scaling ions Ca^{2+} and CO_3^{2-} , to production systems.

In production systems

- i) CO_2 evolution from the aqueous phase to the vapour phase. More generally, the partition of CO_2 between all phases present in the system – water, vapour, and liquid.
- ii) Aqueous acid equilibrium to model the pH increase caused by CO_2 evolution from the aqueous phase.
- iii) CaCO_3 scale precipitation (note that the co-precipitation of CaCO_3 with other scales is also considered).

These processes are addressed individually, and then coupled together, throughout the chapters of this thesis. In particular, in Chapter 3, an aqueous scale prediction model is built that calculates: i) the precipitation of scale, including not only CaCO_3 , but also FeCO_3 , FeS , BaSO_4 , SrSO_4 , and CaSO_4 ; ii) the acid equilibria, including the carbonate

system ($\text{CO}_2/\text{HCO}_3^-/\text{CO}_3^{2-}$), the sulphide system ($\text{H}_2\text{S}/\text{HS}^-/\text{S}^{2-}$), and organic acids; and iii) the rock-brine equilibrium (dissolution/precipitation of CaCO_3 rock).

In Chapter 4, Vapour-Liquid Equilibrium (VLE) calculations are addressed. In particular, the solubility of single-component CO_2 gas in water and brine and the solubility of CO_2 - H_2S - CH_4 gas mixtures in water are modelled. To this end, several Equations of State (EOS) are implemented, including the Soave-Redlich-Kwong (SRK) and Peng-Robinson (PR) EOS. A high accuracy EOS proposed by Duan and Sun to model the solubility of CO_2 in an aqueous phase is also implemented. In addition, VLE models are coupled with the scale prediction model developed in Chapter 3, and an impact study of VLE calculations on scale prediction calculations is carried out. Although I acknowledge that newer EOS perform better than cubic-EOS for predicting density, etc., I opt to implement “well established” cubic EOS such as SRK and PR EOS for their simplicity and robustness.

In Chapter 5, multiphase flash calculations are considered to calculate the partition of components, including CO_2 , between water, vapour, and liquid phases, and coupled with scale prediction calculations developed in Chapter 3. In addition, an algorithm is developed to calculate the CaCO_3 scaling profile in the production systems as a function of decreasing pressure (and temperature) from commonly available (and incomplete) production data.

In Chapter 6, the reactive flow and transport of aqueous components in the reservoir is calculated using a 1D reactive transport model developed in this work for a CO_2 WAG injection schedule. This model is then coupled with a depressurisation algorithm in the wellbore that calculates the precipitation of CaCO_3 scale in the production system. Also, the effect of kinetics on rock-brine interactions in the reservoir is addressed.

2. Literature review

2.1 Aqueous electrolyte systems

The core of any scale prediction software is its **activity model**, i.e. the model that calculates the non-ideal behaviour of aqueous electrolyte systems. The Pitzer model is an activity electrolyte model that is widely used in the oil and gas industry in the context of scale prediction calculations (e.g. Atkinson et al., 1991, Morgenthaler et al., 1993, Azaroual et al., 2001, Bezerra et al., 2003, Al-khaldi et al., 2011, Kan and Tomson, 2010, Shen et al., 2017). This model was first introduced by Pitzer in 1973 (Pitzer, 1973) as an improvement of the Debye-Hückel theory for concentrated electrolyte solutions, and developed in the subsequent years (Pitzer and Mayorga, 1973, Pitzer and Mayorga, 1974, Pitzer and Kim, 1974, Pitzer, 1975, Silvester and Pitzer, 1978, Pitzer, 1995). The original papers by Pitzer can obviously be used to implement the Pitzer model. However, a more practical approach would be to follow the description of the Pitzer model detailed in Pedersen et al., 2015. Also, for a comprehensive exposition of the Pitzer model, the reader is referred to the thermodynamic textbook “Thermodynamics” by Gilbert N. Lewis and Merle Randall revised and updated in the 3rd edition by Pitzer himself (Pitzer, 1995).

Although the Pitzer model seems to be the preferred model for many scale prediction applications – mainly due to the availability of experimental data which results in very good accuracy in the calculation of activity coefficients for high salinity environments –, there are other electrolyte models available in the literature. In fact, in recent years there has been an increased interest in calculating the non-ideal behaviour of aqueous phases by means of an equation of state, rather than an activity coefficient model. In this context, Figure 2.1 shows a possible classification of electrolyte models (based on the textbook by Georgios M. Kontogeorgis, 2010).

Also, other electrolyte models rather than the Pitzer model have been used in the context of scale prediction calculations, such as the Bromley-Zemaitis activity model (Anderko, 2000) and the UNIQUAC model (Chakravarty et al., 2015, Chakravarty and Thomsen, 2015, Figueroa et al., 2016). In fact, the UNIQUAC model has also been used in

combination with the Pitzer model to calculate activity coefficients in mixed-solvent electrolyte systems (Wang et al., 2002).

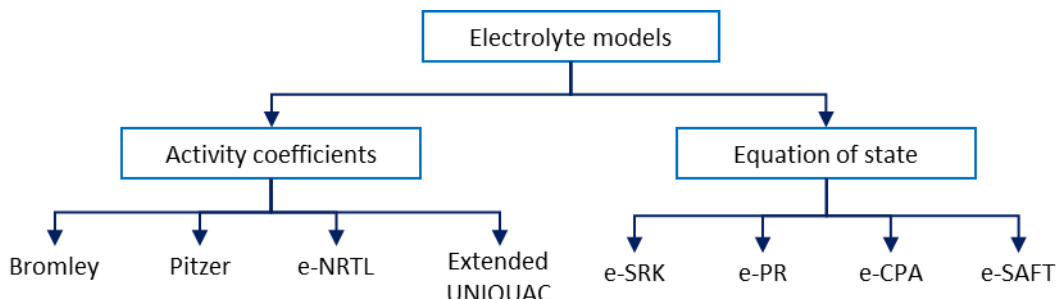


Figure 2.1 – Classification of electrolyte models (based on the textbook by Georgios M. Kontogeorgis, 2010)

There are two main commercial codes used by companies to perform scale prediction calculations in the oil and gas industry, namely Scalechem – developed and distributed by OLI Systems, USA – and Multiscale – developed by NTNU and distributed by Expro Petrotech, Norway (e.g. Collins et al., 2004, Ramstad et al., 2005, Simpson et al., 2005, Jordan et al., 2008, Jones et al., 2006, Jordan and Mackay, 2007, Gomes et al., 2012, Zhang et al., 2015). ScaleSoftPitzer developed by the Brine Chemistry Consortium at Rice University is also commonly used (e.g. Yuan et al., 2004, Chen et al., 2007, Raju, 2009, Zuluaga et al., 2011). ScaleChem uses the Bromley-Zemaitis activity model developed by Bromley, 1973, and Zemaitis, 1980, whereas Multiscale and ScaleSoftPitzer use the Pitzer model. In addition to these software, there are also other software that are used in the context of scale predictions, albeit to a less extent, such as Geochemist's Workbench (Aqueous Solutions LLC, US), Downhole SAT (French Creek Software, US), Multiflash (KBC Advanced Technologies, UK), OKscale (University of Oklahoma, US), and PHREEQC (USGS, US).

Given the models available in the literature for electrolyte systems, and the know-how accumulated by groups involved in the development of scale prediction software, I believe that the Pitzer model is the best option for building a scale prediction model.

2.2 Vapour-liquid equilibrium

The development of Vapour-Liquid Equilibrium (VLE) calculations follow the development of Equations of State (EOS) which relate state variables in a mathematical equation and thus describe the state of matter as a function of physical conditions. One of the most important EOS is the ideal gas law introduced in 1834 by Clapeyron (Clapeyron, 1834) which relates pressure, volume, and temperature for a hypothetical ideal gas. Notwithstanding its many limitations, this EOS can be used to model the behaviour of gases that approximately show ideal gas behaviour.

For gases that do not approximate the ideal gas behaviour, the ideal gas law is not sufficiently accurate. The ideal gas law considers that gas molecules do not occupy volume, i.e. they are treated as point particles, and that they do not attract or repulse other gas molecules. In this context, van der Waals proposed in 1873 a modification to the ideal gas law that accounted for the volume occupied by (real) gas molecules and for the attraction between gas molecules (van der Waals, 1873). This work resulted in the well-known van der Waals (vdW) equation that laid the foundations for many cubic EOS used today.

Arguably one of the most important contribution for the development of cubic EOS was that of Redlich and Kwong. These authors proposed in 1949 a modification of the vdW EOS (Redlich and Kwong, 1949) by introducing two coefficients that proved to give very good results for many gaseous systems, at a time where about 200 EOS had already been proposed (Valderrama, 2003). Following the work of Redlich and Kwong, many researchers proposed cubic EOS that are nowadays commonly used in the oil and gas industry, including the Redlich-Kwong EOS modified by Soave (Soave, 1972) and the Peng-Robinson EOS (Peng and Robinson, 1976) – i.e. SRK and PR EOS, respectively. Other cubic EOS available in the literature include the PR EOS modified by Stryjek and Vera (PRSV 1 and 2) (Stryjek and Vera, 1986b, and Stryjek and Vera, 1986a), the Patel-Teja (PT) EOS and its modification by Valderrama (VPT) (Patel and Teja, 1982, and Valderrama, 1990, respectively), the Elliott-Suresh-Donohue (ESD) EOS (Elliott et al., 1990), among others.

Cubic EOS are widely used in the oil and gas industry for their accuracy and simplicity. However, there are other types of EOS available in the literature. Figure 2.2 shows a

possible classification of EOS (adapted from the work of Valderrama, 2003), which include not only cubic EOS, but also non-cubic, virial-type, and molecular based EOS.

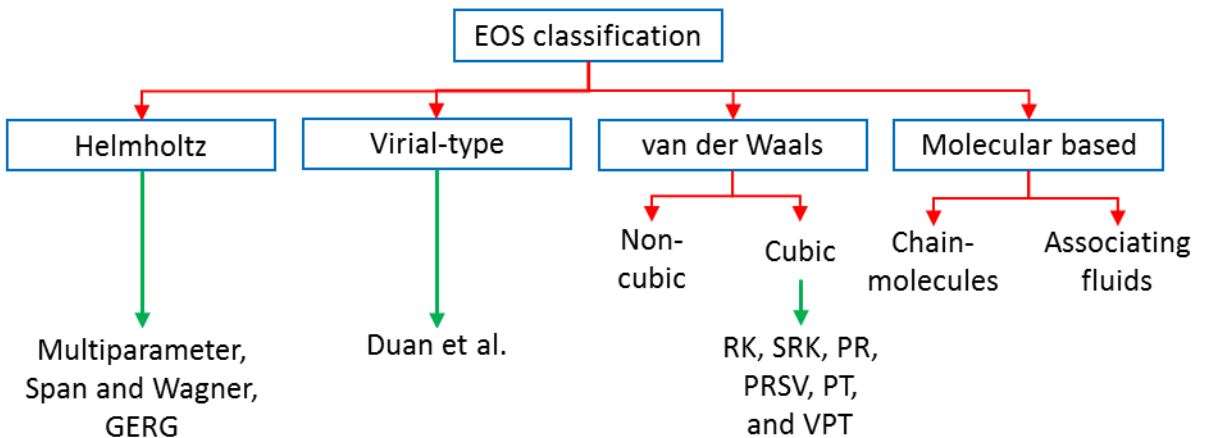


Figure 2.2 – Classification of EOS (adapted from Valderrama, 2003).

For example, molecular based EOS for associating fluids include the Statistical Association Fluid Theory (SAFT) and Cubic-Plus-Association (CPA) EOS. SAFT EOS was introduced by Walter G. Chapman, 1988, George Jackson, 1988, Chapman et al., 1990, and Huang and Radosz, 1990, and based on the work of Wertheim (Wertheim, 1984a, Wertheim, 1984b, Wertheim, 1986a, and Wertheim, 1986b). SAFT EOS was then developed by others (e.g. Fu and Sandler, 1995, Kraska and Gubbins, 1996a, Kraska and Gubbins, 1996b, Blas and Vega, 1998, Gil-Villegas et al., 1997, Gross and Sadowski, 2001, von Solms et al., 2003, Valtz et al., 2004, Shadloo and Peyvandi, 2017). On the other hand, CPA EOS was first introduced by Kontogeorgis et al., 1996, and then developed by others (e.g. Derawi et al., 2004, Oliveira et al., 2007, Voutsas et al., 2007, Haghghi et al., 2009, Riaz et al., 2013, Bjørner and Kontogeorgis, 2016, Frost et al., 2016, Palma et al., 2017). Literature on VLE in general and EOS in particular is vast and I can argue that every research group involved in VLE calculations has its own approach. This is because different R&D groups work with different technical applications, i.e. they usually use a particular EOS that is tuned with a particular experimental dataset and applied in a particular context. There are many textbooks that explore this diversity on the VLE literature (e.g. Sandler, 1994, Danesh, 1998, Pedersen et al., 2015, Firoozabadi, 2016). In fact, I can say that, currently, there is no EOS that can be used to accurately describe the state of matter of all substances and for all physical conditions.

2.3 Multiphase flash calculations

There are mainly two ways to address phase equilibrium calculations (Privat et al., 2016): one based on the equality of chemical potentials, and another based on the minimisation of the Gibbs energy. Figure 2.3 shows schematically a typical multiphase problem: given the molar composition of a hydrocarbon stream F , pressure, and temperature, calculate the number of phases in thermodynamic equilibrium in the system, and the molar composition of each phase.

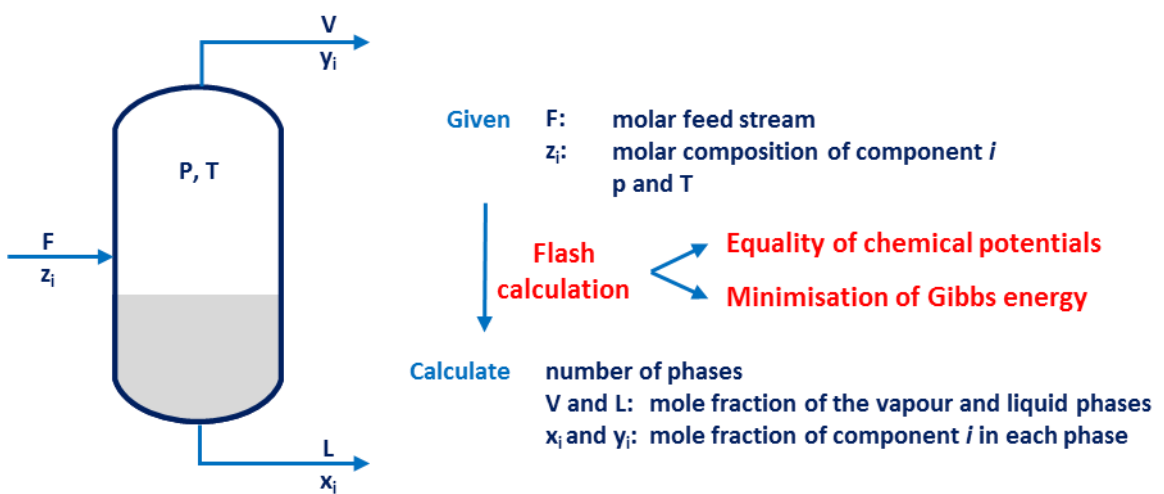


Figure 2.3 – Two-phase PT-flash problem: calculation of the liquid and vapour molar streams, V and L , and respective compositions, from the molar stream of the feed, F , and its composition.

To better understand these two approaches, I review here the argument of Baker et al., 1982. These authors noted that all solution techniques to phase equilibrium calculations, including these two, must satisfy three restrictions. In their words, these restrictions are: i) material balance must be preserved; ii) the chemical potentials for each component must be the same in all phases; and iii) the system of predicted phases at the equilibrium state must have the lowest possible Gibbs energy at the system temperature and pressure.

The solution procedure based on the equality of chemical potentials considers the first and second restrictions, but not the third. As noted above, the first two requirements are necessary, but not sufficient, i.e. the third requirement must also be satisfied. Hence, this procedure is usually coupled with a stability test to assess if there is another equilibrium state with a lower Gibbs energy. This approach is widely studied in the petroleum industry for its simplicity and robustness, particularly in the context of compositional

reservoir simulation (e.g. Firoozabadi and Pan, 2002, Okuno et al., 2010, Nichita and Graciaa, 2011).

On the other hand, the solution procedure based on the minimization of Gibbs energy considers all three requirements, but it has been found to have poorer performance than the former (see for example Pan and Firoozabadi, 2003). This observation is not surprising since the minimisation of the Gibbs energy is a nonlinear optimisation problem constrained to linear equalities and inequalities (as detailed in Trangenstein, 1985), whereas the procedure based on the equality of chemical potentials is essentially a root-finding problem. Nevertheless, this solution procedure is also used to solve multiphase flash calculations (e.g. Sun and Seider, 1995, Lucia et al., 2000, Nichita et al., 2002, Teh and Rangaiah, 2002, Rossi et al., 2009, Néron et al., 2012, Snider et al., 2015).

Although an extensive literature survey on phase flash calculations goes beyond the scope of this work, I briefly highlight here the contributions which I consider as very influential in this area. In 1954, Rachford and Rice published a pioneer work in the form of a technical note (Rachford and Rice, 1952) introducing a flash algorithm suitable for “digital computing machines” that strongly shaped the course of scientific research in the area of flash calculations. Their work resulted in the well-known *Rachford-Rice equation* which is widely applied in the petroleum industry to solve phase equilibria by means of the solution procedure based on the equality of chemical potentials discussed above, and it is still object of ongoing research in present days (e.g. Gaganis et al., 2012, Nichita and Leibovici, 2013, Yan and Stenby, 2014).

This procedure, as noted, does not guarantee that the system is at its lowest possible Gibbs energy. In this context, Michelsen (1982a and b) proposed a test based on the *tangent-plane criterion* as formulated by Baker et al., 1982, to check if a system is at its lowest possible Gibbs energy, or not. Michelsen took a step forward by ensuring that the third restriction discussed above is also satisfied, and thus rendering the procedure based on the equality of chemical potentials very appealing for its simplicity, efficiency and robustness. In fact, stability tests as proposed by Michelsen are commonly run in compositional reservoir simulations prior to a more expensive flash calculation (Haugen and Beckner, 2013). The reason for this is straightforward: if the stability test guarantees that there is no state with a lower Gibbs energy, then the system is already at equilibrium and performing a flash calculation is redundant.

Another interesting advance in flash calculations was suggested in 1982 by Li and Nghiem regarding the value for the mole fraction of the vapour phase (V in Figure 2.3) in a PT-flash calculation based on the equality of chemical potentials. According to these authors, the mole fraction of the vapour phase “can take any value” (Li and Nghiem, 1982), i.e. it can take a value higher than one or lower than zero – which is physically not possible, – since the restrictions i) and ii) to phase equilibrium calculations defined previously are still satisfied. This suggestion contributed to the definition of the concept of *negative flash* introduced later in 1989 in a paper by Whitson and Michelsen. These authors established the procedure for the flash calculation where V could take values higher than one and lower than zero, but still constrained to the limits V_{\min} and V_{\max} , i.e., they established the procedure for the negative flash. In addition, they also identified a range of applications for this new concept, including the calculation of the Minimum Miscibility Pressure (MMP) and the determination of the phase type in compositional reservoir simulation (liquid and vapour). The concept of the negative flash was then extensively studied and applied by others (e.g. Leibovici and Neoschil, 1995, Iranshahr et al., 2010, and Yan and Stenby, 2012), and became a well-established procedure alongside a “standard” flash calculation.

The advances in compositional reservoir simulation go hand in hand with the development of multiphase flash calculations and I can argue that reservoir simulation has indeed become a driving force for the development of multiphase flash techniques. A clear example of this liaison is the development of *reduced methods* to speed up simulations. The idea of using reduced methods is to decrease the number of variables that are required to be solved in flash calculations in order to reduce computational cost. The reduced method concept was first introduced by Michelsen, 1986 and then further extended and studied by others (e.g. Jensen and Fredenslund, 1987, Hendriks and van Bergen, 1992, Firoozabadi and Pan, 2002, Li and Johns, 2006, Nichita and Graciaa, 2011, and Haugen and Beckner, 2013).

The literature on flash calculations is vast and there are many other important contributions that are not covered here. For further reading on the subject, I refer to the textbook of Firoozabadi, 2016, for general considerations on phase equilibria, and to the textbook of Michelsen and Mollerup, 2007 for the numerical implementation of flash algorithms.

2.4 Reactive transport

Reactive transport modelling is widely used in the Earth Sciences disciplines, including in geochemistry, hydrology, and fluid dynamics. For example, it has been used to model bio-remediation processes (e.g. Prechtel and Knabner, 2002, Fang et al., 2009, Yabusaki et al., 2011), CO₂ storage processes (e.g. Kirste, 2013, Suchodolska and Labus, 2016, Gao et al., 2017), transport of nuclear waste contaminants (e.g. Spycher et al., 2003b, Salas et al., 2014, Seher et al., 2016), groundwater contamination (e.g. Zhu et al., 2001, Nath et al., 2008, Bailey et al., 2013), among other processes.

In particular, reactive transport modelling can be used to address mineral dissolution reactions, fluid flow, and transport of components through porous media, and thus it can be used to study the formation of CaCO₃ scale in CO₂ WAG processes. In fact, geochemical modelling is an important “thread” of reactive transport modelling, as discussed in Steefel et al. (2005), and many studies on this topic have been reported in the literature in the past decades (e.g. Reed, 1982, McNab, 1997, Xu et al., 2006, Fahrner et al., 2011, Navarre-Sitchler and Jung, 2017).

Given the many applications of reactive transport modelling, the literature on the subject is vast and diverse. However, the development of reactive transport modelling software goes hand in hand with the introduction of new R&D projects, and I can argue that groups involved in the development of these software packages have indeed become a driving force to the development of reactive transport modelling itself. Thus, I highlight the contributions to reactive transport modelling of the groups involved in the development of PHREEQC – developed by Parkhurst and Appelo (Parkhurst and Appelo, 1999) –, TOUGHREACT – developed as an extension of TOUGH2 V2 (Pruess et al., 1999, Xu et al., 2006, Xu et al., 2011), CrunchFlow – developed by Steefel and co-workers (Carl I. Steefel and Molins, 2016)), and PFLOTRAN – developed by Lichtner and co-workers (Lichtner et al., 2015).

There are many textbooks that address geochemistry in reactive transport modelling, and I recommend the textbooks of Lasaga (1998) for the a good theoretical exposition, and Bethke (2008) for the implementation of numerical algorithms.

3. Aqueous electrolyte model

The precipitation of CaCO_3 scale in production wells in CO_2 WAG schemes is a complex process involving CO_2 dissolution in the aqueous phase, CaCO_3 rock dissolution in the reservoir, re-precipitation of CaCO_3 in production wells due to depressurisation, etc. Thus, modelling this process is also complex, resulting in a collection of models that address each step of the process individually, and ultimately calculating the amount of scale that precipitates in production systems. In this chapter, I build an aqueous electrolyte model that calculates the precipitation of CaCO_3 scale from an initially specified aqueous solution. This model is then developed in subsequent chapters to address the overall process of CaCO_3 precipitation in CO_2 WAG production wells.

Modelling the precipitation of CaCO_3 from an aqueous solution is, in itself, a complex issue, since it requires accounting for all parameters that impact the precipitation of CaCO_3 , such as the precipitation of other scales (e.g. FeCO_3 , FeS , BaSO_4 , etc.), reactions that contribute to the system pH, pressure, temperature, and salinity of the system, etc. In fact, building an aqueous CaCO_3 scale prediction model requires building a *general* aqueous scale prediction model.

The objective in this chapter is to build an aqueous scale prediction model that calculates the precipitation of CaCO_3 scale from aqueous compositional data. The model should consider:

- i) Calculations at common oilfield pressures, temperatures, and salinities.
- ii) CaCO_3 co-precipitation with other common oilfield scales, particularly FeCO_3 , FeS , BaSO_4 , SrSO_4 , and CaSO_4 .
- iii) Include common oilfield species that contribute to the system pH, including CO_2 , H_2S and organic acids.

The question may arise here: why build another aqueous scale prediction model when there are at least 3 or 4 already existing commercial models? The answer to this question is as follows: i) firstly, all commercial models are essentially “black boxes” and for the later work on transport and kinetics, I must have an in-house model so that I can incorporate it into the University codes; ii) I also have a novel formulation of the aqueous

scaling problem which involves equation reduction for all possible scaling scenarios and which is guaranteed to give a unique solution to the scaling equations (explained below); iii) my in-house model has been incorporated into an 1D carbonate reservoir transport code and an approximate method has been developed to carry out *kinetic* transport (i.e. non-equilibrium scaling); iv) I require this model to incorporate into a kinetic wellbore scaling model (work in progress; not reported in this thesis).

3.1 Thermodynamic model

3.1.1 Equilibrium constants

Consider the following general chemical reaction at constant pressure and temperature where a and b are the stoichiometric coefficients:



The condition for thermodynamic equilibrium is given by:

$$\Delta G = b\mu_B - a\mu_A \quad (3.2)$$

Where ΔG is the change in Gibbs energy and μ_A and μ_B are respectively the chemical potential of components A and B . Generalising for any chemical reaction with m components, the condition for thermodynamic equilibrium is written as:

$$\sum_{i=1}^m v_i \mu_i = 0 \quad (3.3)$$

Where v_i is the stoichiometric coefficient of component i . v_i is positive for products and negative for reactants. Considering the definition of chemical potential,

$$\mu_i = \mu_i^0 + RT \ln a_i \quad (3.4)$$

where a_i and μ_i^0 are the activity and the standard chemical potential of component i , and noting that $\sum v_i \mu_i^0 = \Delta G^0$, then, by combining Equations (3.3) and (3.4), the following general expression for the thermodynamic equilibrium is obtained:

$$\Delta G^0 = -RT \ln \prod_{i=1}^m (a_i)^{\nu_i} = -RT \ln K^0 \quad (3.5)$$

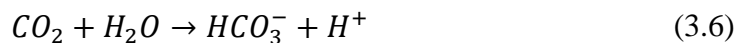
$K^0 = \prod(a_i)^{\nu_i}$ is the thermodynamic equilibrium constant defined as a function of the Gibbs energy. The thermodynamic equilibrium constants are used next to build a thermodynamic scale prediction model. The thermodynamic data used here was adapted from Kaasa, 1998.

3.1.2 System of equations for scale prediction calculations

Scale prediction modelling is based on solving a nonlinear system of equations consisting of: i) acid equilibrium reactions; ii) mineral precipitation reactions; iii) mass balance equations; and iv) the equation for the electrical neutrality of solutions (or in general a *charge balance* equation). These equations are detailed below.

3.1.2.1 Acid equilibrium reactions

Acid equilibrium equations relevant in the context of oilfield scales as studied here are given by the following reactions:



These equations describe the well-known aqueous CO₂/bicarbonate (HCO₃⁻)/carbonate (CO₃²⁻) system. In addition, sulphide species also contribute to the acid equilibrium, as shown in the following reactions (note the similarity between the carbonate and the sulphide systems with both having two dissociation reactions):



Furthermore, organic acids commonly present in petroleum fluids also contribute to the acid equilibrium. Thus, the equation for the dissociation of organic acids is also considered as:



Where HA is a general organic acid.

The thermodynamic equilibrium constants, K^0 , for Equations (3.6) to (3.11) are then written respectively as:

$$K_{CO_2,1}^0 = \frac{m_{H^+} m_{HCO_3^-}}{m_{CO_2}} \frac{\gamma_{H^+} \gamma_{HCO_3^-}}{\gamma_{CO_2} a_{H_2O}} \quad (3.12)$$

$$K_{CO_2,2}^0 = \frac{m_{H^+} m_{CO_3^{2-}}}{m_{HCO_3^-}} \frac{\gamma_{H^+} \gamma_{CO_3^{2-}}}{\gamma_{HCO_3^-}} \quad (3.13)$$

$$K_{H_2O}^0 = m_{OH^-} m_{H^+} \frac{\gamma_{H^+} \gamma_{OH^-}}{a_{H_2O}} \quad (3.14)$$

$$K_{H_2S,1}^0 = \frac{m_{H^+} m_{HS^-}}{m_{H_2S}} \frac{\gamma_{H^+} \gamma_{HS^-}}{\gamma_{H_2S}} \quad (3.15)$$

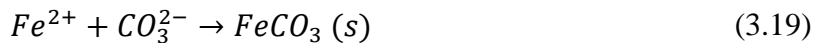
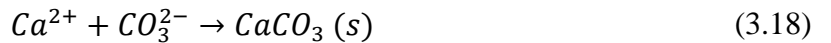
$$K_{H_2S,2}^0 = \frac{m_{H^+} m_{S^{2-}}}{m_{HS^-}} \frac{\gamma_{H^+} \gamma_{S^{2-}}}{\gamma_{HS^-}} \quad (3.16)$$

$$K_{HA}^0 = \frac{m_{H^+} m_{A^-}}{m_{HA}} \frac{\gamma_{H^+} \gamma_{A^-}}{\gamma_{HA}} \quad (3.17)$$

Where m and γ are respectively the molality and the activity coefficient of the respective component.

3.1.2.2 Mineral precipitation reactions

The mineral precipitation reactions considered here are for the precipitation of CaCO_3 , FeCO_3 , FeS , BaSO_4 , SrSO_4 , and CaSO_4 . These equations are written as:





If I consider that the sulphate ion, SO_4^{2-} , is fully dissociated in the pH range of interest (approximately between $pH = 3$ and $pH = 8$ for most oilfield applications), then I can make an important distinction between pH-dependent and pH-independent scales. Since carbonate and sulphide ions, CO_3^{2-} and S^{2-} , react to form, respectively, HCO_3^- and CO_2 , and HS^- and H_2S in the pH range of interest, as shown in Equations (3.6) to (3.10), the mineral scales $CaCO_3$, $FeCO_3$, and FeS are thus strongly dependent on the acid equilibrium. In other words, these scales are dependent on the pH of the system. This means that predicting mineral scale precipitation for pH-dependent scales, as opposed to pH-independent scales, must include acid equilibrium reactions.

The thermodynamic equilibrium constants, K^0 , for Equations (3.18) to (3.61) are given by:

$$K_{sp, CaCO_3}^0 = m_{Ca^{2+}} m_{CO_3^{2-}} \gamma_{Ca^{2+}} \gamma_{CO_3^{2-}} \quad (3.24)$$

$$K_{sp, FeCO_3}^0 = m_{Fe^{2+}} m_{CO_3^{2-}} \gamma_{Fe^{2+}} \gamma_{CO_3^{2-}} \quad (3.25)$$

$$K_{sp, FeS}^0 = m_{Fe^{2+}} m_{S^{2-}} \gamma_{Fe^{2+}} \gamma_{S^{2-}} \quad (3.26)$$

$$K_{sp, BaSO_4}^0 = m_{Ba^{2+}} m_{SO_4^{2-}} \gamma_{Ba^{2+}} \gamma_{SO_4^{2-}} \quad (3.27)$$

$$K_{sp, SrSO_4}^0 = m_{Sr^{2+}} m_{SO_4^{2-}} \gamma_{Sr^{2+}} \gamma_{SO_4^{2-}} \quad (3.28)$$

$$K_{sp, CaSO_4}^0 = m_{Ca^{2+}} m_{SO_4^{2-}} \gamma_{Ca^{2+}} \gamma_{SO_4^{2-}} \quad (3.29)$$

3.1.2.3 Mass conservation equations

Mass balance equations are set such that mass is conserved between initial (usually user input data) and equilibrium states. For example for carbon, the following equations are obtained:

$$m_{CO_2} + m_{HCO_3^-} + m_{CO_3^{2-}} + m_{CaCO_3} + m_{FeCO_3} = \sum m_{initial} \quad (3.30)$$

Where

$$\sum m_{initial} = m_{CO_2,initial} + m_{HCO_3^-,initial} + m_{CO_3^{2-},initial} \quad (3.31)$$

$m_{CO_2,initial}$, $m_{HCO_3^-,initial}$, and $m_{CO_3^{2-},initial}$ are the user input data. Similar equations are derived for *all* other components involved in the calculations.

3.1.2.4 Equation for the electrical neutrality of solutions

The equation for the electrical neutrality of solutions is set such that the sum of the positive charges in solution equals the sum of the negative charges as:

$$\sum_{i=1}^N z m_{i, initial} = \sum_{i=1}^N z m_{i, equilibrium} = 0 \quad (3.32)$$

Where i is the ion, N is the total number of ions, and z is the charge of the ion.

3.1.2.5 Numerical scheme

The above system of equations is the basis of all scale precipitation models, and it can be solved by applying numerical methods, such as the Newton-Raphson method. In addition, this system can be manipulated algebraically in order to be solved in reduced space, as demonstrated in the Appendix. However, there is a pitfall that needs to be carefully addressed: mineral precipitation reactions should only be included in the calculations *if the respective scale precipitates*. However, the system of equations must be solved in order to know if a particular scale is predicted to precipitate or not. For example, consider that CaCO_3 and FeCO_3 are both supersaturated in solution and, therefore, both scales can potentially precipitate. However, the precipitation of one of the scales, say CaCO_3 , can render the other scale, FeCO_3 , under-saturated. This can happen simply due to a pH shift, or a common ion effect (in this example, the consumption of CO_3^{2-}), etc. Then, the equation for the precipitation of the under-saturated mineral should not be included in the model, since it is not verified.

In this context, I develop an innovative algorithm that guarantees that the correct thermodynamic solution is always achieved. This algorithm follows the steps:

- i) All possible scaling systems are identified. These systems have in common the equations for the acid equilibrium, the equations for the conservation of mass, and the equation for the electrical neutrality of solutions, but differ in whether the equations for the mineral precipitation are considered, or not. Considering the precipitation reactions of CaCO_3 , FeCO_3 , and FeS , then there are eight possible options, as shown in Table 3.1. In fact, there are 2^n possible options, where n is the number of pH-dependent scales (in this case, $n = 3$).

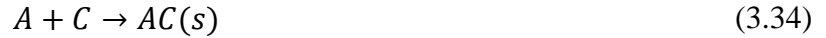
Table 3.1 – Options 1 to 8 identify whether or not the mineral precipitation reaction for CaCO_3 , FeCO_3 , and FeS is present in the overall system of equations.

Option	CaCO_3	FeCO_3	FeS
1			
2			✓
3	✓		
4		✓	
5	✓		✓
6		✓	✓
7	✓	✓	
8	✓	✓	✓

- ii) Since the correct option (Table 3.1) is not known a priori, I derive a separate set of equations for each of the eight possible cases and *all eight possible systems are solved*. I do this in the full knowledge that 7 of these are “wrong”!
- iii) The correct system is then selected based on two criteria: a) the concentrations of all species must be positive; and b) mineral scales cannot be supersaturated, i.e. the saturation ratio for CaCO_3 , FeCO_3 , and FeS must be lower or equal to one. These criteria **guarantee** finding the correct thermodynamic solution, since there cannot be more than one valid solution. In fact, below I show mathematically that the thermodynamically correct solution is *unique* for a given set of initial conditions. This is an important calculation since it guarantees that the solution found always corresponds to a global minimum in Gibbs energy.

Proof for the existence of a unique thermodynamic solution for a scaling system with a common ion effect

Consider the system for the precipitation of two general salts, AB and AC, with a common ion A, as:



Then, I have:

$$K_{sp}(AB) = m_A m_B \quad (3.35)$$

$$K_{sp}(AC) = m_A m_C \quad (3.36)$$

If I consider the precipitation reactions of AB and AC, and if I consider the definition of Saturation Ratio (SR), then at thermodynamic equilibrium I have:

$$\begin{cases} 1 = \frac{m_A m_B}{K_{sp}(AB)} \\ 1 = \frac{m_A m_C}{K_{sp}(AC)} \end{cases} \Leftrightarrow \begin{cases} m_A = \frac{K_{sp}(AB)}{m_B} \\ m_A = \frac{K_{sp}(AC)}{m_C} \end{cases} \Rightarrow \frac{\frac{K_{sp}(AB)}{m_B}}{\frac{K_{sp}(AC)}{m_C}} \Leftrightarrow \frac{m_C}{m_B} = \frac{K_{sp}(AC)}{K_{sp}(AB)} \quad (3.37)$$

Note that if there is precipitation of salts, then the SR is equal to one at equilibrium. However, if the salt is under-saturated, then the SR is lower than one.

If I consider the precipitation reaction of AB only, then I have:

$$\begin{cases} 1 = \frac{m_A m_B}{K_{sp}(AB)} \\ 1 > \frac{m_A m_C}{K_{sp}(AC)} \end{cases} \Leftrightarrow \begin{cases} m_A = \frac{K_{sp}(AB)}{m_B} \\ m_A < \frac{K_{sp}(AC)}{m_C} \end{cases} \Rightarrow \frac{\frac{K_{sp}(AB)}{m_B}}{\frac{K_{sp}(AC)}{m_C}} < \frac{m_C}{m_B} \Leftrightarrow \frac{m_C}{m_B} < \frac{K_{sp}(AC)}{K_{sp}(AB)} \quad (3.38)$$

Likewise, if I consider the precipitation reactions of AC only, then I have:

$$\begin{cases} 1 > \frac{m_A m_B}{K_{sp}(AB)} \\ 1 = \frac{m_A m_C}{K_{sp}(AC)} \end{cases} \Leftrightarrow \begin{cases} m_A < \frac{K_{sp}(AB)}{m_B} \\ m_A = \frac{K_{sp}(AC)}{m_C} \end{cases} \Rightarrow \frac{\frac{K_{sp}(AC)}{m_C}}{\frac{K_{sp}(AB)}{m_B}} < \frac{m_C}{m_B} \Leftrightarrow \frac{m_C}{m_B} > \frac{K_{sp}(AC)}{K_{sp}(AB)} \quad (3.39)$$

Equations (3.37), (3.38), and (3.39) clearly show that if one system is valid, then the others cannot be.

Also for the case when precipitation reactions are not considered, I can show that only one system is thermodynamically valid. In detail, if no precipitation reactions are considered, then I have:

$$\begin{cases} 1 > \frac{m_A m_B}{K_{sp}(AB)} \\ 1 > \frac{m_A m_C}{K_{sp}(AC)} \end{cases} \Leftrightarrow \begin{cases} m_B < \frac{K_{sp}(AB)}{m_A} \\ m_C < \frac{K_{sp}(AC)}{m_A} \end{cases} \quad (3.40)$$

If I now consider, for example, that the system for the precipitation reactions of salts AB and AC is also valid, then I have:

$$m_C = m_B \frac{K_{sp}(AC)}{K_{sp}(AB)} \quad (3.41)$$

$$m_A = \frac{K_{sp}(AB)}{m_B} \quad (3.42)$$

Combining Equations (3.41), (3.42), and (3.43) I obtain:

$$m_B \frac{K_{sp}(AC)}{K_{sp}(AB)} < m_B \frac{K_{sp}(AC)}{K_{sp}(AB)} \quad (3.43)$$

Which is clearly a contradiction. Or, in other words, I can say that both systems cannot be simultaneously valid.

For further information on building a scale prediction model, readers are referred to Rafal et al. (1994), Kaasa (1998), and Pedersen et al. (2015).

3.1.3 Pitzer electrolyte model

The activity coefficients of ions and neutral components were calculated using the Pitzer equations. The Pitzer equations were first introduced by Pitzer in 1973 (Pitzer, 1973) as an improvement of the Debye-Hückel theory for concentrated electrolyte solutions, and developed in the subsequent years (Pitzer and Mayorga, 1973, Pitzer and Mayorga, 1974, Pitzer and Kim, 1974, Pitzer, 1975, Silvester and Pitzer, 1978, Pitzer, 1995).

Considering a solution with w_w kg of solvent and n_i, n_j, \dots moles of solute i, j, \dots the total excess Gibbs energy of a solution in molality G^{Em} is given by:

$$\frac{G^{Em}}{RT} = w_w f + \frac{1}{w_w} \sum_{ij} \lambda_{ij} n_i n_j + \frac{1}{w_w^2} \sum_{ijk} \mu_{ijk} n_i n_j n_k \quad (3.44)$$

In this equation f captures essentially the Debye-Hückel long-range effects of Coulomb forces between ions, whereas the second and third virial coefficients, λ and μ , capture the short-range effects between pairs and triplets of ions, respectively. Note that the matrices for λ_{ij} and μ_{ijk} are symmetric (i.e. $\lambda_{ij} = \lambda_{ji}$, etc.). Pitzer developed a system of equations which was based on the Debye-Hückel theory but considered the ionic strength dependence of the second virial coefficient λ . In principle, this must yield an improvement in matching experimental data since it has further parameterisation (more free parameters) and it correctly reduces to the Debye-Hückel model in very dilute electrolyte solutions.

Pitzer noted that only specific combinations of λ and μ are measurable for an electrolyte solution containing the cations c, c', \dots , and the anions a, a', \dots , and thus defined the following variables:

$$B_{ca} = \lambda_{ca} + \frac{v_c}{2v_a} \lambda_{cc} + \frac{v_a}{2v_c} \lambda_{aa} \quad (3.45)$$

$$\Phi_{cc'} = \lambda_{cc'} - \frac{z_{c'}}{2z_c} \lambda_{cc} - \frac{z_c}{2z_{c'}} \lambda_{c'c'} \quad (3.46)$$

$$C_{ca} = \frac{3}{2} \left(\frac{\mu_{cca}}{z_c} + \frac{\mu_{cca}}{z_a} \right) \quad (3.47)$$

$$\Psi_{cc'a} = 6\mu_{cc'a} - \frac{3z_c}{z_c}\mu_{cca} - \frac{3z_c}{z_{c'}}\mu_{c'c'a} \quad (3.48)$$

Where v is the number of ions per molecule of electrolyte and z is the charge of the ion. $\Phi_{aa'}$ and $\Psi_{aa'c}$ are defined in a similar manner to $\Phi_{cc'}$ and $\Psi_{cc'a}$. Then, after converting the composition to molalities (i.e., $m_i = n_i/w_w$), the equation for the total excess Gibbs energy is re-written as:

$$\begin{aligned} \frac{G^{Em}}{w_w RT} = & f + 2 \sum_c \sum_a m_c m_a \left[B_{ca} + \left(\sum_c m_c z_c \right) C_{ca} \right] \\ & + \sum_{c>c'} \sum_{a>a'} m_c m_{c'} \left[2\Phi_{cc'} + \sum_a m_a \Psi_{cc'a} \right] \\ & + \sum_{a>a'} \sum_{n>n'} m_a m_{a'} \left[2\Phi_{aa'} + \sum_c m_c \Psi_{aa'c} \right] + 2 \sum_n \sum_c m_n m_c \lambda_{nc} \\ & + 2 \sum_n \sum_a m_n m_a \lambda_{na} + 2 \sum_{n< n'} \sum_c m_n m_{n'} \lambda_{nn'} + \sum_n m_n^2 \lambda_{nn} + \dots \end{aligned} \quad (3.49)$$

The index n identifies neutral components for second-order terms. Third-order terms for neutral species are not included. The activity of water and the osmotic and activity coefficients, respectively a_{H_2O} , ϕ and γ , are defined alongside as:

$$\ln a_{H_2O} = -\phi M_{H_2O} \sum_i m_i \quad (3.50)$$

$$\phi - 1 = -\frac{(\partial G^{Em}/\partial w_w)_{n_i}}{RT \sum_i m_i} \quad (3.51)$$

$$\ln \gamma_i = \left(\frac{\partial G^{Em}/w_w RT}{\partial m_i} \right)_{w_w, m_j, j \neq i} \quad (3.52)$$

Lastly, the expressions for the calculation of the osmotic and the activity coefficients of cation M , anion X and neutral component N (i.e., ϕ , γ_M , γ_X and γ_N), in mixed electrolyte solutions are obtained by taking the appropriate differentiations in Equations (3.51) and (3.52):

$$\begin{aligned}
(\phi - 1) = & \frac{2}{\sum_i m_i} \left[\frac{-A_\phi I^{3/2}}{(1 + bI^{1/2})} + \sum_c \sum_a m_c m_a (B_{ca}^\phi + ZC_{ca}) \right. \\
& + \sum_{c < c'} \sum_{a'} m_c m_{c'} \left(\Phi_{cc'}^\phi + \sum_a m_a \Psi_{cc'a} \right) \\
& \left. + \sum_{a < a'} \sum_c m_a m_{a'} \left(\Phi_{aa'}^\phi + \sum_c m_c \Psi_{caa'} \right) \right] \quad (3.53)
\end{aligned}$$

$$\begin{aligned}
\ln \gamma_M = & z_M^2 F + \sum_a m_a (2B_{Ma} + ZC_{Ma}) + \sum_c m_c \left(2\Phi_{Mc} + \sum_a m_a \Psi_{Mca} \right) \\
& + \sum_{a < a'} \sum_c m_a m_{a'} \Psi_{Maa'} + z_M \sum_c \sum_a m_c m_a C_{ca} \quad (3.54)
\end{aligned}$$

$$\begin{aligned}
\ln \gamma_X = & z_X^2 F + \sum_c m_c (2B_{cX} + ZC_{cX}) + \sum_a m_a \left(2\Phi_{Xa} + \sum_c m_c \Psi_{cXa} \right) \\
& + \sum_{c < c'} \sum_X m_c m_{c'} \Psi_{cc'X} + |z_X| \sum_c \sum_a m_c m_a C_{ca} \quad (3.55)
\end{aligned}$$

$$\ln \gamma_N = 2 \sum_c m_c \lambda_{Nc} + 2 \sum_a m_a \lambda_{Na} + \sum_{ca} m_c m_a \xi_{Nca} \quad (3.56)$$

ξ_{Nca} is a ternary parameter that accounts for interactions between a neutral component, a cation, and an anion. In the above expressions, the function F is defined as:

$$\begin{aligned}
F = & -A_\phi \left[\frac{I^{1/2}}{(1 + bI^{1/2})} + \frac{2}{b} \ln(1 + bI^{1/2}) \right] + \sum_c \sum_a m_c m_a B'_{ca} \\
& + \sum_{c < c'} \sum_{a'} m_c m_{c'} \Phi'_{cc'} + \sum_{a < a'} \sum_c m_a m_{a'} \Phi'_{aa'} \quad (3.57)
\end{aligned}$$

Where b has a value of $1.2 \text{ kg}^{1/2} \text{mol}^{1/2}$. The ionic strength I , the function Z and the Debye-Hückel parameter A_ϕ are defined as:

$$I = \frac{1}{2} \sum_i m_i |z_i|^2 \quad (3.58)$$

$$Z = \sum_i m_i |z_i| \quad (3.59)$$

$$A_\phi = \frac{1}{3} \sqrt{2\pi N_0 d_w} \left(\frac{e^2}{4\pi \epsilon_0 D k T} \right)^{3/2} \quad (3.60)$$

In the expression to calculate A_ϕ , N_0 is the Avogadro number ($6.022 \times 10^{23} \text{ mol}^{-1}$), d_w is the density of the solvent in kg/m^3 , e is the electronic charge ($1.602 \times 10^{-19} \text{ C}$), ϵ_0 is the permittivity of vacuum ($8.85419 \times 10^{-12} \text{ C}^2 \text{ N}^{-1} \text{ m}^{-2}$), D is the dielectric constant and k is the Boltzman constant ($1.381 \times 10^{-23} \text{ J K}^{-1}$). Pedersen and Christensen (2007, p. 383) suggested an expression proposed by Mørk, 1989, to calculate the dielectric constant of water as a function of the temperature t , in $^\circ\text{C}$. This expression is given in Equation (3.61). Also, a table with values for the Debye-Hückel parameter A_ϕ is given by Pitzer (1995, p. 544) for various temperatures.

$$D = 87.740 - 0.4008t + 9.398 \times 10^{-4}t^2 - 1.410 \times 10^{-6}t^3 \quad (3.61)$$

Equations (3.62) to (3.64) give, respectively, the ionic strength dependence of the second virial parameters B_{MX}^ϕ , B_{MX} and B'_{MX} .

$$B_{MX}^\phi = \beta_{MX}^{(0)} + \beta_{MX}^{(1)} \exp(-\alpha_1 \sqrt{I}) + \beta_{MX}^{(2)} \exp(-\alpha_2 \sqrt{I}) \quad (3.62)$$

$$B_{MX} = \beta_{MX}^{(0)} + \beta_{MX}^{(1)} g(\alpha_1 \sqrt{I}) + \beta_{MX}^{(2)} g(\alpha_2 \sqrt{I}) \quad (3.63)$$

$$B'_{MX} = \frac{1}{I} \left[\beta_{MX}^{(1)} g'(\alpha_1 \sqrt{I}) + \beta_{MX}^{(2)} g'(\alpha_2 \sqrt{I}) \right] \quad (3.64)$$

α_1 has a value of $2 \text{ kg}^{1/2} \text{ mol}^{1/2}$. For 2-2 electrolytes (e.g., Ca^{2+} and SO_4^{2-}) α_1 is shifted to 1.4 and α_2 equals $12 \text{ kg}^{1/2} \text{ mol}^{1/2}$. The function g and its ionic strength derivative are given by:

$$g(x) = \frac{2}{x^2} [1 - (1 + x) \exp(-x)] \quad (3.65)$$

$$g'(x) = -\frac{2}{x^2} \left[1 - \left(1 + x + \frac{x^2}{2} \right) \exp(-x) \right] \quad (3.66)$$

Third-virial parameters C_{MX} are often given as a function of the more commonly tabulated values C_{MX}^ϕ through the expression:

$$C_{MX} = \frac{C_{MX}^\phi}{2\sqrt{|z_M z_X|}} \quad (3.67)$$

The second-virial parameters Φ_{ij}^ϕ and Φ_{ij} and its derivative Φ'_{ij} are given respectively by:

$$\Phi_{ij}^\phi = \theta_{ij} + {}^E\theta_{ij} + I{}^E\theta'_{ij} \quad (3.68)$$

$$\Phi_{ij} = \theta_{ij} + {}^E\theta_{ij} \quad (3.69)$$

$$\Phi'_{ij} = {}^E\theta'_{ij} \quad (3.70)$$

θ_{ij} and ${}^E\theta_{ij}$ are contributions to the mixing parameter Φ that arise from the asymmetrical mixing of pairs of ions with the same sign. While θ_{ij} is independent of the ionic strength and specific to the ion pair i and j , ${}^E\theta_{ij}$ has a dependency on the ionic strength and, consequently, has a nonzero derivative. The expressions used to calculate ${}^E\theta_{ij}$ and ${}^E\theta'_{ij}$ are given by:

$${}^E\theta_{ij}(I) = \frac{z_i z_j}{4I} [J(x_{ij}) - 1/2J(x_{ii}) - 1/2J(x_{jj})] \quad (3.71)$$

$${}^E\theta'_{ij}(I) = -\frac{{}^E\theta_{ij}(I)}{I} + \frac{z_i z_j}{4I^2} [x_{ij} J'(x_{ij}) - 1/2 x_{ii} J'(x_{ii}) - 1/2 x_{jj} J'(x_{jj})] \quad (3.72)$$

Where

$$x_{ij} = 6z_i z_j A_\phi \sqrt{I} \quad (3.73)$$

The expressions used to evaluate $J(x)$ and $J'(x)$ are rather complex for practical purposes. Pitzer, 1975, proposed an alternative expression for $J(x)$, given here by Equation (3.74). A table with values for $J(x)$ and $J'(x)$ is also presented in this reference (it can be used for comparison purposes).

$$J(x) = [4 + 4.581(x^{-0.7237}) \exp(-0.0120x^{0.528})]^{-1} \quad (3.74)$$

Pitzer assumed that the third-virial coefficient is independent of the ionic strength and it can be neglected when all three ions have the same sign (Pitzer and Kim, 1974).

Values for the parameters used in the Pitzer equations can be found in the original papers by Pitzer (and in the subsequent related literature), or in many other references that collect and provide these data (e.g. Pedersen et al., 2015).

3.2 Results and discussion

3.2.1 Pitzer electrolyte model

My implementation of the Pitzer equations was compared with results obtained by using Multiscale (version 7.1.0.16). Figure 3.1 show an example of this comparison study for increasing concentrations of Na^+ , K^+ , Ca^{2+} , Mg^{2+} , Ba^{2+} , and Fe^{2+} , using chloride, Cl^- , as the counter-ion. In detail, activity coefficients were calculated from low to high salinity values, i.e. for a wide range of ionic strengths, at 1 bar and 25 °C. Note that the Pitzer equations approximate the Debye-Hückel limiting law for low ionic strength solutions (low salinity).

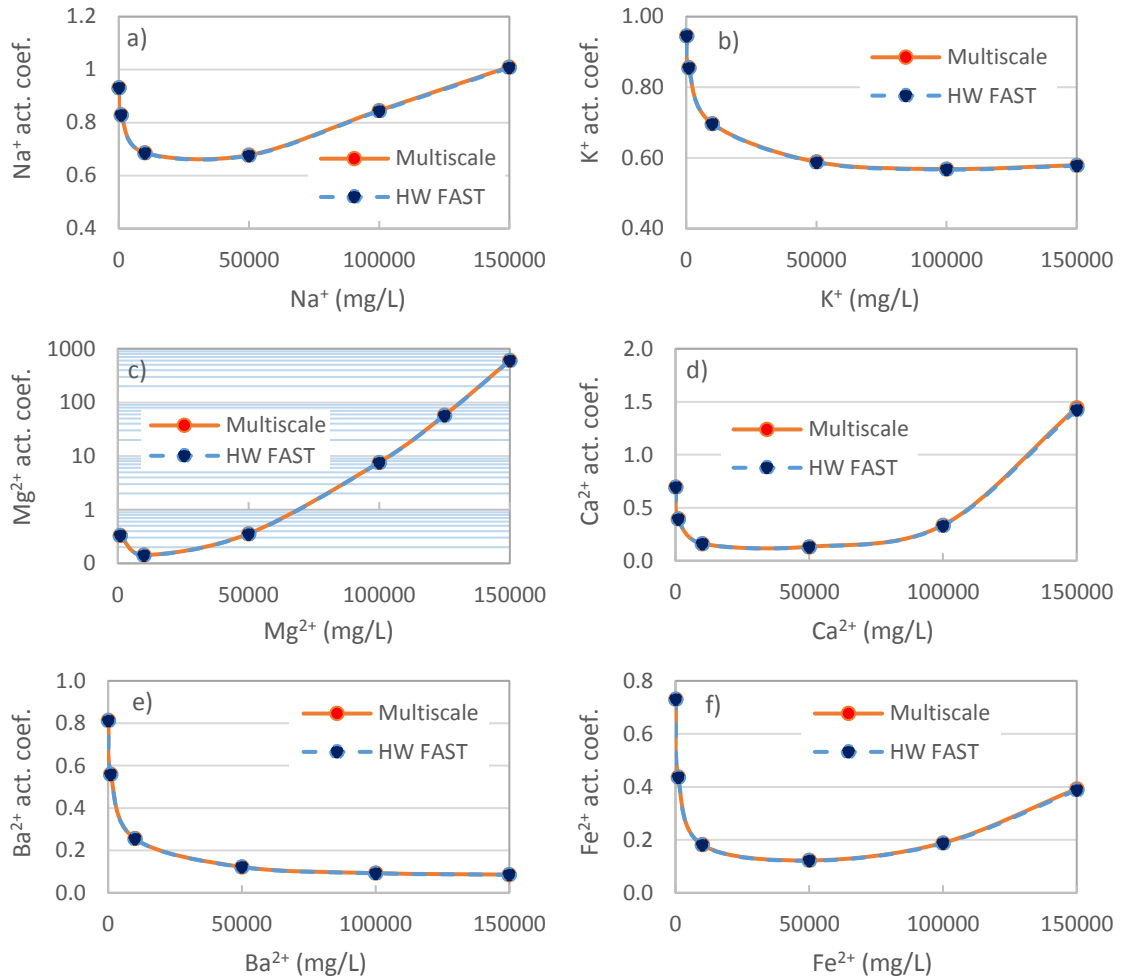


Figure 3.1 – Calculation of activity coefficients for Na^+ , K^+ , Mg^{2+} , Ca^{2+} , Ba^{2+} , and Fe^{2+} [a), b), c), d), e), and f) on figure] by using my code (HW FAST) and Multiscale.

Results in Figure 3.1 show excellent agreement between my implementation of the Pitzer equations and Multiscale for the conditions tested.

The Pitzer equations are a *semi-empirical* model, i.e. their theoretical formulation considers parameters that are fitted to experimental data. In fact, this semi-empirical nature makes the model open to novel parameterisation studies (e.g. Rard and Wijesinghe, 2003). Consequently, the calculation of activity coefficients using the Pitzer equations is dependent on the database used for the estimation of parameters. In other words, if two models use the Pitzer equations to calculate activity coefficients, but they have different databases, then the calculation of activity coefficients is also necessarily different.

Having obtained excellent agreement between my implementation of the Pitzer equations and the implementation of Multiscale, I re-run the calculations, but I now compare my results with results obtained by using PHREEQC (PHREEQC Interactive, Version 3.3.3.10424). Note that PHREEQC is also used to conduct scale prediction studies (e.g. Vazquez et al., 2013, Kazemi Nia Korrani et al., 2014, Abouie et al., 2017). Figure 3.2 shows the results for this comparison study. I emphasise that I used exactly the same data as before (Figure 3.1).

Results in Figure 3.2 show poor agreement between my model and PHREEQC for the calculation of activity coefficients using the Pitzer equations, with the exception for K^+ [Figure 3.2 b)]. However, I can identify two trends depending on the ionic strength: for low ionic strengths (low salinity), both models *roughly* agree on the calculation of the activity coefficients, since both models approximate the Debye-Hückel limiting law. However, for high ionic strengths, the two models have consistently different values (I particularly emphasise the calculation of the Mg^{2+} activity coefficient [Figure 3.2 c]), with several orders of magnitude difference between the two models), due to the use of different databases.

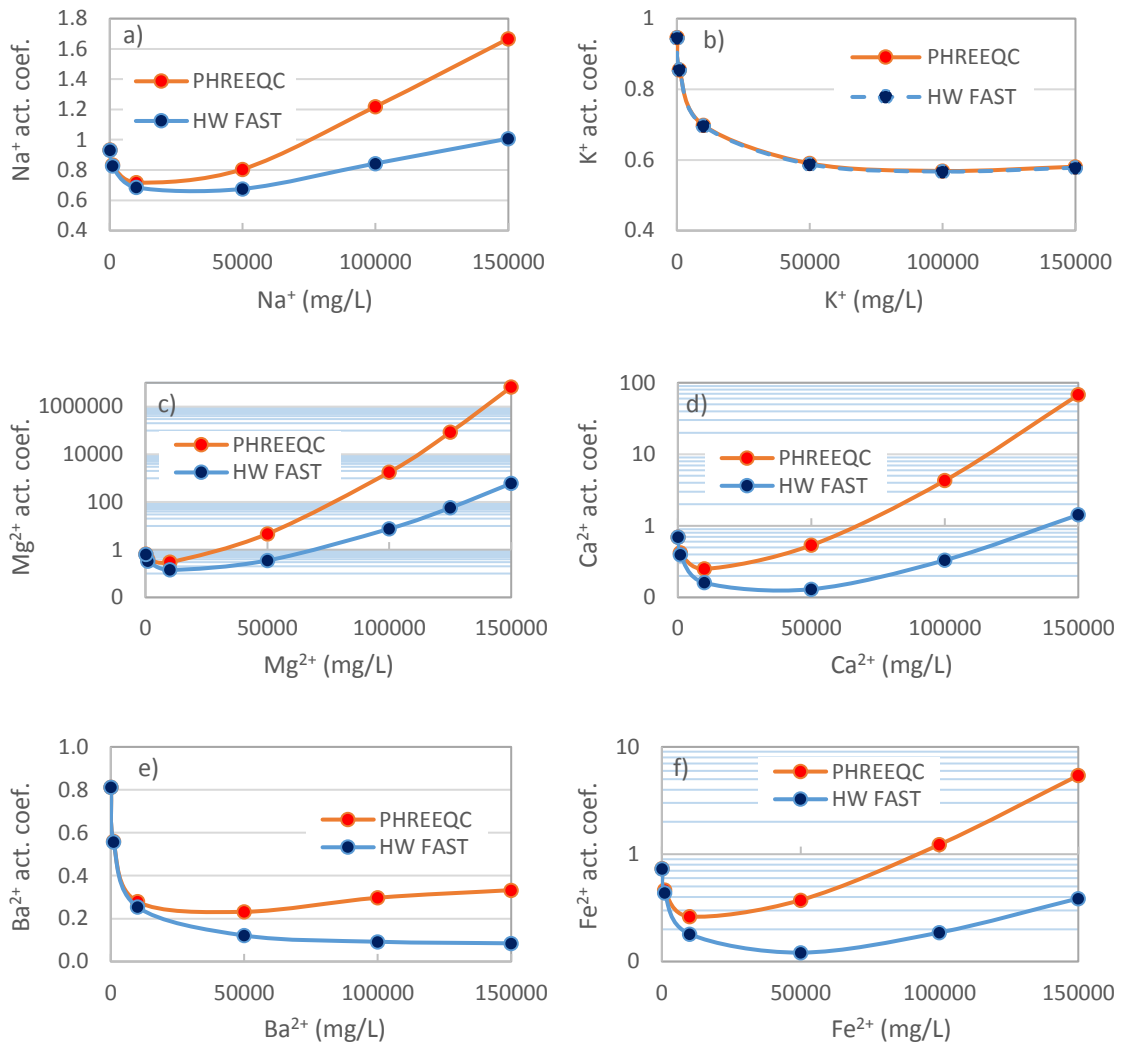


Figure 3.2 – Calculation of activity coefficients for Na^+ , K^+ , Mg^{2+} , Ca^{2+} , Ba^{2+} , and Fe^{2+} [a), b), c), d), e), and f) on figure] by using my code (HW FSAT) and PHREEQC.

Both Multiscale and PHREEQC are well-established industry software used for scale prediction calculations. I have clearly demonstrated excellent agreement between my implementation of the Pitzer equations and Multiscale, and poor agreement when I performed the same comparison using PHREEQC. In this context, I can infer that Multiscale and PHREEQC calculate different activity coefficients at high ionic strengths, although they both use the Pitzer equations as the activity model. These results are a clear indication of the importance of databases for semi-empirical models.

The previous point should be contextualised with common scale prediction calculations: most scale prediction calculations involve brines with a salinity close to, or higher than,

the salinity of seawater, which is around 35 000 TDS for the North Sea seawater. Analysing again the results shown in Figure 3.1 and Figure 3.2, these models calculate *roughly* the same activity coefficient for this salinity. In other words, for most common scale prediction calculations in seawater-like brines, having different Pitzer databases should not impact significantly the calculation of the amount of scale. However, if the calculation is performed at higher ionic strengths, then the difference in the amount of scale predicted by different models will emerge.

Having obtained different results by comparing my model against two different models (Multiscale and PHREEQC), a comparison with actual experimental data is advisable. As noted previously, my model uses the same thermodynamic data as reported in Kaasa, 1998. I now compare, as an example, solubility data for two common oilfield scales, namely CaCO_3 and BaSO_4 , and for NaCl – which is commonly found in oilfield brines. In these data, the activity coefficients are accounted for according to the following equation (exemplified for NaCl):

$$K_{sp}^0(\text{NaCl}) = m_{\text{NaCl}}^2 \cdot \gamma_{\text{Na}^+} \cdot \gamma_{\text{Cl}^-} \quad (3.75)$$

Where $K_{sp}^0(\text{NaCl})$, is the solubility product of NaCl (note that solubility products are key in building scale prediction models), and γ_{Na^+} and γ_{Cl^-} are, respectively, the activity coefficients of Na^+ and Cl^- . In this context, Figure 3.3 shows the comparison between experimental solubility data and the results predicted by my model.

Results in Figure 3.3 show very good agreement between my model and experimental solubility data.

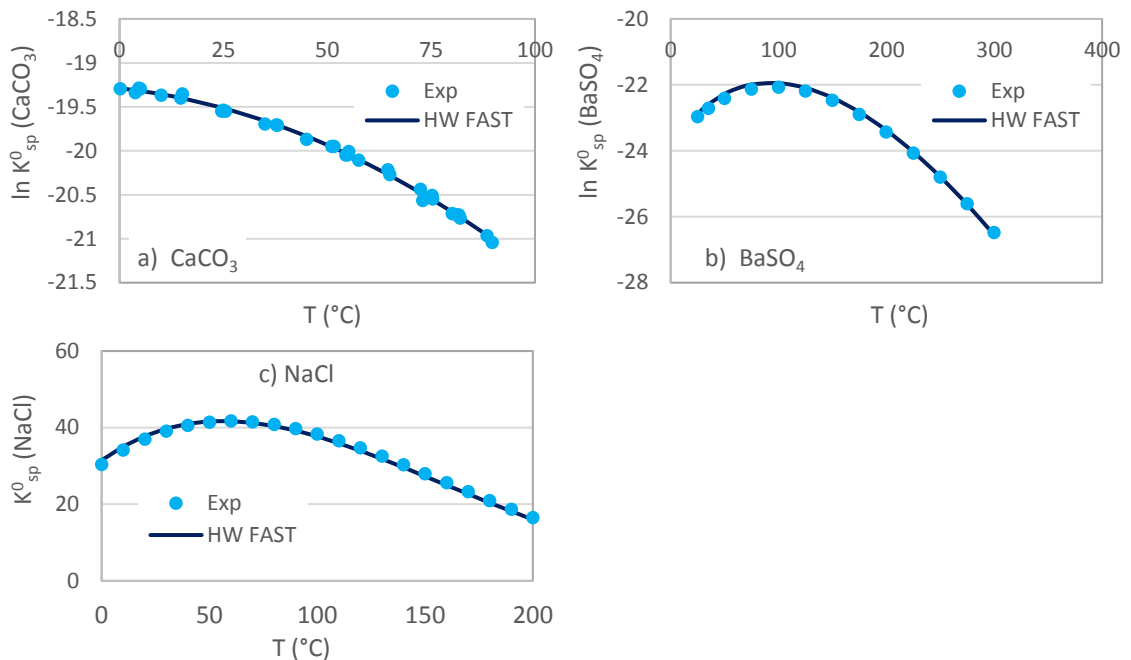


Figure 3.3 – Comparison between experimental solubility data and respective estimation using my model for thee salts: a) CaCO_3 – experimental data taken from Plummer and Busenberg, 1982; b) BaSO_4 – experimental data taken from Blount, 1977; and c) NaCl – experimental data taken from Wood, 1976.

3.2.2 General scale prediction calculations

Activity coefficients are used to calculate stoichiometric equilibrium constants. Then, these constants are used to calculate the amount of scale precipitation. This means that an error introduced in the calculation of activity coefficients has an impact on the calculation of the amount of precipitated scales. However, for comparison purposes with Multiscale, I can overcome this issue by using directly in my model the values for the equilibrium constants provided in Multiscale output file. This way, any deviation between the two models is not related to errors introduced in calculating activity coefficients, although I have clearly demonstrated excellent agreement between both models in calculating activity coefficients.

I note that any brine chemistry, temperature and pressure could be used for a comparison study. As an example, I opt to show in Figure 3.4 the prediction of the precipitation of CaCO_3 , FeS , FeCO_3 , BaSO_4 , SrSO_4 , and CaSO_4 at 100 bar and 60 °C for increasing concentrations of the cation involved in the precipitation of the salt.

Results shown in Figure 3.4 again show excellent agreement between my model and Multiscale for the calculation of the amount of precipitated CaCO_3 , FeS , FeCO_3 , BaSO_4 , SrSO_4 , and CaSO_4 . The very small differences between the results obtained for the two models can be attributed to numerical errors, since both models use a different mathematical formulation which leads to different round-off errors (for further details on Multiscale mathematical formulation, see Kaasa, 1998).

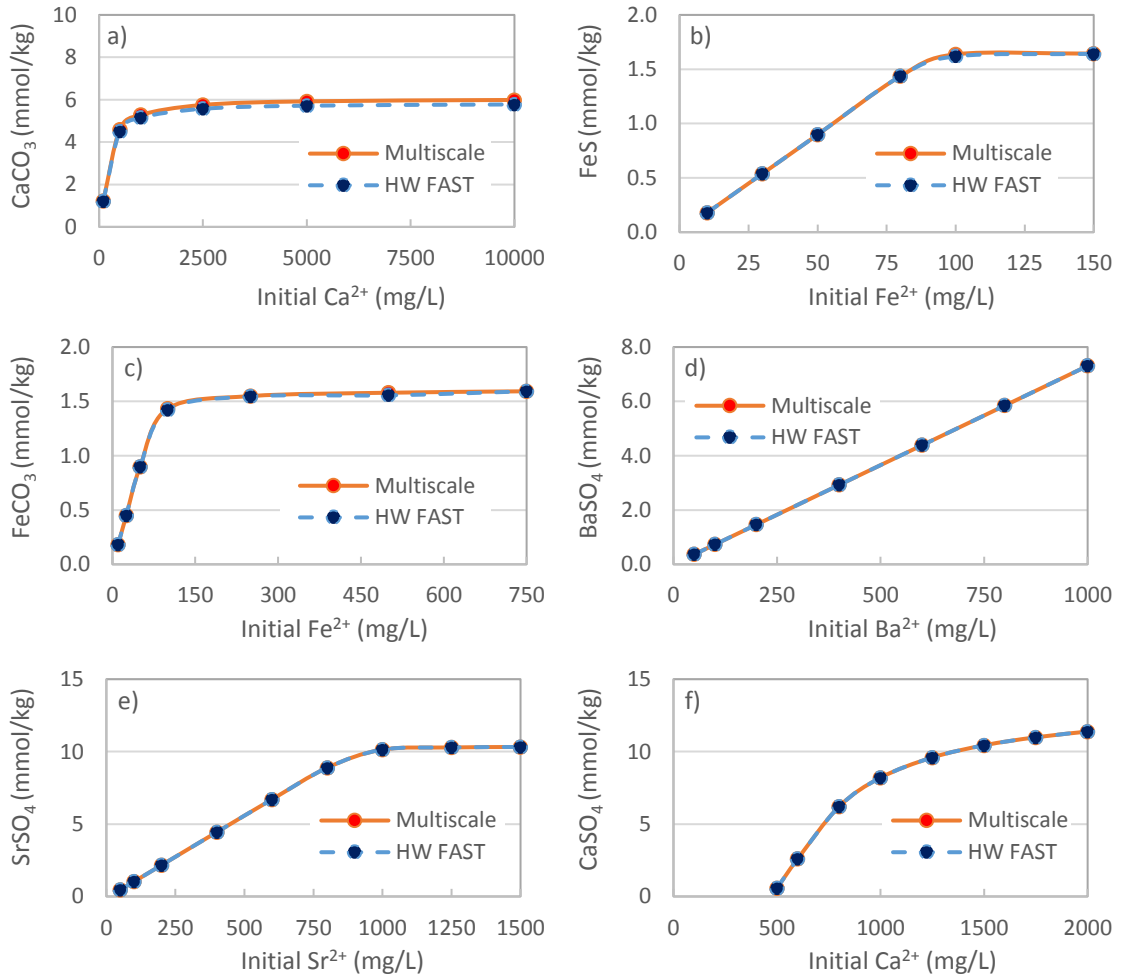


Figure 3.4 – Calculation of CaCO_3 , FeS , FeCO_3 , BaSO_4 , SrSO_4 , and CaSO_4 [a), b), c), d), e), and f) on figure] by using my code (HW FAST) and Multiscale.

3.2.3 Solubility of CaCO_3 scale

The aqueous scale prediction model is now tested for the precipitation of CaCO_3 scale. The mechanism for CaCO_3 scale formation in CO_2 WAG processes results from the evolution of CO_2 from the aqueous phase to the vapour phase, as will be discussed later. However, I can already test the impact of changing key species to CaCO_3 scale

precipitation using the aqueous model, namely species that contribute to the acid equilibrium such as CO_2 , HCO_3^- , and organic acids.

Table 3.2 presents the water composition used in calculations (data adapted from Mackay and Martins de Souza, 2014). In addition, pressure of 100 bar and a temperature of 80 °C were assumed.

Table 3.2 – Water composition used to study the solubility of CaCO_3 scale (adapted from Mackay and Martins de Souza, 2014).

Component	Concentration (mg/L)
Na^+	25265
K^+	495
Mg^{2+}	875
Ca^{2+}	2090
Ba^{2+}	35
Sr^{2+}	210
Fe^{2+}	0
Cl^-	44375
SO_4^{2-}	0
CO_2	-
HCO_3^-	145
CO_3^{2-}	-
pH	7

The precipitation of CaCO_3 for the water composition presented in Table 3.2 was calculated for varying initial concentrations of aqueous CO_2 , as shown in Figure 3.5. In addition, Figure 3.5 also shows results for the CaCO_3 saturation ratio, the concentration of Ca^{2+} , and pH for varying initial concentrations of aqueous CO_2 .

Results in Figure 3.5 show that:

- The precipitation of CaCO_3 scale decreases with increasing concentration of initial CO_2 [Figure 3.5 a)]. In fact, for concentrations of 250 mg initial CO_2/L and higher, there is no more CaCO_3 precipitation. These results show a very important feature of the carbonate/ CaCO_3 system: CaCO_3 scale precipitation is dependent on the concentration of CO_2 in solution. Note that these calculations are for a fixed solution. In a “real” field case, then a solution with $[\text{CO}_2] > 250\text{mg/L}$ would not scale but if the CO_2 repartitioned into the vapour phase, then it would lead to a scaling problem (explained in detail later).

- The saturation ratio of CaCO_3 decreases with increasing initial concentration of CO_2 [Figure 3.5 b)]. For concentrations of 250 mg initial CO_2/L and higher, the CaCO_3 saturation ratio is lower than 1 ($\log \text{SR} < 1$), i.e. the system is undersaturated with respect to CaCO_3 .
- The trend for the concentration of Ca^{2+} [Figure 3.5 c)] follows the trend of CaCO_3 precipitation: as the precipitation of CaCO_3 decreases with increasing initial concentration of CO_2 , the concentration of Ca^{2+} increases.
- Increasing the initial concentration of CO_2 decreases the pH [Figure 3.5 c)], thus causing the increase in CaCO_3 solubility.

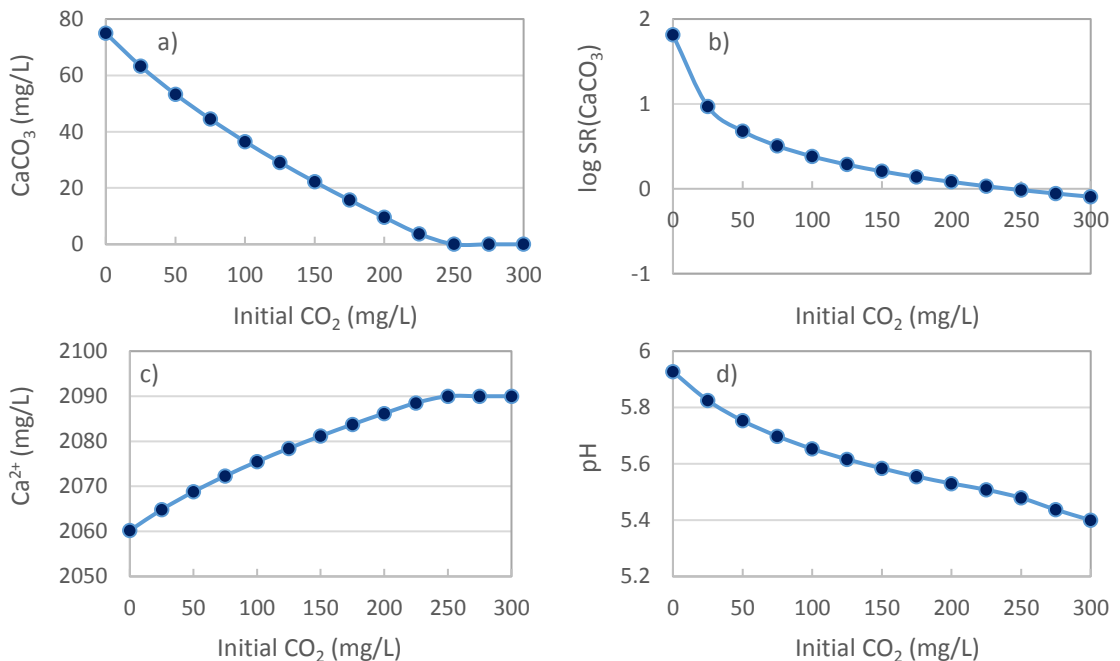


Figure 3.5 – Results for the precipitation of CaCO_3 scale as a function of initial CO_2 [a] on figure]. The CaCO_3 saturation ratio, the concentration of Ca^{2+} , and the pH are also plotted as a function of initial CO_2 [b), c), and d) on figure].

In fact, this last point is probably the most important point in understanding the dependence of the solubility of CaCO_3 with all other components in the system. However, a note of caution should be given when statements are made such as “the increasing pH causes calcite precipitation”. In fact, in satisfying the set of equilibrium equations described above, all of the variables change to achieve a final equilibrium state

– one variable does not “cause” the other; they are a coupled set of non-linear equations.
I review the equation for the precipitation of CaCO_3 :



The saturation ratio equation for Equation (3.76) is then defined as:

$$SR_{\text{CaCO}_3} = \frac{m_{\text{Ca}^{2+}} m_{\text{CO}_3^{2-}}}{K_{sp, \text{CaCO}_3}} \quad (3.77)$$

The saturation ratio can be thought as the “driving force” for scale formation. Thus, increasing the saturation ratio causes a decrease in the solubility of the scale. It is evident from Equation (3.77) that increasing the concentration of CO_3^{2-} increases the saturation ratio, and vice-versa (the saturation ratio is directly proportional to the concentration of CO_3^{2-}). This is the reason why the solubility of CaCO_3 scale is dependent on species that impact the system pH, since a change in the system pH causes a change in the concentration of CO_3^{2-} . In detail, Figure 3.6 shows conceptually how carbon species partition in solution as CO_2 , HCO_3^- , and CO_3^{2-} as a function of pH.

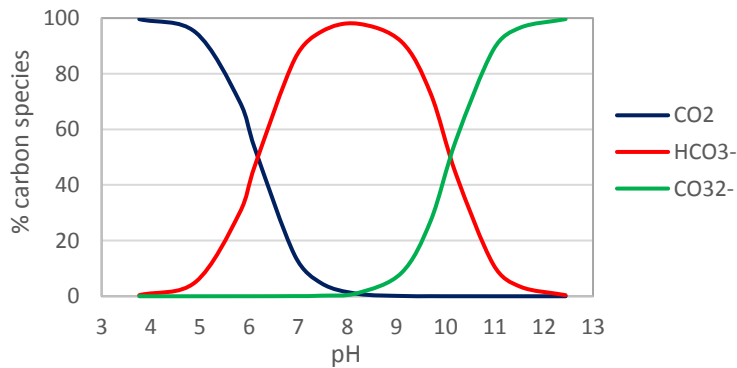


Figure 3.6 – Partition of CO_2 , HCO_3^- , and CO_3^{2-} in solution as a function of pH.

From Figure 3.6, it is clear that increasing the system pH causes an increase in the concentration of CO_3^{2-} , and vice-versa. Note that for acidic pH levels, the concentration of CO_3^{2-} is very low, but it is not zero. Thus, if a component causes the system pH to decrease, then the concentration of CO_3^{2-} decreases as well and, consequently, the solubility of CaCO_3 increases. This is the reason why I can use the system pH to analyse

how components impact the solubility of CaCO_3 scale (but keeping the above cautionary remark in mind!).

Organic acids also contribute to the system pH and, thus, they have an impact on the solubility of CaCO_3 . Figure 3.7 shows the precipitation of CaCO_3 as a function of the organic acids concentration for the water composition presented previously in Table 3.2.

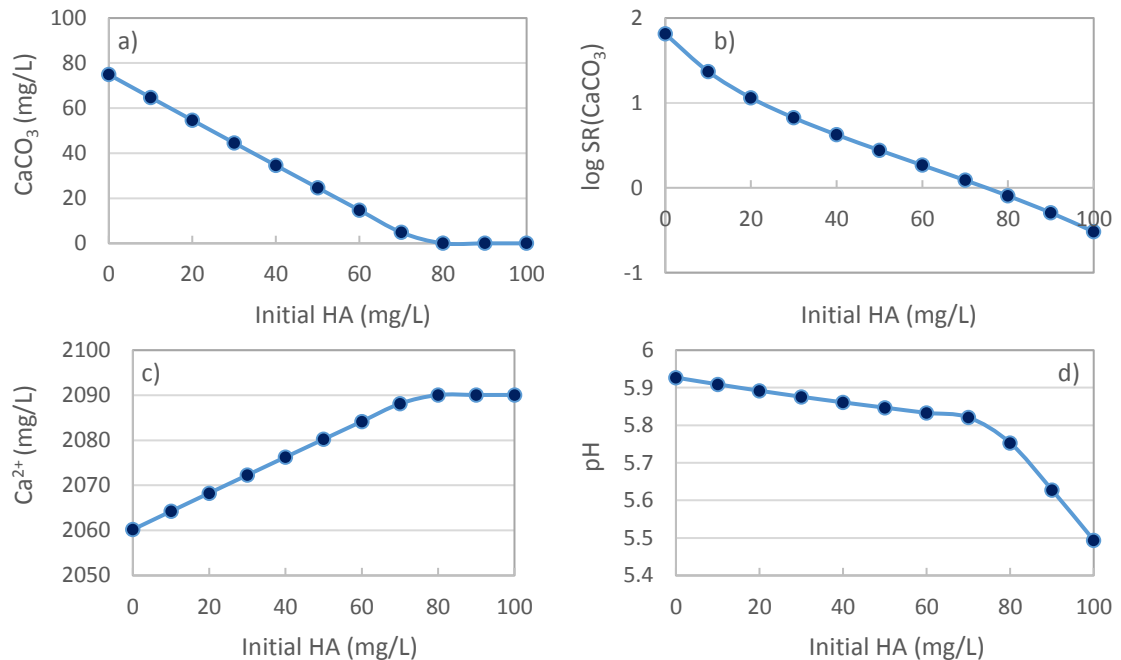


Figure 3.7 – Results for the precipitation of CaCO_3 scale as a function of initial concentration of organic acids [a] on figure]. The CaCO_3 saturation ratio, the concentration of Ca^{2+} , and the pH are also plotted as a function of initial concentration of organic acids [b), c), and d) on figure].

Results in Figure 3.7 show that the precipitation of CaCO_3 decreases with increasing concentration of organic acids, since the system pH decreases with increasing concentration of organic acids [Figure 3.7 d)]. In addition, these results show the buffering capacity of CaCO_3 : increasing the concentration of organic acids is “compensated” by having more CaCO_3 in solution and, thus, the solution’s pH does not change abruptly. Once all CaCO_3 is in solution, i.e. for a concentration of organic acids higher than approximately 70 mg/L, the pH decreases sharply with the increase of organic acids [Figure 3.7 d)].

The initial system pH – that relates to the initial concentration of H^+ using the pH definition – also impacts the precipitation of CaCO_3 . At this point, it is important to

clarify the difference between the initial pH and the equilibrium pH (or the system pH): the initial pH is the pH used as input in the thermodynamic model, whereas the equilibrium pH is the pH of the system after running a thermodynamic equilibrium calculation. Figure 3.8 shows the precipitation of CaCO_3 as a function of the initial pH for the water composition presented previously in Table 3.2.

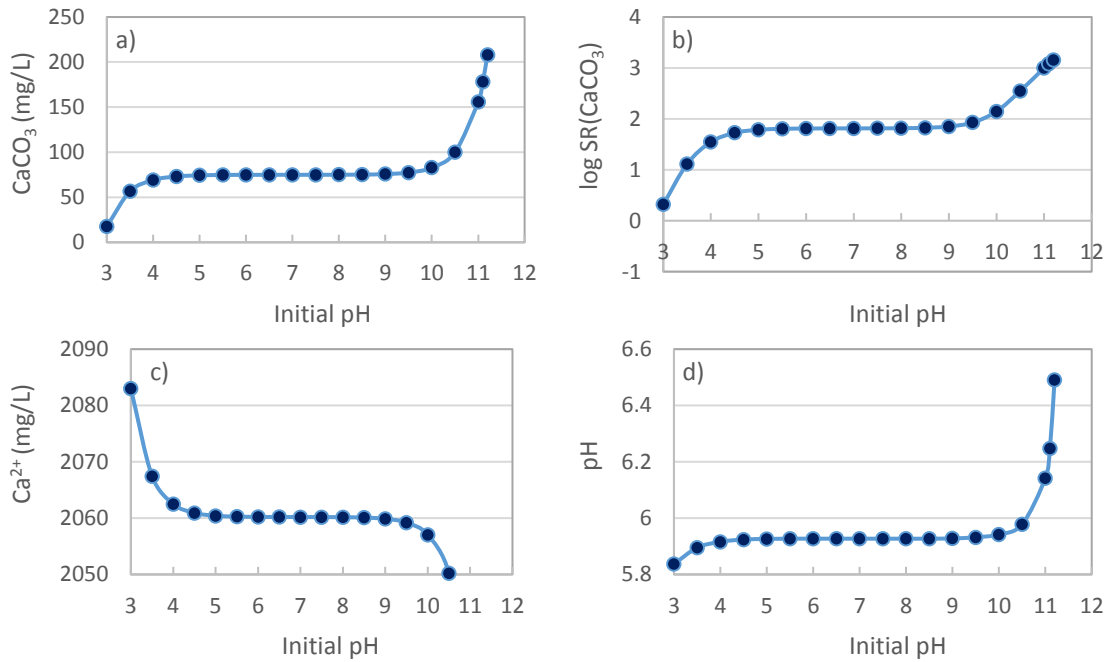


Figure 3.8 – Results for the precipitation of CaCO_3 scale as a function of initial pH [a] on figure]. The CaCO_3 saturation ratio, the concentration of Ca^{2+} , and the pH are also plotted as a function of initial pH [b), c), and d) on figure].

Results in Figure 3.8 show that the precipitation of CaCO_3 has a plateau for initial pH values between approximately 4 and 10. As seen, the precipitation of CaCO_3 depends on the system pH. Thus, analysing the system pH (equilibrium pH) as a function of the initial pH [Figure 3.8 d)], it is clear that the system pH has a plateau for initial pH values between 4 and 10 – and this is the reason why CaCO_3 also has a plateau. In addition, I can say that the system is not really sensitive to the initial pH value used for the range 4 to 10. This observation is somehow expected, since there is also HCO_3^- in the system which contributes dominantly to the acid equilibrium.

An important point to note in the definition and specifying the “initial pH” described above, is that it must be done (or the equations are incomplete). In my code, this is very explicit and it is clearly evident exactly what is done. However, in various commercial

codes this may be done in a rather “default” fashion which may not be transparent to the user. For example, it is evident from the results in Figure 3.8 above, that a rather benign assumption would be to set initial pH = 7. But, something is done in all codes to specify an “initial pH”, and the user should be completely clear exactly what this is.

3.2.4 Co-precipitation of CaCO_3 with FeCO_3 and FeS

CaCO_3 can co-precipitate with other pH-dependent scales such as FeCO_3 and FeS , and the precipitation of one scale can impact the precipitation of the other scales. For example, the precipitation of FeCO_3 in a solution super-saturated with respect to CaCO_3 and FeCO_3 , can render the solution under-saturated with respect to CaCO_3 . In other words, the precipitation of FeCO_3 can impact the solubility of CaCO_3 . Although a calculation is required to assess which pH-dependent scales precipitate for a given set of initial conditions, it is nevertheless important to have an *approximate idea* of the difference in orders of magnitude between the solubility products of the different scales. The solubility products in $(\text{mol/L})^2$ for CaCO_3 , FeCO_3 , and FeS , at 1 bar and 25°C are given by (Möller, 2015):

$$K_{sp, \text{ CaCO}_3} = 3.4 \times 10^{-9} \quad (3.78)$$

$$K_{sp, \text{ FeCO}_3} = 3.1 \times 10^{-11} \quad (3.79)$$

$$K_{sp, \text{ FeS}} = 8 \times 10^{-19} \quad (3.80)$$

Thus, for these conditions I have $K_{sp, \text{ FeS}} << K_{sp, \text{ FeCO}_3} < K_{sp, \text{ CaCO}_3}$, i.e. FeS has by far the lowest solubility of the three scales, followed by FeCO_3 and then CaCO_3 . This means that, although I require a calculation to know which scale(s) precipitates for a given set of initial conditions, I can nevertheless make educated guesses in this respect. For example, in a CO_2 and H_2S -rich environment, if Fe^{2+} is present, then it should most probably precipitate preferentially as FeS . If Ca^{2+} is also present, then FeCO_3 should precipitate preferentially to CaCO_3 (if there is sufficient excess Fe^{2+} in solution after FeS precipitation).

Although I can have an indication of which scale precipitates for a given set of initial conditions, I always require a calculation to accurately assess scaling potentials. In fact,

I will show below that, depending on the conditions, there are *transition zones* for the precipitation of CaCO_3 , FeCO_3 , and FeS . Table 3.3 presents the water composition used in a simulation to exemplify the co-precipitation of CaCO_3 and FeCO_3 in a CO_2 -environment. Calculations were carried out at 100 bar and 80 °C.

Table 3.3 – Water composition used to study the co-precipitation of CaCO_3 scale with FeCO_3 and FeS
(adapted from Mackay and Martins de Souza, 2014).

Component	Concentration (mg/L)
Na^+	25265
K^+	495
Mg^{2+}	875
Ca^{2+}	100
Ba^{2+}	35
Sr^{2+}	210
Fe^{2+}	30
Cl^-	44375
SO_4^{2-}	0
CO_2	-
HCO_3^-	0 to 5000
CO_3^{2-}	-
pH	7

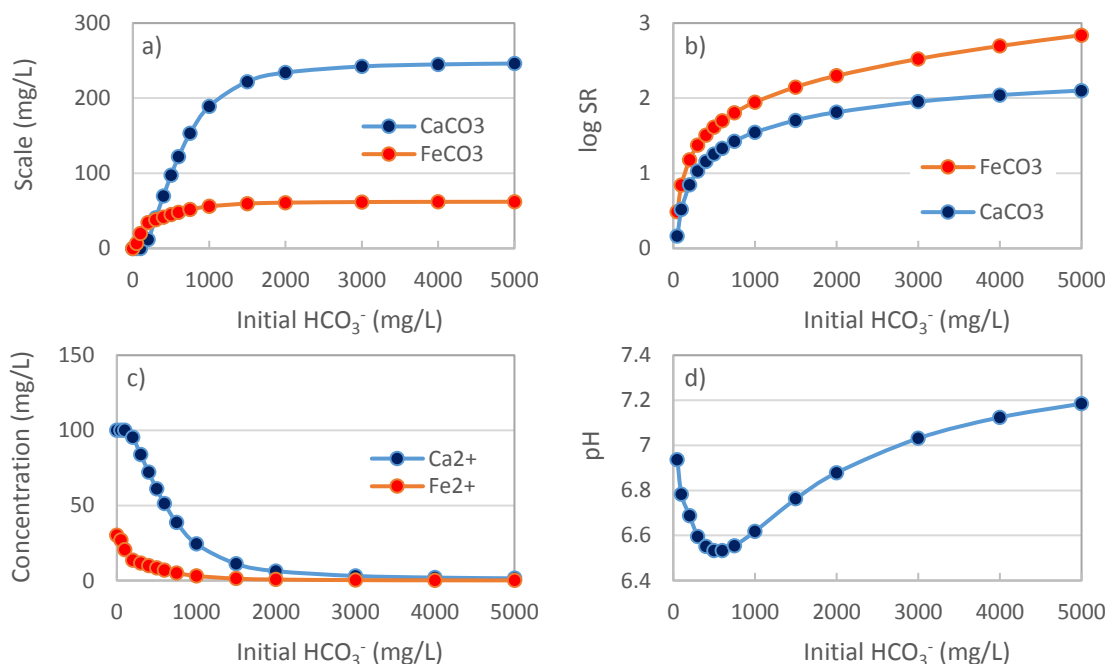


Figure 3.9 – Results for the precipitation of CaCO_3 and FeCO_3 scales as a function of initial HCO_3^- [a] on figure]. The CaCO_3 and FeCO_3 saturation ratios, the concentrations of Ca^{2+} and Fe^{2+} , and the pH are also plotted as a function of initial HCO_3^- [b), c), and d) on figure].

The initial concentration of HCO_3^- was varied between 0 and 5000 mg/L and the precipitation of CaCO_3 and FeCO_3 was assessed, as well as the respective saturation ratios, the concentrations of Ca^{2+} and Fe^{2+} , and the pH, as shown in Figure 3.9.

Results in Figure 3.9 show that:

- Both CaCO_3 and FeCO_3 precipitate in the system [Figure 3.9 a)]. For low HCO_3^- concentrations, the precipitation of FeCO_3 is higher than it is for CaCO_3 . However, as the concentration of HCO_3^- increases, the precipitation of CaCO_3 eventually exceeds the precipitation of FeCO_3 .
- Although the concentration of Ca^{2+} is higher than the concentration of Fe^{2+} , 100 and 30 mg/L, respectively, the saturation ratio for FeCO_3 is higher than it is for CaCO_3 [Figure 3.9 b)]. This is due to the difference in the respective solubility products, i.e. the solubility product for FeCO_3 is significantly lower than it is for CaCO_3 .
- The concentrations of Ca^{2+} and Fe^{2+} [Figure 3.9 c)] follow the inverse trend of that of the precipitation of CaCO_3 and FeCO_3 , respectively.
- There are two factors that contribute to the pH profile in Figure 3.9 d): precipitation of CaCO_3 and FeCO_3 that reduces the concentration of CO_3^{2-} , thus decreasing the pH; and the addition of HCO_3^- to the system, causing an increase in the pH.

If H_2S is also present in the system, then Fe^{2+} can also precipitate as FeS . In this context, I run another simulation to assess the precipitation of CaCO_3 , FeCO_3 , and FeS by using the same conditions as in Table 3.3 (setting the concentration of HCO_3^- equal to 1000 mg/L) for 100 bar and 80 °C, but changing the initial concentration of H_2S between 0 and 600 mg/L, as shown in Figure 3.10.

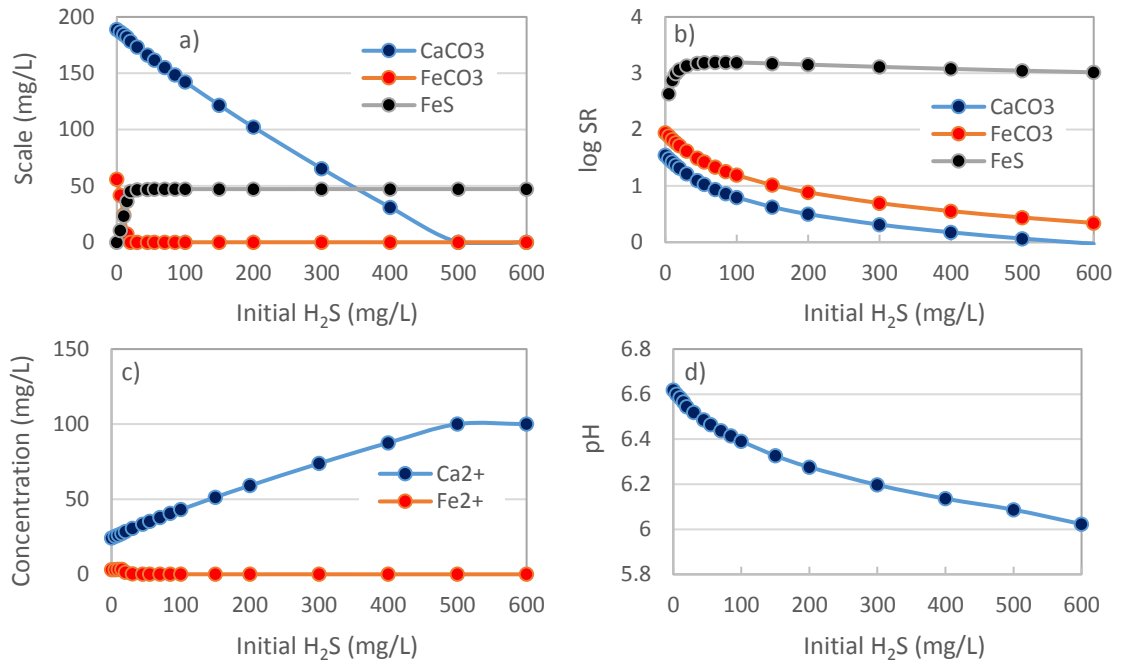


Figure 3.10 – Results for the precipitation of CaCO_3 , FeCO_3 , and FeS scales as a function of initial H_2S [a) on figure]. The CaCO_3 , FeCO_3 , and FeS saturation ratios, the concentrations of Ca^{2+} and Fe^{2+} , and the pH are also plotted as a function of initial H_2S [b), c), and d) on figure].

Results in Figure 3.10 show that:

- For very low concentrations of H_2S , Fe^{2+} precipitates preferentially as FeCO_3 [Figure 3.10 a)], despite the saturation ratio of FeS being higher than the saturation ratio of FeCO_3 [Figure 3.10 b)]. This behaviour is due to S^{2-} being the limiting reactant in the FeS precipitation reaction for low concentrations of H_2S . There is a clear inversion of the precipitation of FeCO_3 and FeS as the concentration of H_2S increases – in fact, if S^{2-} is not the limiting reactant, then all Fe^{2+} available precipitates as FeS .
- The precipitation of CaCO_3 decreases with increasing concentrations of H_2S [Figure 3.10 a)]. This behaviour is expected since the pH decreases with increasing concentrations of H_2S [Figure 3.10 d)], and, as seen before in Section 3.2.3, if the pH decreases, then the solubility of CaCO_3 increases.
- Due to the very low solubility of FeS , the concentration of Fe^{2+} in solution is negligible [Figure 3.10 c)]. In fact, this is an important feature of sulphide systems: if there is a source of Fe^{2+} in an H_2S -rich system – for example, from

corrosion of steel pipes –, then virtually all Fe^{2+} *should* precipitate as FeS . This is a generalisation that needs to be confirmed with calculations – in fact, for very acidic pH levels, it is possible to have Fe^{2+} in solution in an H_2S -rich environment. However, this feature of the sulphide system can be used as a rule of thumb in many scenarios.

I extend the discussion in this last point to study a scenario where Fe^{2+} initially precipitates as FeS , but then it changes with increasing concentration of HCO_3^- to precipitate preferentially as FeCO_3 . Figure 3.11 shows these results for the initial conditions presented in Table 3.3 (the concentration of H_2S is now fixed at 10 mg/L) for 100 bar and 80 °C.

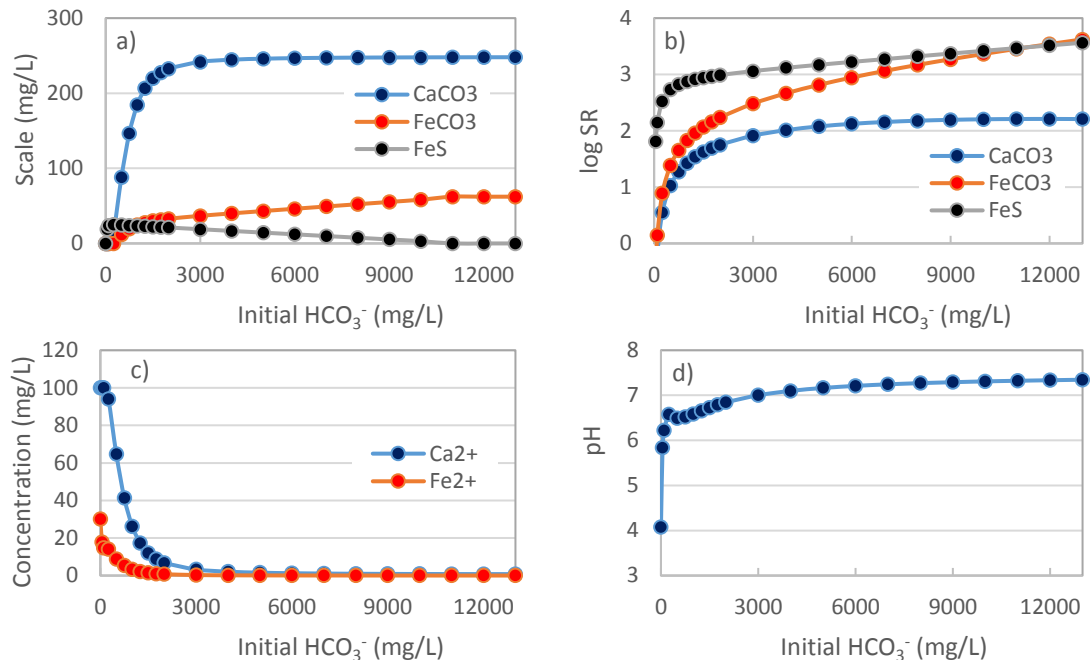


Figure 3.11 – Results for the precipitation of CaCO_3 , FeCO_3 , and FeS scales as a function of initial HCO_3^- [a] on figure]. The CaCO_3 , FeCO_3 , and FeS saturation ratios, the concentrations of Ca^{2+} and Fe^{2+} , and the pH are also plotted as a function of initial HCO_3^- [b), c), and d) on figure].

Results in Figure 3.11 show that Fe^{2+} precipitates preferentially as FeS for low concentrations of HCO_3^- , but this preference is inverted to FeCO_3 for high concentrations of HCO_3^- . It is important to understand these “transition zones” in designing scale management strategies – e.g. in the selection of parameters for sensitivity analyses.

Results in Figure 3.9, Figure 3.10, and Figure 3.11 clearly show the inter-dependence of the precipitation of CaCO_3 with FeCO_3 , and FeS . Thus, it is always necessary to account for the precipitation of all pH-dependent scales when running calculations to assess the precipitation of CaCO_3 .

3.2.5 *Mixing of two chemically incompatible waters*

In carbonate reservoirs, CaCO_3 scale forms in CO_2 -rich production systems due to an autoscaling process, as explained previously. CaCO_3 can also form due to the mixing of two chemically incompatible waters, but this is a different scale formation mechanism. Understanding these two mechanisms is fundamental in modelling CaCO_3 scale. In an autoscaling process as studied here, CaCO_3 forms as a *continuum* process, i.e. it forms as pressure changes in the production system – this change is not usually abrupt, and it often occurs over long lengths in the production system. (I note that more sudden changes can occur such as when fluids go through an Electrical Submersible Pump [ESP]). However, when CaCO_3 scale forms due to the mixing of two waters, there is a *thermodynamic shock*, and this process of scale formation can be thought of as being *discrete*, i.e. scale precipitates promptly at the mixing point.

Alongside CaCO_3 , BaSO_4 is a common oilfield scale. In fact, BaSO_4 formation due to the mixing of two chemically incompatible waters is one of the most common scaling issues. In detail, BaSO_4 forms due to the mixing of seawater, which is rich in sulphate ions, SO_4^{2-} , with formation water, which is rich in barium ions, Ba^{2+} . My model can also easily deal with such a mechanism.

Table 3.4 presents the composition of the formation water and seawater used in calculations (data adapted from Mackay and Martins de Souza, 2014). Calculations were run at 1 bar and 25°C.

Figure 3.12 shows the results obtained for the precipitated mass of BaSO_4 , SrSO_4 , and CaSO_4 , and respective saturation ratios as a function of the mixing percentage between formation water and seawater.

Table 3.4 – Formation water and seawater compositions used to study the scale formation mechanism due to the mixing of two chemically incompatible waters (adapted from Mackay and Martins de Souza, 2014).

Component	Formation water mg/L	Seawater mg/L
Na^+	25265	10319
K^+	495	397
Mg^{2+}	875	1379
Ca^{2+}	2090	446
Ba^{2+}	35	0
Sr^{2+}	210	8
Cl^-	44375	17203
SO_4^{2-}	0	3000
pH	7	7

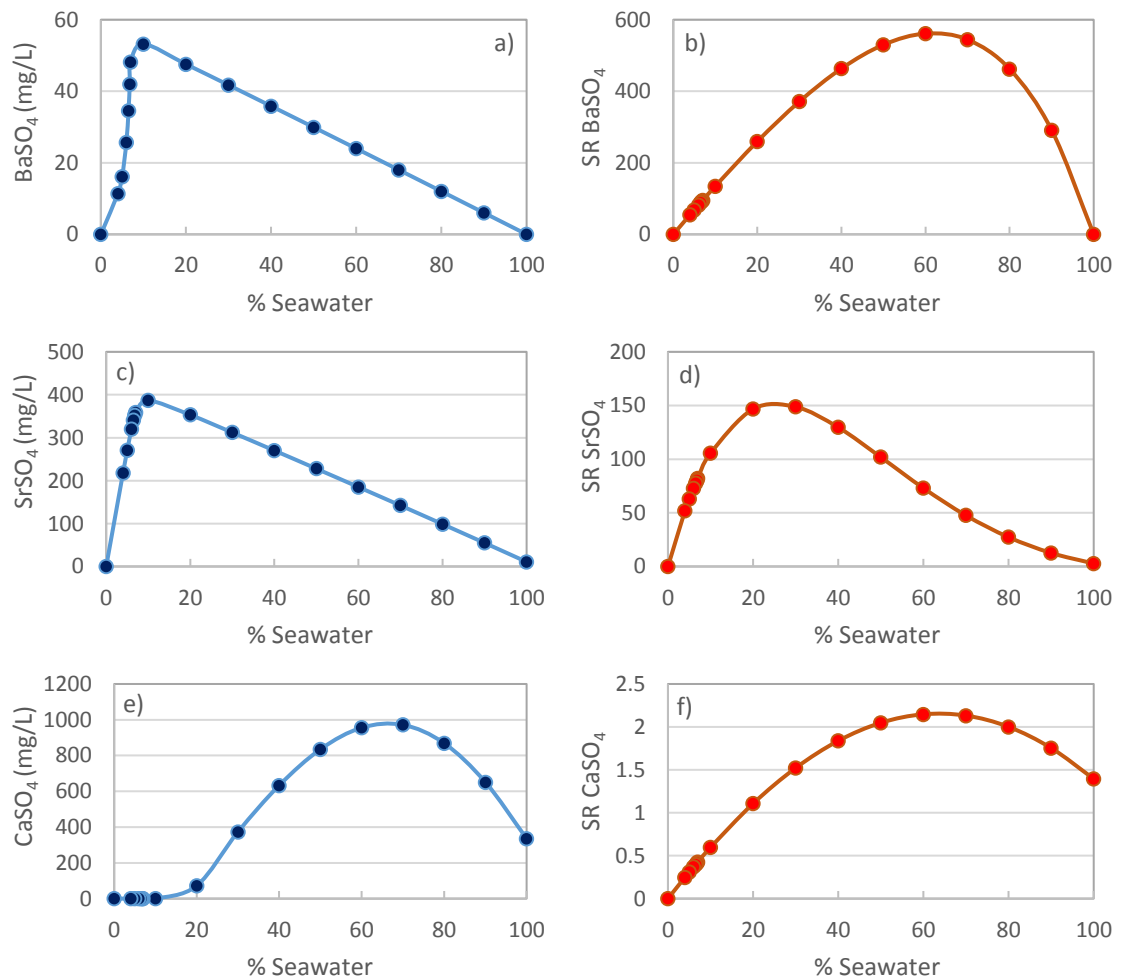


Figure 3.12 – Precipitation of BaSO_4 , SrSO_4 , and CaSO_4 as a function of the percentage of seawater [a), c), and e) on figure], and respective saturation ratios [b), d), and f) on figure].

Alongside the results showed in Figure 3.12, I also plot the concentration of the scaling ions, i.e. Ba^{2+} , Sr^{2+} , Ca^{2+} , and SO_4^{2-} , as a function of the mixing percentage between formation water and seawater, as shown in Figure 3.13.

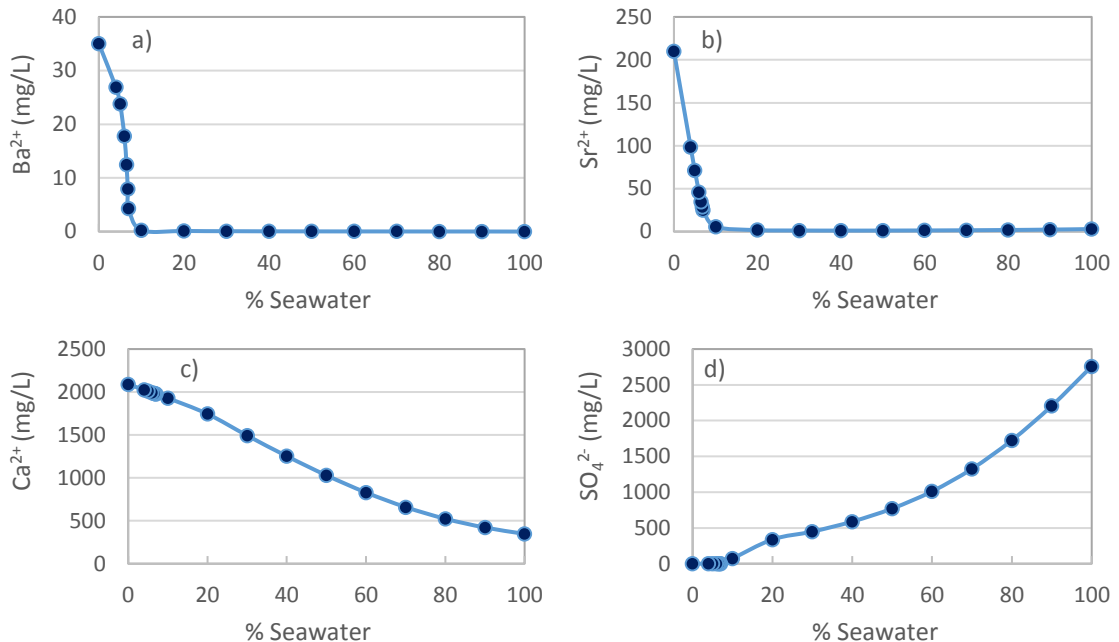


Figure 3.13 – Concentrations of Ba^{2+} , Sr^{2+} , Ca^{2+} , and SO_4^{2-} as a function of the percentage of seawater [a), b), c), and d) on figure].

Results in Figure 3.12 and Figure 3.13 show that:

- All Ba^{2+} and Sr^{2+} in solution precipitate as BaSO_4 and SrSO_4 , respectively – note that for a low percentage of seawater, SO_4^{2-} is the limiting reactant.
- Ca^{2+} precipitates as CaSO_4 , but not entirely, since CaSO_4 is much more soluble than BaSO_4 and SrSO_4 .

These results are in agreement with the results found in the literature for sulphate scales (e.g. Shaw et al., 2012). CaCO_3 scale formation in CO_2 WAG processes, as studied here, should be addressed as an autoscaling process, and not as a mixture of two chemically incompatible waters. In fact, this distinction between scale formation mechanisms has many implications, including: i) in the modelling approach, ii) in the design of laboratory experiments, iii) in the selection of scale inhibitor deployment techniques, etc. These implications will be further addressed in Chapter 5. However, I note that both

mechanisms of scale formation can co-exist, and, if so, they must be modelled accordingly.

3.3 Conclusions and recommendations

Modelling the precipitation of CaCO_3 scale in CO_2 WAG production systems due to de-pressureurisation starts inevitably with modelling the precipitation of CaCO_3 . CaCO_3 is a pH-dependent scale, i.e. its solubility depends on the pH of the system, and so this scale depends on all species that have an impact on the system pH such as CO_2 , H_2S , organic acids, etc. In addition, the precipitation of other pH-dependent scales such as FeCO_3 and FeS also impact the acid equilibrium – and thus the solubility of CaCO_3 –, and, therefore, they must also be accounted for. In sum, building an aqueous model to predict the precipitation of CaCO_3 requires building a *general* scale prediction model.

In this context, an aqueous scale prediction model has been built using the Pitzer equations as the electrolyte model. The following points have been addressed in this chapter:

- Pitzer electrolyte model. The Pitzer equations have been implemented and results for the calculation of activity coefficients were compared with the results obtained by using Multiscale – a good match has been obtained by using both models. In addition, experimental solubility data for CaCO_3 , BaSO_4 , and NaCl has been used to validate the model. Furthermore, these equations have been used to calculate activity coefficients of ions – Na^+ , K^+ , Cl^- , HCO_3^- , etc. – which have then been used to calculate the non-ideal behaviour of aqueous phases.
- One novel feature of the aqueous electrolyte model presented here is that I solve the (reduced) equations for *all* the possible scaling cases which occur (e.g. 8 cases if there are 3 possible insoluble scales in the system), and then identify the *unique* one which is correct (a proof of uniqueness is supplied).
- General scale prediction calculations. My aqueous scale prediction model has the facility of calculating the precipitation of CaCO_3 , FeCO_3 , FeS , BaSO_4 , SrSO_4 , and CaSO_4 for water chemistries commonly found in the context of oilfield scale. A simulation using my model for the precipitation of these scales has been

performed; then, results have been compared, and thus validated, with the results obtained for the same simulation by using Multiscale.

- Solubility of CaCO_3 scale. I have clearly shown that the solubility of CaCO_3 depends on the acid equilibrium, and that the solubility of CaCO_3 increases as the pH of the system decreases. Further, I have demonstrated the impact of components that contribute to the system pH, such as CO_2 , H_2S , and organic acids, on the precipitation of CaCO_3 scale.
- Co-precipitation of CaCO_3 with FeCO_3 and FeS . I have clearly shown the inter-dependency of the precipitation of pH-dependent scales, exemplified in my simulations with CaCO_3 , FeCO_3 , and FeS scales. In addition, I have shown that there are transition zones, i.e. conditions for which a small perturbation in the system causes the scale precipitation profile to change abruptly, that should therefore be considered in sensitivity analyses.
- Mixing of two chemically incompatible waters. CaCO_3 scale forms in CO_2 WAG production systems due to an *autoscaling* mechanism. Another important scale formation mechanism is the mixing of two chemically incompatible waters. These two mechanisms are inherently *different*, and they should be modelled accordingly. I have shown that my model can simulate scale formation due to the mixing of two chemically incompatible waters (in the example run here, I have tested the *classical* mixing of seawater and formation water).

The electrolyte model that calculates the non-ideal behaviour of the aqueous phase is key in scale prediction calculations. For the electrolyte systems found in the context of oilfield scale, I believe that the Pitzer model is the most complete model, since it relies on readily available experimental data. In fact, the oil industry has arguably been a driving force for generating experimental data required from many oilfield related applications, such as the prediction of mineral scale precipitation as studied here. However, other electrolyte models are currently being developed, and attention should be paid to Equations of State that calculate the non-ideal behaviour of the aqueous phase for electrolyte systems, since they have the potential of calculating phase equilibria (for solid, water, vapour, and liquid) by using only one equation, and thus avoiding issues in using different thermodynamic models, such as using different thermodynamic reference states, etc.

4. Vapour-Liquid Equilibrium

In CO₂ WAG schemes, the dissolution of gaseous CO₂ in the aqueous phase in the reservoir causes the dissolution of CaCO₃ rock that can then re-precipitate as CaCO₃ scale during production. In fact, the evolution of CO₂ from the aqueous phase to the vapour phase due to the decrease of pressure during production is the driving force for this mechanism of CaCO₃ scale precipitation. In addition, the solubility of gaseous H₂S in the aqueous phase also impacts the dissolution and precipitation of CaCO₃, since it affects the system pH. Thus, the solubility of acid and sour gases, i.e. CO₂ and H₂S, in water must be addressed in the context of CaCO₃ scale precipitation in CO₂ WAG schemes.

The solubility of acid and sour gases in water is modelled in thermodynamics by utilizing Vapour-Liquid Equilibrium (VLE) calculations. However, there are many VLE models available in the literature. This observation is patent in the availability of Equations of State (EOS) to model the non-ideal behaviour of a vapour phase – e.g. Soave-Reddlich-Kwong, Peng-Robinson, Patel-Teja, Duan and Sun, among others. Here, in my model I actually implement 6 VLE models with EOS that are commonly used in the oil and gas industry (e.g. SRK and PR EOS), or that have been developed specifically to model the solubility of CO₂ in the aqueous phase (e.g. Duan and Sun EOS), although other VLE models could also be considered. I note that even some prominent commercial software models, e.g. Scalechem, only have one EOS implemented (SRK) and there is no evidence that this is the “best” for all applications.

Thus, the objective in this chapter is to couple VLE calculations with the aqueous scale prediction model developed in Chapter 3 in the context of CaCO₃ scale precipitation in CO₂ WAG schemes. In particular, my work programme to achieve this has carried out the following tasks:

- i) Review of VLE models available in the literature.
- ii) Validation of 6 VLE models with experimental data.
- iii) Study the impact of different VLE models on scale prediction calculations.
- iv) Model the precipitation of CaCO₃ in production systems due to the evolution of CO₂ from the water to the vapour phase caused by depressurisation.

4.1 Thermodynamic models

The condition for thermodynamic equilibrium of a liquid mixture with a vapour at a specific pressure and temperature is given, for every component i in the mixture, by:

$$f_i^L = f_i^V \quad (4.1)$$

Where f_i^L and f_i^V are respectively the fugacities of component i in the liquid and vapour phases. VLE calculations are generally categorised into two groups, depending on the treatment of the non-ideal behaviour in the liquid phase (Springer et al., 2012) where the notation below should be read as, γ = activity, φ = EOS:

- $\gamma - \varphi$ approach, where an activity model such as NRTL, UNIQUAC, Pitzer, etc. is used to describe the behaviour of the aqueous phase and an EOS is used to describe the behaviour of the vapour phase.
- $\varphi - \varphi$ approach, where an EOS is used to describe the behaviour of both liquid and vapour phases.

4.1.1 $\gamma - \varphi$ approach

In the $\gamma - \varphi$ approach, the fugacity of component i in the liquid phase is expressed in terms of activity coefficients, γ_i , as:

$$f_i^L = a_i f_i^0 = \gamma_i x_i f_i^0 \quad (4.2)$$

Where a_i x_i and f_i^0 are the activity, the aqueous molar fraction and the standard-state fugacity of component i in the mixture, respectively. The standard-state fugacity dependence with pressure at constant temperature is given by:

$$\left(\frac{\partial \ln f_i^0}{\partial P} \right)_T = \frac{v_i^\infty}{RT} \quad (4.3)$$

Where v_i^∞ is the partial molar volume at infinite dilution of component i . Henry's law is now introduced as:

$$H_{i,j} = \lim_{x_i \rightarrow 0} \frac{f_i^L}{x_i} \quad (4.4)$$

Where $H_{i,j}$ is the Henry's constant for solute i in solvent j . Equation (4.3) is then integrated from the vapour pressure of the solvent to the working pressure giving:

$$f_i^0 = H_{i,j} \exp \int_{P_{vp}}^P \frac{v_i^\infty}{RT} dP \quad (4.5)$$

The fugacity of component i in the vapour phase is given by:

$$f_i^V = y_i \phi_i^V P \quad (4.6)$$

Combining Equations (4.1), (4.2), (4.5) and (4.6) yields:

$$y_i \phi_i^V P = x_i \gamma_i H_{i,j} \exp \int_{P_{vp}}^P \frac{v_i^\infty}{RT} dP \quad (4.7)$$

Lastly, assuming that v_i^∞ is constant in the pressure range between the vapour pressure of the solvent and the operating pressure and after some algebraic manipulations, Equation (4.7) becomes:

$$x_i = \frac{y_i \phi_i^V P}{\gamma_i H_{i,j}} \exp \left[-\frac{(P - P_{vp}) \bar{v}_i^\infty}{RT} \right] \quad (4.8)$$

Equation (4.8) is the working equation for VLE calculations in the $\gamma - \varphi$ approach. For water, the fugacity is given by:

$$f_w^L = \gamma_w^L \phi_w^{sat} P_w^{sat} x_w(T) \exp \left[\frac{v_w^{sat}(T)}{RT} (P - P_w^{sat}) \right] \quad (4.9)$$

Where the subscript w stands for water and the superscript sat stands for saturated.

4.1.2 $\varphi - \varphi$ approach

In the $\varphi - \varphi$ approach, an EOS is used to describe the behaviour of both the liquid and vapour phases. Hence, Equation (4.1) becomes:

$$x_i \phi_i^L = y_i \phi_i^V \quad (4.10)$$

For a binary system of components 1 and 2 (for example, CO₂ and H₂O), Equation (4.10) can be re-written as:

$$\begin{cases} x_1\phi_1^L = y_1\phi_1^V \\ (1-x_1)\phi_2^L = (1-y_1)\phi_2^V \end{cases} \quad (4.11)$$

Privat et al., 2013 suggested an algorithm to solve Equation (4.11) and find the molar compositions of components 1 and 2 in the liquid and vapour phases at a given pressure and temperature. This algorithm considers the following steps (also shown in Figure 4.1):

1. Take an initial guess for $x_1^{(0)}$ and $y_1^{(0)}$ [for example, $x_1^{(0)} = 0.01$ and $y_1^{(0)} = 0.99$].
2. Calculate the fugacity coefficients for components 1 and 2 in the liquid and vapour phases using an EOS.
3. Check convergence by setting $\delta = [|x_1\phi_1^L - y_1\phi_1^V| + |(1-x_1)\phi_2^L - (1-y_1)\phi_2^V|]^{(k)}$. If $\delta < \varepsilon$ (where ε is the precision), then the algorithm has converged and the procedure is terminated.
4. Calculate $x_1^{(k+1)}$ and $y_1^{(k+1)}$ as:

$$\begin{cases} x_1^{(k+1)} = \left[\frac{\phi_1^V(\phi_2^V - \phi_2^L)}{\phi_1^L\phi_2^V - \phi_1^V\phi_2^L} \right]^{(k)} \\ y_1^{(k+1)} = x_1^{(k+1)} \left(\frac{\phi_1^L}{\phi_1^V} \right)^{(k)} \end{cases} \quad (4.12)$$

5. Set $k = k + 1$ and return to step 2.

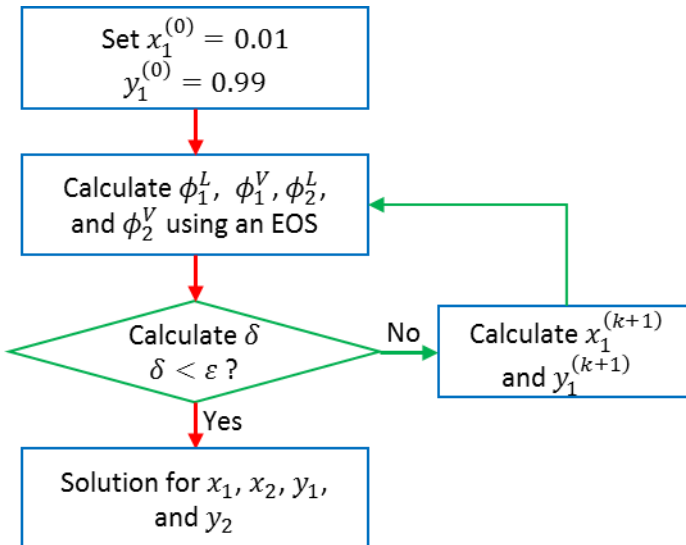


Figure 4.1 - Flowchart of the iterative algorithm for calculating the molar compositions of the liquid and vapour phases of a binary system at a given pressure and temperature (adapted from Privat et al., 2013).

The above procedure can be generalised for multicomponent mixtures (e.g. Privat et al., 2013) and, in this case, linear programming techniques should be utilized for maximum computational efficiency.

4.1.3 Equations of State (EOS) and fugacity coefficients

An EOS is used to calculate the fugacity coefficients of component i in the vapour and liquid phases, ϕ_i^V and ϕ_i^L respectively. Figure 4.2 shows a possible classification of the various EOS available in the literature (adapted from Valderrama, 2003). In this work, I investigate the virial-type EOS as proposed by Duan and Sun, 2003 and the cubic EOS.

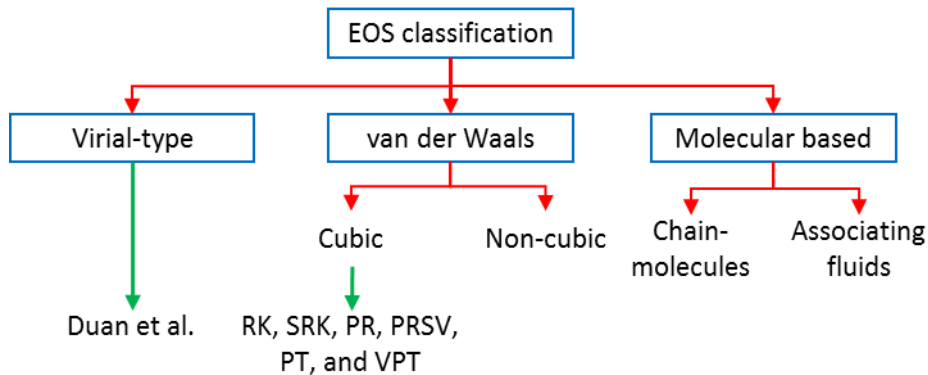


Figure 4.2 – Classification of the EOS available in the literature (adapted from Valderrama, 2003). I investigate the virial and cubic van der Waals-type EOS.

Most common cubic EOS can be described in only one general expression with four parameters a , b , u and w (Muller and Olivera-Fuentes, 1989) as:

$$P = \frac{RT}{v - b} - \frac{a}{v(v + ub) + wb^2} \quad (4.13)$$

Alternatively, Equation (4.13) can be written in terms of the compressibility factor, Z , as:

$$Z^3 + [(u - 1)B - 1]Z^2 + [(w - u)B^2 - uB + A]Z - [w(B^2 + B^3) + AB] = 0 \quad (4.14)$$

Where

$$A = \frac{aP}{(RT)^2}; \quad B = \frac{bP}{RT} \quad (4.15)$$

Parameters u and w for six common EOS used in VLE calculations are given in Table 4.1 (van der Waals EOS is also included here for its historical value).

Table 4.1 – Parameters u and w for Equation (4.13) for seven different EOS.

Equation of state	Abbreviation	u	w
van der Waals, 1873	vdW	0	0
Redlich and Kwong, 1949	RK	1	0
Soave, 1972	SRK	1	0
Peng and Robinson, 1976	PR	2	-1
Stryjek and Vera, 1986b	PRSV	2	-1
Patel and Teja, 1982	PT	$(b + c)/b$	$-c/b$
Valderrama, 1990	VPT	$(b + c)/b$	$-c/b$

Parameters a , b and c for SRK, PR, PRSV, PT and VPT EOS are given by:

$$a = \Omega_a \frac{(RT_c)^2}{P_c} \alpha; \quad b = \Omega_b \frac{RT_c}{P_c}; \quad c = \Omega_c \frac{RT_c}{P_c} \quad (4.16)$$

Values for Ω_a , Ω_b and Ω_c are given in Table 4.2.

Table 4.2 – Ω_a , Ω_b and Ω_c values for SRK, PR, PRSV, PT and VPT EOS to be used in Equation (4.16). Z_c is the critical compressibility factor. Values for ζ_c in the PT EOS can be found in the original paper.

	Ω_a	Ω_b	Ω_c
Soave, 1972	0.42747	0.08664	0
Peng and Robinson, 1976	0.45724	0.07780	0
Stryjek and Vera, 1986b	0.457235	0.077796	0
Patel and Teja, 1982	$3\zeta_c^2 + 3(1 - 2\zeta_c)\Omega_b + \Omega_b^2 + 1 - 3\zeta_c$	Smallest positive root of: $\Omega_b^3 + (2 - 3\zeta_c)\Omega_b^2 + 3\zeta_c^2\Omega_b - \zeta_c^3 = 0$	$1 - 3\zeta_c$
Valderrama, 1990	$0.66121 - 0.76105Z_c$	$0.02207 + 0.20868Z_c$	$0.57765 + 1.87080Z_c$

The α function is equal to $1/T_r^{1/2}$ for the RK EOS. For the remaining EOS identified in Table 4.1, the α function can be written in the general form:

$$\alpha = [1 + F(1 - T_r^{1/2})]^2 \quad (4.17)$$

Where $T_r = T/T_c$ is the reduced temperature and F is a function specific to the EOS being used, as identified in Table 4.3. For water, I have used the α function as described in Coquelet et al., 2004.

Table 4.3 – Function F to be used in Equation (4.17). ω and Z_c are the acentric factor and the critical compressibility factor. κ_1 values are given in the original paper by Stryjek and Vera, 1986b. F values are given in the original paper by Patel and Teja, 1982.

EOS	Function F
SRK	$0.480 + 1.574\omega - 0.176\omega^2$
PR	$0.37464 + 1.54226\omega - 0.26992\omega^2$
PRSV	$\kappa_0 + \kappa_1(1 + T_r^{1/2})(0.7 - T_r)$ where $\kappa_0 = 0.378893 + 1.4897153\omega - 0.17131848\omega^2 + 0.0196554\omega^3$
PT	F is treated as an adjustable empirical parameter
VPT	$0.46283 + 3.58230(\omega Z_c) + 8.19417(\omega Z_c)^2$

In a gas mixture, parameters a , b , u and w are dependent on the composition according to the mixing rule used. For gas mixtures, a , b and c in Equation (4.16) should be replaced

by a_{mix} , b_{mix} and c_{mix} . a_{mix} , b_{mix} and c_{mix} are calculated using a mixing rule and, with the exception of RK EOS, all other EOS identified in Table 4.1 use the classical van der Waals mixing rules:

$$a_{mix} = \sum_i \sum_j x_i x_j (a_i a_j)^{1/2} (1 - k_{ij}); \quad b_{mix} = \sum_i x_i b_i; \quad c_{mix} = \sum_i x_i c_i \quad (4.18)$$

Where k_{ij} is the Binary Interaction Coefficient (BIP) between the components i and j . The fugacity coefficient of component i in the mixture is defined as (Prausnitz et al., 1999):

$$\ln \phi_i = \frac{1}{RT} \int_V^\infty \left[\left(\frac{\partial P}{\partial n_i} \right)_{T,V,n_j} - \frac{RT}{V} \right] dV - \ln Z \quad (4.19)$$

Equation (4.19) can be re-written in terms of the compressibility factor, Z , as shown in Equations (4.21), (4.23) and (4.25) for SRK, PR and PT EOS, respectively. In practice, the calculation of fugacity coefficients is preceded by the calculation of the compressibility factor. The expressions to calculate compressibility factors are thus also written explicitly in Equations (4.20), (4.22) and (4.24) for the respective EOS. A general expression to calculate fugacity coefficients and respective thermodynamic derivation can be found in Muller and Olivera-Fuentes, 1989, and (Poling et al., 2001).

Redlich-Kwong EOS modified by Soave (SRK)

$$Z^3 - Z^2 + (A - B - B^2)Z - AB = 0 \quad (4.20)$$

$$\ln \phi_i = \frac{b_i}{b}(Z - 1) - \ln(Z - B) - \frac{A}{B} \left(2 \frac{a_i^{0.5}}{a^{0.5}} - \frac{b_i}{b} \right) \ln \left(1 + \frac{B}{Z} \right) \quad (4.21)$$

Peng-Robinson (PR) EOS

$$Z^3 - (1 - B)Z^2 + (A - 3B^2 - 2B)Z - (AB - B^2 - B^3) = 0 \quad (4.22)$$

$$\ln \phi_i = \frac{b_i}{b}(Z - 1) - \ln(Z - B) - \frac{A}{2\sqrt{2}B} \left(2 \sum_j y_j a_{ij} - \frac{b_i}{b} \right) \ln \left(\frac{Z + (\sqrt{2} + 1)B}{Z - (\sqrt{2} - 1)B} \right) \quad (4.23)$$

Patel-Teja (PT) EOS

$$Z^3 + (C - 1)Z^2 + (A - 2BC - B - C - B^2)Z - (BC - B^2C - AB) = 0 \quad (4.24)$$

$$\begin{aligned} RT \ln \phi_i = & -RT \ln(Z - B) + RT \left(\frac{b_i}{v - b} \right) - \frac{1}{d} \sum_j y_j a_{ij} \ln \left(\frac{Q + d}{Q - d} \right) + \frac{a(b_i + c_i)}{2(Q^2 - d^2)} \\ & + \frac{a}{8d^3} [c_i(3b + c) + b_i(3c + b)] \left[\ln \left(\frac{Q + d}{Q - d} \right) + \frac{2Qd}{Q^2 - d^2} \right] \end{aligned} \quad (4.25)$$

$$\text{Where } v = ZRT/P, \quad Q = v + \frac{b+c}{2} \quad \text{and} \quad d = \sqrt{bc + \frac{(b+c)^2}{4}}$$

4.1.4 Søreide and Whitson solubility model

Søreide and Whitson, 1992, proposed a model to calculate the solubility of hydrocarbon mixtures in brine (NaCl salinity) at high pressures and temperatures. These authors proposed two modifications to the PR EOS. First, the attraction term a in the PR EOS was modified to include the dependency of NaCl salinity and pure water reduced temperature. Second, following the modification proposed by Peng and Robinson, 1980, of the PR EOS to include two sets of Binary Interaction Parameters (BIPs) for water-hydrocarbon mixtures, Søreide and Whitson derived their own expressions for both aqueous and non-aqueous BIPs, k_{ij}^{AQ} and k_{ij}^{NA} . Thus, the following expression was proposed for calculating the α -term for water as a function of NaCl salinity (c_{sw} , in molality) and pure water reduced temperature, T_r :

$$\alpha^{1/2} = 0.4530[1 - T_r(1 - 0.0103c_{sw}^{1.1})] + 0.0034(T_r^{-3} - 1) \quad (4.26)$$

And the following expressions were proposed to calculate the aqueous and non-aqueous BIPs for CO₂, H₂S and CH₄:

$$\begin{aligned} k_{ij}^{AQ}(\text{CO}_2/\text{NaCl brine}) &= -0.31092(1 + 0.15587c_{sw}^{0.7505}) \\ &+ 0.23580(1 + 0.17837c_{sw}^{0.979})T_{r,i} \\ &- 21.2566 \exp(-6.7222T_{r,i} - c_{sw}) \end{aligned} \quad (4.27)$$

$$k_{ij}^{AQ}(H_2S/NaCl \text{ brine}) = -0.20441 + 0.23426T_{r,i} \quad (4.28)$$

$$\begin{aligned} k_{ij}^{AQ}(CH_4/NaCl \text{ brine}) \\ = & [1.1120 - 1.7369\omega_i^{-0.1}] [1 + (4.7863 \times 10^{-13}\omega_i^4)c_{sw}] \\ & + (1.1001 + 0.8360\omega_i)T_{r,i}(1 + 1.4380 \times 10^{-2}c_{sw}) \\ & + (-0.15742 - 1.0988\omega_i)T_{r,i}^2(1 + 2.1547 \times 10^{-3}c_{sw}) \end{aligned} \quad (4.29)$$

Non-aqueous BIPs for binary mixtures of water and CO₂, H₂S, and CH₄ are presented in Table 4.4. The $\varphi - \varphi$ approach was thus used to calculate the vapour-liquid equilibrium.

Table 4.4 – Non-aqueous BIPs for binary mixtures of water and CO₂, H₂S and CH₄.

Component	k_{ij}^{NA}
CO ₂	0.1896
H ₂ S	$0.19031 - 0.05965T_{r,H_2S}$
CH ₄	0.4850

4.1.5 Duan et al. CO₂ solubility model

Duan and Sun, 2003, proposed a model for CO₂ solubility in water and brine for temperatures from 0 to 260 °C, pressures from 0 to 2000 bar, and ionic strengths from 0 to 4.3 m. These authors developed a virial-type EOS to model the behaviour of the vapour phase and used the Pitzer equations to model the behaviour of the aqueous phase. This model has limited application since it only considers pure CO₂, but it can nevertheless be used in laboratory experiments. The working expression for the CO₂ solubility in water and brine is given by:

$$\begin{aligned} \ln \frac{y_{CO_2}P}{m_{CO_2}} = & \frac{\mu_{CO_2}^{l(0)}}{RT} - \ln \varphi_{CO_2} + \sum_c 2\lambda_{CO_2-c}m_c + \sum_a 2\lambda_{CO_2-a}m_a \\ & + \sum_c \sum_a \zeta_{CO_2-c-a}m_c m_a \end{aligned} \quad (4.30)$$

Where m_{CO_2} is the CO₂ molality, $\mu_{CO_2}^{l(0)}$ is the standard chemical potential, φ_{CO_2} is the fugacity coefficient, and λ and ζ are Pitzer second and third-order interaction parameters,

respectively (c stand for cations and a for anions). The molar fraction of CO₂ in the vapour phase, y_{CO_2} , is given by:

$$y_{CO_2} = \frac{P - P_{H_2O}}{P} \quad (4.31)$$

Where P_{H_2O} is the pure water pressure. Duan and Sun, 2003 proposed the following expression to calculate P_{H_2O} :

$$P = (P_c T / T_c) [1 + c_1(-t)^{1.9} + c_2 t + c_3 t^2 + c_4 t^3 + c_5 t^4] \quad (4.32)$$

Where T is the temperature in K, $t = (T - T_c)/T_c$, T_c and P_c are the critical temperature and pressure of water ($T_c = 647.29$ K and $P_c = 220.85$ bar), and the parameters $c_1 - c_5$ are given in Table 4.5.

Table 4.5 – Parameters $c_1 - c_5$ for Equation (4.32).

Parameters	
c_1	-38.640844
c_2	5.8948420
c_3	59.876516
c_4	26.654627
c_5	10.637097

$\mu_{CO_2}^{l(0)}/RT$, λ 's and ζ 's are calculated using the following expression:

$$\begin{aligned} Par(T, P) = & c_1 + c_2 T + c_3/T + c_4 T^2 + \frac{c_5}{(630 - T)} + c_6 P + c_7 P \ln T + \frac{c_8 P}{T} \\ & + \frac{c_9 P}{(630 - T)} + \frac{c_{10} P^2}{(630 - T)^2} + c_{11} T \ln P \end{aligned} \quad (4.33)$$

Where the parameters $c_1 - c_{11}$ are given in Table 4.6.

Table 4.6 – Parameters for Equation (4.33).

Parameters	$\mu_{CO_2}^{l(0)}/RT$	λ_{CO_2-Na}	$\zeta_{CO_2-Na-Cl}$
c_1	28.9447706	-0.411370585	3.36389723e-4
c_2	-0.0354581768	6.07632013e-4	-1.98298980e-5
c_3	-4770.67077	97.5347708	
c_4	1.02782768e-5		
c_5	33.8126098		
c_6	9.04037140e-3		
c_7	-1.14934031e-3		
c_8	-0.307405726	-0.0237622469	2.12220830e-3
c_9	-0.0907301486	0.0170656236	-5.24873303e-3
c_{10}	9.32713393e-4		
c_{11}		1.41335834e-5	

$\ln \varphi_{CO_2}$ is calculated using the following expression (developed by Duan et al., 1992):

$$\begin{aligned} \ln \varphi_{CO_2} = Z - 1 - \ln Z + \frac{a_1 + a_2/T_r^2 + a_3/T_r^3}{V_r} + \frac{a_4 + a_5/T_r^2 + a_6/T_r^3}{2V_r^2} \\ + \frac{a_7 + a_8/T_r^2 + a_9/T_r^3}{4V_r^4} + \frac{a_{10} + a_{11}/T_r^2 + a_{12}/T_r^3}{5V_r^5} + \frac{a_{13}}{2T_r^3 a_{15}} \quad (4.34) \\ \times \left[a_{14} + 1 - \left(a_{14} + 1 + \frac{a_{15}}{V_r^2} \right) \times \exp \left(-\frac{a_{15}}{V_r^2} \right) \right] \end{aligned}$$

In this expression, Z is given by $Z = P_r V_r / T_r$, where P_r and T_r are the reduced pressure and temperature, respectively. V_r is calculated by solving the following expression (using, for example, the Newton-Raphson routine):

$$\begin{aligned} \frac{P_r V_r}{T_r} = 1 + \frac{a_1 + a_2/T_r^2 + a_3/T_r^3}{V_r} + \frac{a_4 + a_5/T_r^2 + a_6/T_r^3}{V_r^2} + \frac{a_7 + a_8/T_r^2 + a_9/T_r^3}{V_r^4} \\ + \frac{a_{10} + a_{11}/T_r^2 + a_{12}/T_r^3}{V_r^5} + \frac{a_{13}}{T_r^3 V_r^2} \left(a_{14} + \frac{a_{15}}{V_r^2} \right) \exp \left(-\frac{a_{15}}{V_r^2} \right) \quad (4.35) \end{aligned}$$

Parameters $a_1 - a_{15}$ for Equations (4.34) and (4.35) are given in Table 4.7.

Table 4.7 – Parameters for Equations (4.34) and (4.35).

Parameters		Parameters (cont.)	
a_1	8.99288497e-2	a_9	-1.77265112e-3
a_2	-4.94783127e-1	a_{10}	-2.51101973e-5
a_3	4.77922245e-2	a_{11}	8.93353441e-5
a_4	1.03808883e-2	a_{12}	7.88998563e-5
a_5	-2.82516861e-2	a_{13}	-1.66727022e-2
a_6	9.49887563e-2	a_{14}	1.39800000e+0
a_7	5.20600880e-4	a_{15}	2.96000000e-2
a_8	-2.93540971e-4		

4.2 Results and discussion

4.2.1 Solubility of CO₂ in water and brine

In modelling the precipitation of CaCO₃ scale in CO₂ WAG processes, the evolution of CO₂ from the aqueous phase to the vapour phase is calculated using a VLE model. There are several VLE models available in the literature, and I have implemented 6 of the most common models used in the oil and gas industry, namely VLE models that use SRK and PR EOS, among others. My approach consists in validating the implementation of the VLE model with experimental data, in line with standard VLE studies available in the literature.

Figure 4.3 shows the comparison between experimental data for the solubility of CO₂ in water as a function of pressure and for 25, 50, and 100 °C with my implementation of the PR EOS using the $\phi - \gamma$ approach. Spycher et al., 2003a, reviewed experimental data on the solubility of CO₂ in water, and readers are referred to the references on this paper for the solubility data presented here.

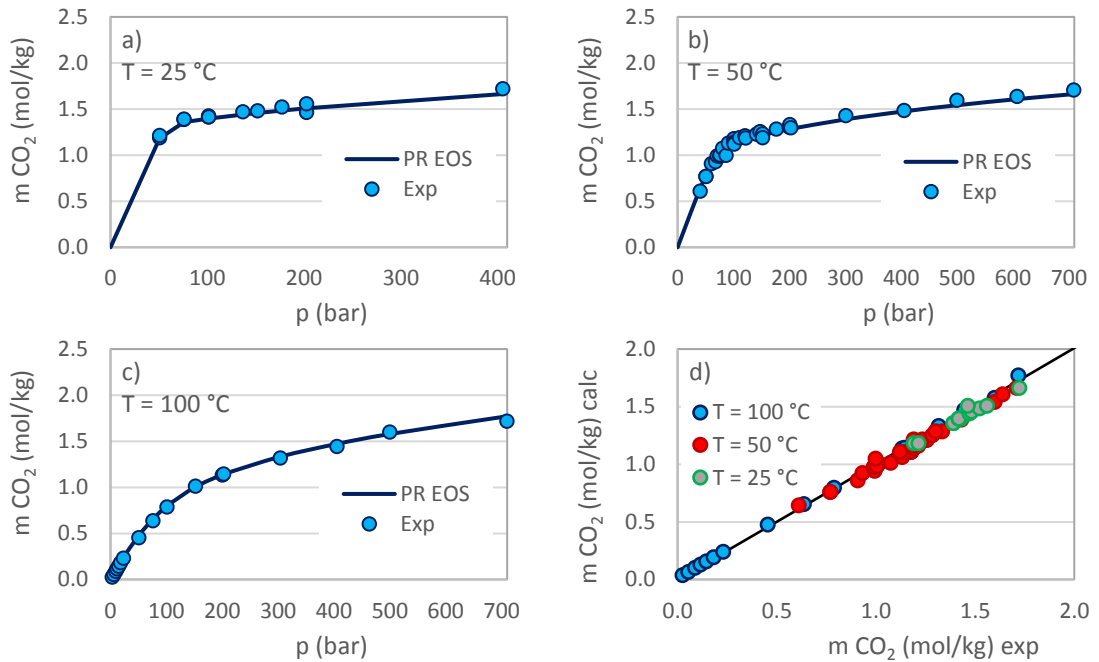


Figure 4.3 – Experimental and calculated (using PR EOS) solubilities of CO_2 in water as a function of pressure for 25, 50, and 100 °C [a), b), and c) on figure]. The calculated solubility of CO_2 is also plotted as a function of the corresponding experimental value [d) on figure].

Results in Figure 4.3 show very good agreement between the experimental data and the VLE model using the PR EOS, even considering that there is always an experimental error associated with measuring the solubility of gases in water.

The same experimental data shown in Figure 4.3 was used to validate my implementation of other VLE models. Figure 4.4 shows the comparison study of these data with my implementation of the VPT EOS using the $\varphi - \gamma$ approach.

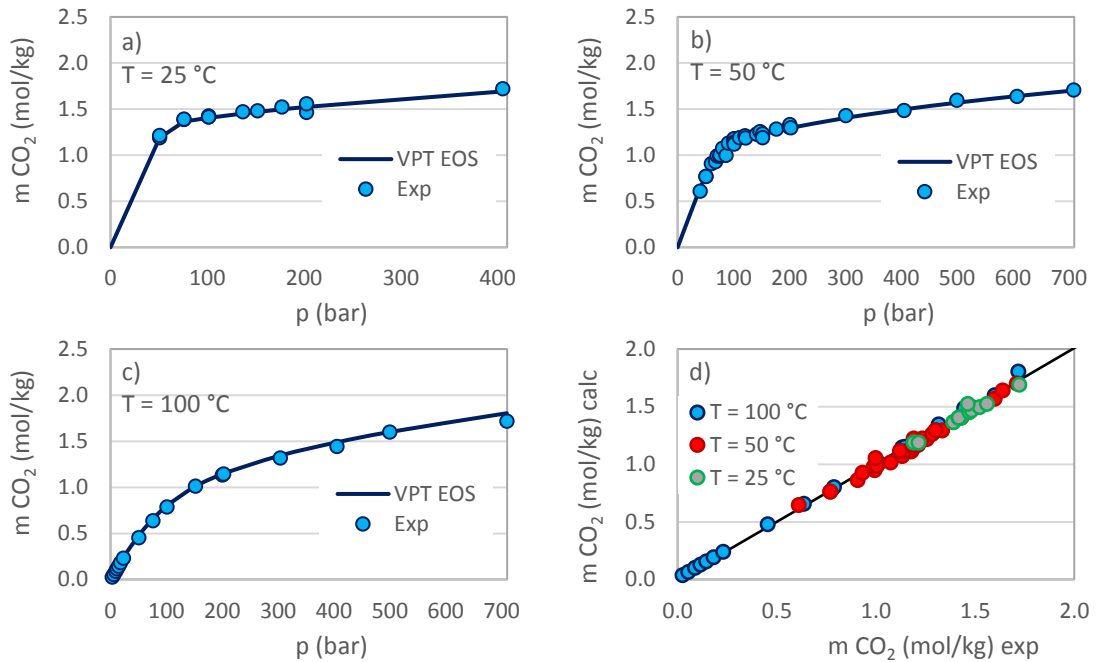


Figure 4.4 – Experimental and calculated (using VPT EOS) solubilities of CO_2 in water as a function of pressure for 25, 50, and 100°C [a), b), and c) on figure]. The calculated solubility of CO_2 is also plotted as a function of the corresponding experimental value [d) on figure].

Results in Figure 4.4 also show very good agreement between the experimental data and the VLE model using the VPT EOS. In fact, it seems that both VLE models are *equally satisfactory* for modelling the solubility of CO_2 in water. It is nevertheless possible to further compare and rank both models using an error analysis. In detail, for each experimental point, the absolute of the relative error (ARD) between the experimental value and the calculated value is determined. Then, an average of all ARD (AARD) is calculated and the model with the lowest AARD can be considered more accurate. For the VLE model using PR EOS, the AARD is 4.11%, and for the VLE model using VPT EOS, the AARD is 3.77%. Hence, considering that the ARDs are higher than the experimental uncertainty, the VLE model using VPT EOS can be considered more accurate than the VLE model using PR EOS *for the set of experimental data tested*.

Ranking VLE models can be misleading, since they depend on the database used for validation. In other words, using a different database for validation purposes can give a different ranking of the VLE models using the above criterion. Another issue to take into consideration is the error analysis. Having the lowest AARD for a VLE model does not necessarily mean that the model outperforms other models. It is possible that a model

has many experimental points with low ARDs, and just a few experimental points with high ARDs. Then, the average of the ARDs, i.e. the AARD, is low for that model. Of course, if I am interested in the conditions in which the model has high ARDs, then the model may not perform as satisfactorily as other models, despite having a lower AARD.

PR and VPT EOS are both cubic EOS. Figure 4.5 shows the comparison study of the same experimental data used before in Figure 4.3 and Figure 4.4 with the VLE model using Duan and Sun EOS, which is a virial-type EOS.

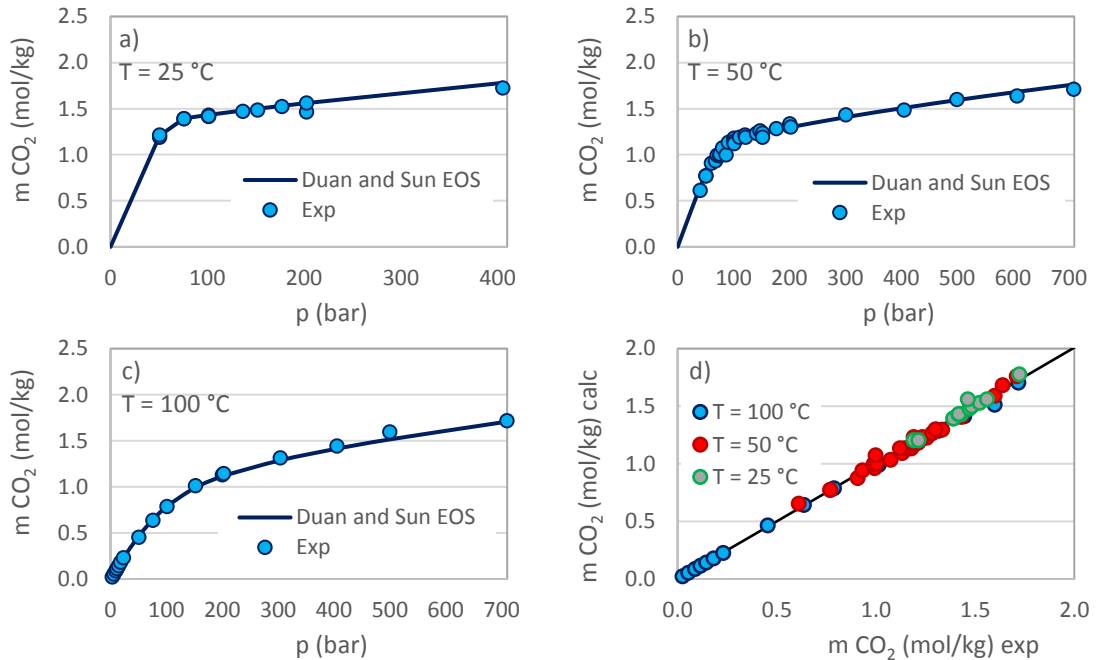


Figure 4.5 – Experimental and calculated (using Duan and Sun EOS) solubilities of CO_2 in water as a function of pressure for 25, 50, and 100 °C [a), b), and c) on figure]. The calculated solubility of CO_2 is also plotted as a function of the corresponding experimental value [d) on figure].

Results in Figure 4.5 also show very good agreement between the experimental data and the VLE model using the EOS proposed by Duan and Sun. In fact, using the AARD as the ranking criterion for the VLE models, the VLE model proposed by Duan and Sun outperforms the models using the PR and VPT EOS, since it has an AARD of 1.64% (as opposed to, as seen previously, 4.11 and 3.77% for PR and VPT EOS, respectively). Table 4.8 summarises the AARD calculated for the VLE models tested here.

Table 4.8 – Average of the Absolute of the Relative Deviation (AARD) for the VLE models tested.

EOS	AARD (%)
SRK	6.04
PR	4.11
PRSV	4.11
PT	3.94
VPT	3.77
Duan and Sun	1.64

Results in Table 4.8 show that the model proposed by Duan and Sun has the lowest AARD of all EOS considered for the experimental dataset tested. However, in a first analysis, it seems that using PR, VPT, or Duan and Sun EOS will not impact significantly scale prediction calculations – I will show below that this observation is fair, except for very specific conditions.

Another important calculation in scale prediction modelling is the calculation of the amount of water present in the vapour phase. The partition of the component H₂O between the aqueous phase and the vapour phase can have a significant impact on scale prediction calculations, since it *concentrates* or *dilutes* the scaling system. This can be very significant in low watercut systems, for example. Here, I have implemented the model proposed by Zirrahi et al., 2010. Figure 4.6 shows the comparison study between experimental data (Spycher et al., 2003a, reviewed experimental data on the water content in the CO₂-rich gas phase and readers are referred to the references on this paper for the solubility data presented here) for the amount of water in the vapour phase as a function of pressure for 25, 50, and 100 °C with my implementation of the model developed by Zirrahi et al., 2010.

Results in Figure 4.6 show good agreement between experimental data and my implementation of the model developed by Zirrahi et al., 2010. However, it is clear that the errors for modelling the water content in the vapour phase are higher than they are for modelling the solubility of CO₂ in water – the AARD for results shown in Figure 4.6 is 8.93%. This is somehow expected since it is more difficult to measure experimentally the water content in a vapour phase, than it is to measure the solubility of CO₂ in water (i.e. the experimental errors are higher for the former). Figure 4.7 shows the calculated values for the water content in the vapour phase as a function of the respective experimental values.

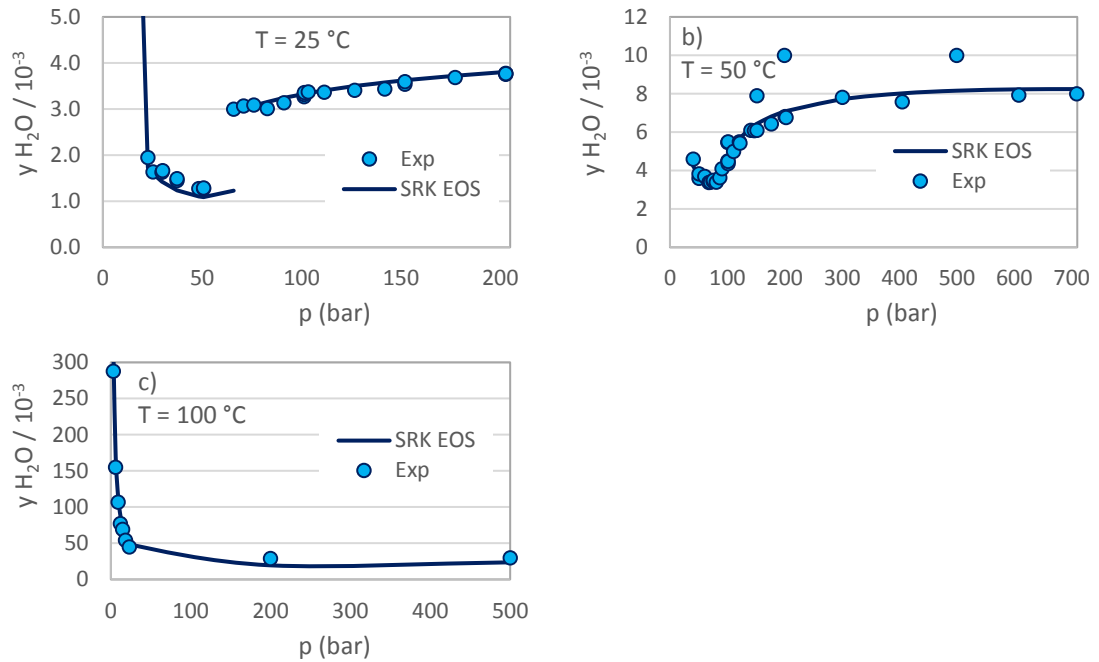


Figure 4.6 – Experimental and calculated (using SRK EOS) values for the water content in a CO₂-rich gas phase as a function of pressure for 25, 50, and 100 °C [a), b), and c) on figure].

Figure 4.7 presents the same data as Figure 4.6, hence also showing good agreement between calculated and measured values.

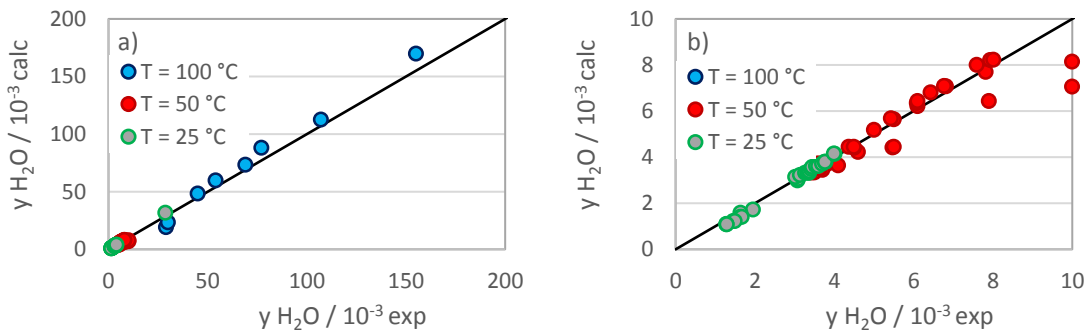


Figure 4.7 – Calculated values for the water content in a CO₂-rich vapour phase using my implementation of the model of Zirrahi et al., 2010, as a function of the respective experimental values. Plot b) zooms the data near the origin of plot a), i.e. for a mole fraction of water between 0 and 10/10⁻³.

Since scale prediction modelling deals with electrolyte systems, the solubility of CO₂ in brine was also investigated. I implemented the model proposed by Søreide and Whitson,

1992, using the $\varphi - \varphi$ approach, and I compared my results with the results presented in the original paper, as shown in Figure 4.8.

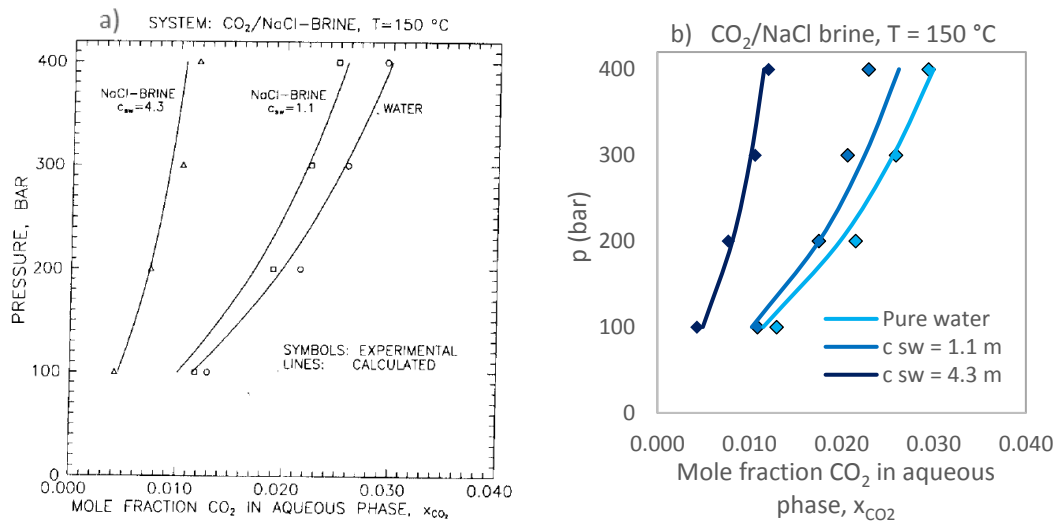


Figure 4.8 – CO_2 solubility in pure water and in brine at 150°C as a function of pressure. a) Plot adapted from the original paper of Søreide and Whitson, 1992. b) My implementation of the model proposed by Søreide and Whitson, 1992.

Results in Figure 4.8 are not entirely satisfactory. I believe that the experimental data used to validate the model – taken from the work of Takenouchi and Kennedy, 1965 – might not have been plotted correctly in the original paper of Søreide and Whitson, 1992. However, the calculated AARD for this model was 6.65 %.

In this context, I have implemented the model proposed by Duan and Sun, 2003, which has used the same experimental data, i.e. the data taken from Takenouchi and Kennedy, 1965, to validate its model. Figure 4.9 shows my implementation of Duan and Sun, 2003, and the plots presented in the original paper.

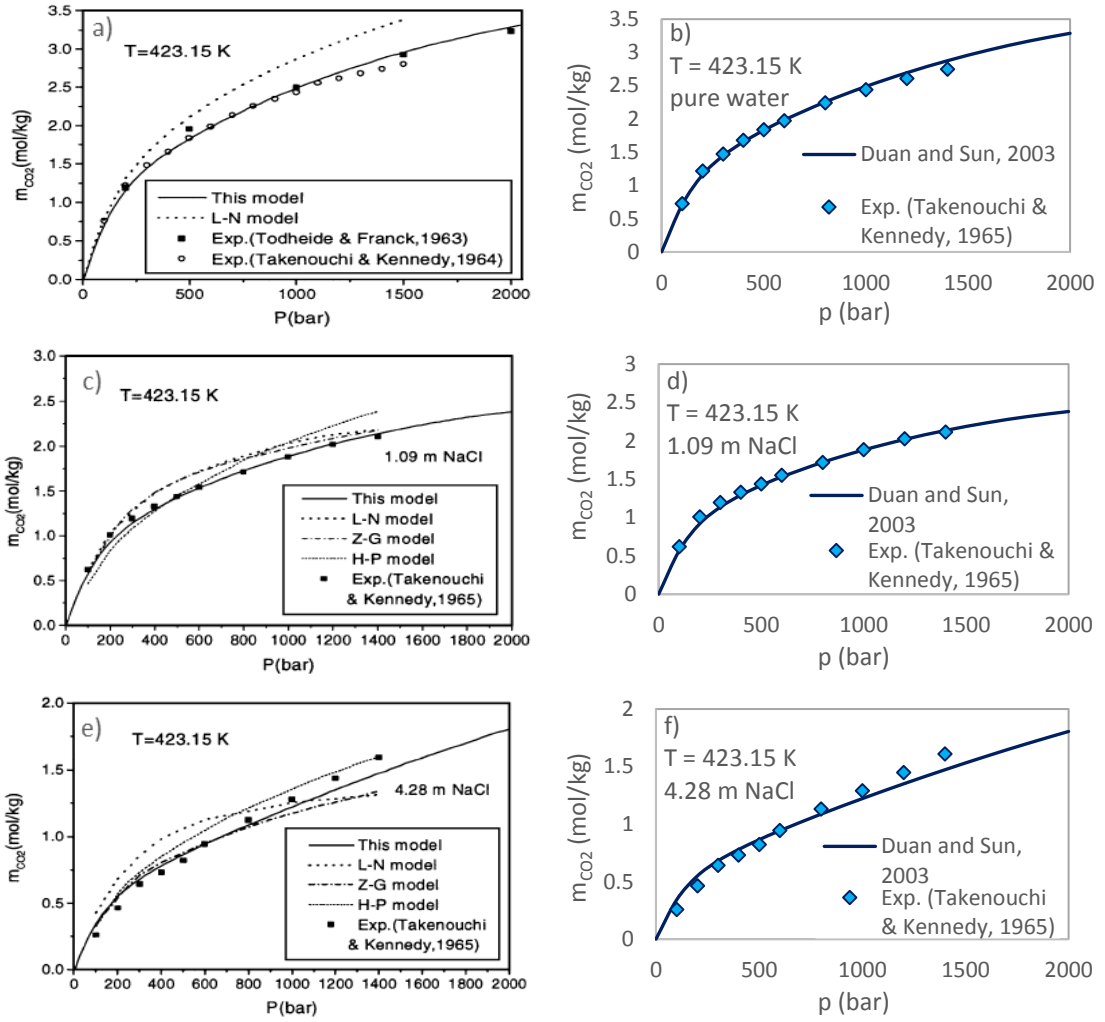


Figure 4.9 – Predicted solubility of CO_2 in water [a) and b) on figure], in 1.09 m NaCl [c) and d) on figure], and in 4.28 m NaCl [e) and f) on figure]. Plots a), c), e) were adapted from the original paper of Duan and Sun, 2003. Plots b), d) and f) correspond to my implementation of the Duan and Sun, 2003 model.

Results in Figure 4.9 show excellent agreement between my implementation of Duan and Sun's model and the results presented in the original paper. The calculated AARD for this model was 4.90 %.

The model developed by Duan and Sun in 2003 has excellent agreement between calculated and measured values for the solubility of CO_2 in water and brine for a wide range of pressures and temperatures, namely for 0 to 260 °C, and for 0 to 2000 bar. These authors used a virial-type EOS developed previously by Duan et al., 1992, and this EOS results from a fitting procedure to experimental data, notwithstanding having a theoretical background. Thus, Duan and Sun's model has the advantage of having excellent

performance in modelling the solubility of CO₂ in water and brine, but it has the disadvantage of being limited to this gas, i.e. this model cannot be used for calculating the solubility of other gases. Note that for example PR EOS is not limited to calculating the solubility of CO₂ in water – it can be used to model the solubility for other gases as well.

4.2.2 Solubility of CO₂, H₂S, and CH₄ gas mixtures in water

As shown above, H₂S also impacts the solubility of pH-dependent scales such as CaCO₃. Thus, I also need to account for the solubility of this gas in the aqueous phase. In addition, although gases other than acid gases (e.g. CH₄, C₂H₆, etc.) do not impact the acid equilibrium, they nevertheless impact the solubility of acid gases in the aqueous phase, and, therefore, they must be accounted for. In this context, I tested a VLE model using SRK, PR, PRSV, PT, and VPT EOS and the $\phi - \gamma$ approach to calculate the solubility of a gas mixture consisting of 60% CO₂, 10% H₂S, and 30% CH₄ in water for different pressures and temperatures, and I compared results with experimental data, as shown in Table 4.9 (readers are referred to the references in Zirrahi et al., 2012, for the experimental data presented here). The BIPs used here for the SRK and PR EOS were taken from Pellegrini et al., 2012. The BIPs for the remaining EOS presented in Table 4.9 were set equal to zero, following the argument presented in Danesh, 1998, p. 156, suggesting that VPT EOS without BIPs can outperform other EOS that use BIPs.

Table 4.9 – Experimental and calculated values for the solubilities of 60% CO₂, 10% H₂S, and 30% CH₄ in water using SRK, PR, PRSV, PT, and VPT EOS.

T (°C)	p (bar)	Experimental (mole fraction)		Calculated (mole fraction)					ARD (%)						
		SRK	PR	PRSV	PT	VPT	SRK	PR	PRSV	PT	VPT				
37.8	48.2	CH ₄	2.76E-04	2.72E-04	2.71E-04	2.71E-04	2.71E-04	1.45	1.81	1.81	1.81	1.81			
		CO ₂	9.30E-03	9.83E-03	9.66E-03	9.66E-03	9.60E-03	9.62E-03	5.67	3.83	3.83	3.17	3.39		
		H ₂ S	5.03E-03	4.73E-03	4.81E-03	4.81E-03	4.63E-03	4.63E-03	6.02	4.45	4.45	7.97	8.01		
76		CH ₄	4.66E-04	4.08E-04	4.09E-04	4.10E-04	4.10E-04	12.45	12.45	12.23	12.02	12.02			
		CO ₂	1.21E-02	1.30E-02	1.27E-02	1.25E-02	1.25E-02	7.35	4.73	4.73	3.29	3.61			
		H ₂ S	5.40E-03	5.75E-03	5.96E-03	5.52E-03	5.53E-03	6.52	10.41	10.43	2.28	2.31			
125.2		CH ₄	7.96E-04	6.45E-04	6.54E-04	6.71E-04	6.73E-04	18.97	17.84	17.84	15.70	15.45			
		CO ₂	1.51E-02	1.52E-02	1.48E-02	1.48E-02	1.42E-02	1.43E-02	0.94	1.87	1.86	5.69	5.21		
		H ₂ S	5.95E-03	5.59E-03	6.16E-03	6.17E-03	5.07E-03	5.10E-03	6.00	3.58	3.63	14.77	14.37		
169.3		CH ₄	9.90E-04	8.22E-04	8.41E-04	8.50E-04	8.54E-04	16.97	15.15	15.05	14.14	13.74			
		CO ₂	1.54E-02	1.59E-02	1.54E-02	1.47E-02	1.48E-02	3.37	0.21	0.23	4.27	3.75			
		H ₂ S	6.08E-03	5.14E-03	5.90E-03	5.90E-03	4.64E-03	4.66E-03	15.44	2.99	2.94	23.62	23.29		
107.2	83.6	CH ₄	3.79E-04	3.51E-04	3.47E-04	3.47E-04	3.49E-04	3.50E-04	7.39	8.44	8.44	7.92	7.65		
		CO ₂	6.98E-03	7.65E-03	7.46E-03	7.46E-03	7.42E-03	7.44E-03	9.63	6.91	6.88	6.30	6.58		
		H ₂ S	3.42E-03	4.09E-03	4.11E-03	4.11E-03	3.99E-03	3.98E-03	19.47	20.12	20.12	16.52	16.37		
129.3		CH ₄	5.78E-04	5.12E-04	5.06E-04	5.06E-04	5.10E-04	5.11E-04	11.42	12.46	12.46	11.76	11.59		
		CO ₂	9.59E-03	1.03E-02	9.97E-03	9.96E-03	9.87E-03	9.91E-03	7.69	3.92	3.89	2.91	3.28		
		H ₂ S	4.47E-03	5.12E-03	5.19E-03	5.19E-03	4.93E-03	4.92E-03	14.63	16.20	16.20	10.22	10.07		
171.7		CH ₄	7.79E-04	6.49E-04	6.39E-04	6.40E-04	6.47E-04	6.49E-04	16.69	17.97	17.84	16.94	16.69		
		CO ₂	1.13E-02	1.22E-02	1.17E-02	1.17E-02	1.15E-02	1.15E-02	7.71	3.15	3.12	1.73	2.19		
		H ₂ S	4.73E-03	5.65E-03	5.78E-03	5.78E-03	5.37E-03	5.36E-03	19.47	22.28	22.28	13.51	13.36		
										AARD (%)	10.25	9.08	9.06	9.36	9.27

Results in Table 4.9 show that:

- PRSV has the lowest AARD (9.06 %) of all EOS tested, and SRK has the highest AARD (10.25 %).
- The VLE models considered have large errors in calculating the solubility of H₂S in water – for example for 107.2 and 83.6 bar, VPT EOS has 16.37 % ARD, which is the lowest ARD of all EOS tested. On the other hand, PR and PRSV have the highest ARD (20.12 %).
- The solubility of CO₂ is calculated satisfactorily using all EOS, particularly using PR, PRSV, PT, and VPT EOS.

Having a state-of-the-art PVT model is not the objective of this thesis. Multiscale and Scalechem – arguably the two most common scale prediction software used by the oil and gas industry – do not have a state-of-the-art PVT model such as the one found in, for example, PVTSim software. I believe that the future of scale prediction modelling is going to be characterised by either scale prediction software incorporating a state-of-the-art PVT model, or by a PVT software incorporating a state-of-the-art scale prediction model. However, I have clearly demonstrated here how the solubility of acid gases in water can be calculated using industry-standard VLE models.

4.2.3 Impact of VLE calculations on scale prediction modelling

As already discussed, there are many VLE models available in the literature. In the context of scale prediction modelling, and particularly for CaCO₃ scale, I require a VLE model that calculates the solubility of CO₂ and H₂S in water. In this context, the following question arises: which VLE model should I use? In my opinion, the answer to this question is straightforward: I should use the VLE model with the lowest error with respect to experimental data. However, I can also pose the following question: what is the impact of not using the VLE model with the lowest error with respect to experimental data on scale prediction modelling?

To answer these questions, I have carried out a series of calculations to assess the precipitation of CaCO₃ by using three different EOS, namely SRK, PR, and VPT EOS.

In particular, I assumed a vapour phase consisting of 10% CO₂ and 90% CH₄, the water chemistry as presented previously in Table 3.2, pressure and temperature of 100 bar and 80°C, and I assessed the precipitation of CaCO₃ as a function of the initial concentration of HCO₃⁻, as shown in Figure 4.10. I note that the gas phase composition depends on the water to gas ratio – this issue is going to be addressed in Chapter 5. For the following calculations, I assume that this composition is constant.

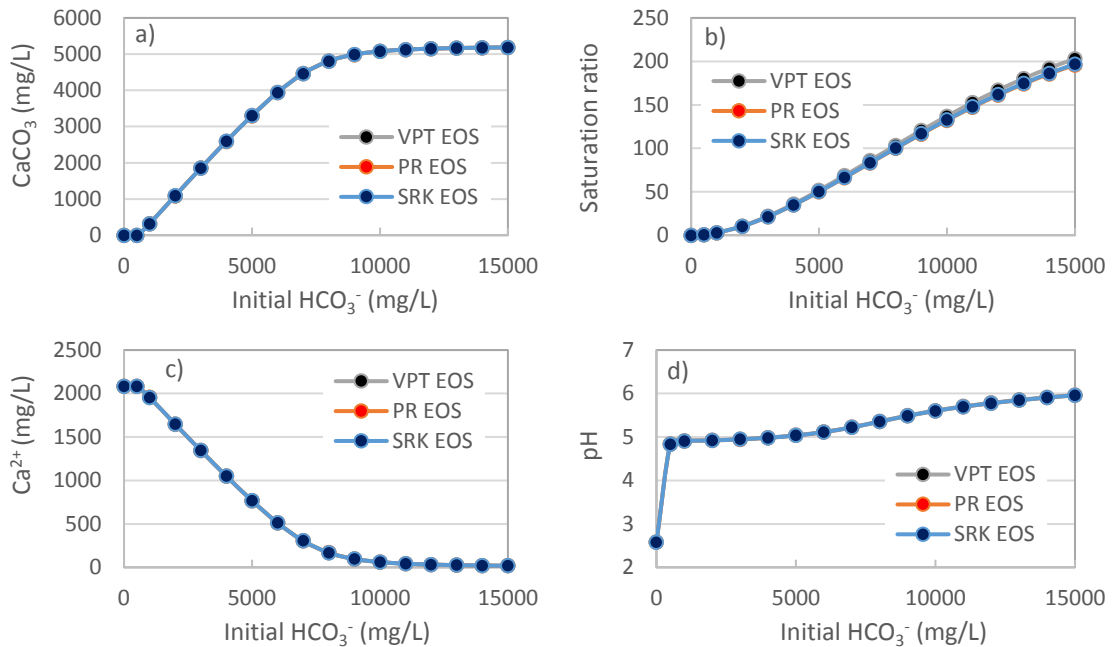


Figure 4.10 – Precipitation of CaCO₃, saturation ratio of CaCO₃, concentration of calcium and pH as a function of the initial HCO₃⁻ by using SRK, PR, and VPT EOS [a), b), c), and d) on figure].

Interestingly, results in Figure 4.10 show that using either SRK, PR, or VPT EOS *apparently* does not impact the precipitation of CaCO₃ [Figure 4.10 a)], since, as seen before in Table 4.8, their respective errors to experimental data are comparable. I can generalise these results by saying that, for many applications, it is not relevant which EOS – as studied here – is used.

However, I acknowledge that, in some situations, the choice of the VLE model does impact scale prediction calculations. In detail, there are scenarios in which a small difference in the concentration of dissolved CO₂ (or H₂S) impacts significantly the precipitation of CaCO₃ – for example, in *transition zones* where a small change in conditions can dictate the precipitation, or not, of scale, or it can dictate the precipitation

of one scale instead of another. In fact, I have already studied transitions zones in Chapter 3 (see Figure 3.9, Figure 3.10, and Figure 3.11). Moreover, I can even use the current example presented in Figure 4.10 to illustrate this point: if I set the initial concentration of HCO_3^- to 590.16 mg/L, i.e. in the transition zone of “no scale” to “ CaCO_3 scale” [Figure 4.10 a)], then the choice of EOS may have a relevant impact on the prediction of CaCO_3 scale. Table 4.10 shows the results for this calculation by using SRK, PR, PRSV, PT, and VPT EOS.

Table 4.10 – Calculation of the precipitation of CaCO_3 scale by using SRK, PR, PRSV, PT, and VPT EOS.

EOS	pH	Ca^{2+} (mg/L)	SR (CaCO_3)	CaCO_3 (mg/L)
SRK	4.901	2081.391	1.0044	1.022
PR	4.9	2081.755	1.0001	0.02
PRSV	4.9	2081.762	1.0000	0
PT	4.909	2078.367	1.0410	9.344
VPT	4.908	2078.708	1.0368	8.409

Results in Table 4.10 show that the pH is practically identical regardless of the EOS used in calculations – and this is expected for the reason explained above. However, the amount of CaCO_3 scale predicted by using different EOS is importantly different: for example, by using PRSV EOS, no CaCO_3 scale is predicted to form, whereas by using PT EOS, 9.344 mg CaCO_3 /L is predicted to form. Comparing both EOS in relative terms, this corresponds to a 100% error.

4.2.4 CaCO_3 scale formation due to de-pressurisation

As seen, in carbonate reservoirs and in CO_2 WAG processes, CaCO_3 scale forms in production systems due to depressurisation. In particular, the evolution of CO_2 from the aqueous phase to the vapour phase in production systems causes the system pH to increase, and CaCO_3 scale to precipitate. This process can now be modelled by coupling VLE calculations with scale prediction calculations for different pressures, i.e. I can now simulate a pressure profile by taking consecutive single point calculations at decreasing pressure values.

In this context, I run a simulation by using the example presented in the previous section, i.e. I assumed a vapour phase consisting of 10% CO₂ and 90% CH₄, the water chemistry as presented previously in Table 3.2, and I calculated the precipitation of CaCO₃ for decreasing values of pressure and temperature – from 100 to 10 bar and from 80 to 60°C, respectively. For this simulation, I used the PR EOS. Results are shown in Figure 4.11.

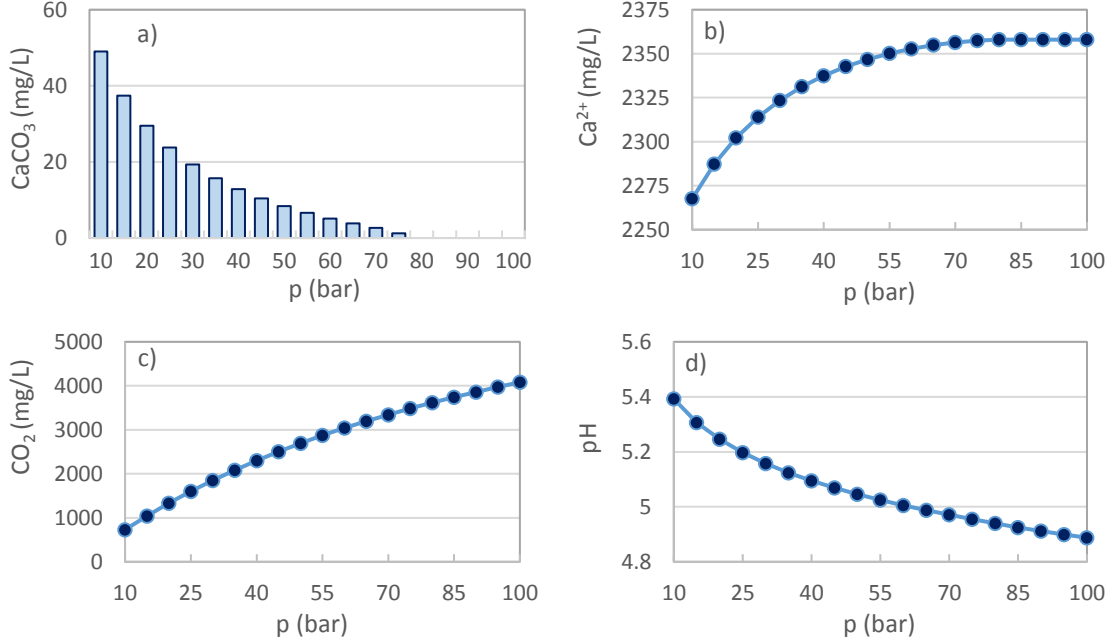


Figure 4.11 – Precipitation of CaCO₃ scale, concentration of Ca²⁺, concentration of CO₂, and pH as a function of pressure [a), b), c), and d) on figure]. Depth is parameterised with pressure, which goes from high pressure downhole to low pressure near surface facilities.

Results in Figure 4.11 a) show that the precipitation of CaCO₃ increases with decreasing pressure. These results are exactly what I was expecting: with decreasing pressure, the CO₂ in the aqueous phase decreases [Figure 4.11 c)], the pH increases [Figure 4.11 d)], and CaCO₃ precipitates [Figure 4.11 a)]. Furthermore, precipitation of CaCO₃ is higher at surface conditions than it is at higher pressure conditions.

Although these results are in agreement with the theory for CaCO₃ scale formation in production systems with a CO₂-rich environment, there is still an important approximation that has been made and that needs to be carefully considered: in these calculations, the composition of the vapour phase did not change with decreasing pressure and temperature, i.e. the composition of the vapour phase was always 10% CO₂ and 90%

CH_4 for all points considered in the calculation. However, when CO_2 evolves from the aqueous phase to the vapour phase, the composition of the vapour phase changes. If the composition of the vapour phase changes, then the solubility of CO_2 in the aqueous phase and the precipitation of CaCO_3 change as well; i.e. these processes are intimately coupled and a full re-equilibration calculation must be carried out in order to solve this problem rigorously. This issue will be dealt with in the next chapter.

4.3 Conclusions and recommendations

The evolution of CO_2 from the aqueous phase to the vapour phase in CO_2 WAG production systems caused by a decrease in pressure, and consequent increase in the system pH, is the driving force for CaCO_3 scale precipitation at these locations. VLE models are used in this context to calculate the evolution of CO_2 from solution as conditions change, or, more generally, they are used to calculate the amount of CO_2 dissolved in solution for a given pressure, temperature, and gas composition.

Standard VLE models used in the oil and gas industry – such as VLE models using SRK, PR, PRSV, PT, VPT, and Duan and Sun EOS – have been implemented and coupled with the aqueous scale prediction model developed previously in Chapter 3. In detail, I have addressed the following in this chapter:

- Solubility of CO_2 in water. VLE models using the $\varphi - \gamma$ approach and SRK, PR, PRSV, PT, VPT, and Duan and Sun EOS were implemented for calculating the solubility of CO_2 in water and validated with experimental data. For the set of experimental data tested, Duan and Sun EOS has been found to have the lowest AARD of all EOS tested – 1.64 %. However, all EOS performed similarly and reasonably well – arguably within experimental uncertainty –, since the highest AARD found was 6.04 % for SRK EOS.

In addition, the water content in a CO_2 -rich vapour phase has been calculated and validated with experimental data with an AARD of 8.93 %.

- Solubility of CO_2 in brine. Søreide and Whitson and Duan and Sun models have been implemented and validated with experimental data. Duan and Sun has been found to perform better than the Soreide and Whitson model, since the AARD

calculated for these models was 4.90 and 6.65%, respectively. In addition, the Duan and Sun model has the advantage of being developed for a wider range of conditions (for 0 to 260 °C, and 0 to 2000 bar).

- Solubility of CO₂, H₂S, and CH₄ gas mixtures in water. VLE models using the $\phi - \gamma$ approach and SRK, PR, PRSV, PT, and VPT EOS were implemented for calculating the solubility of a gas mixture consisting of 60% CO₂, 10% H₂S, and 30% CH₄ in water for pressures and temperatures up to 107.2 °C and 171.7 bar and validated with experimental data. For the set of experimental data tested, the PRSV EOS has been found to perform better than the other EOS studied with an AARD of 9.06 %. However, results are comparable for all EOS, since the highest AARD found was 10.25 % for SRK EOS.
- VLE models using SRK, PR, PRSV, PT, and VPT EOS have been found to have little impact on scale prediction calculations for the conditions tested here. These results are expected and they can be generalised to other conditions, since the AARDs found for the EOS tested here are very similar (see Table 4.8). However, for conditions in which a small error introduced by the VLE model has a big impact on scale precipitation, e.g. in transition zones where a small perturbation in the system can cause scale to precipitate, attention must be paid to the EOS selected. In fact, VLE models with the lowest AARD with respect to a *relevant* experimental database should *always* be chosen – this ensures that errors introduced in scale prediction calculations by VLE models are always the lowest they can possibly be.
- CaCO₃ scale formation due to de-pressurisation. A de-pressurisation algorithm has been designed to model the precipitation of CaCO₃ scale in production systems in CO₂-rich environments due to CO₂ evolution from the aqueous phase to the vapour phase. However, this algorithm considers that the vapour phase composition does not change with decreasing pressure – an approximation that will be dealt with in the next chapter. An example calculation has been run showing that CaCO₃ precipitation increases as pressure decreases, thus indicating that the precipitation of this scale is more severe at topside facilities than it is at lower locations.

CaCO_3 scale, and pH-dependent scales in general, are dependent on the partition of acid gases including CO_2 between the phases in the system (water, vapour, liquid). Thus, scale prediction models need to incorporate a state-of-the-art PVT model to accurately calculate the precipitation of scale, under all (T and P) conditions. I believe that there is a gap in the oil and gas industry in this field, since state-of-the-art scale prediction models do not incorporate state-of-the-art PVT models, and vice-versa. State-of-the-art PVT models now implement more advanced EOS than the *traditional* SRK or PR EOS such as the Cubic-Plus-Association (CPA) EOS and the Statistical Associating Fluid Theory (SAFT) EOS, and scale prediction models should adapt their in-built PVT models to account for these more advanced EOS, and thus improve their modelling capabilities.

5. Multiphase flash calculations

The precipitation of CaCO_3 scale in CO_2 -rich production systems has been calculated in the previous chapter considering the evolution of acid gases from the aqueous phase to the vapour phase due to depressurisation. However, in many CO_2 WAG scenarios, a liquid hydrocarbon phase is also present, and it may influence the partitioning of CO_2 (and H_2S) between the water and vapour phases. Changing the partition coefficient of CO_2 between these phases, and particularly changing the amount of CO_2 dissolved in the aqueous phase, directly impacts scale prediction calculations, including the prediction of CaCO_3 scale precipitation.

The partition of CO_2 and H_2S between the liquid, vapour, and water phases is dependent on the partition of other hydrocarbon components present in the system between these phases. This means that a *general* multi-phase flash algorithm is required to calculate the partition of acid and sour gases between all the phases present in the system. Then, the flash algorithm must be coupled with the scale prediction model developed in Chapter 3 to calculate the amount of CaCO_3 scale that can deposit in CO_2 WAG production systems.

In addition, input data for the *composition of reservoir fluids* – i.e. for the composition of water, vapour, and liquid – is required to run the multi-phase flash and scale prediction models, and to calculate the precipitation of CaCO_3 scale in production systems; i.e. I need to know the downhole compositions of all three phases, liquid/water/vapour. However, this information is seldom available, and must be calculated from surface data. Surface data are commonly obtained by sampling fluids at specific surface locations, such as wellheads and separators. Thus, calculating reservoir fluid compositions from surface data must also be considered.

In this context, the following objectives are considered in this chapter:

- i) Characterisation of petroleum reservoir fluids and their phase behaviour during production.
- ii) Implementation of a 3-phase flash algorithm to model the partition of hydrocarbons between liquid, vapour, and water phases.

- iii) Calculation of reservoir fluid compositions (water, vapour, and liquid).
- iv) Calculation of CaCO_3 scale precipitation profile in CO_2 WAG production systems.

5.1 Petroleum reservoir fluids

The amount of acid gases dissolved in the aqueous phase must be known to calculate the precipitation of scale, and CaCO_3 in particular, in CO_2 and/or H_2S rich environments. However, acid gases partition differently between water, vapour, and liquid phases, depending on the conditions of the system (e.g. T, P, salinity etc.). And these vary from reservoir conditions to surface conditions, i.e. from high to low pressures and temperatures. For example, in a 3-phase liquid/vapour/water system, the amount of CO_2 in the aqueous and oilic phases is higher at reservoir conditions where the pressure is high, than it is at surface conditions where the pressure is low. The amount of CO_2 in the vapour phase is then lower at reservoir conditions than it is at surface conditions. Therefore, PVT calculations, including EOS selection and tuning to field data, phase behaviour modelling, etc., are all integral parts of the associated reservoir system scale prediction calculations.

In this context, Figure 5.1 presents a common classification of petroleum reservoir fluids, according to the shape of their phase diagram and position of the critical point, into black oils, volatile oils, retrograde gases, wet gases, and dry gases, and it identifies the pressure and temperature path of fluids travelling from reservoir to topside. The discussion presented below has been adapted from McCain Jr., 1990, and readers are referred to this textbook for further details on the classification of petroleum reservoir fluids. Pedersen et al. (2015) also provide a good description on the subject.

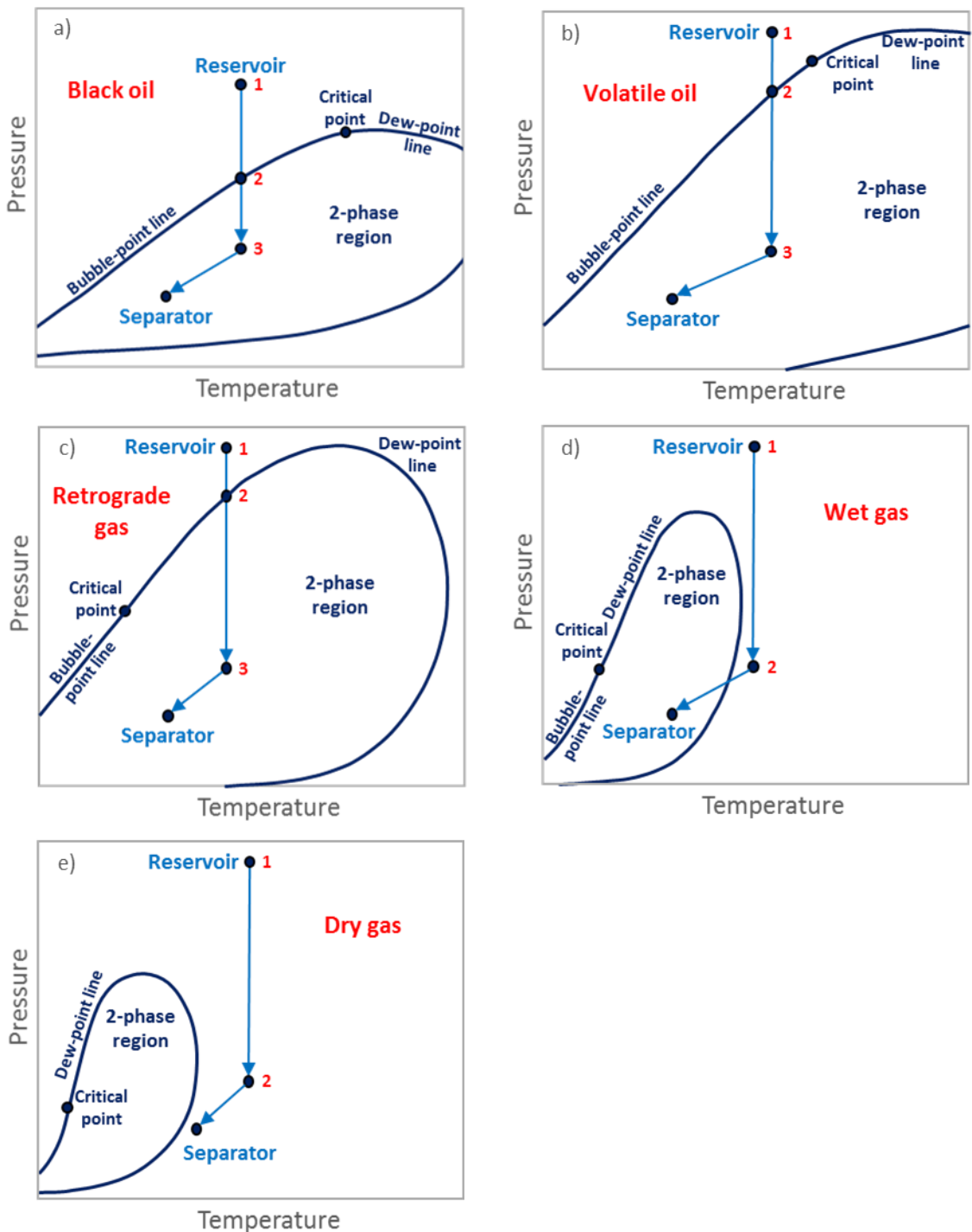


Figure 5.1 – Phase diagram of black oil, volatile oil, retrograde gas, wet gas, and dry gas [a), b), c), d), and e) on figure]. The p-T path of fluids travelling from reservoir to separator is identified in these plots.

From Figure 5.1 I note the following with respect to each fluid:

- Black oils: Figure 5.1 a) shows the typical shape of the phase diagram for black oils. Point 1 identifies the pressure and temperature of fluids in the reservoir, and

line 1-3 identifies the reduction in pressure at constant temperature that takes place in the reservoir as fluids are produced. Point 2 identifies the bubble point pressure and is situated along the line 1-3. Thus, some gas may be liberated as free gas in the reservoir as fluids are produced. When fluids enter the production system – identified in point 3 – and transported up the well to the surface, there is a decrease in pressure and temperature, and additional gas is evolved from the oil to the gas phase, causing some shrinkage of the oil. However, black oils have relatively large amounts of liquid arriving at the separator.

- Volatile oil: the difference between volatile oils and black oils is the position of their critical points – although the critical temperature of both fluids is higher than reservoir temperature, the critical temperature for volatile oils is much lower than black oils. Also, the phase diagram for volatile oils dictates that generally there is some reduction of pressure below the bubble point in the reservoir, i.e. the path along the line 2-3 in Figure 5.1 b), causing the evolution of large quantities of gas from the oil.
- Retrograde gas: the critical temperature for retrograde gases is lower than reservoir temperature, as opposed to black oils and volatile oils, as shown in Figure 5.1 c). Also, retrograde gases have less of the heavy hydrocarbons, causing the phase diagram to be to some extent smaller than these fluids. Some liquid condensates as the gas travels in the reservoir and reaches the dew point pressure [point 2 in Figure 5.1 c)], and as it travels along the 2-3 and 3-separator lines.
- Wet gas: the reservoir temperature is higher than the temperature in the phase envelope region. The reduction of pressure in the reservoir identified in line 1-2 in Figure 5.1 d) due to production does not result in the condensation of liquid. However, there is liquid at the separator, since separator conditions lie within the phase envelope.
- Dry gas: separator conditions lie outside the phase envelope for dry gases, as opposed to wet gases. This means that no hydrocarbon liquid is present at the separator. In fact, dry gases are mainly constituted by methane.

From Figure 5.1 I emphasise that the partition of components between phases, and even the number of phases, changes as fluids travel from reservoir to surface. The prediction of scale precipitation thus changes accordingly.

5.2 Calculation of reservoir fluids composition from surface samples

In order to calculate the precipitation of CaCO_3 scale that forms due to a depressurisation effect, I require not only PVT calculations to model the partition of components between phases, but I also require to know the composition of fluids in the reservoir (hydrocarbon phases and water). By knowing the composition of fluids in the reservoir, including water, I can then apply a depressurisation algorithm, i.e. a calculation at decreasing values of pressure (and temperature), to assess the scale precipitation profile in the production system. Calculating reservoir fluid compositions is achieved by sampling fluids at surface and reconstructing the respective composition in the reservoir by using the principle of mass conservation, as explained below.

5.2.1 Re-conciliation of separator outlet streams and the principle of mass conservation

The most common sampling points in the production system are downhole (less frequent), at the wellhead and at the separator (most common). Downhole sampling gives good indication of the composition of fluids in the reservoir, since fluids have not yet significantly changed due to the inherent change of pressure and temperature associated with production. However, downhole sampling is both expensive and infrequent, since production must be interrupted for sampling. Wellhead sampling is often carried out when the separator handles production from different wells. Separator sampling is probably the most common sampling point in the production system.

There is an important issue relating to scale management associated with sampling at surface locations that I am going to address here. This is that sampling at surface locations gives no indication per se of the amount of scaling ions that have already precipitated and deposited as scale upstream of the sampling point. However, in scale prediction calculations I must use the composition of the brine before scale occurs, and not after.

For example, if CaCO_3 scale precipitates and deposits upstream of the sampling point, then measuring the concentration of Ca^{2+} at the sampling point gives no indication per se of the amount of Ca^{2+} that entered the production system and precipitated as CaCO_3 . However, this amount of Ca^{2+} is required in scale prediction calculations to assess CaCO_3 scaling potential in the production system. In other words, the amount of Ca^{2+} in the reservoir brine that enters the wellbore – the quantity I must use in CaCO_3 scale prediction calculations – is equal, by mass balance, to the amount of Ca^{2+} in the separator brine *plus* all the Ca^{2+} that has precipitated as CaCO_3 scale upstream of the separator, as shown schematically in Figure 5.2.

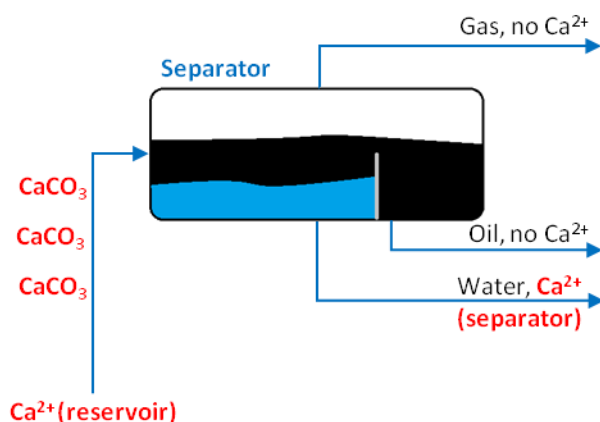


Figure 5.2 – The concentration of Ca^{2+} in the reservoir is equal by mass balance to the concentration of Ca^{2+} at the separator plus all the Ca^{2+} that precipitates between these two locations as CaCO_3 scale.

The calculation of reservoir fluid compositions from fluid sampling is based on the principle of mass conservation, as seen in Figure 5.2 for Ca^{2+} . Figure 5.3 shows a generic case where fluid sampling is carried out in the liquid, vapour, and water outlet streams of a separator. Then, the composition of reservoir fluids is calculated by knowing the mass of *all* streams that leave the separator. In particular, this calculation is achieved by *reconciling* the separator outlet streams, and by performing a phase equilibrium calculation at reservoir conditions.

Gas Chromatography (GC) and True Boiling Point (TBP) distillation are two standard tests used to characterise petroleum reservoir fluids (Pedersen and Christensen, 2007, p.13). Figure 5.4 shows the steps involved in calculating the compositions of reservoir fluids from samples in the separator, including the GC and TBP tests for the liquid and vapour phases.

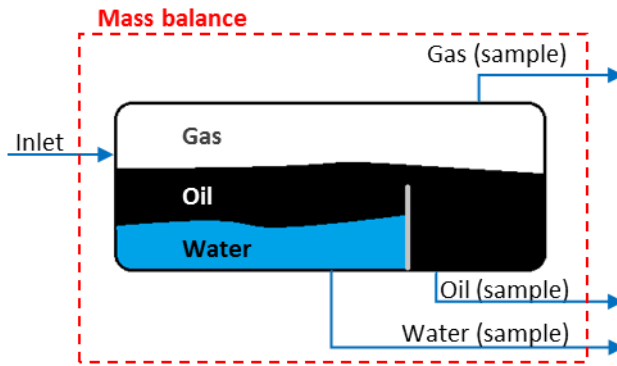


Figure 5.3 – The total mass of fluids is obtained by performing a mass balance to the separator and by reconciling the vapour, liquid, and water streams.

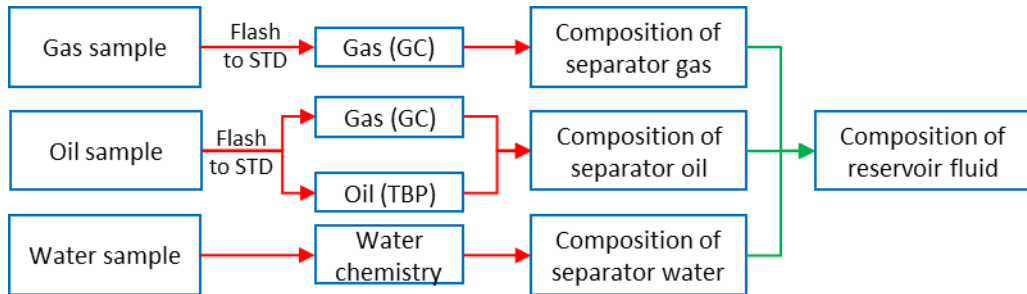


Figure 5.4 – The composition of reservoir fluids is obtained by measuring the composition of vapour, liquid, and water samples at the separator.

The principle of mass conservation is also used to calculate the compositions of reservoir fluids from a downhole sample. The compositions of reservoir fluids are obviously independent of the sampling point. Thus, provided that there is no accumulation of mass in the production system (e.g. deposition of scale, wax, asphaltenes, etc.), then calculating reservoir fluid compositions from different sampling points should give the same result. In fact, analysis of data from two different sampling points may be used to confirm calculations. In addition, I note that downhole and separator sampling are intrinsically different, and that they are dependent on the type of fluid being produced.

Even if the calculation of the compositions of reservoir fluids gives the same answer by using two different sampling points in the production system, this does not mean that the actual reservoir fluid compositions have been obtained. To this end, samples must be *representative* of the reservoir fluids, which does not always occur. For example, if a black oil is below the bubble point pressure in the reservoir [line 2-3 in Figure 5.1 a)],

then some liberation of free gas takes place; oil and gas are then produced at different rates and the calculation of the composition of reservoir fluids from samples is not necessarily accurate. In fact, “at reservoir pressures below the bubble point, no sampling method will give a sample representative of the original reservoir mixture.” (in McCain Jr. 1990, p. 258). Good practice recommendations for getting a representative reservoir sample, including sampling techniques, can be found in API Recommended Practice 44, 2003.

Obtaining the composition of reservoir fluids from samples is a complex issue. It involves selecting the appropriate sampling techniques for the type of fluid being produced (black oil, volatile oil, gas condensate, etc.), selecting and tuning an equation of state to field data to build a phase diagram, accounting for the mass of all components in all phases (either measured or calculated) at sampling points, etc. Although guidelines and best practices are available, these calculations should be carried out, in my opinion, using a case-by-case approach. This is simply because every system has its own specificities (e.g. type of oil, pressure and temperature conditions, layout of the production system, etc.). However, I emphasise that the mass conservation principle is always used, irrespective of the system being considered.

5.2.2 Oil-Gas-Water (OGW) flash

As mentioned previously, petroleum reservoir fluids are typically classified into five groups (Figure 5.1): black oil, volatile oil, gas condensate, wet gas and dry gas. With the exception of dry gas, all of these fluids have a liquid and vapour phase present at the separator. If I assume that water is also always present, then I always have a three phase system consisting of liquid, vapour, and water at the separator. In the reservoir, I can also have a three phase system for black oils and volatile oils below the bubble point pressure, and for retrograde gases below the dew point pressure. For these cases, I can use an Oil-Gas-Water (OGW) flash algorithm to calculate phase equilibria and scale precipitation in the production system, and particularly CaCO_3 scale caused by CO_2 evolution from the aqueous phase.

My implementation of the OGW flash follows the approach proposed by Li and Nghiem, 1986. In a three-phase system consisting of a water-rich phase and liquid and gaseous

hydrocarbon phases with n_c components, the condition for thermodynamic equilibrium for every component i in the mixture at a specific pressure and temperature is given by:

$$\ln K_{iv} + \ln \phi_i^v - \ln \phi_i^l = 0 \quad i = 1, \dots, n_c \quad (5.1)$$

$$\ln K_{iw} + \ln \phi_i^w - \ln \phi_i^l = 0 \quad i = 1, \dots, n_c \quad (5.2)$$

Where K_{im} and ϕ_i^m are, respectively, the partition and the fugacity coefficients of component i in phase m (i.e. in the liquid, l , vapour, v , and water, w , phases). In this formulation, I have $K_{il} = 1$.

The OGW flash calculation consists of solving simultaneously Equations (5.3) and (5.4) to find the molar fraction of the liquid, vapour, and water phases (F_l , F_v , and F_w , respectively) where x_i and z_i are, respectively, the molar fraction and the initial feed of component i . I also have $F_l + F_v + F_w = 1$.

$$\sum_{i=1}^{N_c} (x_i^v - x_i^l) = \sum_{i=1}^{N_c} \frac{z_i(K_{iv} - 1)}{F_l + F_v K_{iv} + F_w K_{iw}} = 0 \quad (5.3)$$

$$\sum_{i=1}^{N_c} (x_i^w - x_i^l) = \sum_{i=1}^{N_c} \frac{z_i(K_{iw} - 1)}{F_l + F_v K_{iv} + F_w K_{iw}} = 0 \quad (5.4)$$

The molar fraction of component i in each phase can then be calculated by using the following expression:

$$y_{im} = K_{im} z_i / \sum_q K_{iq} F_q \quad \begin{matrix} i = 1, \dots, n_c \\ m = l, v, w \\ q = l, v, w \end{matrix} \quad (5.5)$$

There are several methods which are available to solve these equations, including the successive substitution method. For further details on how to implement numerical solution methods for these equations, see Michelsen and Mollerup, 2007.

The vapour and liquid hydrocarbon phases are modelled with an Equation of State (EOS), whereas the solubility in the aqueous phase is modelled by Henry's law. Here, I used the

Peng-Robinson (PR) EOS (Soave, 1972). My implementation of Henry's law follows strictly the paper of Li and Nghiem, 1986.

5.2.3 Coupling OGW with scale predictions: equilibration of fluids with reservoir rock

To calculate scaling profiles in the production system, and particularly CaCO_3 scale that forms in production wells due to CO_2 evolution from the aqueous phase, the composition of reservoir fluids that enter the production system must be known. As mentioned previously, downhole sampling provides a good indication of the composition of fluids present in the reservoir, and, if downhole sampling is not an option, then the composition of reservoir fluids can be calculated from surface samples.

I now design an algorithm that calculates the compositions of reservoir fluids, including water, by using i) data from surface sampling, ii) the OGW flash introduced in Section 5.2.2, and iii) scale prediction modelling introduced in Chapter 3. I use the PR EOS to solve the OGW flash at reservoir conditions by using surface data as input, thus fixing the compositions of the liquid, vapour, and (partially) aqueous phases. The composition of CO_2 and H_2S in the aqueous phase is fixed by this calculation. However, CO_2 and H_2S can react in solution to form, respectively, HCO_3^- and CO_3^{2-} [Equations (3.6) and (3.7)], and HS^- and S^{2-} [Equations (3.9) and (3.10)]. Also, as seen, CO_2 and H_2S are involved in the precipitation (or dissolution) reactions of CaCO_3 , FeCO_3 , and FeS [Equations (3.18), (3.19), and (3.20)] – in fact, carbonate reservoirs function as a pH-buffer, and, in CO_2 -rich environments, I usually have CaCO_3 dissolution. This means that I have to iteratively correct the amount of aqueous CO_2 and H_2S to account for the respective depletion (or addition) by these processes, i.e. I have to add (or remove) mass to the system. This calculation is illustrated in Figure 5.5.

The composition of the reservoir fluids and the total mass of the scaling system is calculated using the algorithm showed in Figure 5.5. This algorithm couples standard PVT calculations with standard scale prediction calculations, and it ensures that thermodynamic equilibrium is established in both calculations, i.e. it finds a global minimum in Gibbs energy for the liquid-vapour-water-solid system.

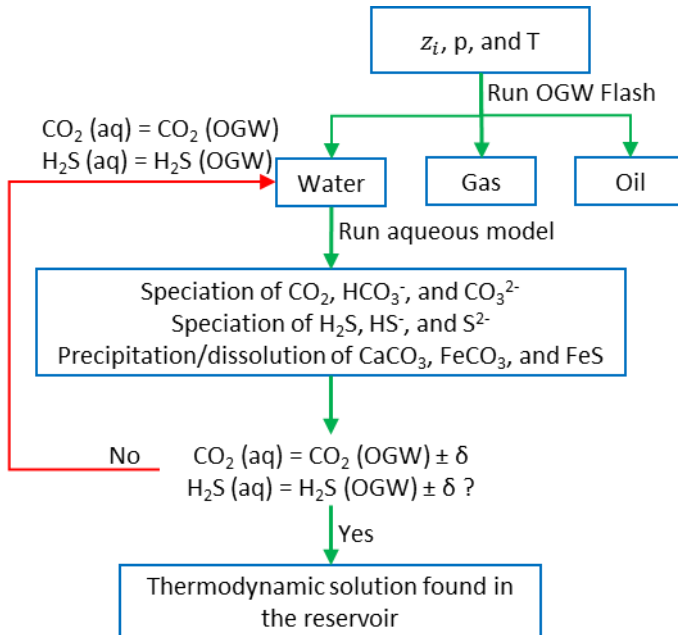


Figure 5.5 – Flowchart for the calculation of the fluid compositions in the reservoir, including the speciation of CO_2 and H_2S in solution as well as carbonate rock-brine interactions.

5.3 Calculation of scale precipitation profiles in production systems

I have shown how to calculate the total mass of components present in reservoir fluids – liquid, vapour, and water – from surface data, and how to calculate the partition of these components between the phases in the reservoir. These fluids then enter the production system, and can precipitate scale. I introduce next an algorithm that calculates scale precipitation profiles in the production system by using the composition of reservoir fluids as input data.

5.3.1 Coupling OGW with scale predictions: precipitation of scale in the production system

When fluids enter the production system and travel up the well to the separator, the total mass of components is conserved (this may include accumulation of scale, wax, asphaltenes, etc. in the system). However, there is an important difference in the context of scale prediction modelling between calculations carried out in the reservoir, as seen in the previous section, and calculations carried out in the production system: in the later,

reservoir rock is no longer present, and, consequently, it is no longer possible to have rock dissolution.

Calculating scale precipitation profiles in the production system is initialised by performing an OGW flash using the total mass of components – which was previously established using the algorithm developed in Section 5.2.3 – at pressure and temperature values of interest. Then, CO₂ and H₂S react in solution according to the acid equilibrium reactions [Equations (3.6) to (3.11)] and can precipitate as carbonate and sulphide scales [Equations (3.18) to (3.20)], thus changing the amount of aqueous CO₂ and H₂S initially predicted by the OGW flash. Then, the initial feed for the OGW flash is iteratively corrected to account for the CO₂ and H₂S reactions, ensuring that the total mass of components is always conserved, as shown in Figure 5.6.

The algorithm presented in Figure 5.6 calculates the amount of scale that precipitates in the production system, which is ultimately my goal. This information is then used to design scale management strategies.

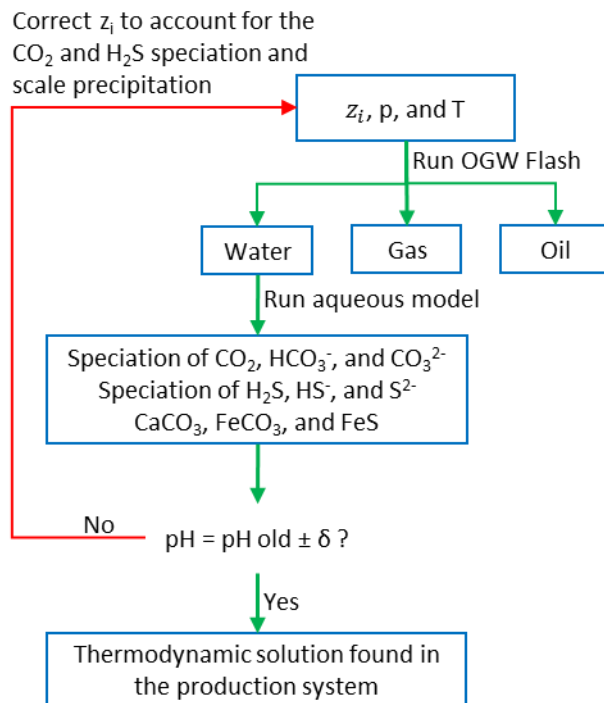


Figure 5.6 – Flowchart for the calculation of the fluid compositions in the production system, including the speciation of CO₂ and H₂S in solution and precipitation of scale.

5.4 Calculation of scaling profiles in the production system that agree with the water chemistry measured at surface sampling points

If scale precipitates and deposits in the production system upstream of the sampling point, then measuring the concentration of the scaling ions at the sampling point gives an incomplete indication by itself of the amount of those ions that have precipitated as scale. However, I know the total amount of all components that are present in the production system by knowing the composition of all phases at the separator, *except*, as noted, for the components that are directly involved in scale precipitation reactions. Components partition differently between the phases in the production system due to different conditions of pressure and temperature, but their total mass is nevertheless the same.

For example for CaCO_3 scale, the only components that are not known are the total mass of calcium, Ca^{2+} , and carbon, $\text{CO}_2/\text{HCO}_3^-/\text{CO}_3^{2-}$. This information is valuable since I can almost completely identify the initial conditions of the system, while identifying key parameters for scale precipitation. For CaCO_3 scale, the *initial conditions* of the system are the total mass of all components except calcium and carbon, and the *key parameters* for scale precipitation are then the total mass of calcium and carbon.

Given the (almost complete) set of initial conditions and key parameters, I can calculate the scaling profile in the production system that is in full agreement with production data. The procedure is explained as follows: first, I assume values for the key parameters identified above; second, I calculate the scaling profile in the production system; third, I compare the calculated values with the measured ones for the composition of components at the sampling point; and fourth, if the calculated and measured values are the same, then I have found the initial values for the key parameters and the scaling profile in the production system that is in agreement with production data; otherwise, if the calculated and measured values are not the same, then I repeat the procedure by changing the initial values for the key parameters. This procedure is shown schematically in Figure 5.7.

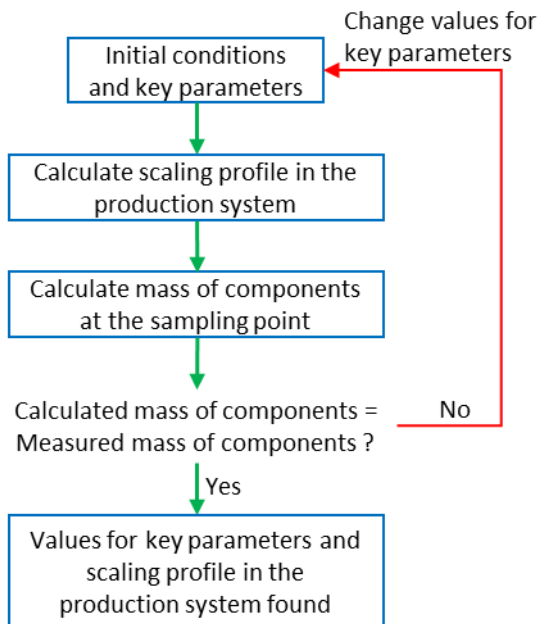


Figure 5.7 – Flowchart for the calculation of the correct water chemistry in the reservoir, and scale profile in the production system.

The procedure explained above results in a set of scale precipitation profiles in the production system as a function of the values given to key parameters, and one of these scale profiles matches production data. As seen, these key parameters are directly involved in the calculation of scale precipitation in the production system – as is the case of Ca^{2+} and $\text{CO}_2/\text{HCO}_3^-/\text{CO}_3^{2-}$ concentrations for CaCO_3 scale. They are, therefore, good candidates for sensitivity analysis studies that can identify worst case scenarios. Thus, this calculation not only calculates the correct set of initial conditions and scale profile in the production system, but also performs a sensitivity analysis on parameters directly involved in precipitation reactions. I can then identify worst case scenarios with respect to scale formation, which is always a valuable piece of information in the design of scale management strategies.

My model is further explained below using a demonstrative example.

5.5 Results and discussion

5.5.1 Oil-Gas-Water (OGW) flash

My implementation of the OGW flash algorithm was compared with the results obtained by using CMG WinProp (version 2015.10.5612.22665). WinProp is a PVT software distributed by the Computer Modelling Group (CMG) for reservoir compositional simulation and used in many contexts in the oil and gas industry. Table 5.1 and Figure 5.8 show an example of the results obtained for this comparison study for a fluid at 40 bar and 68 °C. The input values required in an OGW flash are the composition of the feed (in mole %), and pressure and temperature. The algorithm then calculates the partition of the several components between the liquid, vapour, and water phases, and the mole percentage of each phase, as shown in Table 5.1. The BIPs used in the calculations were taken from Winprop – readers are referred to Winprop’s manual for the calculation of BIPs.

The results in Table 5.1 and Figure 5.8 show very good agreement between my implementation of the OGW flash and Winprop’s for the conditions tested. In addition, I have performed other comparison studies for different conditions of feed, temperature, and pressure, and I obtained very similar results to those presented in Table 5.1 and in Figure 5.8.

Table 5.1 – Comparison of the OGW flash results obtained by using my code and Winprop at 40 bar and 68 °C (PR EOS was used).

Component	mole % Feed	HW FAST			Winprop		
		Water	Liquid	Vapour	Water	Liquid	Vapour
H ₂ O	30	99.93490	0.29828	0.76426	99.93458	0.31724	0.80203
CO ₂	0.715	0.01319	0.38216	1.32109	0.01258	0.42134	1.30169
CH ₄	37.486	0.04420	12.94690	73.18200	0.04402	12.94561	73.16612
C ₂	5.960	0.00492	5.59786	9.88249	0.00491	5.59555	9.88015
C ₃	6.934	0.00284	11.93940	8.80969	0.00284	11.93206	8.80796
nC ₄	3.793	0.00087	9.95075	3.12453	0.00087	9.94377	3.12424
nC ₅	2.536	0.00013	8.49351	1.17717	0.00013	8.48735	1.17727
nC ₆	1.971	0	7.49275	0.47310	0.00003	7.48739	0.47323
nC ₇	10.606	0	42.89940	1.26668	0.00004	42.86968	1.26729
Phase		29.56730	23.33220	47.10050	29.56730	23.34790	47.08470

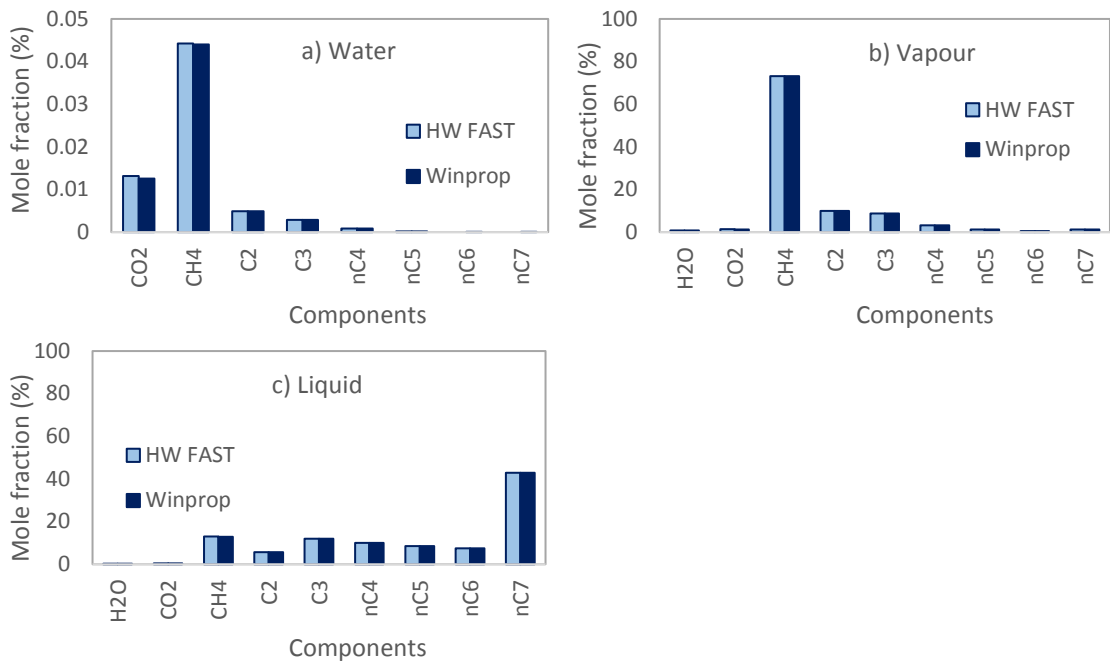


Figure 5.8 – Partition of components between the water, vapour and liquid phases [a), b), and c) on figure] – these are the same results as the ones presented in Table 5.1.

5.5.2 Calculation of reservoir fluid compositions from surface samples

As introduced in Section 5.2.3, reservoir fluid compositions can be calculated from analysing surface samples and by using the principle of mass conservation. It is also necessary to perform an equilibrium calculation of these fluids with reservoir rock to obtain a thermodynamic equilibrium between all phases, i.e. an equilibrium calculation between solid, water, and hydrocarbon phases.

Thus, the input for the algorithm presented in Section 5.2.3 consists of: i) reservoir pressure and temperature; ii) total hydrocarbon feed, including water; and iii) aqueous electrolyte chemistry. Then, the partition of components between all phases (solid, water, vapour, and liquid) in the reservoir is calculated. Knowing the composition of the fluids in the reservoir is the first step to calculate scaling profiles in the production system, as discussed later.

Table 5.2 and Table 5.3 present the initial conditions used in a demonstrative example to calculate the composition of reservoir fluids from surface data. The initial input is simplified to study the partition of components between phases that have a direct impact on the CO₂/carbonate system, including CaCO₃ rock dissolution/precipitation. These

components are $\text{CO}_2/\text{HCO}_3^-/\text{CO}_3^{2-}$ and Ca^{2+} . However, I present later in Table 5.7 an example that uses field data.

Table 5.2 – Equilibrium calculation of water, liquid, and vapour phases at 100 bar and 80 °C.

mole %	Initial (feed)	Equilibrium (in the reservoir)		
		Water	Liquid	Vapour
H ₂ O	30	99.62380	0.49197	0.65581
CO ₂	10	0.28397	9.37395	17.85890
CH ₄	40	0.09223	27.69230	80.00470
nC ₈	20	0.00002	62.44180	1.48058
Phase		29.7017	31.1004	39.1979

Table 5.3 – Equilibrium calculation of the aqueous phase with reservoir rock at 100 bar and 80 °C.

m (mg/L)	Initial	Equilibrium
CO ₂	0	5691.83
HCO ₃ ⁻	200	746.73
CO ₃ ²⁻	0	0.02870
Ca ²⁺	2000	2171.13
pH	7	5.091

The partition of components in the water, vapour, and liquid phases presented in Table 5.2 is shown schematically in Figure 5.9.

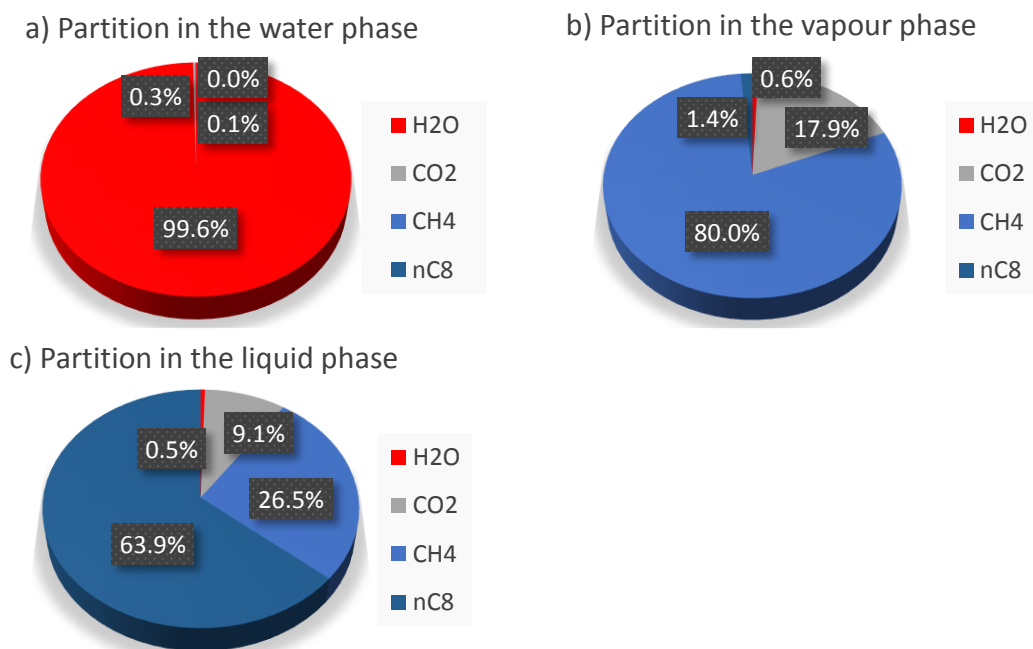


Figure 5.9 – The partition of components presented in Table 5.2 in the water, vapour, and liquid phases [a), b), and c) on figure].

The results in Table 5.2, Table 5.3, and Figure 5.9 show that:

- H₂O is (obviously) the main component in the aqueous phase (99.62380 mole %). CO₂ accounts for 0.28397 mole % of this phase and its concentration is 5691.83 mg/L. Note that this value is established by the OGW flash, although CO₂ is also an input in the electrolyte model. By doing so, I am assuming that CO₂ in the aqueous phase is given by a PVT study, as is usually the case (measurements of CO₂ in the aqueous phase may not be reported). CH₄ and nC8 account for 0.09223 and 0.00002 mole %, respectively. This shows that, in general terms, the solubility of hydrocarbons in the water phase decreases as its molecular weight increases.
- The vapour phase is mainly composed of CH₄ (80.00470 mole %) and CO₂ (17.85890 mole %). The liquid phase is composed by the hydrocarbon components (CH₄ and nC8), but CO₂ and H₂O are also present. In fact, CO₂ and H₂O account for 9.37395 and mole % and 0.49197 mole % of the phase, respectively. As discussed below (Table 5.6), the amount of H₂O present in the liquid phase in the reservoir is going to partition into the aqueous phase as fluids are produced, causing some dilution of the components present in this phase, including scaling ions. This, of course, will have an impact on the amount of scale that precipitates in the production system.
- The initial input for the concentrations of CO₂, HCO₃⁻, CO₃²⁻, and Ca²⁺, and for the pH in the aqueous phase is not at thermodynamic equilibrium. After an equilibrium calculation with the hydrocarbon phases and carbonate rock, the equilibrium quantities of these components are found. Thus, there is carbonate rock dissolution, since the concentration of Ca²⁺ increases from 2000 to 2171.13 mg/L. In addition, the pH at thermodynamic equilibrium is 5.091, indicating that carbonate rock buffers the system in CO₂-rich (acid) environments.

Another valuable item of information in calculating the composition of the reservoir fluids is to determine the partition of components between the phases. Thus, Figure 5.10 shows the partition of the total number of moles of each component, i.e. H₂O, CO₂, CH₄, and nC8, between the water, vapour, and liquid phases in the reservoir.

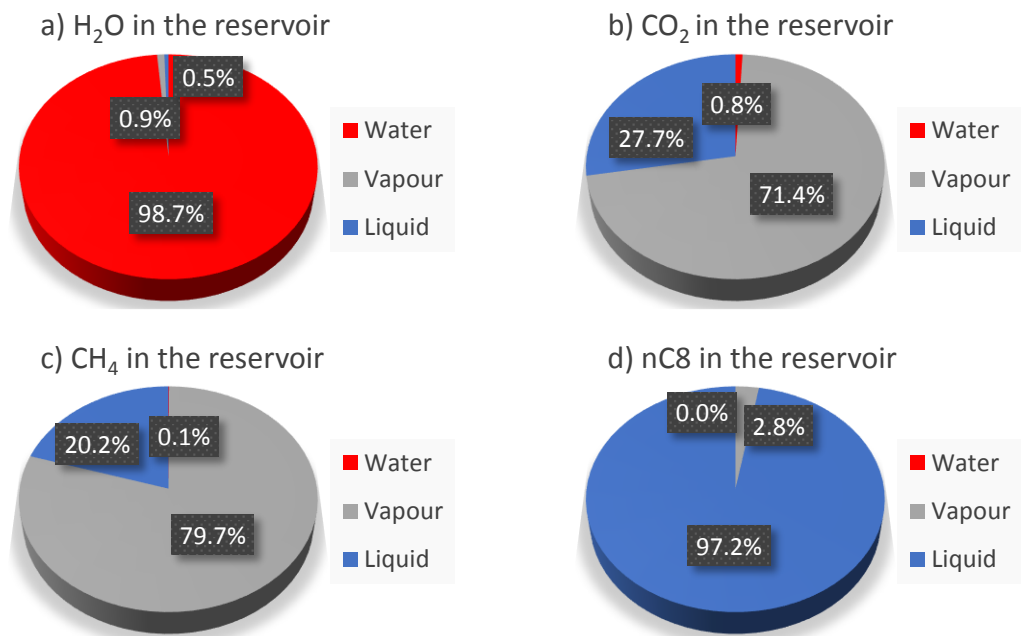


Figure 5.10 – Partition of the total number of moles of H₂O, CO₂, CH₄, and nC8, between the water, vapour, and liquid phases in the reservoir [a), b), c), and d) on figure].

The results in Figure 5.10 show that: i) H₂O is mainly present in the aqueous phase - 98.7% of the total moles of H₂O are in this phase; ii) CO₂ is mainly present in the vapour and liquid phases; iii) CH₄ is also mainly present in the vapour and liquid phases, but more in the vapour phase; and iv) nC8 is mainly present in the liquid phase.

Knowing the partition of components between the phases is important for scale prediction calculations. As discussed below, pressure and temperature decrease as fluids are produced, thus changing the partitioning of components between the phases. This change has an impact on the scaling potential of the several scales in the production system.

5.5.3 Calculation of scale precipitation profiles in production systems

As introduced in Section 5.3.1, scale precipitation profiles can be calculated using the composition of fluids in the reservoir. I have shown in the previous section an example that calculates the composition of reservoir fluids from surface data. This calculation sets the total mass of each component, since carbonate rock can dissolve, i.e. mass can be added to the system, and, also, aqueous CO₂ can be added to account for the depletion of

CO_2 from the $\text{CO}_2/\text{HCO}_3^-/\text{CO}_3^{2-}$ equilibrium. However, in the production system, the total mass of all components is conserved and equal to the total mass found in the previous equilibrium calculation in the reservoir. Then, phase equilibrium and scale prediction calculations are carried out at decreasing values of pressure and temperature to simulate production according to the algorithm shown in Figure 5.6.

The reservoir fluid compositions calculated in the previous section and shown in Table 5.2 and Table 5.3 are now used to calculate the respective scale precipitation profile in the production system. To this end, pressure was varied from 100 to 10 bar taking pressure steps of 5 bar; temperature was also varied, linearly, between 80 and 60 °C; and the amount of scale formed was calculated at each pressure step, which is ultimately my goal.

Figure 5.11 shows the profile of the CO_2 , HCO_3^- , pH, and Ca^{2+} concentrations in the production system, i.e. the evolution of the concentration of these species as they travel from reservoir (100 bar) to separator (10 bar).

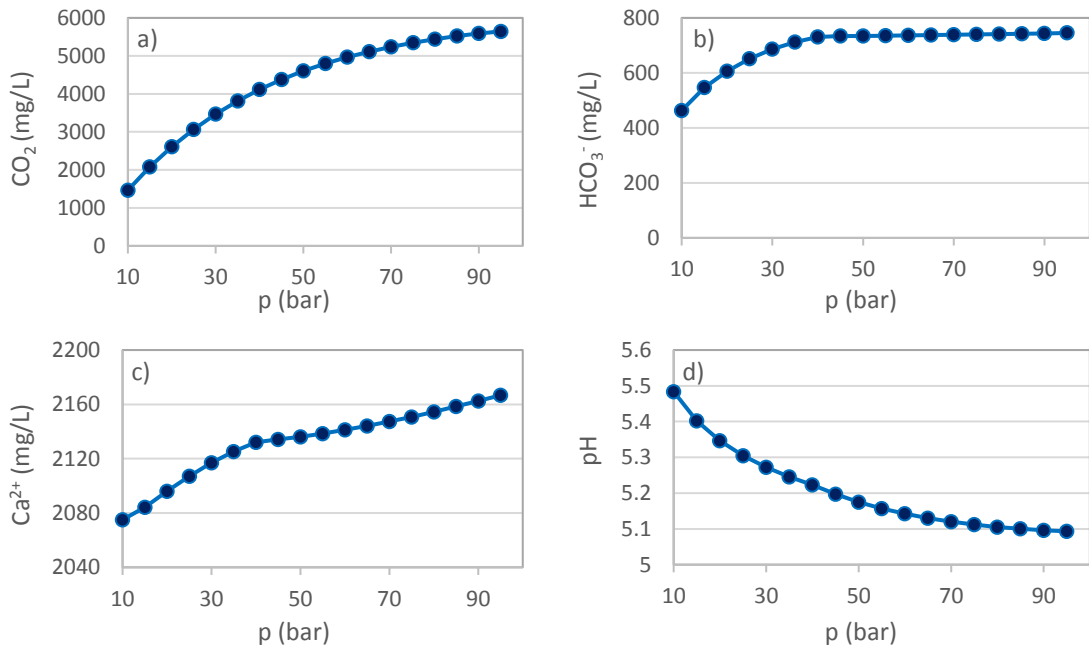


Figure 5.11 – Profiles of the concentrations of CO_2 , HCO_3^- , Ca^{2+} , and pH in the production system [a), b), c), and d) on figure].

The results in Figure 5.11 show that: i) the concentration of aqueous CO₂ decreases as fluids travel to the surface – in fact, the evolution of CO₂ from the aqueous phase to the vapour phase is the driving force for CaCO₃ precipitation in CO₂-rich production systems (as studied here); ii) the concentration of HCO₃⁻ also decreases; iii) the pH increases as fluids are produced due to the CO₂ evolution from the aqueous phase; and iv) the concentration of Ca²⁺ decreases somewhat moderately from 100 bar to around 40 bar due to water condensation, and then sharply between 40 bar and 10 bar due to water condensation and CaCO₃ precipitation (see CaCO₃ scale precipitation profile below).

I can now compare the partition of components between the liquid, vapour, and water phases for reservoir conditions, shown previously in Figure 5.10, and for surface conditions, shown in Figure 5.12 for separator conditions (10 bar).

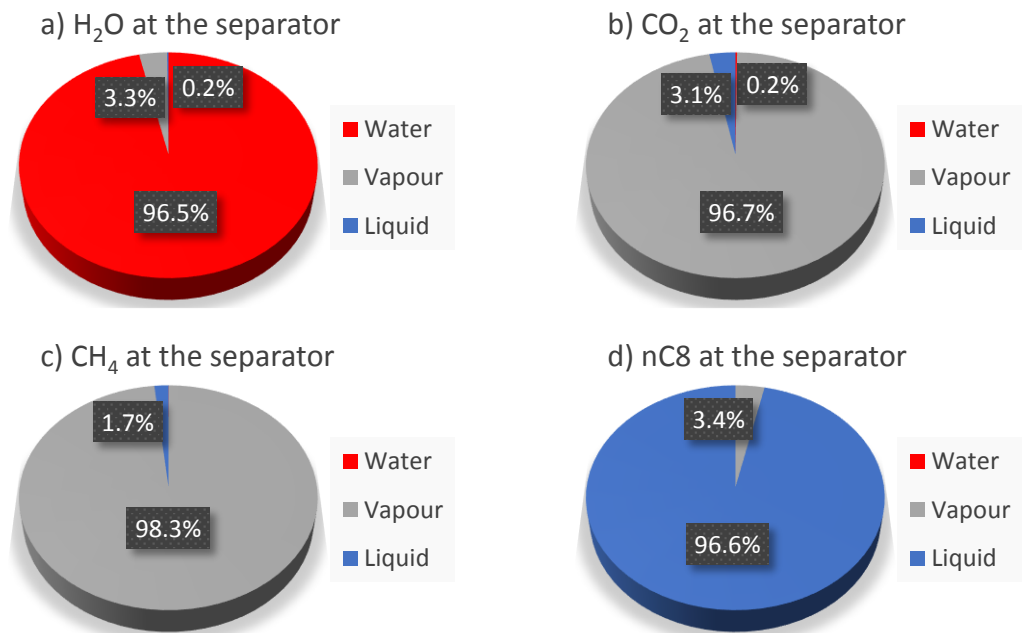


Figure 5.12 – Partition of the total number of moles of H₂O, CO₂, CH₄, and nC8, between the water, vapour, and liquid phases at the separator [a), b), c), and d) on figure].

The results in Figure 5.12 show that: i) as in the reservoir, the component H₂O is mainly present in the aqueous phase; also, H₂O evolves from the liquid phase (0.49197% in the reservoir) to the vapour and aqueous phases (0.2% in the liquid phase at the separator) – this means that there is condensation of water during production, which dilutes the

concentration of components in the aqueous phase, including scaling ions; ii) CO₂ is now mainly present in the vapour phase – note the reduction from 27.7% in the liquid phase in the reservoir to 3.1% at the separator – this clearly shows that VLE calculations are not sufficient to model the phase behaviour of CO₂, and consequently the precipitation of scale, including CaCO₃, when there is also a liquid phase present in the system; iii) CH₄ is also mainly present in the vapour phase; and iv) nC₈ is mainly present in the liquid phase, as in the reservoir.

Figure 5.13 shows the CaCO₃ scale precipitation profile in the production system for the initial conditions presented in Table 5.2 and Table 5.3.

The results in Figure 5.13 clearly show that CaCO₃ scale precipitates in the production system at pressures equal to and lower than 40 bar, and that precipitation increases as pressure decreases. Also, the worst point in the production system with respect to CaCO₃ precipitation is where pressure has its lowest value, which, in this case, is at the separator (i.e. at 10 bar).

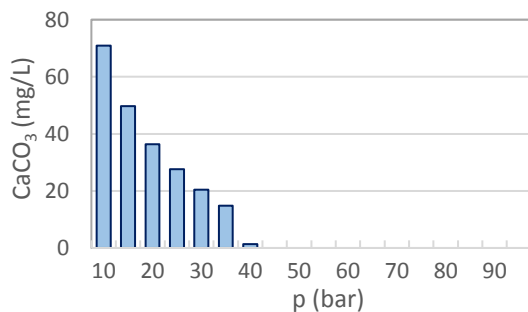


Figure 5.13 – Profile for the precipitation of CaCO₃ scale in the production system.

These results indicate that continuous downhole injection of CaCO₃ scale inhibitor may be an option to prevent scale formation, since scale does not precipitate downhole in the reservoir completions. This solution may be preferable to more expensive squeeze treatments, provided it can equally well “protect” the well. Thus, we must be quite certain that scale does not precipitate upstream of the scale inhibitor injection point, and have a remediation strategy should this scenario occur.

I can argue that knowing and understanding the system is the best way to take informed decisions. For example, I know that CaCO₃ scale forms in CO₂-rich production wells due

to a depressurisation effect – but what is the role of temperature? The solubility of CaCO_3 scale, contrary to most oilfield scales, decreases with increasing temperature. Thus, the solubility of CaCO_3 increases when temperature decreases during production. Figure 5.14 shows a re-run of the previous example, but instead of varying the temperature between 80 and 60 °C, I kept the temperature constant and equal to reservoir temperature (80 °C). Note that both simulations – results shown in Figure 5.13 and Figure 5.14 – have the same starting point, i.e. a calculation at 80°C and 100 bar. However, this point is not shown in Figure 5.13 and Figure 5.14 – these plots already consider a 5 bar pressure step due to depressurisation (i.e. starting point at 95 bar).

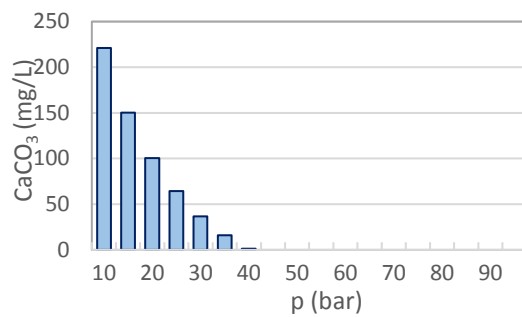


Figure 5.14 – Profile for the precipitation of CaCO_3 scale in the production system at constant temperature.

Results in Figure 5.14 show that CaCO_3 scale deposits everywhere in the production system, from downhole to separator. Also in these results, CaCO_3 scale is predicted to form more severely at the separator. Furthermore, the cumulative amount of CaCO_3 scale that deposits in the production system is clearly higher than in the previous results. This means that temperature has a very important role in suppressing CaCO_3 scale (at lower T) in production systems, and, in fact, these results clearly show that I must carefully include the effect of temperature when studying the precipitation of CaCO_3 due to a depressurisation effect. In the context of results in Figure 5.14, opting for CaCO_3 scale inhibitor continuous downhole injection would no longer be an *easy* decision to take.

Another interesting point in modelling CaCO_3 scale due to a depressurisation effect is the choice of the pressure step included in calculations. Once fluids enter the production well, there is a small decrease in pressure and, consequently, a small amount of CaCO_3 can precipitate. However, fluids are still close to the thermodynamic equilibrium that

was previously established in the reservoir. For this reason, it is not likely that the completion is the worst point in the production system with respect to CaCO_3 scale formation, or that CaCO_3 precipitation is very severe at this location. As fluids move away from the reservoir and to the surface, each pressure step renders the system in a new thermodynamic equilibrium that can result, again, in the precipitation of a small amount of CaCO_3 scale. In fact, I should think of CaCO_3 scale precipitation in production wells as a *continuum*, rather than as a discrete, process.

The choice of pressure step used in calculations has an impact on results, and ultimately in the design of the scale management strategy. Figure 5.15 shows the profile of CaCO_3 scale precipitation in the wellbore as a function of pressure and as a function of pressure step assumed in calculations. In particular, Figure 5.15 a) shows the results assuming a pressure step of 5 bar – these are the same data as shown previously in Figure 5.13 –, and they show the results assuming a lower pressure step, namely 1 bar. Figure 5.15 b) plots the same data as Figure 5.15 a), but it adds the results assuming a higher pressure step, this time assuming 10 bar. Figure 5.15 c) and Figure 5.15 d) further include more data, including a single point calculation in Figure 5.15 d), i.e. data for a pressure step equal to the difference between reservoir pressure and separator pressure. However, these results in Figure 5.15 must be interpreted carefully and correctly. The **cumulative** amount of calcite scale is exactly the same for all cases, and this is equal to the amount of scale by taking one step from reservoir to separator conditions. The cumulative amount of scale coming up the wellbore converges as a larger number of steps are taken and this is the correct underlying quantity of the system if all calcite deposition occurs *at equilibrium*.

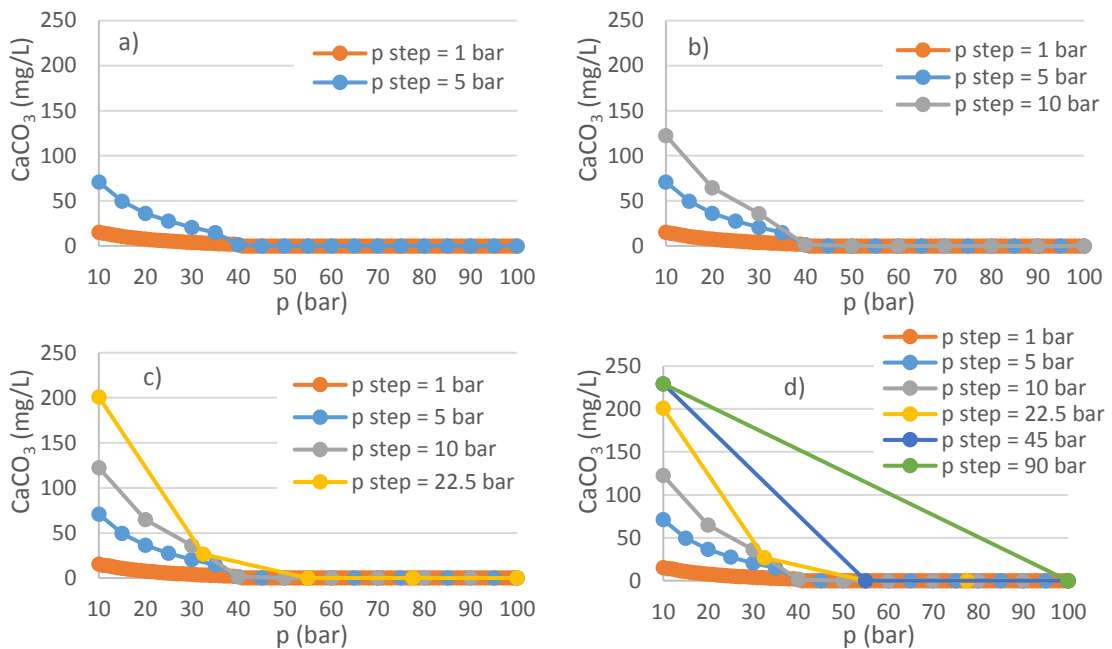


Figure 5.15 – Precipitation of CaCO_3 scale in the production system for different pressure steps.

If calculating scale precipitation by taking only one step from the reservoir to the separator, then this would represent a very “worst case” scenario and it is unlikely to be correct or representative for the actual scaling problem in that well. Suppose I took, say, 4 steps to perform the scaling calculations, then at the first of these I would be stating that the scaling problem was at the SR which was found at this point. Thus, it appears to be rather arbitrary what size of pressure step I should take in this calculation. Also, it implies that the actual scaling problem I should use in the laboratory to select a SI to prevent calcite formation is also rather arbitrary. However, I believe that a resolution of this issue is to:

- (i) Calculate the correct (converged) cumulative scaling profile for calcite in the well.
- (ii) Use this to examine where some critical SR may occur in the well if first precipitation is seen at some point X. At the present moment, this is a **decision** not a rigorous correct value (see (iii) below).
- (iii) This cumulative scaling profile should be used in conjunction with a wellbore kinetic scaling model which has been formulated within FAST and is currently

being developed (not presented here). This kinetic model will give a more rational basis to the choice of point X in step (ii) above.

These results clearly show that the precipitation of CaCO_3 scale in production wells in CO_2 -rich environments that forms due to a depressurisation effect should be treated as a continuum process, or as a mixed continuum (very small pressure steps) and discrete process. I extend this discussion by noting that the traditional scale inhibitor selection programmes are designed for cases where there is a *thermodynamic shock* [single point calculation, as seen in the green data points in Figure 5.15 d)], even if I am dealing with an autoscaling, or *continuum*, process [light blue data points in Figure 5.15 a)]. A clear example is the use of Tube Blocking Tests (TBT) methods to assess performance of scale inhibitors performance. In these tests, two solutions – typically, one having a scaling cation (e.g. Ca^{2+}) and another having a scaling anion (e.g. HCO_3^-) – are brought together at representative pressure and temperature, and scale upon mixing. Scale inhibitors are then screened, both qualitatively and quantitatively, for their performance at inhibiting scale formation.

Although these tests rank scale inhibitors for their capacity to inhibit a particular scale, they are nevertheless not testing scale inhibition of an autoscaling process, but rather of a thermodynamic shock. This may be one of the reasons why heuristics proliferated in the oil industry when companies have to deal with CaCO_3 scale (e.g. Zhang et al., 2015). There are many reasons why testing the correct scale formation mechanism should be considered. For example, to assess the correct induction time for scale formation, the correct scale morphology, etc. Again, I believe that this can only be placed on a fully rational basis by developing the kinetic wellbore model referred to above.

5.5.4 Example of a calculation in a CO_2 and H_2S -rich environment

As seen in Chapter 3, CaCO_3 scale is a pH-dependent scale, and, consequently, it is dependent on other species that contribute to the acidity of the system, such as H_2S and FeS . I now run an example similar to the example presented in Sections 5.5.2 and 5.5.3, but I include $\text{H}_2\text{S}/\text{HS}^-$ and Fe^{2+} in the system. Table 5.4 and Table 5.5 present the initial conditions used in the simulation, and the results obtained for the equilibrium calculation with the reservoir by using the algorithm presented in Section 5.2.3.

Table 5.4 – Equilibrium calculation of water, liquid, and vapour phases at 100 bar and 80 °C.

mole %	Initial (feed)	Equilibrium (in the reservoir)		
		Water	Liquid	Vapour
H ₂ O	30	99.56330	0.52895	0.66317
CO ₂	4	0.11691	3.89133	7.29706
H ₂ S	6	0.22380	9.63120	7.31561
CH ₄	40	0.09600	28.95730	83.27390
nC ₈	20	0.00002	56.99120	1.45031
Phase		29.7095	34.1740	36.1165

Table 5.5 – Equilibrium calculation of the aqueous phase with reservoir rock at 100 bar and 80 °C.

m (mg/L)	Initial	Equilibrium
CO ₂	0	2290.43
HCO ₃ ⁻	200	474.69
CO ₃ ²⁻	0	0.02801
H ₂ S	0	4068.08
HS ⁻	500	312.67
S ²⁻	0	0
Ca ²⁺	2000	1993.05
Fe ²⁺	30	0.03027
pH	7	5.297

The results in Table 5.4 and Table 5.5 can be analysed in a similar manner as the results presented previously in Table 5.2 and Table 5.3. However, I further note the following: i) H₂S is now present in the system and, as for CO₂, the aqueous amount of H₂S (4068.08 mg/L) is set by the OGW flash; ii) 30 mg/L Fe²⁺ is used as input, but after the equilibrium calculation with the reservoir, this amount reduces to 0.03027 mg/L – Fe²⁺ precipitates in the reservoir as FeS. However, there is still a trace of Fe²⁺ that enters the production system.

After running an equilibrium calculation with the reservoir, fluids are brought to surface, and scaling profiles in the production system are calculated. Figure 5.16 shows the profiles for the concentrations of CO₂/HCO₃⁻ and H₂S/HS⁻ in the production system.

As expected, the concentrations of CO₂/HCO₃⁻ and H₂S/HS⁻ decrease with decreasing pressure, since CO₂ and H₂S evolve from the aqueous phase to the vapour phase. This evolution of gases causes an increase in the pH, as shown in Figure 5.17.

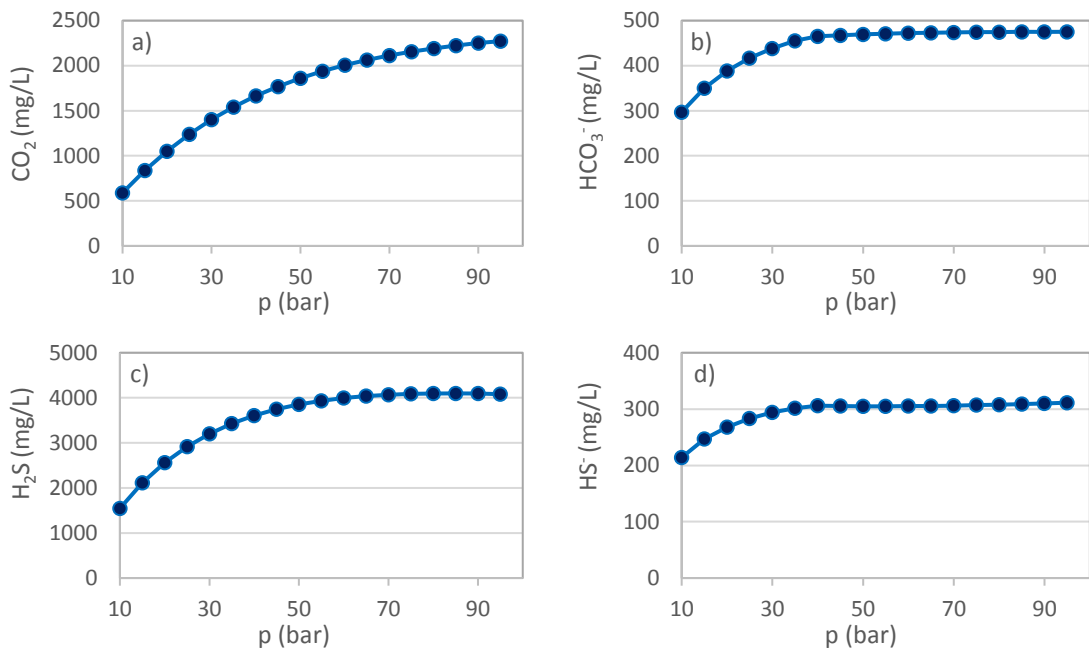


Figure 5.16 – Profiles of the concentrations of CO_2 , HCO_3^- , H_2S and HS^- in the production system [a), b), c), and d) on figure].

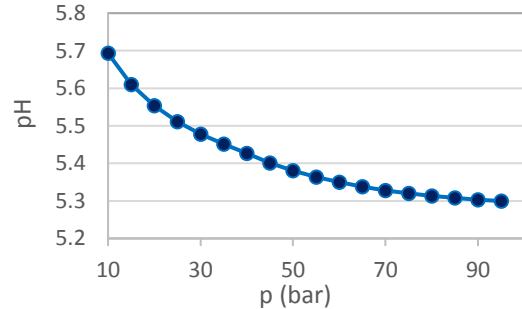


Figure 5.17 – pH profile in the production system.

In this simulation, CaCO_3 is predicted to precipitate [Figure 5.18 c)] for the reasons already discussed, but, interestingly, FeS is also predicted to precipitate, as shown in Figure 5.18 d). Note that there is only a trace amount of Fe^{2+} coming from the reservoir (0.03027 mg/L).

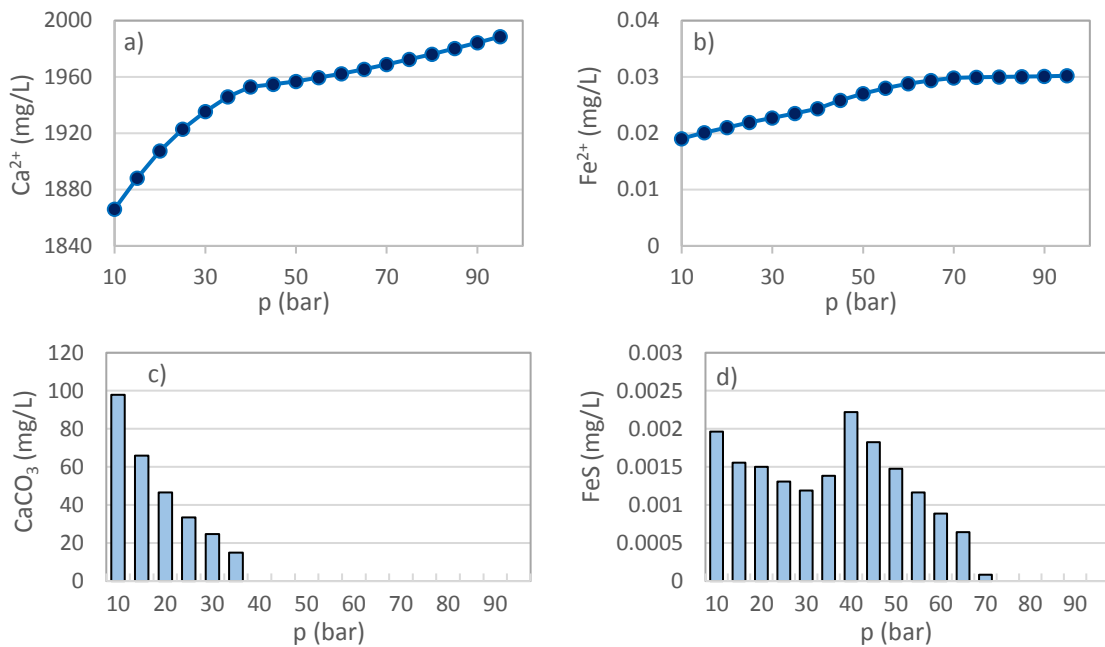


Figure 5.18 – Profiles of the concentrations of Ca^{2+} , Fe^{2+} , CaCO_3 , and FeS in the production system [a), b), c), and d) on figure].

The results in Figure 5.18 a) and c) show that the profile for the concentration of Ca^{2+} and precipitation of CaCO_3 in the production system is very similar to the profiles shown previously in Figure 5.11 d) and Figure 5.13, respectively. In this system, FeS starts to precipitate at 70 bar and increases steadily until the pressure is reduced to 40 bar. Then, this trend is disrupted because CaCO_3 also starts to precipitate. These results clearly show the interdependence of the precipitation of pH-dependent scales.

In addition, Figure 5.18 b) shows that the concentration of Fe^{2+} is approximately constant from 100 bar to 70 bar, which, at a first glance, is not in accordance with results shown in Figure 5.18 a) for the concentration of Ca^{2+} : in this pressure range, it is clear that the concentration of Ca^{2+} decreases due to water condensation. Thus, the concentration of Fe^{2+} should also decrease in this pressure range. And, in fact, it does, although it is not clear in the results shown in Figure 5.18 b). In this context, Table 5.6 presents the concentrations of Ca^{2+} and Fe^{2+} in the production system, and the respective dilution factors.

Table 5.6 – Dilution factors for the concentrations of Ca^{2+} , and Fe^{2+} in the production system.

p (bar)	Ca^{2+} (mg/L)	Fe^{2+} (mg/L)	Ca^{2+} dilution factor	Fe^{2+} dilution factor	Error
95	1988.62	0.03021	1.00216	1.00216	0.00000
90	1984.34	0.03014	1.00208	1.00208	0.00000
85	1980.22	0.03008	1.00200	1.00200	0.00000
80	1976.27	0.03002	1.00191	1.00191	0.00000
75	1972.50	0.02996	1.00182	1.00362	0.00180
70	1968.92	0.02985	1.00172	1.01559	0.01388
65	1965.55	0.02939	1.00160	1.02121	0.01961
60	1962.41	0.02878	1.00147	1.02791	0.02643
55	1959.52	0.02800	1.00132	1.03601	0.03470
50	1956.95	0.02703	1.00113	1.04605	0.04492
45	1954.74	0.02584	1.00089	1.05877	0.05788
40	1953.01	0.02440	1.00361	1.03793	0.03432
35	1945.98	0.02351	1.00537	1.03329	0.02791
30	1935.58	0.02276	1.00654	1.03729	0.03075
25	1923.00	0.02194	1.00817	1.04357	0.03540
20	1907.42	0.02102	1.01016	1.04496	0.03480
15	1888.23	0.02012	1.01178	1.05548	0.04370
10	1866.24	0.01906	-	-	-

From Table 5.6 it is clear that the concentrations of Ca^{2+} and Fe^{2+} have the same dilution factor from 100 to 70 bar.

Although the main mechanism of CaCO_3 scale formation studied here is due to CO_2 evolution from the aqueous phase to the vapour phase, and consequent increase in the pH, I should always take into consideration that water evaporation and condensation are also important autoscaling mechanisms for CaCO_3 precipitation (e.g. McCartney et al., 2014).

5.5.5 Field case example

Extending the previous examples to a field case scenario is somewhat straightforward. Table 5.7 presents the initial input for a field hydrocarbon composition – adapted from Pedersen et al. (2015, p. 42) –, and Table 5.8 and Figure 5.19 present a comparison of this calculation with Winprop. Table 5.9 presents the results for the equilibrium calculation of the aqueous phase – adapted from Mackay and Martins de Souza (2014) – with carbonate rock.

Table 5.7 – Equilibrium calculation of fluids with the reservoir at 100 bar and 80 °C. Oil composition data adapted from (Pedersen et al., 2015) and water composition data adapted from Mackay and Souza).

mole %	Initial (feed)	Equilibrium (in the reservoir)		
		Water	Liquid	Vapour
H ₂ O	10	99.83500	0.45537	0.61450
CO ₂	2.827	0.06616	2.18456	4.06583
N ₂	0.545	0.00077	0.20427	1.00663
C1	45.536	0.08738	25.9755	75.0545
C2	8.606	0.00795	8.51609	10.5234
C3	5.760	0.00207	7.70751	5.00494
iC4	1.012	0.00020	1.58488	0.64506
nC4	2.441	0.00040	4.00231	1.37364
iC5	0.896	0.00004	1.62555	0.34534
nC5	1.244	0.00004	2.30534	0.43027
C6	1.581	0	3.14941	0.32386
C7	2.551	0	5.29736	0.30352
C8	2.746	0	5.83398	0.19298
C9	1.698	0	3.65658	0.06945
C10	1.254	0	2.72115	0.03026
C16	11.303	0	24.78010	0.01588
Phase		9.5323	45.5844	44.8832

Table 5.8 – Comparison of the OGW flash results obtained by using my code and Winprop at 100 bar and 80°C (PR EOS was used).

Component	mole %	HW FAST			Winprop		
		Feed	Water	Liquid	Vapour	Water	Liquid
H ₂ O	10	99.83500	0.45537	0.61450	99.82441	0.47849	0.63911
CO ₂	2.827	0.06616	2.18456	4.06583	0.06731	2.32686	3.92546
N ₂	0.545	0.00077	0.20427	1.00663	0.00088	0.19863	1.01503
C1	45.536	0.08738	25.9755	75.0545	0.09565	26.02321	75.15944
C2	8.606	0.00795	8.51609	10.5234	0.0087	8.51398	10.52833
C3	5.760	0.00207	7.70751	5.00494	0.00227	7.69642	5.0035
iC4	1.012	0.00020	1.58488	0.64506	0.00022	1.58135	0.64474
nC4	2.441	0.00040	4.00231	1.37364	0.00044	3.9924	1.37297
iC5	0.896	0.00004	1.62555	0.34534	0.00004	1.62072	0.34517
nC5	1.244	0.00004	2.30534	0.43027	0.00005	2.29829	0.43003
C6	1.581	0	3.14941	0.32386	0.00002	3.13867	0.32377
C7	2.551	0	5.29736	0.30352	0.00001	5.2783	0.30356
C8	2.746	0	5.83398	0.19298	0	5.81245	0.1931
C9	1.698	0	3.65658	0.06945	0	3.64291	0.06953
C10	1.254	0	2.72115	0.03026	0	2.71091	0.03031
C16	11.303	0	24.7801	0.01588	0	24.68642	0.01596
Phase		9.5323	45.5844	44.8832	9.5119	45.7574	44.7307

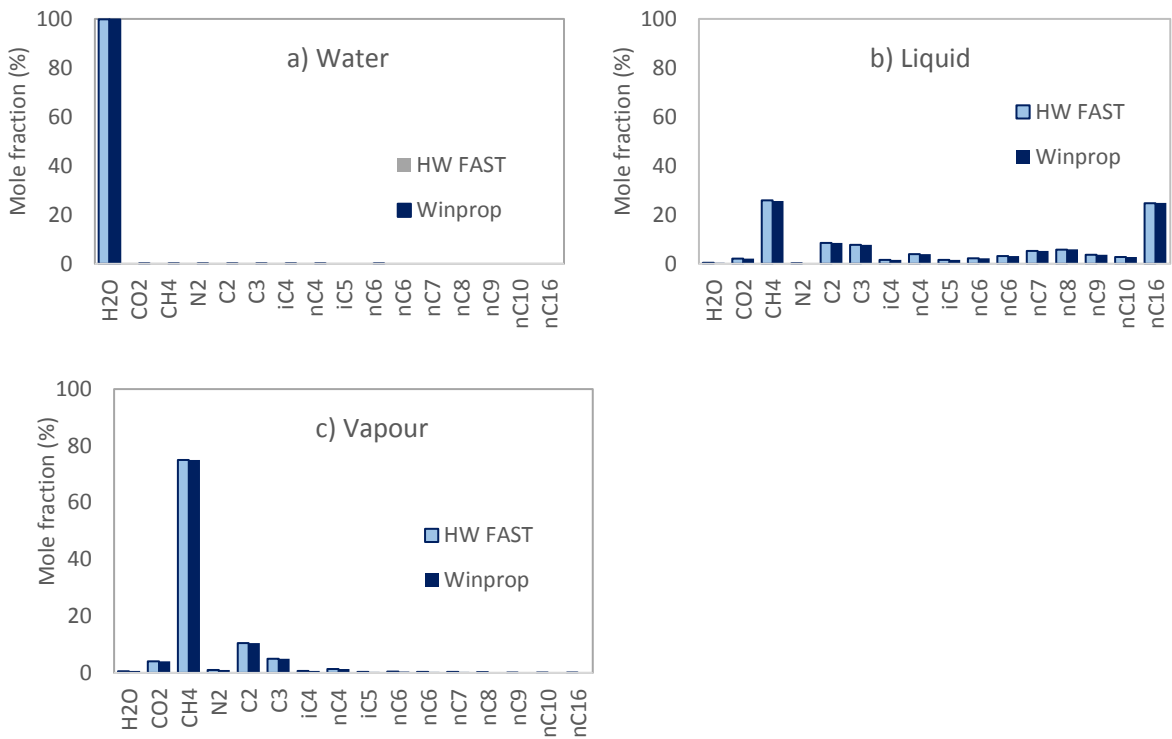


Figure 5.19 – Partition of components between the water, liquid, and vapour phases [a), b), and c) on figure] – these are the same results as the ones presented in Table 5.8.Table 5.1

Table 5.9 – Equilibrium calculation of the aqueous phase with reservoir rock at 100 bar and 80 °C.

m (mg/L)	Initial	Equilibrium
Na ⁺	25265	25280.53
K ⁺	495	495.30
Mg ²⁺	875	875.54
Ca ²⁺	2090	2254.72
Ba ²⁺	35	35.02
Sr ²⁺	210	210.13
Fe ²⁺	0	0
Cl ⁻	44375	43238.48
SO ₄ ²⁻	0	0
CO ₂	-	1178.48
HCO ₃ ⁻	145	642.97
CO ₃ ²⁻	-	0.21072
pH	7	5.546

The results in Table 5.8 and Figure 5.19 show very good agreement between my implementation of the OGW flash and Winprop's for the conditions tested.

In the example presented in Table 5.7, I highlight the initial feed of CO₂ – which accounts for 2.827 mole % of the total feed –, H₂O (10 mole % of the total feed), and light-ends

that account for the majority of the total feed (45.536 mole % CH₄). In the reservoir, all components partition between the water (9.5323 mole %), vapour (44.8832 mole %), and liquid (45.5844 mole %). In addition, I emphasise the concentration of Ca²⁺ in the reservoir (2254.72 mg/L), which indicates that some dissolution of rock has taken place during the equilibrium calculation of the fluids with carbonate rock.

Furthermore, I extend the discussion to note that this calculation follows the algorithm presented previously in Figure 5.5, and thus I note that the OGW flash calculation is solved in a first instance (Table 5.7), followed by a brine-rock equilibrium calculation (Table 5.9), i.e. there are two distinct calculations that have been coupled together. In other words, the total mass of the system is being calculated in this step.

The depressurisation algorithm introduced in Section 5.3 is then applied to these fluids, and the CaCO₃ scaling profile in the production system is calculated, as shown in Figure 5.20.

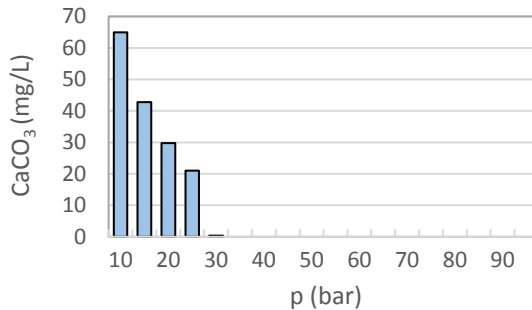


Figure 5.20 – CaCO₃ scale profile in the production system.

Results in Figure 5.20 show that the system presented in Table 5.7 has a potential for CaCO₃ scale at topside facilities, and that a scale management strategy should be considered accordingly.

The examples I have shown so far suggest that, according to my model, CaCO₃ is often predicted to precipitate in the production system in CO₂-rich systems. I can argue that this is exactly what should happen for the following reasons:

- In the reservoir, the carbonate system, which includes the species Ca²⁺, HCO₃⁻, and CaCO₃, is at thermodynamic equilibrium. This means that the SR(CaCO₃) =

1, and that a small change of conditions (pressure, temperature, salinity, pH, etc.) causes dissolution or precipitation of CaCO_3 rock, so that a new equilibrium is established, i.e. the condition $\text{SR}(\text{CaCO}_3) = 1$ is again obtained.

- In the production system, conditions change and the equilibrium previously established in the reservoir is necessarily disrupted such that $\text{SR}(\text{CaCO}_3)$ becomes higher or lower than 1. This equilibrium can then be shifted to cause supersaturation of CaCO_3 , i.e. $\text{SR}(\text{CaCO}_3) > 1$, causing scale precipitation, or it can be shifted to cause under-saturation of CaCO_3 , i.e. $\text{SR}(\text{CaCO}_3) < 1$, and, in this case, no scale precipitates or dissolves (there is no rock to be dissolved).
- The key point is then to find in which direction the system is evolving, i.e. if conditions are changing favouring under-saturation of CaCO_3 or supersaturation, and which factors influence this behaviour. I have identified here CO_2 evolution from the aqueous phase to the vapour phase as the driving force for CaCO_3 scale formation, and this *always* happens in CO_2 -rich production systems due to depressurisation. Assuming that fluids are always at equilibrium with carbonate rock, then I *always* have a potential scaling system.
- Certainly, there are factors that shift the system to under-saturation of CaCO_3 in the production system, as also seen here, such as a decrease in temperature, and water condensation. In the end, it is a balance between all contributing factors, but CO_2 evolution from the aqueous phase to the vapour phase caused by depressurisation has probably the highest weight of these factors in many production scenarios.

For these reasons, I can argue that I should *always expect* CaCO_3 scale precipitation in production systems in carbonate or carbonate-rich reservoirs and in CO_2 -rich environments.

5.5.6 Calculation of scaling profiles in the production system that agree with the water chemistry measured at surface sampling points

I have shown so far a procedure to calculate reservoir fluid compositions and scaling profiles in the production system. However, there is an inconsistency in the results with produced data that needs to be carefully addressed: the water chemistry calculated at surface conditions using my model does not match the observed data for the scaling ions. I review in Table 5.10 the example shown previously for the calculation of reservoir fluid compositions from surface samples. Note that the concentration of Ca^{2+} measured at the sampling point (separator) was 2000 mg/L, as highlighted in Table 5.10.

Table 5.10 – Equilibrium calculation of fluids with the reservoir at 100 bar and 80 °C.

m (mg/L)	Initial	Equilibrium
CO_2	0	5691.83
HCO_3^-	200	746.73
CO_3^{2-}	0	0.02870
Ca^{2+}	2000	2171.13
pH	7	5.091

However, after calculating the CaCO_3 scaling profile in the production system [Figure 5.21 a)], the concentration of Ca^{2+} predicted at the separator is not the same as the concentration of Ca^{2+} measured at this location, as highlighted in Figure 5.21 b).

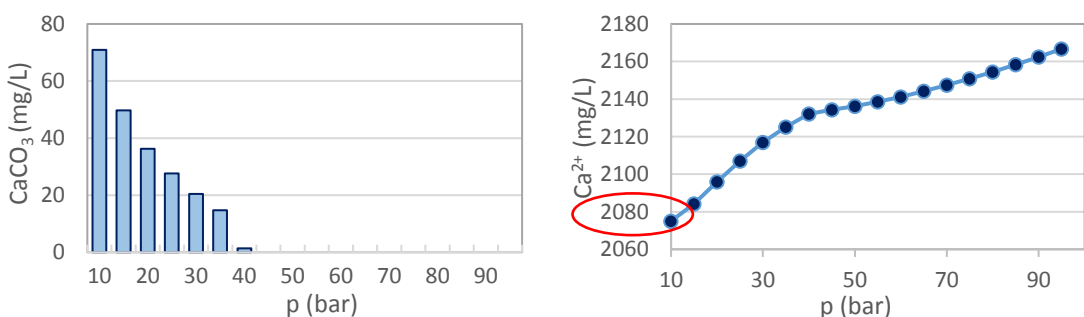


Figure 5.21 – CaCO_3 scale (left) and concentration of Ca^{2+} profile (right) in the production system. Note that the concentration of Ca^{2+} calculated at separator conditions (10 bar) is not 2000 mg/L.

As explained previously, the concentration of CO_2 in the aqueous phase is fixed by the PVT calculation. I can then vary the initial values for the concentrations of HCO_3^- (or CO_3^{2-} , or both) and Ca^{2+} until I obtain, after running a simulation, the correct

concentration of Ca^{2+} at the separator. To accomplish this, I plot in Figure 5.22 the concentration of Ca^{2+} that I obtain at the separator by varying the initial concentrations of HCO_3^- and Ca^{2+} in the reservoir from 0 to 1000 mg/L and from 0 to 3000 mg/L, respectively.

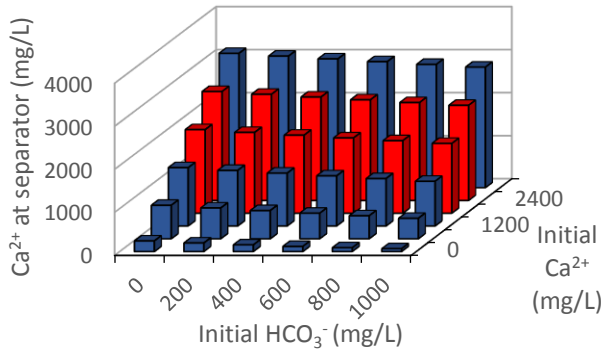


Figure 5.22 – Concentration of Ca^{2+} calculated at separator conditions (10 bar) for different values of initial concentrations of Ca^{2+} and HCO_3^- .

From Figure 5.22, it is understandable that if I fix, for example, 0 mg/L for the initial HCO_3^- concentration (note that this concentration is before an equilibrium calculation with carbonate rock and fluids in the reservoir), then I find that 1858.32 mg/L of the initial Ca^{2+} concentration gives 2000 mg/L of Ca^{2+} at the separator. In fact, in this context there is unique reciprocity between values of initial Ca^{2+} and HCO_3^- concentrations: for each value of initial Ca^{2+} concentration, there is an unique correspondent value of initial HCO_3^- concentration such that the concentration of Ca^{2+} at the separator is 2000 mg/L, and vice versa. The red columns in Figure 5.22 identify lower and upper limits of this reciprocity: for example, if I fix 0 mg/L for the initial HCO_3^- concentration and increase the initial concentration of Ca^{2+} starting from zero, then the first 4 columns have values lower than 2000 mg Ca^{2+} /L at the separator, and the last two have values higher than 2000 mg Ca^{2+} /L.

Figure 5.23 presents the results obtained by using a correct set of initial conditions for the equilibrium calculation in the reservoir [Figure 5.23 a)] and for the Ca^{2+} concentration profile in the production system [Figure 5.23 b)]. Note that the Ca^{2+} concentration at the separator, i.e. at 10 bar, is now 2000 mg/L, as highlighted in Figure 5.23 b).

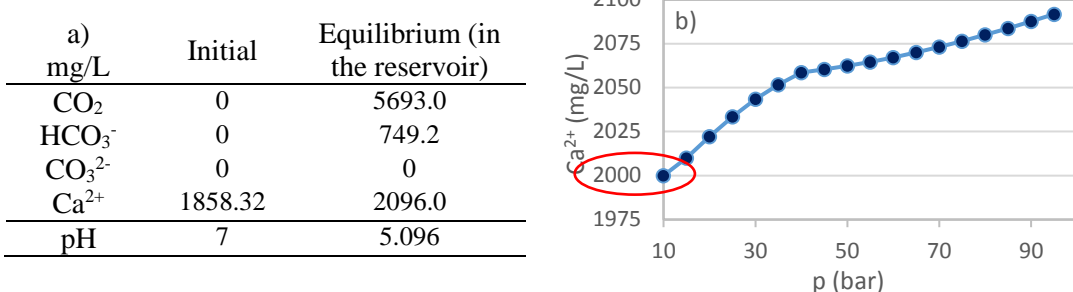


Figure 5.23 – a) Equilibrium calculation of fluids with the reservoir at 100 bar and 80 °C; and b) concentration of Ca²⁺ profile in the production system. Note that the concentration of Ca²⁺ calculated at separator conditions (10 bar) is 2000 mg/L.

The results in Figure 5.23 show that using a correct set of initial conditions allows getting a match between calculated and measured values for the concentration of Ca²⁺ at the separator. Furthermore, I note that I could have used *any* set of correct initial conditions to obtain the correct scaling profile in the production system, as shown in Figure 5.24.

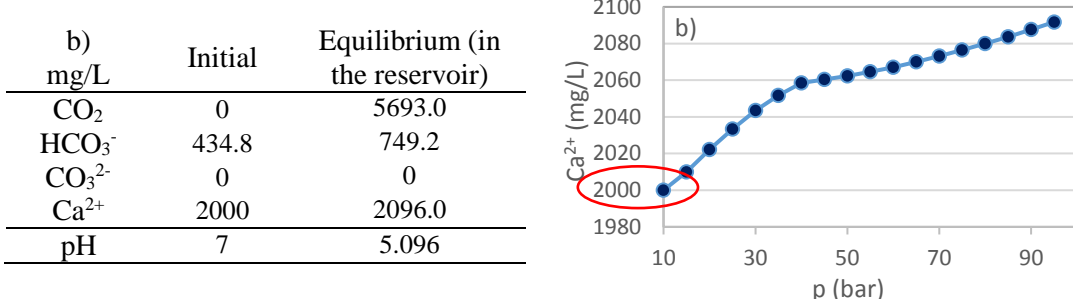


Figure 5.24 – a) Equilibrium calculation of fluids with the reservoir at 100 bar and 80 °C using different initial conditions compared to the ones used in Figure 5.23; and b) concentration of Ca²⁺ profile in the production system. Note that the concentration of Ca²⁺ calculated at separator conditions (10 bar) is 2000 mg/L.

Obviously, the calculated composition for the water present in the reservoir in equilibrium with carbonate rock and hydrocarbon fluids can even be used as the “true” set of initial conditions, although this step is redundant after finding one correct set of initial conditions that match the measured data at the separator, since the solution is unique.

Figure 5.25 shows the profiles in the production system for the concentration of Ca^{2+} and CaCO_3 scale that is in agreement with production data. This is the information required to design scale management strategies.

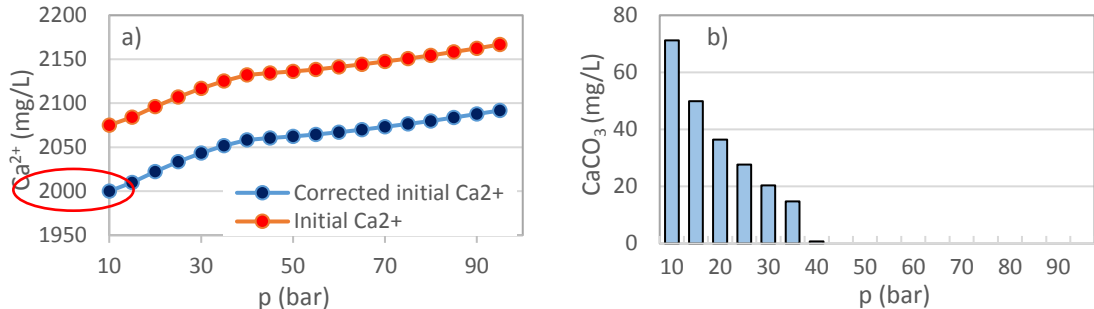


Figure 5.25 – a) Concentration of Ca^{2+} in the production system for the non-corrected and corrected cases; and b) CaCO_3 scale precipitation profile in the production system.

Table 5.11 shows the calculated values for the aqueous concentrations of Ca^{2+} and $\text{CO}_2/\text{HCO}_3^-/\text{CO}_3^{2-}$ in the reservoir and at the separator, and the respective measured values at the separator.

Table 5.11 – Comparison between measured and calculated values for the brine composition at separator conditions.

mg/L	Calculated reservoir brine	Calculated separator brine	Separator brine
CO_2	5693.0	1466.15	-
HCO_3^-	749.2	465.53	200
CO_3^{2-}	0	0.036	-
Ca^{2+}	2096.0	2000.00	2000

The results in Table 5.11 show excellent agreement between the calculated and measured values for the concentration of Ca^{2+} at the separator, and that the calculated concentration of HCO_3^- at the separator is higher than the measured concentration. This difference can be attributed to the uncertainty in measuring HCO_3^- concentrations, due to, for example, the possibility of having CO_2 evolution from a sample when bringing it to atmospheric pressure, and consequent HCO_3^- loss.

So far, I have proposed a procedure to calculate carbonate scale precipitation in production systems that matches observed data. However, it is desirable to run sensitivity

analyses on key parameters to answer “what if” questions and to identify worst case scenarios.

In order to identify worst case scenarios with respect to scale precipitation, I propose varying critical parameters for the specific process, such as the concentrations of components that are directly involved in precipitation reactions. For CaCO_3 scale, these components are Ca^{2+} and HCO_3^- . Figure 5.26 presents the results for the precipitation of CaCO_3 in the worst point of the production system – which is, in this case, at the separator, where the pressure has its lowest value – as a function of the initial concentration of Ca^{2+} and HCO_3^- .

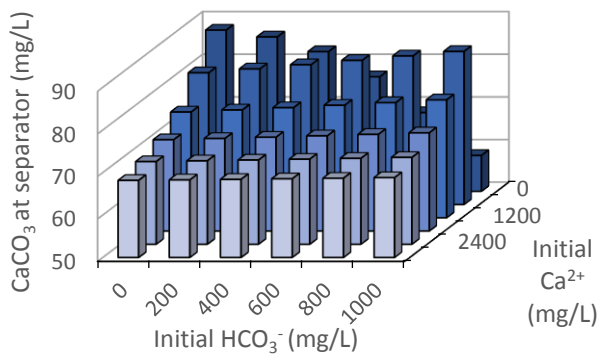


Figure 5.26 – Concentration of CaCO_3 calculated at separator conditions (10 bar) for different values of initial concentrations of Ca^{2+} and HCO_3^- .

The results in Figure 5.26 show that the worst case scenario corresponds to having zero for the initial concentrations of Ca^{2+} and HCO_3^- . Obviously, the concentrations of these two components are not zero after performing an equilibrium calculation with the carbonate rock and fluids in the reservoir.

Figure 5.27 shows the CaCO_3 scaling profile in the production system for the three cases studied here, i.e. for the case where I did not correct the concentration of Ca^{2+} in the production system, for the case where I corrected the concentration of Ca^{2+} , and for the worst case scenario.

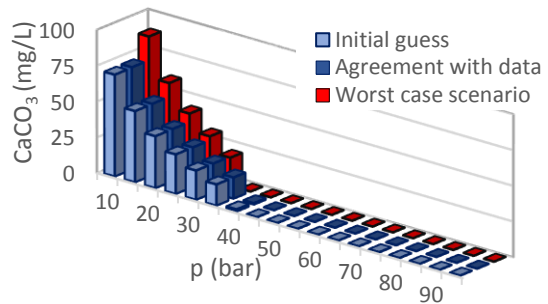


Figure 5.27 – CaCO_3 scale precipitation profile in the production system for the non-corrected case, the corrected case, and the worst case scenario.

Results in Figure 5.27 suggest that, for the present study, the CaCO_3 precipitation profile in the production system would not be significantly affected by using the concentrations of components measured at the separator as initial conditions for the model. Also, the worst case scenario is not significantly different from the correct CaCO_3 scaling profile, suggesting that the system is not very sensitive with respect to the initial concentrations of Ca^{2+} and HCO_3^- used in the model. A conservative scale management strategy would then use the worst case scenario to address CaCO_3 scale in the production system.

5.6 Conclusions and recommendations

The precipitation of CaCO_3 scale in CO_2 WAG processes depends on the partition of CO_2 between all the phases in the system, including liquid. This means that CaCO_3 scale precipitation depends not only on the conditions of the system such as pressure, temperature, etc., but also on the type of hydrocarbon fluid in the system (black oil, volatile oil, retrograde gas, wet gas, or dry gas). In this context, I have extended the scale precipitation model to account for the partition of components, including CO_2 and H_2S , between water, vapour, and liquid phases. In addition, I have developed a procedure that calculates CaCO_3 scaling profiles in CO_2 -rich production systems from commonly available compositional data. In detail, I have addressed the following in this chapter:

- Oil-Gas-Water (OGW) flash calculation. The OGW algorithm proposed by Li and Nghiem, 1986, has been implemented and further validated by comparing results obtained by using my implementation and results obtained by using the PVT software Winprop. In addition, this algorithm has been coupled with the aqueous scale prediction model developed previously in Chapter 3, for two types of calculations: in the reservoir, where the total mass of the system is found; and in the production system, where the mass of the system is conserved.
- Calculation of reservoir fluid compositions from surface samples. A procedure for calculating the composition of water, vapour, and liquid in the reservoir from surface compositional data has been developed. This procedure consists in determining the total mass of the combined water, vapour, and liquid phases at a surface sampling location, and then calculating the partition of components at reservoir conditions by using the OGW flash algorithm and accounting for the principle of mass conservation.
- Calculation of scaling profiles in production systems. Having determined the composition of fluids in the reservoir, an algorithm for calculating the precipitation of CaCO_3 scale in the production system has been developed, by also using the OGW flash routine and the principle of mass conservation. I note that this calculation is one of the main objectives of the thesis, i.e. calculating the CaCO_3 scale precipitation in CO_2 -rich production systems.

- Calculation of scaling profiles in production systems that fully agree with production data. Having calculated the precipitation of CaCO_3 scale in the production system, I have verified that the calculated concentration of Ca^{2+} at the sampling location did not match the measured one. This is because the concentration of Ca^{2+} calculated for reservoir conditions from surface data is not accurate, since CaCO_3 scale precipitates upstream of the sampling point. Thus, a procedure has been developed to find the correct concentration of Ca^{2+} in the reservoir such that the calculated concentration of Ca^{2+} at the sampling location agrees with the measured one.

Having a state-of-the-art PVT model is key to calculate mineral scale precipitation, especially if components involved in scale precipitation partition between all phases in the system, such as CO_2 which is involved in the precipitation of CaCO_3 and partitions between the aqueous, vapour, and liquid phases. Although I have implemented here common PVT models that are widely used in the oil industry, there is room for improvement. In fact, I believe that scale prediction models must have the same PVT capabilities as the most advanced PVT software available in the industry. This way, and in this context, scale prediction calculations will be as accurate as they can possibly be.

6. Reactive transport

In a CO₂ WAG process, CO₂ and water are alternatively injected in the reservoir for tertiary oil recovery. This means that the transport of fluids in the reservoir and their production is dependent on the injection schedule, and, consequently, so is the precipitation of CaCO₃ scale in production systems. This cyclic nature of CO₂ WAG processes can be modelled in the context of CaCO₃ scale precipitation in production wells by using a 1D reactive transport model.

In particular, this model can calculate the reactive flow and transport of components – Na⁺, Cl⁻, Ca²⁺, HCO₃⁻, etc. – through a porous medium, and thus account for rock-brine interactions in the reservoir. In fact, the dissolution of CaCO₃ rock in the reservoir into Ca²⁺ and CO₃²⁻ (and HCO₃⁻) ions, followed by the transport of these components to the production system, and subsequent re-precipitation of CaCO₃ scale at this location, is the mechanism for CaCO₃ scale formation in CO₂ WAG processes (as studied here). Therefore, modelling rock-brine equilibrium and transport of components in the reservoir must be included in the study of CaCO₃ scale formation in CO₂ WAG processes.

In this context, the following objectives are considered in this chapter:

- i) Develop a 1D reactive transport model to account for the reactive flow and transport of components commonly encountered in oilfield water compositions (Na⁺, Cl⁻, Ca²⁺, Fe²⁺, HCO₃⁻, etc.).
- ii) Validate the reactive transport model with experimental data.
- iii) Model the precipitation of CaCO₃ scale in CO₂ WAG processes by: a) using the reactive transport model to calculate rock-brine interactions and transport of components in the reservoir; and b) using the scale prediction model developed in the previous chapters coupled with the reactive transport model to calculate CaCO₃ scale precipitation in CO₂ WAG production systems.
- iv) Study the effect of kinetics on the carbonate/CaCO₃ system.
- v) Apply the reactive transport model to calculate the capacity of natural occurring FeCO₃ rock to scavenge H₂S.

6.1 1D reactive transport model

As seen in Chapter 3, the various species directly involved in the CO₂/carbonate system are CO₂, Ca²⁺, HCO₃⁻, CO₃²⁻, H⁺, and OH⁻ as well as calcite itself, CaCO₃. I denote this vector of unknowns, \underline{c} , where $\underline{c} = (c_1, c_2, c_3, \dots)^T$. Thus, to model flow in a CO₂ WAG system, each component must be transported according to a typical 1D advection-dispersion equation as follows:

$$\frac{\partial c_i}{\partial t} = D_i \frac{\partial^2 c_i}{\partial x^2} - v_i \frac{\partial c_i}{\partial x} + R_i(\underline{c}) \quad (6.1)$$

Where c_i is the concentration of species i , D_i is the corresponding dispersion coefficient, v_i is the velocity and $R_i(\underline{c})$ is the reaction rate of species i (which may depend on all other species j present, where $i \neq j$). This equation is well known in the theory of transport in porous media (Lasaga, 1998). Any suitable numerical scheme may be used to solve this set of transport equations and I apply a single point upwind explicit scheme to solve this set of transport equations directly, as (Ferziger and Peric, 2002, pp. 143-148):

$$c_i^{n+1} = c_i^n + \left[D \frac{\Delta t}{\Delta x^2} (c_{i+1}^n + c_{i-1}^n - 2c_i^n) - v \frac{\Delta t}{\Delta x} (c_i^n - c_{i-1}^n) \right] \quad (6.2)$$

6.2 Studying the effect of kinetics in the reactive transport model

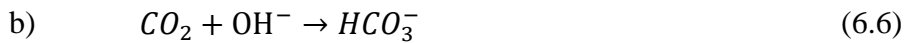
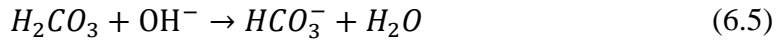
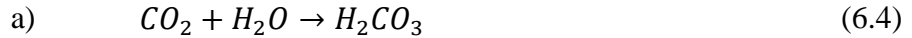
Predicting the precipitation of CaCO₃ in production systems can be a challenge due to the complexity of the scaling system, namely the partition of key components, such as CO₂, between all the phases in the system. Another factor that can add to the complexity of the system is the introduction of kinetics in the thermodynamic model. If kinetics play a relevant role in the precipitation of CaCO₃ scale, then thermodynamic calculations might not suffice to determine the correct amount of CaCO₃ scale that precipitates in production systems.

Introducing kinetics in the thermodynamic models developed in the previous chapters is out of the scope of this thesis. Introducing kinetics in a thermodynamic model adds a degree of complexity to the system, and there might be relevant kinetic data which are

not readily available in the literature. For example, I review here Equation (3.6) introduced in Chapter 3 for the speciation of CO₂ into HCO₃⁻:

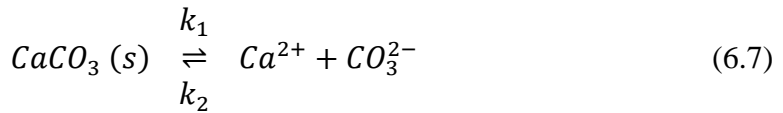


In a kinetic model, this equation should be re-written as two parallel and competing reactions as:



In thermodynamics, Equations (6.3) and (6.4)-(6.6) are equivalent, since the net result is the same. However, in a kinetic model, I have to consider the different rate laws for Equations a) and b) separately (Lasaga, 1998, pp. 47-51). In fact, having one reaction much slower than the other can impact scaling systems, such as the CaCO₃ scaling system as studied here [e.g. the rate of dissolution of carbonate rock can be limited by the kinetics of reactions a) and b) above].

Rate laws not only introduce a degree of complexity in thermodynamic calculations, but also introduce new experimental parameters that need to be specified. For example, Equations (6.7) and (6.8) show respectively the reaction for the CaCO₃ dissolution/precipitation (forward and reverse reactions) and corresponding rate law (Lasaga, 1998, pp. 82-93).



$$-\frac{dm_{CaCO_3}}{dt} = \frac{A}{V} k_2 K_{sp}^n (1 - \Omega^n) \quad (6.8)$$

Where A/V is the CaCO₃ specific area (area/solution volume), k₂ is the CaCO₃ precipitation rate constant, n is a positive constant, and Ω is the CaCO₃ saturation ratio. In a thermodynamic model, I require knowledge of only the solubility product of CaCO₃ for reaction (6.7). In a kinetic model, I require, in addition, to know k₂ and n, and their

respective dependence on pressure and temperature (and maybe even salinity). However, I can argue that these data are not readily available in the literature.

Although introducing kinetics in a thermodynamic model is not straightforward, I can nevertheless use a thermodynamic formulation to study the *effect of kinetics* on scaling systems by taking an expeditious approach. This approach is explained as follows: in thermodynamic calculations, I always have an initial state and an equilibrium state. If kinetics are considered, then the equilibrium state may not be reached during the period of the calculation, and the system *halts somewhere in between the initial and the equilibrium states*. Thus, I can calculate the equilibrium state and apply a *pseudo kinetic factor* that brings the system to a point in between the initial and equilibrium states. This concept is shown schematically in Figure 6.1: the initial state is defined by the initial concentration of the species in the system; the thermodynamic model is run to find the equilibrium concentration of the species, i.e. to find the equilibrium state; and then the pseudo kinetic factor ζ ($0 \leq \zeta \leq 1$) is applied to the equilibrium concentrations to find the concentration of the species that lie between the initial and the equilibrium states, as shown in Equation (6.9). This is an approximation, since I am performing a linear interpolation between initial and equilibrium states, and this is most probably not strictly correct in a kinetic model. However, it can be used to study the effect of kinetics on CaCO_3 scale precipitation.

$$c_{i, \text{initial}} = \zeta c_{i, \text{equilibrium}} \quad (0 \leq \zeta \leq 1) \quad (6.9)$$

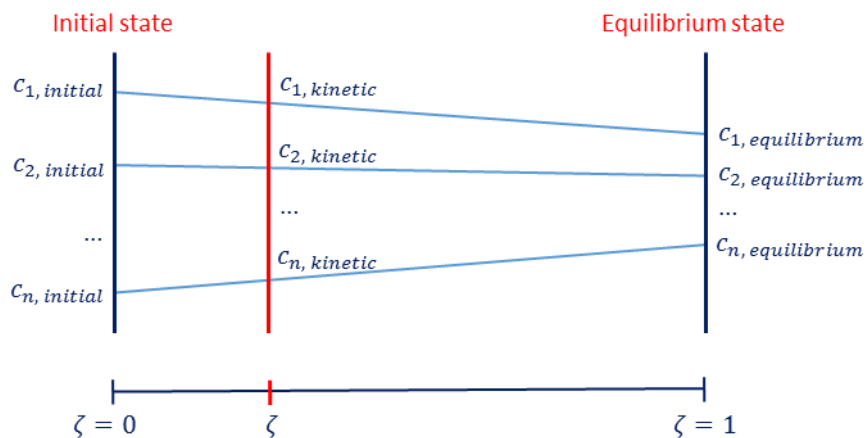


Figure 6.1 – Linear interpolation of initial and equilibrium thermodynamic states.

This approach can then be applied in the reaction term in Equation (6.1).

In transport theory, the Damköhler number can be used to relate reaction timescales with transport timescales. This number is defined as follows:

$$Da = \frac{\text{reaction rate}}{\text{convective transport rate}} \quad (6.10)$$

Equation (6.10) shows that if $Da \geq 1$, then the reaction rate is higher than the convective transport rate and the system *has the time* for reactions to take place. On the other hand, if $0 \leq Da < 1$, then the convective transport rate is higher than the reaction rate, and the system *has not the time* for reactions to take place completely. If $Da = 0$, then reactions do not take place at all, and there is only transport of components. It is interesting to note that the pseudo kinetic factor ζ introduced previously relates with the Damköhler number for $0 \leq Da < 1$.

6.3 Reactive transport coupled with scale predictions in production systems

Considering the reactive transport model presented above and the scale prediction and VLE models presented in Chapters 3 and 4, respectively, I propose the following model to address CaCO_3 scale dissolution in a carbonate reservoir and the subsequent precipitation in CO_2 WAG production wells:

1. Injection profile and reactive transport

In a CO_2 WAG scheme, the injection profile alternates between the injection of a CO_2 -rich vapour phase and water. Since CO_2 must dissolve in water to react with CaCO_3 rock in the reservoir, I assume that the injection of the CO_2 slug is represented by the injection of water saturated with CO_2 at reservoir pressure and temperature. In other words, the injection profile consists of the alternated injection of seawater and CO_2 -saturated seawater. This assumption simplifies the model by considering the reactive transport of only one phase, while capturing the main effects of rock dissolution which are relevant to CaCO_3 dissolution and re-precipitation in production wells. In reality, not all CO_2 will come into contact

with water in the reservoir and dissolve rock, so my assumption allows working in a worst case scenario.

2. Depressurisation

I assume that the flowing water composition in the last block of the reactive transport simulation is essentially the same as the composition of the water that enters the wellbore. Then, this water *is brought to surface* by varying pressure and temperature, with both pressure and temperature decreasing as the produced brine is transported up the well to the surface. The consequent evolution of CO₂ from the aqueous phase to the vapour phase is calculated by using the VLE model, and the precipitation of CaCO₃ scale at each point of the production system is then calculated using the scale prediction model. This gives a scale deposition profile of calcite up the well.

Steps 1 and 2 above are explained in detail by presenting the calculations for a field example in the next section.

6.4 Results and discussion

6.4.1 *Model validation with laboratory data*

Experimental data from the Flow Assurance and Scale Team (FAST) database has been used to validate the reactive transport model. As noted previously, in a CO₂-WAG scheme, the rock-brine interactions play a fundamental role. In particular, the dissolution of calcite in the reservoir due to the more acidic environment is key to the subsequent re-precipitation of CaCO₃ at the production wells. This process can be studied with an experiment consisting of flooding a calcite (CaCO₃)-packed column with seawater at different pH-levels and assessing the profile for the dissolution of calcite, as show in Figure 6.2.

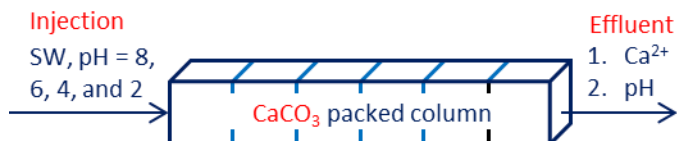


Figure 6.2 – CaCO_3 -packed column flooded with seawater at different pH levels. The effluent is then measured for the pH and concentration of Ca^{2+} .

The column used in the experiment was packed with crushed calcite rhombs (crushed calcite rhombs supplied by Northern Geological Supplies of Bolton, Lancashire, and sieved to a grain size between 100 and 315 μm ; column diameter and length of 1.5 and 13.6 cm) and flooded with synthetic seawater (SSW) at 15 mL/h flowrate. The composition of SSW is presented in Table 6.1. The injection of SSW with different pH-values was carried out where 10 PV slugs of four brines with pH values of 8, 6, 4, and 2, were sequentially injected. An in-line pH probe was used to continuously measure the effluent pH and thus minimise potential pH-measuring errors due to CO_2 off-gassing. The effluent was collected and the concentration of calcium was then assayed using ICP-OES.

Table 6.1 – Composition of the injection brine – synthetic seawater (SSW).

Ion	mg/L
Na^+	10890
Ca^{2+}	428
Mg^{2+}	1368
K^+	460
SO_4^{2-}	2960
Cl^-	19773

Figure 6.3 shows the experimental and modelling results obtained for the pH measured at the effluent stream as a function of the pore volume injected.

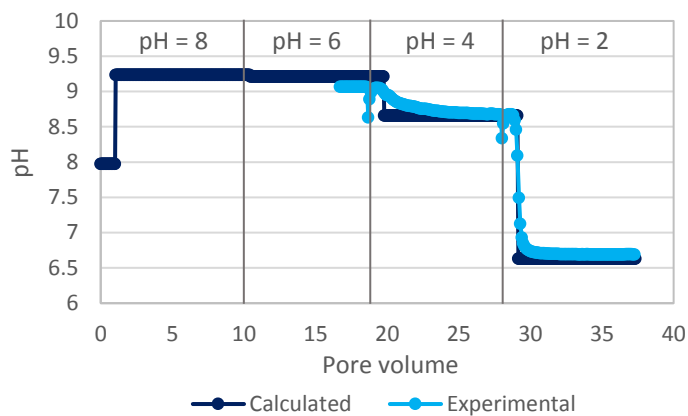


Figure 6.3 – pH as a function of the PV injected for the calculated and experimental values.

The results in Figure 6.3 show very good agreement between calculated and measured values for the effluent pH. In addition, these results show that:

- i) Initially, the water present in the column has a pH of approximately 8. This water is displaced when injection starts, and after 1 PV injection of SSW with pH = 8 all of this water has been displaced from the column (at least, in the numerical simulation).
- ii) The injection of SSW with pH = 8 causes the pH in the effluent to shift from 8 to approximately 9.5, indicating that some dissolution of CaCO₃ has taken place (increase in CO₃²⁻ ions).
- iii) The injection of SSW with pH = 6 practically does not perturb the system, since the pH in the effluent is approximately the same as for the previous injection wave (SSW with pH = 8), i.e. pH measured is also approximately 9.5. The injection of SSW with pH = 4 slightly perturbs the system, since the pH in the effluent shifts from 9.5 to approximately 8.6.
- iv) The injection of SSW with pH = 2, i.e., the injection of a very acidic brine, causes a considerable perturbation in the system, since the pH in the effluent shifts from 8.6 to approximately 6.7. However, the injection of this brine shows how CaCO₃ rock buffers the system: the injection of a very acidic brine

does not cause a very acidic environment, since CaCO_3 rock dissolves and re-establishes the pH (due to an increase in CO_3^{2-} ions).

Figure 6.4 shows the experimental and modelling results obtained for the concentration of Ca^{2+} measured at the effluent stream as a function of the pore volume injected.

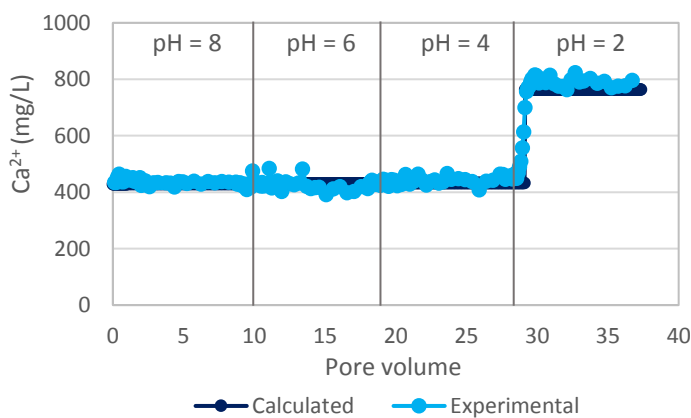


Figure 6.4 – Concentration of Ca^{2+} as a function of the PV injected for the calculated and experimental values.

The results in Figure 6.4 show very good agreement between calculated and measured values for the concentration of Ca^{2+} at the effluent stream. In addition, these results show that:

- i) No significant dissolution of calcite occurs caused by the injection of SSW with pH 8, 6 and 4, since there is no apparent change in the effluent concentration of Ca^{2+} .
- ii) However, the observed change in effluent pH for the pH 4 injected brine does indicate that some reaction is taking place and a *very* slight increase in Ca^{2+} is predicted.
- iii) The injection of SSW with pH 2 causes an increase in the concentration of Ca^{2+} in the effluent due to the significant dissolution of calcite in the column and a significant drop in the pH levels to 6.7 (Figure 6.3).

The results in Figure 6.3 and Figure 6.4 clearly demonstrate that my model accurately predicts the CaCO_3 rock dissolution/precipitation, including the acid equilibrium

behaviour, and the transport of components through a porous medium for the conditions tested.

6.4.2 *CaCO_3 scale in CO_2 -WAG*

6.4.2.1 *Model input for a field case scenario*

I used data from a field case reported previously by Mackay and Martins de Souza (2014) to run the simulations. In particular, I used data for the injection and formation water compositions and the reservoir pressure and temperature, although my model can be readily applied to other field conditions. For this case, the reservoir pressure and temperature are 169 bar and 62.7 °C, and the injection and formation water compositions are presented in Table 6.2.

Table 6.2 – Formation and injection water compositions used in simulations. Adapted from Mackay and Martins de Souza (2014).

Components	Formation water	Seawater
Na^+	25265	10319
K^+	495	397
Mg^{2+}	875	1379
Ca^{2+}	2090	446
Ba^{2+}	35	0
Sr^{2+}	210	8
Fe^{2+}	0	0
Cl^-	44375	17203
SO_4^{2-}	0	3000
HCO_3^-	145	150

The input data for the reactive transport model are presented in Table 6.3.

Table 6.3 – Input data used in the reactive transport simulation.

Flow rate (bbl/day), $Q =$	1000
Time step (days), $\Delta t =$	2.52
Grid size (m), $\Delta x =$	100
Porosity, $\Phi =$	0.4
Dispersion (m^2/s), $D =$	0
Number of grid Blocks, $N =$	20
Cross-sectional area (m^2), $A =$	10

The CO₂ WAG injection schedule is shown in Table 6.4. As explained above, the injection profile consists of the alternating injection of ordinary seawater and CO₂-saturated water. I assume that the CO₂-rich vapour phase is composed of 80% CO₂ and 20% CH₄ (in mole percent) from which I calculate the amount of CO₂ (and CH₄) dissolved in the CO₂-saturated brine using a VLE model (PR EOS). I chose an injection profile which will render results easy to interpret – the injection of 0.5 PV of each slug (CO₂ and water) and 1.5 PV for the last seawater slug, although I could have used any other CO₂ WAG injection profile schedule.

Table 6.4 – CO₂ and seawater injection profile schedule.

Pore volume	Slug
0.5	CO ₂
0.5	Seawater
0.5	CO ₂
0.5	Seawater
0.5	CO ₂
1.5	Seawater

6.4.2.2 *Dissolution in the near-wellbore region of the injector*

Here I assume initially that the CO₂ slug (i.e. the water saturated with CO₂) is in thermodynamic equilibrium with the carbonate rock (as calcite, CaCO₃). However, in later calculations, this assumption will be relaxed and the effects of kinetics within the reservoir will be investigated. However, whether the fluids are fully in equilibrium with the rock or not, there will always be *some* degree of dissolution or precipitation when injecting a reactive CO₂/water slug.

Figure 6.5 shows the impact of injecting alternatively CO₂ and water on CaCO₃ rock dissolution (negative values) and precipitation (positive values) for this example.

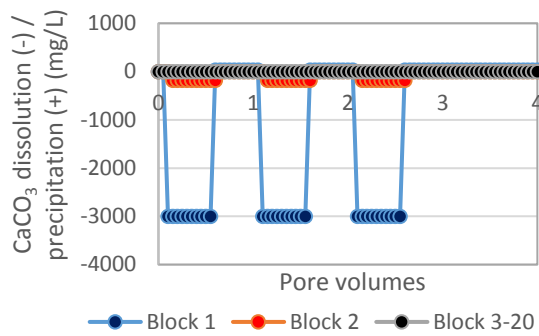


Figure 6.5 – CaCO_3 dissolution (negative values) and precipitation (positive values) as a function of the pore volumes injected for the CO_2 -WAG injection profile schedule identified in Table 6.4.

The results in Figure 6.5 show that CO_2 WAG injection causes rock dissolution in the near-wellbore region of the injector (negative values), i.e. in blocks 1 and 2, and no dissolution or precipitation deeper within the reservoir or in the near-wellbore region of the producer (the value is very close to zero), i.e. in blocks 3 to 20. Furthermore, the dissolution of rock has a cyclic behaviour depending on which slug is being injected: for the CO_2 slug, i.e. for 0 to 0.5, 1 to 1.5, and 2 to 2.5 of pore volumes injection, the dissolution of rock is enhanced, being dissolved approximately 3000 mg/L of rock in the first block. This dissolution of CaCO_3 rock causes an increase of Ca^{2+} and CO_3^{2-} ions (present actually as HCO_3^- ions at these lower pH values) in the aqueous phase that are subsequently transported to production wells where they will then re-precipitate as CaCO_3 scale.

6.4.2.3 *Boundaries for CaCO_3 scale: concept of CO_2 and seawater waves*

As seen from the results in Figure 6.5, the CO_2 WAG injection profile has a cyclic behaviour. This leads directly to a cyclic behaviour in production results, depending on which “wave” – CO_2 or water – is being analysed. Figure 6.6 shows a snapshot of the pH vs. distance profile in the reservoir for four “times, T” (i.e. pore volumes injected), viz. at $T = 0.5, 1, 1.5$, and 2 PV (see Table 6.4).

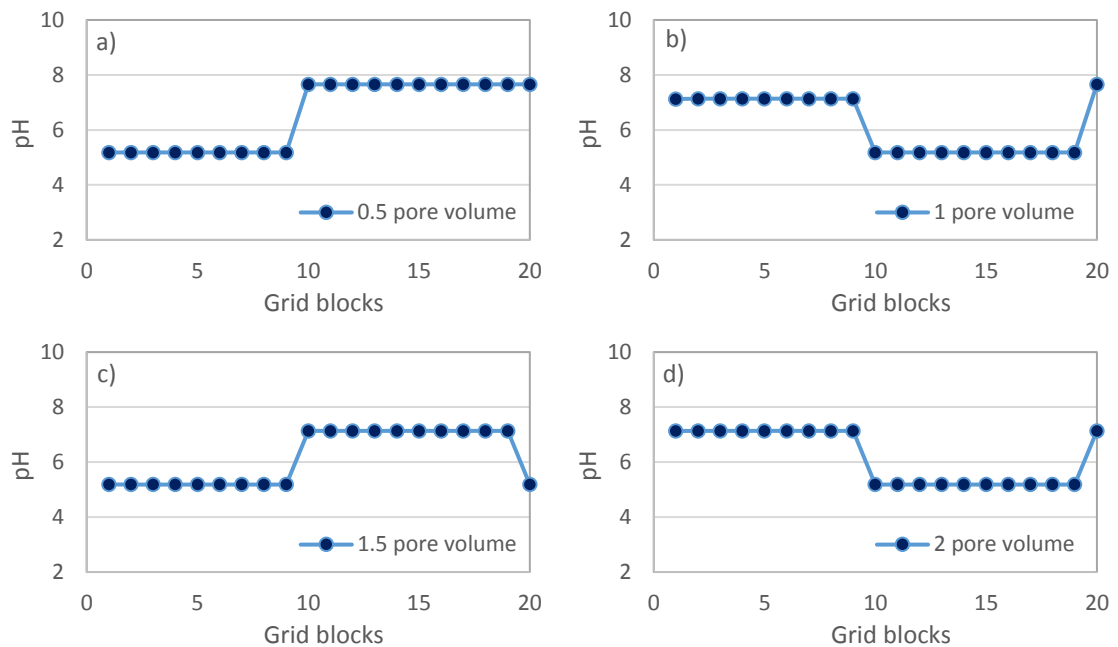


Figure 6.6 – pH profile in the reservoir as a function of 0.5, 1, 1.5, and 2 pore volumes injected [a), b), c), and d) on figure].

Results in Figure 6.6 show that, for example at $T = 0.5$ PV injection [Figure 6.6 a)], there are two pH levels: 5.2 for blocks 1 to 10 which corresponds to the injection of the CO_2 slug, and 7.7 for blocks 10 to 20 which corresponds to original pH of the formation water (in equilibrium with CaCO_3 rock). If I then analyse the plot for $T = 1$ PV of injection [Figure 6.6 b)], I see that the injection of seawater causes the pH to shift from 5.2 to 7.1. And a similar analysis can be made for the $T = 1.5$ and $T = 2$ PV injection cases in Figure 6.6 c) and d), respectively.

If these various waves of seawater, CO_2 and formation water propagate to the producer (which they do in this 1D calculation), then these results suggest that I have three different production regimes depending on which wave is being produced, i.e. depending on whether formation water is being produced, or it is the CO_2 wave, or the seawater wave. In fact, I can clearly identify these three different production profiles in the results shown in Figure 6.7. Figure 6.7 plots the concentration of components (exemplified by Ca^{2+} and pH) in the last block of the reactive transport simulation as a function of the pore volume injected. Note that it is precisely these concentrations/compositions that enter the wellbore.

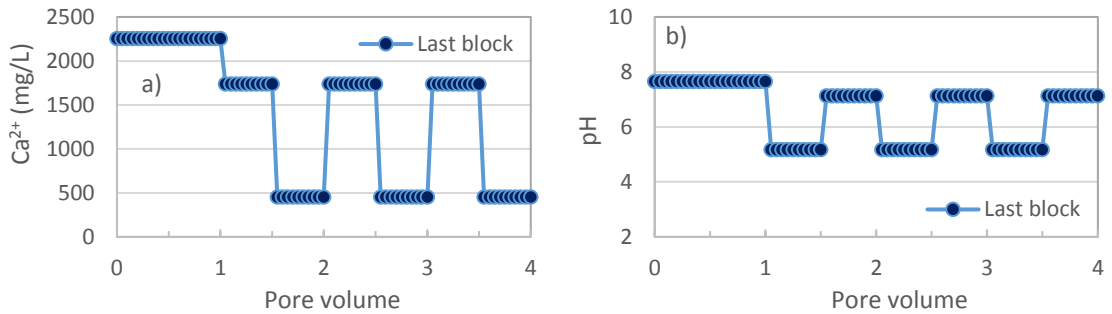


Figure 6.7 – Concentration of Ca^{2+} and pH in the last block of the reactive transport simulation as a function of the pore volumes injected [a) and b) on figure, respectively]. These concentrations are the same as the concentrations of the fluids that enter the wellbore. Three distinguishable production stages can be seen: formation water production, CO_2 and seawater waves.

Results in Figure 6.7 show that, for example for the concentration of Ca^{2+} [Figure 6.7 a)], the formation water wave ($2256 \text{ mg Ca}^{2+}/\text{L}$) corresponds to the injection of $T = 1 \text{ PV}$, the CO_2 saturated brine waves ($1738 \text{ mg Ca}^{2+}/\text{L}$) correspond to the injection of $T = 1$ to 1.5 , 2 to 2.5 , and 3 to 3.5 PV , and the seawater waves ($454 \text{ mg Ca}^{2+}/\text{L}$) correspond to the injection of $T = 1.5$ to 2 , 2.5 to 3 , and 3.5 to 4 PV .

6.4.2.4 *CaCO_3 scale precipitation in the production system*

The three production regimes were identified in the previous section, as follows: a) production of formation water, b) production of the CO_2 saturated brine waves, and c) production of the seawater waves. Given the very different aqueous phase compositions for each of these cases, I expect quite different behaviour for each with respect to CaCO_3 scale precipitation in the wellbore. Using the different predicted fluid compositions for each of these cases in a scaling calculation in the wellbore, I obtain the calcite deposition profiles shown in Figure 6.8 a), b), and c). Note that in these plots, I parameterise “depth” with pressure which goes from high pressure downhole to lower pressure near the surface facilities. Further, in these calculations I have assumed that the temperature was constant and equal to reservoir temperature.

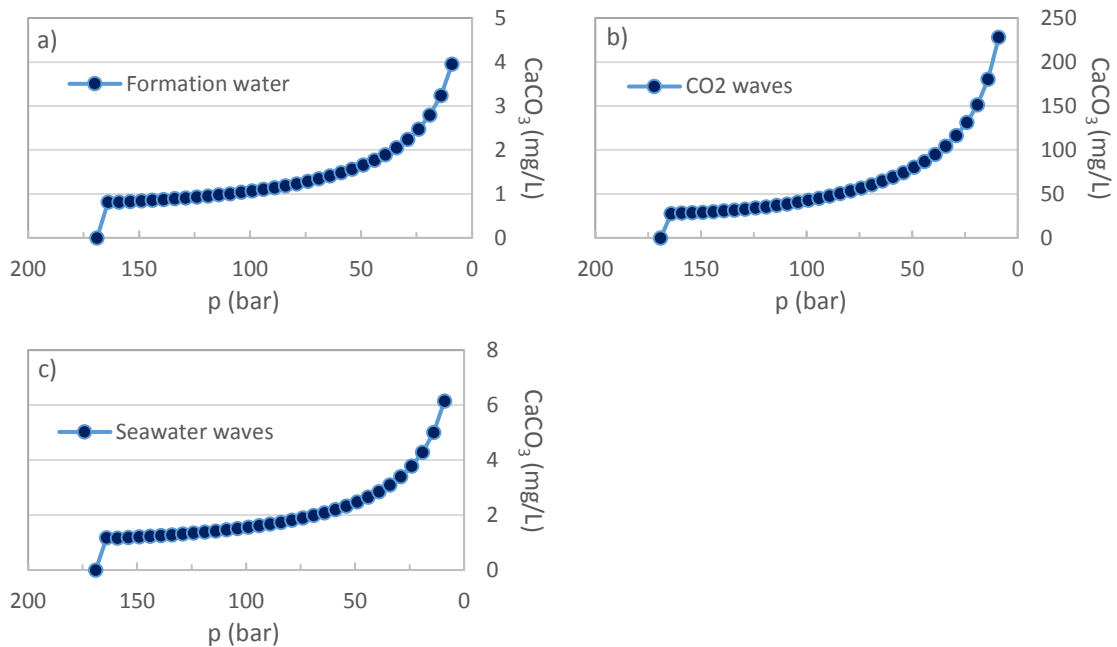


Figure 6.8 – Precipitation of CaCO_3 for the formation water, CO_2 , and seawater waves as fluids move from the reservoir to surface, i.e. from high to low pressure [a), b) and c) on figure].

The results in all plots in Figure 6.8 show that no CaCO_3 scale forms at reservoir pressure, i.e. 169 bar, since, at reservoir conditions, the rock-brine system is at equilibrium (the SR for CaCO_3 is 1, SR = 1). However, as fluids enter the wellbore and pressure decreases by a small value, 5 bar in the simulations, I then calculate that CaCO_3 precipitation occurs for all production waves – 0.813 mg CaCO_3/L for the formation water wave, 27.842 mg CaCO_3/L for the CO_2 saturated brine waves, and 1.174 mg CaCO_3/L for the seawater waves.

I can already identify a clear difference between the impacts of the three waves on CaCO_3 precipitation downhole. The CO_2 saturated brine waves are considerably more severe in terms of calcite deposition than formation water and seawater waves, due the high levels of Ca^{2+} and bicarbonate (HCO_3^-) which these waves deliver to the wellbore because of the high calcite dissolution. As pressure decreases to surface conditions, CaCO_3 precipitates in a gradual manner, being more severe at surface conditions for all three waves. However, CO_2 saturated brine waves cause a degree of CaCO_3 precipitation considerably higher than the formation and seawater waves: for example for 10 bar (close to typical separator pressures), I calculate the precipitation of 228.2 mg CaCO_3/L for the CO_2 saturated brine waves as opposed to 3.9 and 6.1 mg CaCO_3/L for the formation water

and seawater waves, respectively. This is expected due to the carbonate rock dissolution described above.

In summary, I can consider the CO₂ saturated brine waves as the worst case scenario with respect to CaCO₃ scale precipitation. The CaCO₃ scale starts to precipitate downhole, but is considerably more severe as the system approaches surface conditions. This information is important for the design of scale management strategies, particularly for the design of preventive measures of CaCO₃ formation.

Figure 6.9 sums up results in a concise way: I plot the precipitation of CaCO₃ scale in the two extremes of the production system, i.e. downhole where the CaCO₃ precipitation is lower and at separator where the CaCO₃ precipitation is higher, as a function of the pore volumes injected. The consequences of these three waves of fluid arriving at the producer well can clearly be identified in Figure 6.9.

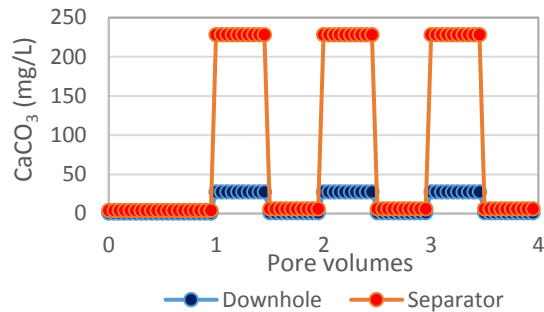


Figure 6.9 – Precipitation of CaCO₃ scale downhole and at the separator as a function of the pore volumes injected.

Results shown in Figure 6.9 show that if the production system is *protected* against CaCO₃ scale for the CO₂ saturated brine waves, i.e. for the worst case scenario, then it is also protected for the formation water and seawater waves. This is a 1D calculation and, in this respect, it will be a “worst case” scenario. Realistically, due to 3D flow effects, I expect the production profiles to lie somewhere in between the extremes identified by my results and scale management strategies should obviously target this reality. There is nevertheless great value in identifying the boundaries of the CaCO₃ scaling regime.

Although I have introduced the concept of seawater and CO₂ saturated brine waves, I recognise that production profiles are not characterised by these “sharp” waves and that

production profiles should lie somewhere in between the boundaries that I have identified in the simulations. Dispersion/mixing in the reservoir due to local rock formation heterogeneity and 3D flow effects (divergent and convergent areal streamlines and vertical heterogeneity or reservoir layering) would tend to spread out these sharp fronts in the reservoir. As a consequence of this, there may be some mitigation of the severity of the calcite deposition at the producers. More accurate fine grid 3D calculations will help to assess the degree of reservoir dispersion which may be expected in specific cases.

Figure 6.10 shows the profile of CaCO_3 scale precipitation in the wellbore as a function of pressure and of pressure step assumed in the calculations: if I assume a small pressure step, say 5 bar as I have done for all calculations, I predict that CaCO_3 precipitates continuously along the production system, and I calculate the precipitation of 228.2 mg CaCO_3/L at the separator (dark blue data points in Figure 6.10). However, if I assume a large pressure step, say 160 bar to exemplify a single point calculation, I predict the precipitation of 2166.0 mg CaCO_3/L at the separator (green data points in Figure 6.10).

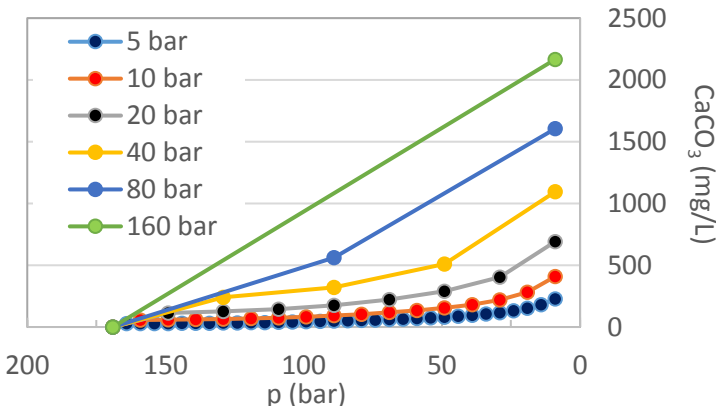


Figure 6.10 – CaCO_3 precipitation in the production system for different pressure steps assumed in the calculations.

The results in Figure 6.10 show the implications of choosing a pressure step in calculations, as already discussed in Section 5.5.3 (see Figure 5.15). Again, I note that my view (expressed above) is that the development of a kinetic wellbore scale deposition model will help to resolve the issue of what size steps to take and what fluid brine compositions and conditions should be used in experiments.

6.4.3 Study of the effect of kinetics on CaCO_3 scale in CO_2 -WAG

The previous example is used to illustrate the effect of kinetics in the reactive transport model, as introduced in Section 6.2. Thus, I review the results that show the dissolution of CaCO_3 rock in the near-wellbore region of the injector:

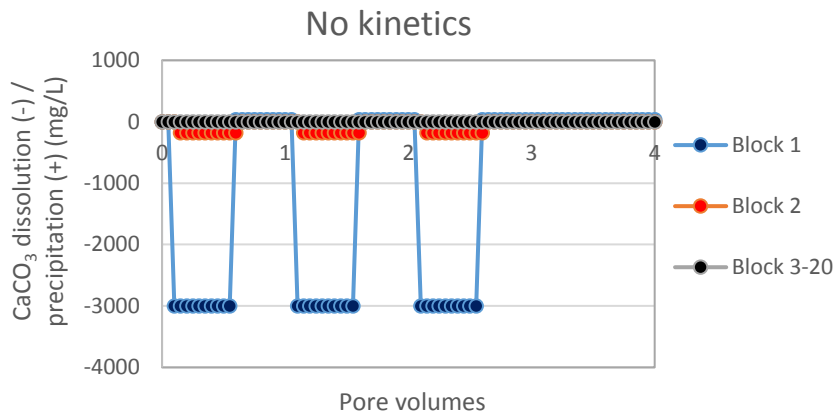


Figure 6.11 – CaCO_3 dissolution (negative values) and precipitation (positive values) as a function of the pore volumes injected for the CO_2 -WAG injection profile shecdule identified in Table 6.4.

Figure 6.11 shows that CaCO_3 dissolution occurs mainly in the first block – dissolution of approximately 3000 mg CaCO_3/L for the CO_2 wave –, since the system *has the time* to reach thermodynamic equilibrium in the first block – in fact, this is always verified in a thermodynamic model. However, short residence times are expected in the near-wellbore region, and, therefore, the reaction rate for the rate-determining reaction might be lower than the convective transport rate [see Equation (6.10)], and the system might not reach thermodynamic equilibrium at this location.

In detail, I consider the radial model presented in Figure 6.12.

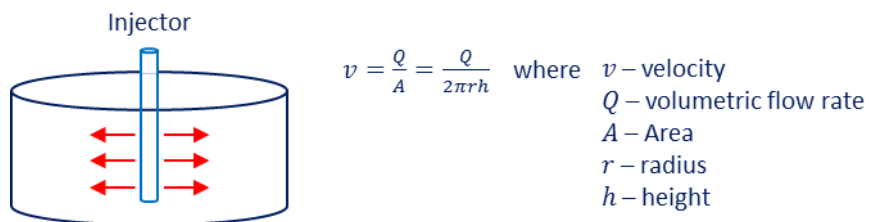


Figure 6.12 – The calculation of velocity in a radial model is different from the 1D model considered here.

In a radial model, residence times in the near-wellbore region of the injector are lower because the velocity of the injection fluid is inversely proportional to the radius, i.e. as the radius increases (distance from the injection well), the area increases, and the velocity decreases. Although the velocity of the injection fluid in my 1D reactive transport model is constant (the volumetric flowrate and area are constant), I can nevertheless study the effect of decreasing velocity in the reservoir by introducing the pseudo kinetic factor, as explained in Section 6.2. I acknowledge that this is a rough approximation, but it might be a very useful technique for many applications (e.g. establishing worst case scenarios, study of trends in the system, etc.).

In this context, I re-run the simulation presented in Figure 6.11, but I set $\zeta = 0.5$, i.e. the system can only reach *half-way* between the initial and equilibrium states, as shown in Figure 6.13.

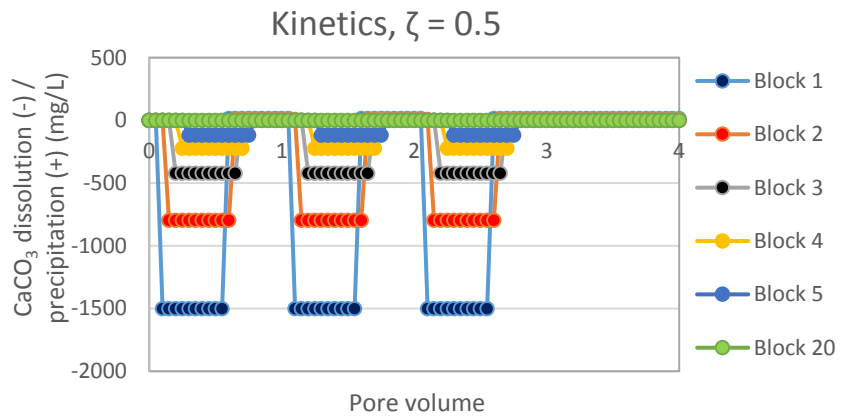


Figure 6.13 – CaCO_3 dissolution (negative values) and precipitation (positive values) as a function of the pore volumes injected for the CO_2 -WAG injection profile shechedule identified in Table 6.4, and with a kinetic factor of 0.5.

Results in Figure 6.13 show that the dissolution in the first block is now half of the amount predicted by the previous simulation, i.e. I now have the dissolution of approximately 1500 mg CaCO_3/L for the CO_2 saturated brine wave. Hence, the system has not reached thermodynamic equilibrium in the first block, and the dissolution of CaCO_3 rock continues in the subsequent blocks.

In addition, I can analyse the dissolution of CaCO_3 as a function of the distance in the reservoir for different PV injected, as shown in Figure 6.14 (note that PV were selected

to coincide with the CO₂ wave, since the CaCO₃ dissolution is higher for this wave than it is for the seawater wave – see Table 6.4 for the CO₂ WAG injection schedule).

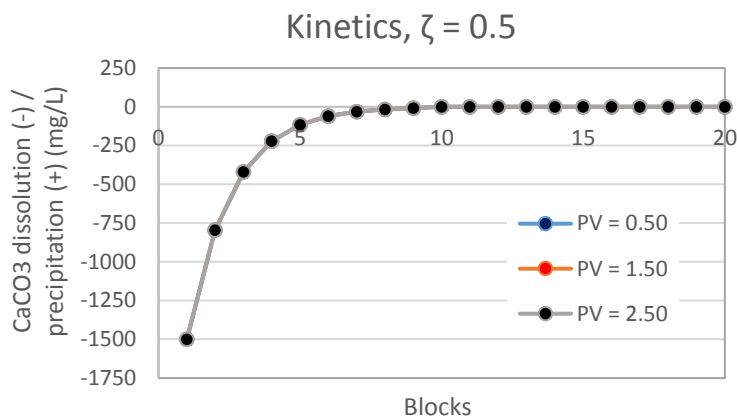


Figure 6.14 – CaCO₃ dissolution (negative values) and precipitation (positive values) as a function of the blocks in the simulation for the CO₂-WAG injection profile schedule identified in Table 6.4, and with a kinetic factor of 0.5.

Results in Figure 6.14 show that the dissolution of CaCO₃ has the highest value near the injector, and that it decreases as fluids flow farther away from the injector. Hence, including kinetics in the reactive transport calculations *shifts* the dissolution of CaCO₃ away from the injector well. However, when fluids reach the producer, i.e. in block 20, there is no longer considerable amount of CaCO₃ rock dissolution, and, therefore, the CaCO₃ precipitation profile in the production system calculated previously (see Figure 6.8) is not really affected by these kinetic effects in the reservoir.

It is a fairly good assumption to consider that fluids are at thermodynamic equilibrium when they reach production wells due to their long residence times in the reservoir. In fact, I can argue that rock dissolution profiles in the near-wellbore region of the injector *does not* really impact the CaCO₃ scaling profile in production systems. However, if I consider a small pseudo kinetic factor, say $\zeta = 0.1$, for demonstration purposes, then kinetic effects can be seen in production systems, as shown in Figure 6.15.

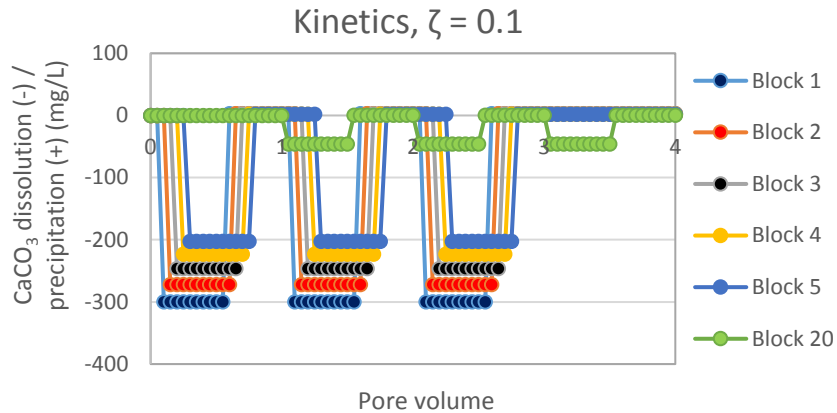
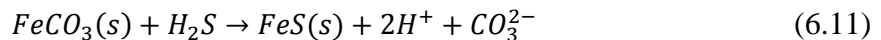


Figure 6.15 – CaCO_3 dissolution (negative values) and precipitation (positive values) as a function of the pore volumes injected for the CO_2 -WAG injection profile schedule identified in Table 6.4, and with a kinetic factor of 0.1.

Results in Figure 6.15 show that there is still rock dissolution taking place in the last block (block 20) for the CO_2 wave. This means that the concentration of the scaling ions Ca^{2+} and HCO_3^- that enter the production system is less than it would be in a thermodynamic calculation, thus impacting the CaCO_3 scaling profile in the production system.

6.4.4 Siderite (FeCO_3) scavenging H_2S in the reservoir

The reactive transport model can be readily extended to other applications. For example, I can model the storage capacity of H_2S in a siderite (FeCO_3)-rich reservoir by natural depletion. Since FeCO_3 is much more soluble than FeS , FeCO_3 dissolves in the reservoir in the presence of H_2S , and Fe^{2+} re-precipitates as FeS , as shown in Equation (6.11).



To exemplify this process, I run a simulation with the following conditions:

- a) Injection in the reservoir of water saturated with H_2S (5 mole % in the vapour phase), as presented in Table 6.5. The composition of the injection and formation waters are also presented in Table 6.5.

- b) Reservoir pressure and temperature: 100 bar and 60 °C. Reservoir rock mineralogy: 59% non-reactive (sandstone), 40% CaCO₃, and 1% FeCO₃.
- c) Transport parameters are presented in Table 6.6.

Table 6.5 – Injection and formation water compositions used in the FeCO₃ scavenging H₂S simulation. The injected water is in equilibrium with a vapour phase containing 10% CO₂, 5% H₂S, and 85% CH₄.

	Injection water	Formation water
y CO ₂ (mol%)	10	-
y H ₂ S (mol%)	5	-
y CH ₄ (mol%)	85	-
m Na ⁺ (mg/L)	10319	25265
m K ⁺ (mg/L)	397	495
m Mg ²⁺ (mg/L)	1379	875
m Ca ²⁺ (mg/L)	446	2090
m Ba ²⁺ (mg/L)	0	35
m Sr ²⁺ (mg/L)	8	210
m Fe ²⁺ (mg/L)	0	0
m Cl ⁻ (mg/L)	17203	44375
m SO ₄ ²⁻ (mg/L)	3000	0
m HCO ₃ ⁻ (mg/L)	150	145
m CO ₃ ²⁻ (mg/L)	0	-
pH	7	7

Table 6.6 – Reactive transport parameters used in the FeCO₃ scavenging H₂S simulation

Flow rate (bbl/day), Q =	1000
Time step (days), Δt =	13.89
Grid size (m), Δx =	0.05
Cross-sectional area (m ²), A =	0.5
Porosity, Φ =	0.4
Dispersion (m ² /s), D =	0
Number of grid blocks, N =	10

Figure 6.16 shows a snapshot of the aqueous concentration of H₂S vs. distance profile in the reservoir for four “times, T” (i.e. pore volumes injected), viz. at T = 1, 10, 20 and 30 PV.

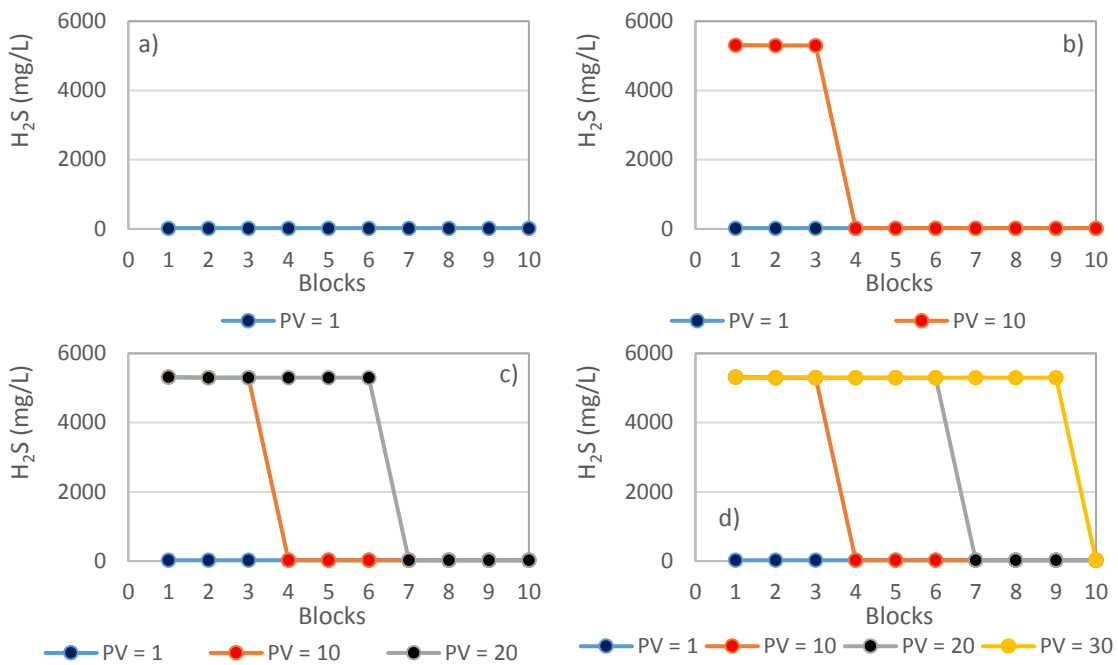


Figure 6.16 – Concentration of H_2S as a function of the number of blocks for several PV injected.

Results in Figure 6.16 show that:

- For $T = 1$ PV injection [Figure 6.16 a)], the concentration of H_2S in the reservoir is approximately zero – this means that all H_2S is being captured in the reservoir as FeS [Equation (6.11)]. In particular, H_2S is being captured mainly in the first block as FeS , causing the depletion of FeCO_3 .
- As injection continues, FeCO_3 in the first block eventually becomes completely depleted (remember that the reservoir rock has only 1% of FeCO_3), and this block loses its capacity to capture H_2S as FeS . Thus, the reaction continues in the next block where there is still FeCO_3 available to react with H_2S , until this block, also, becomes completely depleted of FeCO_3 , and so on. In this context, I can affirm that there is a *FeCO_3 dissolution front*, and that when this front reaches the last block, the reservoir loses its capacity to capture H_2S by the means described in Equation (6.11).
- Figure 6.16 b) shows the reservoir at $T = 10$ PV injection. These results show that the first three blocks are completely depleted of FeCO_3 and that the FeCO_3 dissolution front is at block 4 where there is still capacity to capture H_2S as FeS (the concentration of H_2S in this block is approximately zero).

- iv) Figure 6.16 c) and d) show respectively the reservoir at $T = 20$ and 30 PV injection. At $T = 30$ PV injection, the FeCO_3 dissolution front is in the last block, and the reservoir is almost completely depleted of FeCO_3 .

Figure 6.17 summarise the results shown in Figure 6.16, by plotting the concentration of H_2S in the reservoir for different PV injected together (i.e. for $T = 1, 10, 20, 30$, and 40 PV injection).

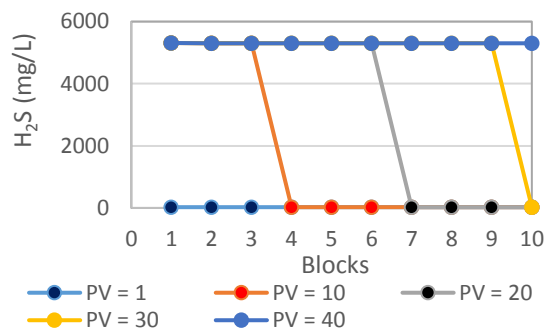


Figure 6.17 – Concentration of H_2S as a function of the number of blocks for several PV injected.

Results in Figure 6.17 show that the reservoir has no longer the capacity to capture H_2S by means of Equation (6.11) after the injection of 40 PV – note that for 40 PV injection, the concentration of H_2S in the reservoir does not change.

Figure 6.18 shows the dissolution front of FeCO_3 (negative values for dissolution, and positive values for precipitation).

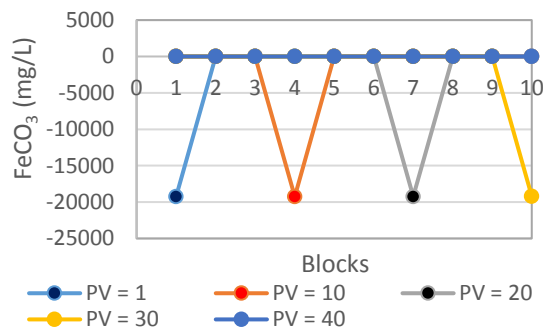


Figure 6.18 – FeCO_3 dissolution (negative values) and precipitation (positive values) as a function of the number of blocks for different pore volumes injected.

Results in Figure 6.18 show that, for example for $T = 10$ PV injection, the FeCO_3 dissolution front is at block 4, and that for $T = 20$ PV injection, it is at block 7.

Complementary to Figure 6.18, Figure 6.19 shows the precipitation of FeS in the reservoir.

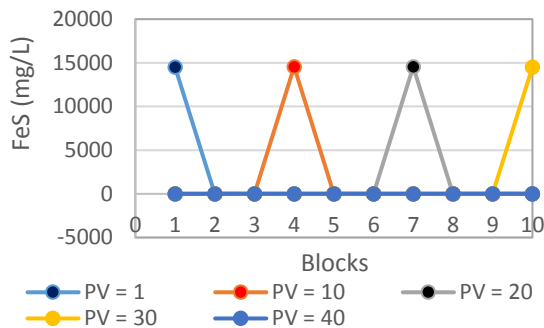


Figure 6.19 – FeS dissolution (negative values) and precipitation (positive values) as a function of the block numbers for different pore volumes injected.

Results in Figure 6.19 can be analysed in parallel with results in Figure 6.18: the FeCO_3 dissolution front match the *FeS precipitation front*. For example for $T = 10$ PV injection, the FeS precipitation front is at block 4, and for $T = 20$ PV injection, it is at block 7.

Ultimately, I would like to calculate the total capacity of the reservoir in capturing H_2S as FeS . To do so, I can plot the concentration of H_2S as a function of the PV injected for the last block (block 10), as shown in Figure 6.20 (note that data for blocks 1 and 5 are also shown).

Results in Figure 6.20 show that the reservoir has the capacity to capture the H_2S present in 31.716 PV.

Considering that Equation (6.11) is quantitative, i.e. that all FeCO_3 available dissolves in the presence of H_2S , and that all Fe^{2+} then re-precipitates as FeS , it is possible to calculate the reservoir capacity to capture H_2S without needing to run a reactive transport calculation. First, the volume of FeCO_3 rock in the reservoir is calculated as follows:

$$V_{\text{FeCO}_3} = A \Delta x (\text{nr of blocks}) (1 - \phi) \eta_{\text{FeCO}_3} \quad (6.12)$$

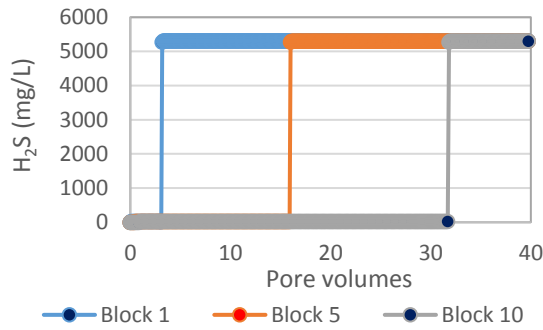


Figure 6.20 – Concentration of H₂S as a function of the pore volumes injected for blocks 1, 5, and 10.

Where η_{FeCO_3} is the FeCO₃ fraction of the rock. Knowing that $\rho_{FeCO_3} = 3900 \text{ kg/m}^3$ and considering the molecular weight of FeCO₃, then:

$$n_{FeCO_3} = \frac{V_{FeCO_3} \rho_{FeCO_3}}{MM_{FeCO_3}} \quad (6.13)$$

Where n_{FeCO_3} is the total amount of FeCO₃ rock in the reservoir (in moles). The amount of aqueous H₂S (in moles) in the injection fluid is given by a VLE calculation (using, in this case, PR EOS). Thus, I have $n_{H_2S} = f(p, T, y_i)$. The PV that calculates H₂S breakthrough is then given by:

$$PV_{H_2S \text{ breakthrough}} = 1 + \frac{n_{FeCO_3}}{n_{H_2S}} \frac{Q_v \Delta x}{A \Delta x (\text{nr of blocks}) \phi} \quad (6.14)$$

In this example, and using Equations (6.12), (6.13), and (6.14), I have:

$$n_{FeCO_3} = 50.49494 \text{ moles}$$

$$n_{H_2S} = 0.164879 \text{ moles}$$

$$PV_{H_2S \text{ breakthrough}} = 1 + \frac{50.49494}{0.164879} \frac{8.3333 \times 10^{-9} \times 1200000.48}{0.5 \times 0.05 \times 10 \times 0.4} = 31.5$$

Values are all in SI units. In the reactive transport calculation, $PV_{H_2S \text{ breakthrough}} = 31.716$ showing that the analytical procedure can be used to confirm results obtained by running a reactive transport calculation.

6.5 Conclusions and recommendations

In a CO₂ WAG process, CO₂ and water are alternatively injected in the reservoir for tertiary oil recovery. This cyclic injection schedule then impacts the production of fluids and the potential for CaCO₃ scale in production systems. A 1D reactive transport model has been developed to simulate the CO₂ WAG reactive flow and transport of components in the reservoir, and then coupled with the scale prediction algorithm developed in the previous chapters to account for the pressure reduction in production systems and consequent precipitation of CaCO₃ scale. In detail, the following points have been addressed in this chapter:

- Reactive transport validation with experimental data. A laboratory experiment consisting of flooding a CaCO₃-packed column with seawater at different pH levels and measuring the pH and the concentration of Ca²⁺ in the effluent stream has been used to validate the reactive transport model. I have shown that the reactive model accurately simulates the reactions occurring in the carbonate (CO₂, HCO₃⁻, and CO₃²⁻)/CaCO₃ system.
- CaCO₃ scale in CO₂-WAG. I have shown that I can use the 1D reactive transport model to simulate the production of fluids according to a CO₂ WAG injection schedule. In particular, I have shown that I can categorise production into three groups according to the CO₂ WAG injection schedule: production of formation water; production of CO₂ saturated brine waves; and production of seawater waves. For each group, the precipitation of CaCO₃ scale in the production system is calculated. This calculation defines the boundaries of the scaling system, and can be used in conjunction with other calculations (e.g. calculations that make use of production data, as presented in Chapter 5) to design strategies, including worst case scenario strategies, to tackle the precipitation of CaCO₃ scale in CO₂ WAG production systems. Furthermore, in the calculations I have shown that the precipitation of CaCO₃ scale in the production system for the CO₂ saturated brine waves is *considerably* more severe than it is for the production of formation water or seawater waves. In fact, I believe that I can generalise this conclusion and state that the precipitation of CaCO₃ in the production system increases with increasing amount of CO₂ in the vapour phase in the reservoir.

- The effect of kinetics on CaCO_3 scale in CO_2 WAG. The effect of kinetics on the carbonate/ CaCO_3 has been addressed by calculating initial and equilibrium thermodynamic states and by assuming that kinetics impede the system in *reaching* the equilibrium state. The concentration of the species in the system is then calculated by linearly interpolation between the two thermodynamic states. I have shown that kinetics can influence the dissolution of CaCO_3 rock in the near-wellbore region of the injector, by *shifting* the dissolution of rock away from the injector well.
- FeCO_3 scavenging H_2S in the reservoir. I have shown that the reactive transport model developed here can not only be applied to study the precipitation of CaCO_3 scale in CO_2 WAG production systems, but it can also be applied to other common issues encountered in oil and gas production such as the production and subsequent re-injection of H_2S in the reservoir for H_2S storage. I have clearly shown how the reactive transport model can be used to calculate the natural capacity of a reservoir to capture H_2S as mineral FeS by reaction with FeCO_3 rock.

Although CO_2 must dissolve in the aqueous phase in the reservoir to react with CaCO_3 rock, and thus CO_2 WAG processes can be modelled in the context of this work as the reactive transport of a single aqueous phase, the model can nevertheless be further extended to also account for the transport of gas and oil in the reservoir. Also, I emphasise the importance of integrating the analysis carried out for the reactive transport model with other relevant studies. For example, the results produced in this chapter can be integrated with results produced by reservoir modelling, or with the results produced in Chapter 5 that account for production data, etc.

7. Conclusions and recommendations

A thermodynamic model has been developed to calculate the precipitation of CaCO_3 scale in CO_2 WAG production systems. This model addresses relevant steps in the formation of CaCO_3 scale in CO_2 WAG production systems individually, and then it couples them together, thus closely simulating the CaCO_3 scaling process as it occurs in CO_2 WAG operations. In particular, the following steps have been modelled and coupled together by using an aqueous electrolyte model, a VLE model, a multiphase flash model, and a reactive transport model, as developed respectively in Chapters 3 to 6:

- i) Dissolution of the CO_2 slug in the aqueous phase in the reservoir, and consequent decrease of the system pH.
- ii) Dissolution of CaCO_3 rock in the reservoir, and consequent increase in Ca^{2+} and CO_3^{2-} ions in the aqueous phase.
- iii) Transport of aqueous components in the reservoir, including the scaling ions Ca^{2+} and CO_3^{2-} , to production systems as a function of the CO_2 WAG injection schedule.
- iv) In production systems, the partition of CO_2 between all phases present in the system (water, vapour, and liquid) due to depressurisation, particularly the evolution of CO_2 from the aqueous phase to the vapour phase, and consequent increase in the system pH.
- v) And the precipitation of CaCO_3 scale in production systems.

The precipitation of CaCO_3 in CO_2 WAG production systems is dependent on all these steps. For example, the precipitation of CaCO_3 is dependent on the concentration of Ca^{2+} . However, the concentration of Ca^{2+} in production systems is dependent on the amount of CaCO_3 rock previously dissolved in the reservoir, which, in turn, is dependent on the amount of CO_2 dissolved in the aqueous phase. Thus, modelling the precipitation of CaCO_3 scale in CO_2 WAG production systems *must* account for all steps identified here. In other words, this scaling process should not be treated as a single point calculation, as it is often the case when dealing with scale formation due to the mixing of two chemically

incompatible waters – in fact, I believe that distinguishing scale formation mechanisms is key to achieving accurate modelling results. By doing so, it is possible to calculate the boundaries of the CaCO_3 scaling system, as shown here, and thus it is possible to design *worst case scenario* strategies to mitigate CaCO_3 scale, which should always be considered in scale management.

In addition, I suggest a new view towards CaCO_3 scale formation based on the simulations run here: *CaCO_3 scale forms always in production systems for carbonate reservoirs and in CO_2 -rich environments*. This view is based on two points: i) in carbonate reservoirs and in CO_2 -rich environments, CaCO_3 rock *always* dissolves such that $\text{SR}(\text{CaCO}_3) = 1$; and ii) in production systems, pressure *always* reduces from reservoir to topside, causing the thermodynamic equilibrium for CaCO_3 scale to *always* evolve to a supersaturated state. This view has immediate implications for CaCO_3 scale management strategies in such conditions – for example, it shifts the question “do I have a CaCO_3 scaling issue?” to “how much CaCO_3 scale do I have to manage and where?” In fact, it should be noted that, for the same reasons, CaCO_3 scale formation is more severe at topside facilities than it is in wellbores. This means that, in some cases, continuous downhole injection of scale inhibitors might suffice to treat CaCO_3 scale, as opposed to the more expensive squeeze treatments.

Furthermore, I highlight the following points which are somehow transversal to all chapters developed in this work, and can be used as starting points for future R&D in scale estimation modelling:

- Databases are critical to semi-empirical thermodynamic modelling. Having an up-to-date experimental database for semi-empirical thermodynamic models is a *sine qua non* of accurate modelling results. In fact, developing experimental databases for new scaling systems should always be prioritised [e.g. for High-Pressure High-Temperature (HPHT) systems, Alkali-Surfactant-Polymer (ASP) EOR systems, etc.).]
- If components partition between all phases in a scaling system, such as the partition of CO_2 between water, vapour, and liquid in CO_2 WAG processes, then state-of-the-art PVT modelling is required. In fact, I believe that this will be a major research topic in scale estimation modelling in the near-future. For

example, the increasing interest in the development of sour reservoirs can be a driving force for the development of scale estimation and PVT modelling, since these systems are associated with sulphide scale and, therefore, they are associated with the partition of H₂S (and CO₂) between the water, vapour, and liquid phases.

- As shown here, models should be used in accordance with the scaling processes that they are addressing, and with the data available. Modelling an autoscaling process as a “mixing of two waters” scaling process, i.e. in single-point calculation manner, is simply not satisfactory. In addition, data required as input in scale estimation models is often not completely available. This means that the modelling approach should target this reality, as shown here in Section 5.4, and avoid the view of “one model fits all”. By doing so, I believe that, for some scaling processes, the accuracy of scale estimation results using thermodynamic models can be greatly improved. Al-khaldi et al., 2011

8. Bibliography

- ABOUIE, A., KORRANI, A. K. N. & SEPEHRNOORI, K. 2017. Aspects of Scale Deposition in a Compositional Coupled Wellbore/Reservoir Simulator, SPE-184507-MS. *SPE International Conference on Oilfield Chemistry*. Montgomery, Texas, USA: Society of Petroleum Engineers.
- AL-KHALDI, M. H., ALJUHANI, A., AL-MUTAIRI, S. H. & GURMEN, M. N. 2011. New Insights into the Removal of Calcium Sulfate Scale, SPE-144158-MS. *SPE European Formation Damage Conference*. Noordwijk, The Netherlands: Society of Petroleum Engineers.
- ALVARADO, V. & MANRIQUE, E. 2010. Enhanced Oil Recovery: An Update Review. *Energies*, 3, 1529.
- ANDERKO, A. M. 2000. Simulation of FeCO₃/FeS Scale Formation Using Thermodynamic and Electrochemical Models, NACE-00102. *CORROSION 2000*. Orlando, Florida, USA: NACE International.
- API RECOMMENDED PRACTICE 44 2003. Sampling Petroleum Reservoir Fluids. 2nd ed.
- ATKINSON, G., RAJU, K. & HOWELL, R. D. 1991. The Thermodynamics of Scale Prediction, SPE-21021-MS. *SPE International Symposium on Oilfield Chemistry*. Anaheim, California, USA: Society of Petroleum Engineers.
- AZAROUAL, M., HURTEVENT, C., KERVEVAN, C., BROCHOT, S. & DURANCE, M. V. 2001. Quantitative Prediction of Scale Deposits Induced by Oil Production: Application of the Thermo-Kinetic Software SCALE2000, SPE-68303-MS. *International Symposium on Oilfield Scale*. Aberdeen, United Kingdom: Society of Petroleum Engineers.
- BAILEY, R. T., GATES, T. K. & HALVORSON, A. D. 2013. Simulating variably-saturated reactive transport of selenium and nitrogen in agricultural groundwater systems. *Journal of Contaminant Hydrology*, 149, 27-45.
- BAKER, L. E., PIERCE, A. C. & LUKS, K. D. 1982. Gibbs Energy Analysis of Phase Equilibria, SPE-9806-PA. *Society of Petroleum Engineers Journal*, 22, 731-742.
- BETHKE, C. M. 2008. *Geochemical and Biogeochemical Reaction Modeling*, 2nd ed., New York, Cambridge University Press.
- BEZERRA, M. C. M., ROSARIO, F. F. & ROCHA, A. A. 2003. Scale Prediction and Remediation for Deep Water Fields, SPE-80403-MS. *International Symposium on Oilfield Scale*. Aberdeen, United Kingdom: Society of Petroleum Engineers.
- BJØRNER, M. G. & KONTOGEOORGIS, G. M. 2016. Modeling derivative properties and binary mixtures with CO₂ using the CPA and the quadrupolar CPA equations of state. *Fluid Phase Equilibria*, 408, 151-169.
- BLAS, F. J. & VEGA, L. F. 1998. Prediction of Binary and Ternary Diagrams Using the Statistical Associating Fluid Theory (SAFT) Equation of State. *Industrial & Engineering Chemistry Research*, 37, 660-674.

- BLOUNT, C. W. 1977. Barite solubilities and thermodynamic quantities up to 300°C and 1400 bars. *American Mineralogist*, 62, 942-957.
- BROMLEY, L. A. 1973. Thermodynamic properties of strong electrolytes in aqueous solutions. *AIChE Journal*, 19, 313-320.
- CARL I. STEEFEL & MOLINS, S. 2016. CrunchFlow: Software for Modeling Multicomponent Reactive Flow and Transport - User's Manual. *Lawrence Berkeley National Laboratory: Earth Sciences Division*.
- CHAKRAVARTY, K. H., FOSBØL, P. L. & THOMSEN, K. 2015. Fine Formation During Brine-Crude Oil-Calcite Interaction in Smart Water Enhanced Oil Recovery for Caspian Carbonates, SPE-177379-MS. *SPE Annual Caspian Technical Conference & Exhibition*. Baku, Azerbaijan: Society of Petroleum Engineers.
- CHAKRAVARTY, K. H. & THOMSEN, K. 2015. Formation of Anhydrite Due to Interaction Between Water Soluble CO₂(aq) and Calcite Mineral During Enhanced Oil Recovery, SPE-178129-MS. *SPE Oil & Gas India Conference and Exhibition*. Mumbai, India: Society of Petroleum Engineers.
- CHAPMAN, W. G., GUBBINS, K. E., JACKSON, G. & RADOSZ, M. 1990. New reference equation of state for associating liquids. *Industrial & Engineering Chemistry Research*, 29, 1709-1721.
- CHEN, H.-J., BURNSIDE, C. A., WIDENER, M. W. & HINRICHSEN, C. J. 2007. Assessment of Barite Scaling Potentials, Sulfate Removal Options, and Chemical Treating Strategies for the Tombua-Landana Development, SPE-106480-MS. *International Symposium on Oilfield Chemistry*. Houston, Texas, USA: Society of Petroleum Engineers.
- CHRISTENSEN, J. R., STENBY, E. H. & SKAUGE, A. 2001. Review of WAG Field Experience. *SPE Reservoir Evaluation & Engineering*, 4, 97-106.
- CLAPEYRON, É. 1834. Mémoire sur la puissance motrice de la chaleur. *Journal de l'École Polytechnique*, XIV, 153–190.
- COLLINS, I. R., STALKER, R. & GRAHAM, G. M. 2004. Sulphate Removal for Barium Sulphate Scale Mitigation a Deepwater Subsea Production System, SPE-87465-MS. *SPE International Symposium on Oilfield Scale*. Aberdeen, United Kingdom: Society of Petroleum Engineers.
- COQUELET, C., CHAPOY, A. & RICHON, D. 2004. Development of a New Alpha Function for the Peng–Robinson Equation of State: Comparative Study of Alpha Function Models for Pure Gases (Natural Gas Components) and Water-Gas Systems. *International Journal of Thermophysics*, 25, 133-158.
- DANESH, A. 1998. *PVT and Phase Behaviour of Petroleum Reservoir Fluids*, Amsterdam, The Netherlands, Elsevier.
- DERAWI, S. O., ZEUTHEN, J., MICHELSEN, M. L., STENBY, E. H. & KONTOGEOORGIS, G. M. 2004. Application of the CPA equation of state to organic acids. *Fluid Phase Equilibria*, 225, 107-113.
- DUAN, Z., MØLLER, N. & WEARE, J. H. 1992. An equation of state for the CH₄-CO₂-H₂O system: I. Pure systems from 0 to 1000°C and 0 to 8000 bar. *Geochimica et Cosmochimica Acta*, 56, 2605-2617.

- DUAN, Z. & SUN, R. 2003. An improved model calculating CO₂ solubility in pure water and aqueous NaCl solutions from 273 to 5333 K and from 0 to 2000 bar. *Chem Geol*, 193, 257-271.
- ELLIOTT, J. R., SURESH, S. J. & DONOHUE, M. D. 1990. A simple equation of state for non-spherical and associating molecules. *Industrial & Engineering Chemistry Research*, 29, 1476-1485.
- FAHRNER, S., SCHAEFER, D. & DAHMKE, A. 2011. Reactive transport modeling to assess geochemical monitoring for detection of CO₂ intrusion into shallow aquifers. *Energy Procedia*, 4, 3155-3162.
- FANG, Y., YABUSAKI, S. B., MORRISON, S. J., AMONETTE, J. P. & LONG, P. E. 2009. Multicomponent reactive transport modeling of uranium bioremediation field experiments. *Geochimica et Cosmochimica Acta*, 73, 6029-6051.
- FIGUEROA, D. C., FOSBØL, P. L. & THOMSEN, K. 2016. Prediction and Experimental Determination of the Solubility of Exotic Scales at High Temperatures - Zinc Sulfide, SPE-179877-MS. *SPE International Oilfield Scale Conference and Exhibition*. Aberdeen, United Kingdom: Society of Petroleum Engineers.
- FIROOZABADI, A. 2016. *Thermodynamics and Applications in Hydrocarbon Energy Production*, New York, USA, McGraw-Hill Education
- FIROOZABADI, A. & PAN, H. 2002. Fast and Robust Algorithm for Compositional Modeling: Part I - Stability Analysis Testing. *SPE Journal*, 7, 78-89.
- FLEMING, N., RAMSTAD, K., ERIKSEN, S. H., MOLDRHEIM, E. & JOHANSEN, T. R. 2007. Development and Implementation of a Scale Management Strategy for Oseberg Sor. *SPE Production & Operations*, 22, 307-317.
- FROST, M., KONTOGEOORGIS, G. M., VON SOLMS, N., HAUGUM, T. & SOLBRAA, E. 2016. Phase equilibrium of North Sea oils with polar chemicals: Experiments and CPA modeling. *Fluid Phase Equilibria*, 424, 122-136.
- FU, Y.-H. & SANDLER, S. I. 1995. A Simplified SAFT Equation of State for Associating Compounds and Mixtures. *Industrial & Engineering Chemistry Research*, 34, 1897-1909.
- GAGANIS, V., MARINAKIS, D. & VAROTSI, N. 2012. A general framework of model functions for rapid and robust solution of Rachford–Rice type of equations. *Fluid Phase Equilibria*, 322–323, 9-18.
- GALP 2016. Shaping Energy: Annual Report and Accounts.
- GAO, J., XING, H., TIAN, Z., PEARCE, J. K., SEDEK, M., GOLDING, S. D. & RUDOLPH, V. 2017. Reactive transport in porous media for CO₂ sequestration: Pore scale modeling using the lattice Boltzmann method. *Computers & Geosciences*, 98, 9-20.
- GEORGE JACKSON, W. G. C., KEITH E. GUBBINS 1988. Phase equilibria of associating fluids. *Molecular Physics*, 65, 1-31.
- GEORGIOS M. KONTOGEOORGIS, G. K. F. 2010. *Thermodynamic Models for Industrial Applications: From Classical and Advanced Mixing Rules to Association Theories*, Chichester, West Sussex, United Kingdom, John Wiley & Sons Ltd.

- GIL-VILLEGRAS, A., GALINDO, A., WHITEHEAD, P. J., MILLS, S. J., JACKSON, G. & BURGESS, A. N. 1997. Statistical associating fluid theory for chain molecules with attractive potentials of variable range. *The Journal of Chemical Physics*, 106, 4168-4186.
- GOMES, R., MACKAY, E. J., DEUCHER, R. H., BEZERRA, M. C. M., ROSARIO, F. F. & JORDAN, M. M. 2012. Impact of Reservoir Reactions on Thermodynamic Scale Predictions, SPE-155255-MS. *SPE International Conference on Oilfield Scale*. Aberdeen, United Kingdom: Society of Petroleum Engineers.
- GROSS, J. & SADOWSKI, G. 2001. Perturbed-Chain SAFT: An Equation of State Based on a Perturbation Theory for Chain Molecules. *Industrial & Engineering Chemistry Research*, 40, 1244-1260.
- HAGHIGHI, H., CHAPOY, A., BURGESS, R., MAZLOUM, S. & TOHIDI, B. 2009. Phase equilibria for petroleum reservoir fluids containing water and aqueous methanol solutions: Experimental measurements and modelling using the CPA equation of state. *Fluid Phase Equilibria*, 278, 109-116.
- HAUGEN, K. B. & BECKNER, B. 2013. A Critical Comparison of Reduced and Conventional EOS Algorithms. *SPE Journal*, 18, 378-388.
- HENDRIKS, E. M. & VAN BERGEN, A. R. D. 1992. Application of a reduction method to phase equilibria calculations. *Fluid Phase Equilibria*, 74, 17-34.
- HUANG, S. H. & RADOSZ, M. 1990. Equation of state for small, large, polydisperse, and associating molecules. *Industrial & Engineering Chemistry Research*, 29, 2284-2294.
- IRANSHAHR, A., VOSKOV, D. & TCHELEPI, H. A. 2010. Generalized negative-flash method for multiphase multicomponent systems. *Fluid Phase Equilibria*, 299, 272-284.
- JENSEN, B. H. & FREDENSLUND, A. 1987. A simplified flash procedure for multicomponent mixtures containing hydrocarbons and one non-hydrocarbon using two-parameter cubic equations of state. *Industrial & Engineering Chemistry Research*, 26, 2129-2134.
- JONES, T., KOGSBOLL, H. H. & KOLDIG, J. 2006. Downhole Scale Management in Gorm, Dan, and Halfdan, and Implications to Industry Trends, SPE-100508-MS. *SPE International Oilfield Scale Symposium*. Aberdeen, United Kingdom: Society of Petroleum Engineers.
- JORDAN, M. M., COLLINS, I. R. & MACKAY, E. J. 2008. Low Sulfate Seawater Injection for Barium Sulfate Scale Control: A Life-of-Field Solution to a Complex Challenge. *SPE Production & Operations*, 23, 192-209.
- JORDAN, M. M. & MACKAY, E. J. 2007. Scale Control in Chalk Reservoirs: The Challenge of Understanding the Impact of Reservoir Processes and Optimizing Scale Management via Chemical Placement and Retention - from the Laboratory to the Field, SPE-105189-MS. *SPE Middle East Oil and Gas Show and Conference*. Manama, Bahrain: Society of Petroleum Engineers.
- KAASA, B. 1998. *Prediction of pH, mineral precipitation and multiphase equilibria during oil recovery*. PhD thesis, Trondheim, Norway, Norwegian University of Science and Technology.

- KAN, A. & TOMSON, M. 2010. Scale Prediction for Oil and Gas Production, SPE-132237-MS. *International Oil and Gas Conference and Exhibition in China*. Beijing, China: Society of Petroleum Engineers.
- KAZEMI NIA KORRANI, A., SEPEHRNOORI, K. & DELSHAD, M. 2014. A Comprehensive Geochemical-Based Approach to Quantify the Scale Problems, SPE-168196-MS. *SPE International Symposium and Exhibition on Formation Damage Control*. Lafayette, Louisiana, USA: Society of Petroleum Engineers.
- KIRSTE, D. 2013. Mineral Saturation State and the Implications for Reaction Rates in Reactive Transport Modeling of CO₂ Storage. *Procedia Earth and Planetary Science*, 7, 432-435.
- KONTOGEOORGIS, G. M., VOUTSAS, E. C., YAKOUMIS, I. V. & TASSIOS, D. P. 1996. An Equation of State for Associating Fluids. *Industrial & Engineering Chemistry Research*, 35, 4310-4318.
- KRASKA, T. & GUBBINS, K. E. 1996a. Phase Equilibria Calculations with a Modified SAFT Equation of State. 1. Pure Alkanes, Alkanols, and Water. *Industrial & Engineering Chemistry Research*, 35, 4727-4737.
- KRASKA, T. & GUBBINS, K. E. 1996b. Phase Equilibria Calculations with a Modified SAFT Equation of State. 2. Binary Mixtures of n-Alkanes, 1-Alkanols, and Water. *Industrial & Engineering Chemistry Research*, 35, 4738-4746.
- LASAGA, A. C. 1998. *Kinetic Theory in the Earth Sciences*, Princeton, New Jersey, USA, Princeton University Press.
- LEIBOVICI, C. F. & NEOSCHIL, J. 1995. A solution of Rachford-Rice equations for multiphase systems. *Fluid Phase Equilibria*, 112, 217-221.
- LI, Y.-K. & NGHIEM, L. X. 1982. The Development of a General Phase Envelope Construction Algorithm for Reservoir Fluid Studies, SPE-11198-MS. *SPE Annual Technical Conference and Exhibition*. New Orleans, Louisiana, USA: Society of Petroleum Engineers.
- LI, Y.-K. & NGHIEM, L. X. 1986. Phase equilibria of oil, gas and water/brine mixtures from a cubic equation of state and henry's law. *The Canadian Journal of Chemical Engineering*, 64, 486-496.
- LI, Y. & JOHNS, R. T. 2006. Rapid Flash Calculations for Compositional Simulation. *SPE Reservoir Evaluation & Engineering*, 9, 521-529.
- LICHTNER, P. C., HAMMOND, G. E., LU, C., KARRA, S., BISHT, G., ANDRE, B., MILLS, R. & KUMAR, J. 2015. PFLOTRAN User Manual: A Massively Parallel Reactive Flow and Transport Model for Describing Surface and Subsurface Processes.
- LUCIA, A., PADMANABHAN, L. & VENKATARAMAN, S. 2000. Multiphase equilibrium flash calculations. *Computers & Chemical Engineering*, 24, 2557-2569.
- MACKAY, E. 2003. Predicting in Situ Sulphate Scale Deposition and the Impact on Produced Ion Concentrations. *Chemical Engineering Research and Design*, 81, 326-332.
- MACKAY, E. & MARTINS DE SOUZA, A. P. 2014. Modelling of CO₂ and Seawater Injection in Carbonate Reservoirs to Evaluate Inorganic Scaling Risk, SPE-

- 169766-MS. *SPE International Oilfield Scale Conference and Exhibition*. Aberdeen, United Kingdom: Society of Petroleum Engineers.
- MCCAIN JR., W. D. 1990. *The Properties of Petroleum Fluids*, Tulsa, Oklahoma, USA, PennWell Publishing Company.
- MCCARTNEY, R. A., DUPPENBECKER, S. S. & CONE, R. 2014. Constraining the Conditions of Scale Deposition in a Gas Condensate Well: A Case Study, SPE-169804-MS. *SPE International Oilfield Scale Conference and Exhibition*. Aberdeen, United Kingdom: Society of Petroleum Engineers.
- MCNAB, W. W. 1997. Simulation of reactive geochemical transport in groundwater using a semi-analytical screening model. *Computers & Geosciences*, 23, 869-882.
- MICHELSEN, M. L. 1986. Simplified flash calculations for Cubic Equations of State. *Industrial & Engineering Chemistry Process Design and Development*, 25, 184-188.
- MICHELSEN, M. L. & MOLLERUP, J. M. 2007. *Thermodynamic Models: Fundamentals & Computational Aspects*, 2nd ed., Holte, Denmark, Tie-Line Publications.
- MÖLLER, D. 2015. *Chemistry for Environmental Scientists*, Berlin, Germany, De Gruyter.
- MORGENTHALER, L. N., LAWSON, J. B., FAIRCLOTH, R. J. & BERKSHIRE, D. C. 1993. Scale Prediction and Control in the Denver Unit CO₂ Flood, SPE-26603-MS. *SPE Annual Technical Conference and Exhibition*. Houston, Texas, USA: Society of Petroleum Engineers.
- MØRK, J. 1989. *Model til beregning af dielektricitetskonstanter i råolie*. MSc thesis, Danish Engineering Academy.
- MULLER, E. A. & OLIVERA-FUENTES, C. 1989. General Expressions for Multicomponent Fugacity Coefficients and Residual Properties from Cubic Equations of State. *Latin American Applied Research*, 19, 99-109.
- NATH, B., JEAN, J.-S., LEE, M.-K., YANG, H.-J. & LIU, C.-C. 2008. Geochemistry of high arsenic groundwater in Chia-Nan plain, Southwestern Taiwan: Possible sources and reactive transport of arsenic. *Journal of Contaminant Hydrology*, 99, 85-96.
- NAVARRE-SITCHLER, A. & JUNG, H. 2017. Complex Coupling of Fluid Transport and Geochemical Reaction Rates: Insights from Reactive Transport Models. *Procedia Earth and Planetary Science*, 17, 5-8.
- NÉRON, A., LANTAGNE, G. & MARCOS, B. 2012. Computation of complex and constrained equilibria by minimization of the Gibbs free energy. *Chemical Engineering Science*, 82, 260-271.
- NICHITA, D. V., GOMEZ, S. & LUNA, E. 2002. Multiphase equilibria calculation by direct minimization of Gibbs free energy with a global optimization method. *Computers & Chemical Engineering*, 26, 1703-1724.
- NICHITA, D. V. & GRACIAA, A. 2011. A new reduction method for phase equilibrium calculations. *Fluid Phase Equilibria*, 302, 226-233.

- NICHITA, D. V. & LEIBOVICI, C. F. 2013. A rapid and robust method for solving the Rachford–Rice equation using convex transformations. *Fluid Phase Equilibria*, 353, 38-49.
- OKUNO, R., JOHNS, R. & SEPEHRNOORI, K. 2010. A New Algorithm for Rachford–Rice for Multiphase Compositional Simulation. *SPE Journal*, 15, 313-325.
- OLIVEIRA, M. B., COUTINHO, J. A. P. & QUEIMADA, A. J. 2007. Mutual solubilities of hydrocarbons and water with the CPA EoS. *Fluid Phase Equilibria*, 258, 58-66.
- PALMA, A. M., OLIVEIRA, M. B., QUEIMADA, A. J. & COUTINHO, J. A. P. 2017. Re-evaluating the CPA EoS for improving critical points and derivative properties description. *Fluid Phase Equilibria*, 436, 85-97.
- PAN, H. & FIROOZABADI, A. 2003. Fast and Robust Algorithm for Compositional Modeling: Part II - Two-Phase Flash Computations. *SPE Journal*, 8, 380-391.
- PARKHURST, D. L. & APPELO, C. A. J. 1999. User's Guide to PHREEQC (Version2) - a Computer Program for Speciation, Batch-Reaction, One-Dimensional Transport, and Inverse Geochemical Calculations. *Water-Resources Investigations Report 99-4259*.
- PATEL, N. C. & TEJA, A. S. 1982. A new cubic equation of state for fluids and fluid mixtures. *Chemical Engineering Science*, 37, 463-473.
- PEDERSEN, K. S. & CHRISTENSEN, P. L. 2007. *Phase Behavior of Petroleum Reservoir Fluids*, Boca Raton, Florida, USA, CRC Press - Taylor & Francis Group.
- PEDERSEN, K. S., CHRISTENSEN, P. L. & SHAIKH, J. A. 2015. *Phase Behavior of Petroleum Reservoir Fluids*, 2nd ed., Boca Raton, Florida, USA, CRC Press, Taylor & Francis Group.
- PELLEGRINI, L. A., MOIOLI, S., GAMBA, S. & CERAGIOLI, P. 2012. Prediction of vapor-liquid equilibrium for reservoir mixtures with cubic equations of state: Binary interaction parameters for acidic gases. *Fluid Phase Equilibria*, 326, 45-49.
- PENG, D.-Y. & ROBINSON, D. B. 1976. A New Two-Constant Equation of State. *Industrial & Engineering Chemistry Fundamentals*, 15, 59-64.
- PENG, D.-Y. & ROBINSON, D. B. 1980. Two- and Three-Phase Equilibrium Calculations for Coal Gasification and Related Processes. in *Thermodynamics of Aqueous Systems with Industrial Applications*. Alberta, Canada: American Chemical Society.
- PITZER, K. & MAYORGA, G. 1974. Thermodynamics of electrolytes. III. Activity and osmotic coefficients for 2-2 electrolytes. *Journal of Solution Chemistry*, 3, 539-546.
- PITZER, K. S. 1973. Thermodynamics of electrolytes. I. Theoretical basis and general equations. *The Journal of Physical Chemistry*, 77, 268-277.
- PITZER, K. S. 1975. Thermodynamics of electrolytes. V. effects of higher-order electrostatic terms. *Journal of Solution Chemistry*, 4, 249-265.
- PITZER, K. S. 1995. *Thermodynamics*, 3rd ed., New York, USA, McGraw-Hill International Editions.

- PITZER, K. S. & KIM, J. J. 1974. Thermodynamics of electrolytes. IV. Activity and osmotic coefficients for mixed electrolytes. *Journal of the American Chemical Society*, 96, 5701-5707.
- PITZER, K. S. & MAYORGA, G. 1973. Thermodynamics of electrolytes. II. Activity and osmotic coefficients for strong electrolytes with one or both ions univalent. *The Journal of Physical Chemistry*, 77, 2300-2308.
- PIZARRO, J. O. D. S. & BRANCO, C. C. M. 2012. Challenges in Implementing an EOR Project in the Pre-Salt Province in Deep Offshore Brasil. Society of Petroleum Engineers.
- PLUMMER, L. N. & BUSENBERG, E. 1982. The solubilities of calcite, aragonite and vaterite in CO₂-H₂O solutions between 0 and 90°C, and an evaluation of the aqueous model for the system CaCO₃-CO₂-H₂O. *Geochimica et Cosmochimica Acta*, 46, 1011-1040.
- POLING, B. E., PRAUSNITZ, J. M. & O'CONNELL, J. P. 2001. *The Properties of Gases and Liquids*, 5th ed., New York, USA, McGraw-Hill.
- PRAUSNITZ, J. M., LICHTENTHALER, R. N. & AZEVEDO, E. G. D. 1999. *Molecular Thermodynamics of Fluid-Phase Equilibria*, Upper Saddle River, New Jersey, USA, Prentice Hall PTR.
- PRECHTEL, A. & KNABNER, P. 2002. Accurate and efficient simulation of coupled water flow and nonlinear reactive transport in the saturated and vadose zone—application to surfactant enhanced and intrinsic bioremediation. *Developments in Water Science*, 47, 687-694.
- PRIVAT, R., JAUBERT, J.-N., BERGER, E., CONIGLIO, L., LEMAITRE, C., MEIMAROGLOU, D. & WARTH, V. 2016. Teaching the Concept of Gibbs Energy Minimization through Its Application to Phase-Equilibrium Calculation. *Journal of Chemical Education*, 93, 1569-1577.
- PRIVAT, R., JAUBERT, J.-N. & PRIVAT, Y. 2013. A simple and unified algorithm to solve fluid phase equilibria using either the gamma–phi or the phi–phi approach for binary and ternary mixtures. *Computers & Chemical Engineering*, 50, 139-151.
- PRUESS, K., OLDENBURG, C. & MORIDIS, G. 1999. *TOUGH2 user's guide, version 2.0*, Berkeley, California, USA, Lawrence Berkeley Laboratory.
- RACHFORD, H. H., JR. & RICE, J. D. 1952. Procedure for Use of Electronic Digital Computers in Calculating Flash Vaporization Hydrocarbon Equilibrium. *Journal of Petroleum Technology*, 4, 327-328.
- RAJU, K. U. 2009. Successful Scale Mitigation Strategies in Saudi Arabian Oil Fields, SPE-121679-MS. *SPE International Symposium on Oilfield Chemistry*. The Woodlands, Texas, USA: Society of Petroleum Engineers.
- RAMSTAD, K., TYDAL, T., ASKVIK, K. M. & FOTLAND, P. 2005. Predicting Carbonate Scale in Oil Producers from High Temperature Reservoirs. *SPE Journal*, 10, 363-373.
- RARD, J. A. & WIJESINGHE, A. M. 2003. Conversion of parameters between different variants of Pitzer's ion-interaction model, both with and without ionic strength dependent higher-order terms. *The Journal of Chemical Thermodynamics*, 35, 439-473.

- REDLICH, O. & KWONG, J. N. S. 1949. On the thermodynamics of solutions; an equation of state; fugacities of gaseous solutions. *Chemical reviews*, 44, 233-244.
- REED, M. H. 1982. Calculation of multicomponent chemical equilibria and reaction processes in systems involving minerals, gases and an aqueous phase. *Geochimica et Cosmochimica Acta*, 46, 513-528.
- RIAZ, M., YUSSUF, M. A., KONTOGEORGIS, G. M., STENBY, E. H., YAN, W. & SOLBRAA, E. 2013. Distribution of MEG and methanol in well-defined hydrocarbon and water systems: Experimental measurement and modeling using the CPA EoS. *Fluid Phase Equilibria*, 337, 298-310.
- ROSSI, C. C. R. S., CARDOZO-FILHO, L. & GUIRARDELLO, R. 2009. Gibbs free energy minimization for the calculation of chemical and phase equilibrium using linear programming. *Fluid Phase Equilibria*, 278, 117-128.
- SALAS, J., SENA, C. & ARCOS, D. 2014. Hydrogeochemical evolution of the bentonite buffer in a KBS-3 repository for radioactive waste. Reactive transport modelling of the LOT A2 experiment. *Applied Clay Science*, 101, 521-532.
- SANDLER, S. I. 1994. *Models for thermodynamic and phase equilibria calculations* (edited by Stanley I. Sandler), New York, USA, Marcel Dekker.
- SEHER, H., NAVARRO, M., ARTMANN, A., LARUE, J., ROLOFF, R. & WEIß, D. 2016. Modelling contaminant transport in generic landfills for decommissioning waste from German nuclear power plants. *Progress in Nuclear Energy*, 89, 46-56.
- SHADLOO, A. & PEYVANDI, K. 2017. The implementation of ion-based ePC-SAFT EOS for calculation of the mean activity coefficient of single and mixed electrolyte solutions. *Fluid Phase Equilibria*, 433, 226-242.
- SHAW, S. S., SORBIE, K. & BOAK, L. S. 2012. The Effects of Barium Sulfate Saturation Ratio, Calcium, and Magnesium on the Inhibition Efficiency -Part I: Phosphonate Scale Inhibitors. *SPE Production & Operations*, 27, 306-317.
- SHEN, D., BHADURI, S., VO, M., CARMAN, P., GUPTA, D. V. S. & PANDEY, Y. 2017. A Novel Solid Inhibitor for Anhydrite Scale Control Under Extreme Well Conditions, SPE-184525-MS. *SPE International Conference on Oilfield Chemistry*. Montgomery, Texas, USA: Society of Petroleum Engineers.
- SILVESTER, L. & PITZER, K. 1978. Thermodynamics of electrolytes. X. Enthalpy and the effect of temperature on the activity coefficients. *Journal of Solution Chemistry*, 7, 327-337.
- SIMPSON, C., GRAHAM, G. M., COLLINS, I. R., MCELHINEY, J. E. & DAVIS, R. A. 2005. Sulphate Removal for Barium Sulphate Mitigation - Kinetic vs. Thermodynamic Controls in Mildly Oversaturated Conditions, SPE-95082-MS. *SPE International Symposium on Oilfield Scale*. Aberdeen, United Kingdom: Society of Petroleum Engineers.
- SNIDER, J., GRIVA, I., SUN, X. & EMELIANENKO, M. 2015. Set based framework for Gibbs energy minimization. *Calphad*, 48, 18-26.
- SOAVE, G. 1972. Equilibrium constants from a modified Redlich-Kwong equation of state. *Chemical Engineering Science*, 27, 1197-1203.

- SØREIDE, I. & WHITSON, C. H. 1992. Peng-Robinson predictions for hydrocarbons, CO₂, N₂, and H₂S with pure water and NaCl brine. *Fluid Phase Equilibria*, 77, 217-240.
- SPRINGER, R. D., WANG, Z., ANDERKO, A., WANG, P. & FELMY, A. R. 2012. A thermodynamic model for predicting mineral reactivity in supercritical carbon dioxide: I. Phase behavior of carbon dioxide–water–chloride salt systems across the H₂O-rich to the CO₂-rich regions. *Chemical Geology*, 322–323, 151-171.
- SPYCHER, N., PRUESS, K. & ENNIS-KING, J. 2003a. CO₂-H₂O mixtures in the geological sequestration of CO₂. I. Assessment and calculation of mutual solubilities from 12 to 100 °C and up to 600 bar. *Geochimica et Cosmochimica Acta*, 67, 3015-3031.
- SPYCHER, N. F., SONNENTHAL, E. L. & APPS, J. A. 2003b. Fluid flow and reactive transport around potential nuclear waste emplacement tunnels at Yucca Mountain, Nevada. *Journal of Contaminant Hydrology*, 62, 653-673.
- STEEFEL, C. I., DEPAOLO, D. J. & LICHTNER, P. C. 2005. Reactive transport modeling: An essential tool and a new research approach for the Earth sciences. *Earth and Planetary Science Letters*, 240, 539-558.
- STRYJEK, R. & VERA, J. H. 1986a. PRSV2: A cubic equation of state for accurate vapor—liquid equilibria calculations. *The Canadian Journal of Chemical Engineering*, 64, 820-826.
- STRYJEK, R. & VERA, J. H. 1986b. PRSV: An improved peng—Robinson equation of state for pure compounds and mixtures. *The Canadian Journal of Chemical Engineering*, 64, 323-333.
- SUCHODOLSKA, K. & LABUS, K. 2016. Simplified Models for Reactive Transport and Chemical Reactions During CO₂ Storage in Saline Aquifers. *Energy Procedia*, 97, 509-514.
- SUN, A. C. & SEIDER, W. D. 1995. Homotopy-continuation method for stability analysis in the global minimization of the Gibbs free energy. *Fluid Phase Equilibria*, 103, 213-249.
- TAKENOUCHI, S. & KENNEDY, G. C. 1965. The solubility of carbon dioxide in nacl solutions at high temperatures and pressures. *American Journal of Science*, 263, 445-454.
- TEH, Y. S. & RANGAIAH, G. P. 2002. A Study of Equation-Solving and Gibbs Free Energy Minimization Methods for Phase Equilibrium Calculations. *Chemical Engineering Research and Design*, 80, 745-759.
- TRANGENSTEIN, J. A. 1985. Minimization of Gibbs Free Energy in Compositional Reservoir Simulation, SPE-13520-MS. *SPE Reservoir Simulation Symposium*. Dallas, Texas, USA: Society of Petroleum Engineers.
- VALDERRAMA, J. O. 1990. A Generalized Patel-Teja Equation of State for Polar and Nonpolar Fluids and Their Mixtures. *Journal of Chemical Engineering of Japan*, 23, 87-91.
- VALDERRAMA, J. O. 2003. The State of the Cubic Equations of State. *Industrial & Engineering Chemistry Research*, 42, 1603-1618.

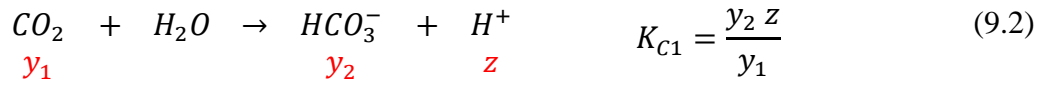
- VALTZ, A., CHAPOY, A., COQUELET, C., PARICAUD, P. & RICHON, D. 2004. Vapour–liquid equilibria in the carbon dioxide–water system, measurement and modelling from 278.2 to 318.2K. *Fluid Phase Equilibria*, 226, 333-344.
- VAN DER WAALS, J. D. 1873. *Over de Continuiteit van den Gas-en Vloeistofstoestand*. PhD thesis, Leiden, The Netherlands, University of Applied Sciences Leiden.
- VAZQUEZ, O., MCCARTNEY, R. A. & MACKAY, E. 2013. Produced-Water-Chemistry History Matching Using a 1D Reactive Injector/Producer Reservoir Model. *SPE Production & Operations*, 28, 369-375.
- VERMA, M. K. 2015. Fundamentals of carbon dioxide-enhanced oil recovery (CO₂-EOR)—A supporting document of the assessment methodology for hydrocarbon recovery using CO₂-EOR associated with carbon sequestration. *U.S. Geological Survey Open-File Report 2015*, 1071, 19 p.
- VON SOLMS, N., MICHELSEN, M. L. & KONTOGEOORGIS, G. M. 2003. Computational and Physical Performance of a Modified PC-SAFT Equation of State for Highly Asymmetric and Associating Mixtures. *Industrial & Engineering Chemistry Research*, 42, 1098-1105.
- VOUTSAS, E., PERAKIS, C., PAPPA, G. & TASSIOS, D. 2007. An evaluation of the performance of the Cubic-Plus-Association equation of state in mixtures of non-polar, polar and associating compounds: Towards a single model for non-polymeric systems. *Fluid Phase Equilibria*, 261, 343-350.
- WALTER G. CHAPMAN, G. J., KEITH E. GUBBINS 1988. Phase equilibria of associating fluids. *Molecular Physics*, 65, 1057-1079.
- WANG, P., ANDERKO, A. & YOUNG, R. D. 2002. A speciation-based model for mixed-solvent electrolyte systems. *Fluid Phase Equilibria*, 203, 141-176.
- WERTHEIM, M. S. 1984a. Fluids with highly directional attractive forces. I. Statistical thermodynamics. *Journal of Statistical Physics*, 35, 19-34.
- WERTHEIM, M. S. 1984b. Fluids with highly directional attractive forces. II. Thermodynamic perturbation theory and integral equations. *Journal of Statistical Physics*, 35, 35-47.
- WERTHEIM, M. S. 1986a. Fluids with highly directional attractive forces. III. Multiple attraction sites. *Journal of Statistical Physics*, 42, 459-476.
- WERTHEIM, M. S. 1986b. Fluids with highly directional attractive forces. IV. Equilibrium polymerization. *Journal of Statistical Physics*, 42, 477-492.
- WHITSON, C. H. & MICHELSEN, M. L. 1989. The negative flash. *Fluid Phase Equilibria*, 53, 51-71.
- WOOD, J. R. 1976. Thermodynamics of brine-salt equilibria — II. The system NaCl-KCl-H₂O from 0 to 200°C. *Geochimica et Cosmochimica Acta*, 40, 1211-1220.
- XU, T., SONNENTHAL, E., SPYCHER, N. & PRUESS, K. 2006. TOUGHREACT—A simulation program for non-isothermal multiphase reactive geochemical transport in variably saturated geologic media: Applications to geothermal injectivity and CO₂ geological sequestration. *Computers & Geosciences*, 32, 145-165.
- XU, T., SPYCHER, N., SONNENTHAL, E., ZHANG, G., ZHENG, L. & PRUESS, K. 2011. TOUGHREACT Version 2.0: A simulator for subsurface reactive transport

- under non-isothermal multiphase flow conditions. *Computers & Geosciences*, 37, 763-774.
- YABUSAKI, S. B., FANG, Y., WILLIAMS, K. H., MURRAY, C. J., WARD, A. L., DAYVAULT, R. D., WAICHLER, S. R., NEWCOMER, D. R., SPANE, F. A. & LONG, P. E. 2011. Variably saturated flow and multicomponent biogeochemical reactive transport modeling of a uranium bioremediation field experiment. *Journal of Contaminant Hydrology*, 126, 271-290.
- YAN, W. & STENBY, E. H. 2012. On multiphase negative flash for ideal solutions. *Fluid Phase Equilibria*, 322–323, 41-47.
- YAN, W. & STENBY, E. H. 2014. On solving the Rachford-Rice equation with higher order methods. *Fluid Phase Equilibria*, 363, 290-292.
- YUAN, M., MOSLEY, J. & HYER, N. 2001. Mineral Scale Control in a CO₂ Flooded Oilfield, SPE-65029-MS. *SPE International Symposium on Oilfield Chemistry*. Houston, Texas, USA: Society of Petroleum Engineers.
- YUAN, M., SMITH, J. K., COOLEY, C. & WILLIAMSON, D. A. 2004. Effective Mineral Scale Control in Canyon Express, Gulf of Mexico, SPE-87429-MS. *6th International Symposium on Oilfield Scale*. Aberdeen, United Kingdom: Society of Petroleum Engineers.
- ZEMAITIS, J. F. 1980. Predicting Vapor-Liquid-Solid Equilibria in Multicomponent Aqueous Solutions of Electrolytes. *Thermodynamics of Aqueous Systems with Industrial Applications*. Washington, DC, USA: American Chemical Society.
- ZHANG, P., ALLAN, K. & HUGH, B. 2015. Selection of Calcium Carbonate Scale Critical Values for Deepwater Production. Society of Petroleum Engineers.
- ZHU, C., HU, F. Q. & BURDEN, D. S. 2001. Multi-component reactive transport modeling of natural attenuation of an acid groundwater plume at a uranium mill tailings site. *Journal of Contaminant Hydrology*, 52, 85-108.
- ZIRRAHI, M., AZIN, R., HASSANZADEH, H. & MOSHFEGHIAN, M. 2010. Prediction of water content of sour and acid gases. *Fluid Phase Equilibria*, 299, 171-179.
- ZIRRAHI, M., AZIN, R., HASSANZADEH, H. & MOSHFEGHIAN, M. 2012. Mutual solubility of CH₄, CO₂, H₂S, and their mixtures in brine under subsurface disposal conditions. *Fluid Phase Equilibria*, 324, 80-93.
- ZULUAGA, E., EVANS, P., NESOM, P., SPRATT, T. & DANIELS, E. 2011. Technical Evaluations to Support the Decision to Reinject Produced Water. *SPE Production & Operations*, 26, 128-139.

9. Appendix

Solving the aqueous non-linear system of equations in reduced space

The following is a reduction technique to solve the aqueous nonlinear system of equations in reduced space.



Charge balance equation:

$$C_0 = 2m_{1,0} + 2m_{2,0} + z_0 - w_0 - x_{2,0} - 2x_{3,0} - y_{2,0} - 2y_{3,0} - v_{2,0} = 0$$

$$C = 2m_1 + 2m_2 + z - w - x_2 - 2x_3 - y_2 - 2y_3 - v_2 = 0$$

Hence,

$$C_0 = 2(m_1 + m_2) + z - w - x_2 - 2x_3 - y_2 - 2y_3 - v_2 \quad (9.10)$$

Mass balance equations:

$$\text{S: } x_{t,0} = x_1 + x_2 + x_3 + x_4 \quad (9.11)$$

$$\text{C: } y_{t,0} = y_1 + y_2 + y_3 + y_4 + y_5 \quad (9.12)$$

$$\text{Fe: } m_{1,0} = m_1 + x_4 + y_5 \quad (9.13)$$

$$\text{Ca: } m_{2,0} = m_2 + y_4 \quad (9.14)$$

$$\text{HA: } v_{t,0} = v_1 + v_2 \quad (9.15)$$

From Equations (9.2) and (9.3) I have:

$$y_1 = \frac{1}{K_{C1}} y_2 z \quad (9.16)$$

$$y_3 = K_{C2} \frac{y_2}{z} \quad (9.17)$$

Then,

$$\begin{aligned} y_1 + y_2 + y_3 &= \left(\frac{1}{K_{C1}} z + 1 + K_{C2} \frac{1}{z} \right) y_2 \\ \text{If } g_C &= \frac{1}{K_{C1}} z + 1 + K_{C2} \frac{1}{z} \text{ then} \\ y_1 + y_2 + y_3 &= g_C y_2 \end{aligned} \quad (9.18)$$

From Equations (9.4) and (9.5) I have:

$$x_1 = \frac{1}{K_{S1}} x_2 z \quad (9.19)$$

$$x_3 = K_{S2} \frac{x_2}{z} \quad (9.20)$$

Then,

$$x_1 + x_2 + x_3 = \left(\frac{1}{K_{S1}} z + 1 + K_{S2} \frac{1}{z} \right) x_2$$

If $g_S = \frac{1}{K_{S1}} z + 1 + K_{S2} \frac{1}{z}$ then

$$x_1 + x_2 + x_3 = g_S x_2 \quad (9.21)$$

From Equations (9.11) and (9.21) I have:

$$x_4 = x_{t,0} - g_S x_2 \quad (9.22)$$

Also from Equation (9.13) I have:

$$x_4 = m_{1,0} - m_1 - y_5 \quad (9.23)$$

Combining Equations (9.7) and (9.9), I obtain:

$$\frac{K_{C4}}{y_3} = \frac{K_{S3}}{x_3} \quad (9.24)$$

Then, combining Equations (9.17) and (9.20) with Equation (9.24), I obtain:

$$x_2 = \frac{K_{S3} K_{C2}}{K_{S2} K_{C4}} y_2$$

If $\kappa = \frac{K_{S3} K_{C2}}{K_{S2} K_{C4}}$ then

$$x_2 = \kappa y_2 \quad (9.25)$$

Combining Equations (9.4) and (9.17) I obtain:

$$m_1 = \frac{K_{C4} z}{K_{C2} y_2} \quad (9.26)$$

Also, combining Equations (9.3) and (9.8) I obtain:

$$m_2 = \frac{K_{C3} z}{K_{C2} y_2} \quad (9.27)$$

From Equations (9.8) and (9.14) I have:

$$y_4 = m_{2,0} - \frac{K_{C3} z}{K_{C2} y_2} \quad (9.28)$$

Combining Equations (9.13), (9.22) and (9.26) I obtain:

$$y_5 = m_{1,0} - \frac{K_{C4} z}{K_{C2} y_2} - (x_{t,0} - g_s x_2) \quad (9.29)$$

From Equations (9.11) and (9.23) I have:

$$\begin{aligned} x_{t,0} &= x_1 + x_2 + x_3 + m_{1,0} - m_1 - y_5 \\ x_{t,0} &= g_s x_2 + m_{1,0} - \frac{K_{C4} z}{K_{C2} y_2} - y_5 \end{aligned} \quad (9.30)$$

Considering that $y_{t,0} = g_c y_2 + y_4 + y_5$ and adding $x_{t,0}$ to $y_{t,0}$ yields:

$$\begin{aligned} x_{t,0} + y_{t,0} &= g_s x_2 + m_{1,0} - \frac{K_{C4} z}{K_{C2} y_2} + g_c y_2 + m_{2,0} - \frac{K_{C3} z}{K_{C2} y_2} \Leftrightarrow \\ \Leftrightarrow g_c y_2 + \kappa g_s y_2 + (m_{1,0} + m_{2,0}) - (x_{t,0} + y_{t,0}) - \frac{z}{y_2} \frac{K_{C3} + K_{C4}}{K_{C2}} &= 0 \end{aligned}$$

If $\alpha_1 = (m_{1,0} + m_{2,0}) - (x_{t,0} + y_{t,0})$ then

$$g_c y_2 + \kappa g_s y_2 + \alpha_1 - \frac{z}{y_2} \frac{K_{C3} + K_{C4}}{K_{C2}} = 0 \quad (9.31)$$

Equation (9.31) is the Newton-Raphson (NR) working equation to be solved for z . The expression to calculate y_2 is derived below.

From Equations (9.25) and (9.20) I obtain:

$$-x_2 - 2x_3 = -\kappa y_2 - 2 \frac{K_{S2}}{z} \kappa y_2 = -\kappa \left(1 + 2 \frac{K_{S2}}{z}\right) y_2 \quad (9.32)$$

From Equations (9.13) and (9.14) I obtain:

$$m_1 + m_2 = m_{1,0} - x_4 - y_5 + m_{2,0} - y_4$$

From Equations (9.22) and (9.25) I have:

$$x_4 = x_{t,0} - \kappa g_S y_2$$

Also, from Equations (9.12) and (9.18) I have:

$$y_4 + y_5 = y_{t,0} - y_2 g_C$$

Then

$$m_1 + m_2 = (m_{1,0} + m_{2,0}) - (x_{t,0} + y_{t,0}) + (\kappa g_S + g_C) y_2$$

If $\alpha_1 = (m_{1,0} + m_{2,0}) - (x_{t,0} + y_{t,0})$ then

$$m_1 + m_2 = \alpha_1 + (\kappa g_S + g_C) y_2 \quad (9.33)$$

Combining Equations (9.1), (9.10), (9.32), and (9.33), and after some algebraic manipulation, I arrive to the following expression for y_2 :

$$y_2 = \frac{C_0 - 2\alpha_1 - \left(z - \frac{K_w}{z}\right)}{2\kappa g_S + 2g_C - \kappa \left(1 + 2 \frac{K_{S2}}{z}\right) - \left(1 + 2 \frac{K_{C2}}{z}\right)} \quad (9.34)$$

After finding z , the remaining variables can be found by back substituting using the equations above.